

UNIVERSITY OF CALGARY

Engineered impurity-doped materials for Quantum Information

Processing applications — nano-structures and disordered materials

by

Thomas Lutz

A THESIS

SUBMITTED TO THE FACULTY OF GRADUATE STUDIES

IN PARTIAL FULFILMENT OF THE REQUIREMENTS FOR THE

DEGREE OF DOCTOR OF PHILOSOPHY

GRADUATE PROGRAM IN PHYSICS AND ASTRONOMY

CALGARY, ALBERTA

DECEMBER, 2017

©Thomas Lutz 2017

Abstract

In this thesis we explore various ways to extend population lifetimes and coherence times of solid-state emitters. We focus on rare-earth-ion doped host materials and silicon vacancy centers in diamond, both of which are used for applications in quantum information processing and quantum communications. Enhanced lifetimes and coherence times would improve the performance of these applications.

One approach investigates the possibility to suppress lattice vibrations that cause decoherence and population relaxation by engineering the phonon density of states through nano-structuring of the emitter's host material. Towards this end we study different materials and methods to obtain the desired nano-materials. Using various optical spectroscopic methods, we show that population dynamics can indeed be influenced by modifying the structure of the surrounding host material. However, we also find that the employed fabrication and synthesis methods often induce crystal damage that, in turn, degrades spectroscopic properties.

As a second approach, we study rare-earth-ions in disordered host materials. Detailed spectroscopic characterizations are presented and we show with the example of an erbium doped fiber that such materials can indeed feature better properties, specifically

longer population lifetimes, than the commonly used bulk crystals. We found optimal operation parameters for the erbium doped fiber which made it possible to use this medium for successful proof of principle experiments demonstrating a multimode quantum memory that operates within the convenient telecom band (around 1550 nm wavelength).

Besides increasing the fundamental knowledge, the results of the studies presented in this thesis are highly relevant for the fields of quantum communications and quantum information processing since nano-structured materials are beginning to be investigated for on-chip implementations of various applications such as quantum memories and quantum gates. In addition, we found that population dynamics driven by detrimental lattice vibrations can indeed be modified in small powder materials and thus, with improved fabrication techniques, the complete suppression of lattice vibrations should be possible, benefiting a plethora of applications.

Preface

Below is a list of papers that are included in this thesis. Papers are listed according to the order in which they are introduced.

- **Paper 1:** "Modification of phonon processes in nano-structured rare-earth-ion-doped crystals" T. Lutz, L. Veissier, C. W. Thiel, R. L. Cone, P. E. Barclay, and W. Tittel, Phys. Rev. A **94**, 013801 (2016)
- **Paper 2:** "Effects of fabrication methods on spin relaxation and crystallite quality in rare-earth-ion doped powders studied using spectral hole burning" T. Lutz, L. Veissier, C. W. Thiel, P. J. T. Woodburn, R. L. Cone, P. E. Barclay, and W. Tittel, Science and Technology of Advanced Materials **17**, 63-70 (2015)
- **Paper 3:** "Effects of mechanical processing and annealing on optical coherence properties of $\text{Er}^{3+}:\text{LiNbO}_3$ powders" T. Lutz, L. Veissier, C. W. Thiel, P. J. T. Woodburn, R. L. Cone, P. E. Barclay, and W. Tittel, J. Lumin **191**, 2-12 (2017)
- **Paper 4:** "Quadratic Zeeman effect and spin-lattice relaxation of $\text{Tm}^{3+}:\text{YAG}$

at high magnetic fields” L. Veissier, C. W. Thiel, T. Lutz, P. E. Barclay, W. Tittel, and Rufus L. Cone, Phys. Rev. B **94**, 205133 (2016)

- **Paper 5:** ”Modification of relaxation dynamics in $\text{Tb}^{3+}:\text{Y}_3\text{Al}_5\text{O}_{12}$ nanopowders” T. Lutz, L. Veissier, P. J. T. Woodburn, R. L. Cone, P. E. Barclay, W. Tittel, and C. W. Thiel, submitted to Phys. Rev. B (2016)
- **Paper 6:** ”Efficient and long-lived Zeeman-sublevel atomic population storage in an erbium-doped glass fiber” E. Saglamyurek, T. Lutz, L. Veissier, M. P. Hedges, C. W. Thiel, R. L. Cone, and W. Tittel, Phys. Rev. B (R) **92**, 241111 (2015)
- **Paper 7:** ”Optical decoherence and spectral diffusion in an erbium-doped silica glass fiber featuring long-lived spin sublevels” L. Veissier, M. Falamarzi, T. Lutz, E. Saglamyurek, C. W. Thiel, R. L. Cone, and W. Tittel, Phys. Rev. B **94**, 195138 (2016)

Acknowledgements

First I would like to thank my supervisors, professors Wolfgang Tittel and Paul Barclay, for making this research possible, for their guidance and for all their support and availability during the years of my Ph.D. There were many times when their advice and fresh ideas resulted in new progress. The work, presented in this thesis, would also not have been possible without Charles Thiel and Lucile Veissier, who were working together with me for countless hours — and nights — and whose knowledge and ideas were invaluable for the achieved success. During all the time in Calgary, I was supported a lot by the whole QC2 group and the group of the Barclay Lab; many fruitful discussions lead to new approaches and solutions. Furthermore, I would like to thank all the people who read my thesis and gave me their feedback as well as Simon Trudel and his group for the help with powder syntheses.

Without the huge support of my whole family, the stay in Canada would not have been possible. I would like to thank them and especially Andrea Araya for being with me during the many happy moments but also for the tireless encouragement, support and motivation during the challenging times of this journey.

Contents

1. Background	1
1.1. Introduction	1
1.2. Rare-earth-ions and their applications	4
1.3. Spectral tailoring and the atomic frequency comb quantum memory .	7
2. Light-matter interaction	12
2.1. Rabi oscillations	12
2.2. Maxwell-Bloch equations	14
2.3. Jaynes Cumings model	15
3. Spectroscopic tools and spectral tailoring	17
3.1. Spectral hole burning	17
3.2. Coherence measurements	22
3.2.1. Two-pulse photon echo	22
3.2.2. Spectral diffusion and three- pulse photon echo	24
3.2.3. Free-induction decay	26

4. Spin lattice relaxation	28
4.1. Orbach theory	29
4.1.1. Direct-phonon process	30
4.1.2. Two-phonon processes	33
5. Phonon suppression in engineered materials	37
5.1. Paper 1: Modification of phonon processes in nanostructured rare-earth-ion-doped crystals	38
5.1.1. Summary	38
5.1.2. Introduction	40
5.1.3. Phonon restriction in Er:Y ₂ SiO ₅	42
5.1.3.1. Restriction in small powder materials	47
5.1.3.2. Restriction in phononic crystals	50
5.1.4. Conclusion	52
5.2. Powder fabrication methods	61
5.2.1. Mechanical processing	61
5.2.2. Chemical synthesis	62
5.3. Paper 2: Effects of fabrication methods on spin relaxation and crystallite quality in rare-earth-ion doped powders studied using spectral hole burning	67
5.3.1. Summary	67
5.3.2. Introduction	70

5.3.3.	Experiment	71
5.3.3.1.	Tm:YAG	71
5.3.3.2.	Spectral hole burning	72
5.3.3.3.	Bulk single crystal reference	73
5.3.4.	Results	74
5.3.4.1.	Crushing and ball milling	75
5.3.4.2.	Effects of annealing	78
5.3.4.3.	Comparison of high- and low-energy ball-milling meth- ods	79
5.3.4.4.	Direct chemical synthesis	82
5.3.5.	Discussion of different characterization methods	84
5.3.6.	Conclusions and Outlook	86
5.4.	Paper 3: Effects of mechanical processing and annealing on optical coherence properties of $\text{Er}^{3+}:\text{LiNbO}_3$ powders	95
5.4.1.	Summary	95
5.4.2.	Introduction	98
5.4.3.	Sample preparation	102
5.4.4.	Optical coherence lifetime measurements	109
5.4.4.1.	Two pulse photon echoes	111
5.4.4.2.	Echo decays in powders of randomly orientated crys- tallites	112
5.4.4.3.	Magnetic field dependence of coherence lifetimes . . .	116
5.4.4.4.	Spectral hole burning	119

5.4.4.5.	Free induction decay and spectral diffusion	124
5.4.5.	Conclusion	128
5.4.6.	Acknowledgments	130
5.5.	Identification and suppression of the direct-phonon process	143
5.6.	Paper 4: Quadratic Zeeman effect and spin-lattice relaxation of Tm ³⁺ :Y ₃ Al ₅ O ₁₂ at high magnetic fields	143
5.6.1.	Summary	144
5.6.2.	Introduction	147
5.6.3.	Quadratic Zeeman shift	149
5.6.3.1.	Theoretical background	149
5.6.3.2.	Measurements of the inhomogeneous line	153
5.6.3.3.	Magnetic field strength dependence	153
5.6.3.4.	Orientation dependence	155
5.6.4.	Nuclear spin-state lifetimes	157
5.6.4.1.	Orientation dependence	158
5.6.4.2.	Spin-lattice relaxation	159
5.6.4.3.	Temperature dependence	160
5.6.4.4.	Magnetic field dependence at 1.6 K	161
5.6.4.5.	Magnetic field dependence at 4 K	161
5.6.4.6.	Model	162
5.6.5.	Conclusion	165
5.6.6.	Acknowledgments	166

5.7. Paper 5: Modification of relaxation dynamics in $\text{Tb}^{3+}:\text{Y}_3\text{Al}_5\text{O}_{12}$ nanopow-	
ders	177
5.7.1. Summary	177
5.7.2. Introduction	182
5.7.3. Experimental Details	184
5.7.4. Time Resolved Fluorescence Measurements	187
5.7.5. Measurement of temperature dependent population re-distribution	195
5.7.6. Conclusion	197
5.7.7. Acknowledgements	198
5.7.8. APPENDIX A: Powder characterization	198
5.7.9. APPENDIX B: Spectroscopic investigations of powder quality	202
5.7.10. APPENDIX C: Local temperature measurement	203
5.8. Silicon vacancy centres in diamond	212
5.9. Phonon suppression in silicon vacancy centers in diamond	213
5.9.1. Resonant interaction	216
5.9.2. Orbital state lifetime measurements	218

6. Effects of spin inhomogeneity in disordered materials on lifetimes and coherence times 222

6.1. Paper 6: Efficient and long-lived Zeeman-sublevel atomic population	
storage in an erbium-doped glass fiber	224
6.1.1. Summary	224
6.1.2. Introduction	228

6.1.3.	Hole burning mechanism and limiting processes	231
6.1.4.	Concentration dependence	236
6.1.5.	Conclusion	238
6.2.	Coherence limiting two-level systems	245
6.3.	Paper 7: Optical decoherence and spectral diffusion in an erbium-doped silica glass fiber featuring long-lived spin sublevels	248
6.3.1.	Summary	248
6.3.2.	Introduction	251
6.3.3.	Experimental details	253
6.3.4.	Two-pulse photon echo measurements – analysis and model . .	254
6.3.5.	Temperature and magnetic field dependence of the effective homogeneous linewidth	258
6.3.5.1.	Spectral diffusion model	261
6.3.6.	Three-pulse photon echo measurements – spectral diffusion at large timescales	264
6.3.7.	Conclusion	265
6.3.8.	Acknowledgments	266
7.	Conclusion	271
8.	Outlook	274
A.	Copyright permissions	276
A.1.	Papers 1,4,5,6,7	276

A.2. Paper 2	276
A.3. Paper 3	278
A.4. Permission of co-authors	278

List of Tables

5.1. Hole widths (Γ) (bold fonts indicate visible side holes), and lifetimes (T_a) of all measured materials at 1.6 K and $B = 1$ T. *ball milled . . .	75
5.2. Powders characterized in the manuscript and their fabrication methods.	105
5.3. Parameters from fitting the experimental data shown in Fig. 5.17 by Eq. 5.12. For all samples, the value of Γ_{\max} was fixed to 1 MHz and the parameter Γ_0 was constrained to be larger or equal than minimum bulk value ($\Gamma_0 = 3$ kHz at 6 T), which lead to $\Gamma_0 = 3$ kHz.	117
5.4. Maximum effective absorption coefficient α_{eff} extracted from SHB measurements, as well as effective linewidths Γ_{eff} extracted from SHB (after a $T_w = 25 \mu\text{s}$), 2PE (heterodyne measurement for samples #3 to #6) and FID (after a $T_w = 5 \mu\text{s}$) measurements at $T = 1.6$ K and $B = 2$ T for different samples. When a double exponential decay was observed, as described in the main text, both decay values are listed. For the bulk crystal, the magnetic field and light polarization were parallel to the c -axis ($\mathbf{B} \parallel \mathbf{E} \parallel c$).	120

5.5.	Nuclear spin-state lifetimes for ions at different sites in a magnetic field of 6 T and at 1.6 K in 1 % Tm ³⁺ :YAG. Each measurement is labeled and displayed in Fig. 5.26.	159
5.6.	Parameters obtained from the 2-dimensional fit of the experimental spin relaxation rate data by Eq. 5.23.	163
6.1.	Parameters for Eq. 6.8 to fit the experimental data, with α_1 in 10^9 s^{-2} , α_2 in $\text{Hz T}^{-1} \text{ K}^{-1}$ and α_3 in Hz T^{-4}	234
6.2.	Parameters resulting from the 2-dimensional fit of Eq. 6.8 to $\Gamma_{\text{eff}}(B, T)$	262

List of Figures

1.1.	a) Radial probability for the electronic wavefunction for the example of Gd^+ , reproduced from [1]. The electrons of the 4f shell are shielded from the environment by the electrons of the 5s/p shells. b) Illustration of the various shells and their filling in case of REIs.	5
1.2.	Inhomogeneously broadened absorption line Γ_{inhom} composed of homogeneously broadened absorption lines Γ_{hom} of individual ions in a different crystal environment. Figure reproduced from [2].	6
1.3.	Energy levels of the Er^{3+} isotopes in a solid. Quantum numbers as described in the main text with m_S the electron spin projection and m_I the nuclear spin projection.	7
1.4.	Generation of an atomic frequency comb with splitting Δ via frequency selective spectral hole burning on the inhomogeneously broadened absorption line Γ_{inh}	8

3.1.	Experimental hole burning sequence, frequency-selective optical pumping moves population from $ g_0\rangle$ to $ a\rangle$. When the hole is read by a laser pulse that is swept in frequency over the extent of the hole this manifests itself in decreased absorption.	18
3.2.	a) Holeburning on an ensemble without inhomogeneous broadening. Two antiholes arise since population is transferred into the upper ground-state. A sidehole arises since the other transition originating from the same level as the pump is also depleted. b) Due to the inhomogeneous broadening the pump (vertical arrows) is simultaneously resonant with various transitions resulting in a symmetric hole-spectrum. Figure reproduced from [3].	21
3.3.	Pulse sequence and phase evolution in a two-pulse photon echo. Diverging lines in the phase evolution correspond to ions affected by a decoherence inducing process. The more ions are affected by such processes, the smaller the echo becomes. Reproduced from [4].	23
3.4.	Pulse sequence in a three-pulse photon echo. See main text for a detailed description.	25
3.5.	a) Pulse sequence for a delayed FID measurement together with the signal observed on the Photodiode b).	27
4.1.	Different phonon processes facilitating transitions between $ a\rangle$ and $ g_0\rangle$, each described in detail in the main text.	30

5.1.	Magnetic field dependence of the spin-flip rate. As described by Equation 5.2, the total rate R (solid red line) is composed of a constant term R_0 (dotted blue line), a spin flip-flop term (green dashed line) and a direct phonon term (orange dash-dotted line), dominant above 1 T. We assume $T = 3$ K, $g = 14$, $R_0 = 0.1$ kHz, $\alpha_D = 5 \times 10^{-4}$ kHz/T ⁵ and $\alpha_{ff} = 2$ kHz.	43
5.2.	Effect of the direct phonon process suppression on the effective homogeneous linewidth. As described by Equation 5.4, Γ_{eff} after $t = 10 \mu\text{s}$ is shown as a function of the magnetic field strength in the presence (blue dashed line) and in the absence (red solid line) of the direct phonon process. We assume the same parameters as in Fig. 5.1 and, in addition, $\Gamma_{\text{max}} = 5 \times 10^{10}$ Hz, $\Gamma_0 = 10$ kHz.	45
5.3.	Simulated phonon density of states in a Y_2SiO_5 nanoparticle with a diameter of 12 nm. Each eigenmode of the spherical particle is represented by a Lorentzian with a width of 1 GHz.	48
5.4.	(a) Unit cell of the proposed phononic crystal structure. The radius of the island is 9.5 nm, the width of the arms is 5 nm, and their length 5 nm. This structure is 7 nm thick. (b) Band structure of the phononic crystal in (a). The band gap (shaded grey) around the center frequency of 178 GHz is clearly visible. (c) Reciprocal lattice [59] showing the points traversed in the band structure.	51
5.5.	Flow diagram of the sol-gel synthesis used to produce YAG powders. For a detailed description see main text.	64

5.6. Schematic of a typical coprecipitation synthesis. The target material forms in the solution of source materials after addition of a base. . . .	65
5.7. Schematic illustrating the process of combustion synthesis with the example of LiNbO_3 . The process is described in detail in the main text.	67
5.8. a) Level structure of Tm:YAG without and with an applied magnetic field. b) Hole burning spectrum of the 1% Tm:YAG bulk crystal together with a fit (red line).	72
5.9. XRD spectra of selected powders together with the reference spectrum (JCPDS # 30-0040) of YAG. a) Chemical synthesis, b) Crytur non-annealed, c) SMC low energy ball milled, d) SMC low energy ball milled and annealed.	76
5.10. SEM images and typical hole burning spectra of the powder obtained after ball-milling the bulk crystal from SMC for two days. a), c) before, and b), d) after annealing at 1400 °C for 4 hours.	88
5.11. a) SEM image of the 1% Tm:YAG powder provided by Crytur, and typical hole burning spectrum b) before and c) after annealing.	89
5.12. SEM image of the 1% Tm:YAG powder after 4 hours of high-energy planetary ball-milling.	89
5.13. SEM image of the synthesized 1% Tm:YAG powder.	90
5.14. Scanning electron microscope images of (a) powder #1 made from a 0.1% $\text{Er}^{3+}:\text{LiNbO}_3$ bulk crystal (SMC) by grinding with a mortar and pestle, (b) powder #2 ball-milled for only 30 min.	106

- 5.15. Scanning electron microscope images (a) powder #3 ball-milled and annealed at 900 C, and (b) powder #6 annealed up to 1100 C. . . . 107
- 5.16. (a) Orientation dependence of the effective linewidth Γ_{eff} in a 0.1% $\text{Er}^{3+}:\text{LiNbO}_3$ bulk crystal measured at $T = 1.6$ K and $B = 2$ T. The magnetic field orientation is rotated by an angle θ from the c -axis of the crystal. The inset shows an example echo intensity decay at $\theta = 0$ i.e. $\mathbf{B} \parallel c$, where the fit of Eq. 5.9 gives $\Gamma_{\text{eff}} = 1/\pi T_{\text{M}} = 3.1$ kHz. The red solid line is an empirical polynomial fit to the experimental $\Gamma_{\text{eff}}(\theta)$ data. (b) Decay of the echo area for the 0.1% $\text{Er}^{3+}:\text{LiNbO}_3$ reference powder. The dashed line corresponds to a fit of a sum of two exponential decays to the experimental data (black dots). The red solid line corresponds to a calculation of the expected decay in the powder due to the orientation dependence of Γ_{eff} in the bulk crystal. . 131
- 5.17. Magnetic field dependence of the effective homogeneous linewidth in 0.1% $\text{Er}^{3+}:\text{LiNbO}_3$ at $T = 3$ K for the bulk crystal (for $\mathbf{B} \parallel c$), the reference powder #1, and a powder ball-milled for 30 min. (powder #2).132
- 5.18. Hole burning spectrum in 0.1% $\text{Er}^{3+}:\text{LiNbO}_3$ (powder #1) at $T = 1.6$ K and $B = 2$ T. Zero detuning corresponds to 1531.882 nm in vacuum. 132
- 5.19. Typical background-subtracted FID decay of the reference powder #1 at $B = 3.9$ T, $T = 1.6$ K and waiting time $t_{\text{w}} = 5 \mu\text{s}$. Solid points are measured values and the solid line is a fit of the FID signal. The inset shows a magnification of the first $1 \mu\text{s}$ of the decay. 133

5.20. Effective homogeneous linewidths at a) $B = 2$ T and b) $B = 3.9$ T at $T = 1.6$ K as a function of the waiting time T_w measured using the delayed FID technique for powders #1, # 3 through #6 and for the bulk crystal. The solid lines are guides to the eye.	134
5.21. Orientation of the six different sites of Tm^{3+} ions in the YAG crystal lattice [14, 15]. Each parallelepiped represents the orientation of the local D_2 point symmetry for a subset of sites. The specific set of x , y , and z axes labeled in the diagram correspond to the local frame of site 1. In our experiment, the light propagates along $[1\bar{1}0]$ and the magnetic field is applied in the plane defined by $[110]$ and $[001]$, forming an angle θ with the $[111]$ axis. Because of the D_2 point symmetry of the sites, the electric transition dipole moment for the specific ground and excited states involved in the 793 nm optical transition is aligned along the local y axis. The gyromagnetic tensor γ_J orientation is also determined by the local frame.	149
5.22. Simplified energy level structure of $\text{Tm}^{3+}:\text{YAG}$, relevant for our study. Represented are the two lowest crystal field levels of the $^3\text{H}_6$ and $^3\text{H}_4$ multiplets [24, 25]. In an external magnetic field, the crystal field level energies vary as B^2 due to the quadratic Zeeman effect, with different coefficients for each level. As a consequence, the optical transition $^3\text{H}_6(1) \rightarrow ^3\text{H}_4(1)$, which has a zero-field frequency of ν_0 , is shifted by $\Delta(B)$. The frequency Δ_{CF} , corresponding to the transition between the two crystal field levels in the ground state, also varies as B^2	167

- 5.23. Inhomogeneous line of a 0.1 % Tm^{3+} :YAG crystal (a) at zero magnetic field and $T = 2$ K, and (b) with a 3 T magnetic field along $[111]$ and at $T = 5$ K. A narrowband laser probed the medium with $\mathbf{k} \parallel [\bar{1}\bar{1}0]$ and $\mathbf{E} \parallel [111]$ (see main text for definitions). The experimental points were fit by a Lorentzian function with a full width at half maximum $\Gamma_{\text{inh}} = 17$ GHz at zero magnetic field. The center frequency is $\nu_0 = 377868$ GHz, and the absorption coefficient is $\alpha_0 = 2.3 \text{ cm}^{-1}$. Because of polarization imperfections, the probe light slightly interacted with ions at sites 2, 4, and 6 that do not experience any shift for $\mathbf{B} \parallel [111]$. In consequence, the model includes two Lorentzian functions for $B = 3$ T. The shift Δ of the strongest line corresponding to ions at sites 1, 3, and 5 is 42.7 GHz. 168
- 5.24. Magnetic field dependence of several inhomogeneous line properties of a 0.1 % Tm^{3+} :YAG crystal at $T = 5$ K and with $\mathbf{B} \parallel \mathbf{E} \parallel [111]$. (a) Frequency shift Δ as a function of the magnetic field strength B . The experimental points were fit by a quadratic function, giving a coefficient $\gamma_2 = 4.69 \pm 0.03 \text{ GHz/T}^2$. (b) Observed nonlinear increase in the inhomogeneous linewidth Γ_{inh} as a function of the magnetic field strength B . The experimental points were fit by a B^2 dependence, giving a broadening coefficient of 0.28 GHz/T^2 . (c) Observed nonlinear decrease in the integrated transition linestrength k as a function of the magnetic field strength B . The experimental points were fit by a B^2 dependence, giving a coefficient of $-1.3 \text{ GHz cm}^{-1} \text{ T}^{-2}$ 169

- 5.25. Transmission spectra for various angles θ of magnetic field with respect to the $[111]$ crystal axis in the plane defined by the $[111]$ and $[\bar{1}\bar{1}2]$, of a 1% Tm^{3+} :YAG crystal at 1.6 K. The strength of the applied magnetic field was 6 T. The polarization of the probing light was (a) along $[111]$, leading to interaction with ions of sites 1, 3, and 5, and (b) along $[\bar{1}\bar{1}2]$ leading to interaction with ions of sites 4 and 6. 170
- 5.26. Frequency shift Δ as a function of the magnetic field angle θ at $B = 6$ T for ions of the site 1 (blue), sites 3 and 5 (yellow), and sites 4 and 6 (green), extracted from the transmission spectra shown in Fig. 5.25. The experimental points are presented together with the expected values (solid lines). The points labeled by letters (A-E) identify configurations for which the spin-state lifetime was measured (see Table 5.5) 171
- 5.27. Spin-lattice relaxation rate as a function of the temperature T for $B = 3$ T in 0.1% Tm :YAG for ions of sites 1, 3, and 5. The magnetic field and the light polarization were along $[111]$, and ions of sites 1, 3, and 5 were thus optically and magnetically equivalent. The experimental points were fit by Eq. 5.23 with the parameters given in Table 5.6. . . 171
- 5.28. Spin-lattice relaxation rate as a function of the magnetic field strength B at $T = 1.6$ K in 0.1% Tm :YAG for ions of sites 1, 3, and 5. The magnetic field and the light polarization were along $[111]$. Ions of sites 1, 3, and 5 were optically and magnetically equivalent. The experimental points were fit by Eq. 5.23 with the parameters given in Table 5.6. . . 172

5.29. Spin-lattice relaxation rate as a function of the magnetic field strength B at $T = 4$ K in 0.1% Tm:YAG for ions of sites 1, 3, and 5. The magnetic field and the light polarization were along [111], so ions of sites 1, 3, and 5 were optically and magnetically equivalent. The experimental points were fit by Eq. 5.23 with the parameters given in Table 5.6. . . .	172
5.30. Relevant energy levels of $\text{Tb}^{3+}:\text{Y}_3\text{Al}_5\text{O}_{12}$ (vertical axis not to scale) for the measurement of population relaxation between the first two crystal-field levels within the $^5\text{D}_4$ excited-state manifold. A pulsed laser excites the ions from the $^7\text{F}_6 a$ ground state to the $^5\text{D}_4 f$ excited state, from where they decay rapidly into $^5\text{D}_4 a$ and b . The resulting fluorescence due to the four $^5\text{D}_4 a/b \rightarrow ^7\text{F}_5 a/b$ transitions are collected, spectrally resolved, and then analyzed.	185
5.31. Fluorescence spectra at 5 K of (a) a 40 nm diameter powder and (b) a 500 nm diameter powder (synthesized via method 1). Each spectrum (black dots) is fit with the sum of four identical Lorentzian lines with the same pairwise energy splitting Δ (Δ'). For $d = 40$ nm the width is 53 GHz and Δ is 40 GHz, and for $d = 500$ nm the width is 13 GHz and Δ' is 39 GHz.	188
5.32. Fluorescence decays $^5\text{D}_4 a \rightarrow ^7\text{F}_5 a$ (red dots) and $^5\text{D}_4 b \rightarrow ^7\text{F}_5 a$ (blue dots) at 1.5 K in large crystallites ($d = 500$ nm). The experimental points are fit with Eq. 5.27 (solid lines), resulting in $T_\alpha = 235 \mu\text{s}$ and $T_\beta = 4$ ms. Inset: relevant level structure and rates associated with the fluorescence decays (see definitions in the main text).	189

5.33. Amplitude ratio α/β obtained from an average of the fits of Eq. 5.27 to the four decays ${}^5\text{D}_4\ a, b \rightarrow {}^7\text{F}_5\ a, b$ as a function of average nanocrystal diameter d for powder 1 (red circles) and powder 2 (blue squares) at 1.5 K. Simulations are depicted using dashed lines. Note that the amplitude of the fast decay has been corrected for the partially overlapping lines as described in the main text. Inset: Characteristic time of the fast decay component as a function of nanocrystal diameter d	191
5.34. Ratio of population n_b/n_a as a function of temperature in the bulk crystal (black squares) and in nanocrystals from method 1 of average diameter $d = 72$ nm (blue triangles) and 40 nm (red dots). Solid lines are best fits using Eq. 5.29, and shaded areas represent uncertainties.	196
5.35. Microscope images of 1% $\text{Tb}^{3+}:\text{Y}_3\text{Al}_5\text{O}_{12}$ created using method 1 and annealed at 1400 C (a), or 900 C (b,c), and from method 2 annealed at 900 C (d). Panels (a,b,d) are SEM images, showing the size distribution of the nanocrystals. Panels (e) and (f) show XRD spectra of powders produced by method 1 and 2, respectively (solid blue lines), and the corresponding reference spectrum (JCPDS # 30-0040; red circles) for YAG. Panel (c) is a high-resolution TEM image showing the crystalline structure (narrow white lines), which can extend over several particles if they are agglomerated.	200
5.36. Particle size (d) dependence of the radiative lifetime of the ${}^5\text{D}_4\ a$ level for powders from method 1 (red circles) and powders from method 2 (blue squares). The solid line shows the expected dependence.	203

5.37. Particle-size-dependence of the inhomogeneous linewidth for powders from method 1 (red circles) and powders from method 2 (blue squares). Inset: Splitting Δ between the $^5\text{D}_4$ a/b levels versus particle size. The solid lines are guides to the eye.	204
5.38. Ratio n_2/n_1 of populations in the ground manifold $^7\text{F}_6$ b/a levels as a function of the temperature T_{set} read by the cryostat sensor for a bulk crystal (black dots) and nanocrystalline powder samples with di- ameters $d = 124 \pm 30$ nm and produced by method 1 (blue squares) and $d = 63 \pm 11$ nm, produced by method 2 (red triangles). The solid line is the fit to a Boltzmann distribution with $\Delta_g = 83.5$ GHz. Note that the large error bar for 3.2 K and $d = 124$ nm is caused by a large uncertainty of the fit to that particular absorption spectrum.	205
5.39. Relevant energy levels of the SiV center in diamond.	213
5.40. Vibrational density of states (DOS) simulations for nanopillars with varying diameter d on a bulk diamond substrate.	215
5.41. Scanning electron microscope images of the fabricated nano pillars. . .	216
5.42. Schematic of the setup used to probe SiV centers in diamond.	216
5.43. Photoluminescence scan across the four transitions of a SiV center in bulk diamond.	217

5.44. a) Time sequence of the two laser pulses used to extract the orbital state lifetime of a SiV center. b) Simplified energy level structure of the SiV. For lifetime measurements, population is excited from the ground state $ g_1\rangle$ (red arrow) and fluorescence from the two excited states $ e_{1/2}\rangle$ (blue arrows) is collected from the phonon sideband. c) Time-resolved fluorescence collected from the phonon sideband. The pump pulse leads to a population inversion in the ground states that manifests itself in a decreased fluorescence during the second pulse. Due to population relaxation $ g_2\rangle \rightarrow g_1\rangle$, the fluorescence during the probe pulse will increase with increasing spacing between the pulses τ .	220
5.45. Exemplary decay of the ratio A_1/A_2 for a SiV in bulk diamond. The population lifetime in the upper ground state $ g_2\rangle$ is extracted by a fit of Eq. 5.30.	221
5.46. Orbital state ($ g_2\rangle$) lifetime of SiV centers in nano-pillars of different diameters. Experimental data is displayed as blue dots, the red line shows the result of our simulations.	221
6.1. Spectral hole area as a function of the waiting time for $B = 500$ G and $T = 0.65$ K. The experimental data is fitted by the sum of two exponential decays with characteristic times $T_a = 1.32 \pm 0.09$ s and $T_b = 25.9 \pm 1.5$ s. The inset shows the fiber absorption profile at $T = 0.8$ K (dashed blue line) and the hole lifetime T_b for various wavelengths (black dots).	229

6.2.	Magnetic field dependent depth of a 200 MHz-wide hole normalized to the depths of a 100 MHz-wide hole at each field, which is not significantly affected by population transfer from an anti-hole. Please note that the absolute hole depth of a narrow hole decreases at $B > 0.06$ T due to decreasing lifetimes, as shown in Fig. 6.5 c). Experimental data is shown by black dots; simulated results are in red.	232
6.3.	Spin relaxation rate $1/T_a$ as a function of temperature at $B = 500$ G. The dashed lines correspond to the different terms of Eq. 6.8: the Er-Er coupling (blue dashed), the direct process (green dotted), and the Raman process (orange dashed dotted).	235
6.4.	Dependence of the rate $1/T_a$ on the magnetic field at $T = 0.8$ K. The solid line shows the theoretical prediction of Eq. 6.8 with the set of parameters in Table 6.2, and the dashed and dotted lines correspond to the individual terms (first term: blue dashed, second term: green dotted, third term: orange dashed dotted).	236
6.5.	a) Dependence of the rate $1/T_b$ on the magnetic field for fibers with different erbium doping concentrations and lengths. b) Absorption profiles of the three fibers. c) Hole depth as a function of magnetic field. All measurements are taken at 0.8 K, at 1532 nm for fibers 1 and 2, and at 1536 nm for fiber 3. Red: fiber 1 (190 ppm, 20 m), black: fiber 2 (200 ppm, 10 m), blue: fiber 3 (1200 ppm, 3 m).	237
6.6.	Schematic of a TLS with barrier height V_0 , well separation L and energy difference Δ	246

6.7.	Two-pulse photon echo peak intensity as a function of the time delay between the two excitation pulses at $T = 0.7$ K for $B = 0.05$ T (blue dots) and $B = 1$ T (yellow dots). The pulse sequence is shown in the inset. The experimental data are fitted by a single-exponential function (dashed lines) with characteristic decay constants $T_2 = 247 \pm 14$ ns and $T_2 = 396 \pm 16$ ns.	254
6.8.	Spectral diffusion processes in a rare-earth ion doped glass. The local environments of the optically probed Er^{3+} ions in the center of the grey circle are perturbed by either direct interaction with fluctuations in the state of neighboring TLS (depicted on the right-hand side), or interaction with fluctuations in the state of other Er^{3+} spins in the local environment driven by TLS or another Er^{3+} ion. Inset: double-well potential-energy structure of the TLS, with asymmetry energy Δ , barrier energy V_0 and well separation L	256
6.9.	Magnetic field dependence of the effective homogeneous linewidth Γ_{eff} at $T = 0.7 \pm 0.05$ K. The dashed lines shows the theoretical prediction of Eq. 6.8 with the set of parameters in Table 6.2.	259
6.10.	Temperature dependence of the effective homogeneous linewidth Γ_{eff} at $B = 0.05$ T and $B = 2$ T. The dashed lines shows the theoretical prediction of Eq. 6.8 with the set of parameters in Table 6.2.	260

6.11. Effective homogeneous linewidth as a function of t_{23} , derived from 3PPE measurements at $T = 0.76$ K at $B = 0.06$ T (empty circles) and $B = 2$ T (filled circles). The experimental data is fitted by Eq. 6.10 with $\gamma = 0.376$ MHz/decade and 0.410 MHz/decade at $B = 0.06$ T and 2 T respectively.	266
A.1. Part of the APS copyright agreement granting me permission to use papers 1,4,5,6,7 in my thesis.	276
A.2. Part of the Journal of Luminescence copyright agreement granting me permission to use paper 2 in my thesis.	277
A.3. Part of the STAM copyright agreement granting me permission to use paper 2 in my thesis.	278
A.4. Email (part 1) from Paul Barclay granting me permission to publish the papers of which he is a co-author.	280
A.5. Email (part 2) from Paul Barclay granting me permission to publish the papers of which he is a co-author.	281
A.6. Email (part 1) from Rufus Cone granting me permission to publish the papers of which he is a co-author.	282
A.7. Email (part 2) from Rufus Cone granting me permission to publish the papers of which he is a co-author.	283
A.8. Email from Mohsen Falamarzi granting me permission to publish the papers of which he is a co-author.	284

A.9. Email from Morgan Hedges granting me permission to publish the papers of which he is a co-author.	285
A.10. Email from Erhan Saglamyurek granting me permission to publish the papers of which he is a co-author.	286
A.11. Email (part 1) from Charles Thiel granting me permission to publish the papers of which he is a co-author.	287
A.12. Email (part 2) from Charles Thiel granting me permission to publish the papers of which he is a co-author.	288
A.13. Email (part 1) from Wolfgang Tittel granting me permission to publish the papers of which he is a co-author.	289
A.14. Email (part 2) from Wolfgang Tittel granting me permission to publish the papers of which he is a co-author.	290
A.15. Email from Lucile Veissier granting me permission to publish the pa- pers of which she is a co-author.	291
A.16. Email from Philip Woodburn granting me permission to publish the papers of which he is a co-author.	292

1. Background

1.1. Introduction

Large-scale quantum networks [5] are an auspicious replacement for today's internet, which is based on the transmission of bits, i.e. zeros and ones, encoded in strong light. In a quantum network, bits are replaced by quantum bits (qubits) [6], which can be in the usual states zero or one, but, unlike classical bits, also in an arbitrary superposition of zero and one. To transmit such qubits they are often encoded into single photons whereas for local processing and storage they are usually encoded in atoms [7].

A quantum network would have distinct advantages compared to its classical counterpart. First, it would allow one to connect distant quantum computers, which are currently being developed since they promise great improvement in computing performance. For example, quantum computer algorithms that can perform factoring [8] of large numbers and searching of databases [9] orders of magnitude faster compared to classical computers already exist. Furthermore, the ability to send qubits, encoded into photons, over long distances is a prerequisite to encrypt communica-

tion between remote parties with information-theoretic security using quantum key distribution (QKD) [10]. Thus, QKD is fundamentally safer than current encryption methods that are based on mathematical algorithms that are expected to be broken eventually (as detailed in the NIST Report on Post-Quantum Cryptography [11]). QKD relies on the fact that quantum states, and hence qubits, cannot be copied (no-cloning theorem [12]) since a quantum measurement has to obey the uncertainty relation [13]. However, it is this inability to create perfect copies of individual qubits that makes it challenging to transmit quantum information over long distances. As a direct consequence of the no-cloning theorem, simple amplification, as used by classical communication networks, is not possible. Therefore, other means of establishing long quantum links, for example quantum repeaters [14, 15], need to be developed.

The realization of large scale quantum networks requires the development of many individual quantum devices. A general problem that is inherently related to the quantum nature and limits the performance of all potential devices is decoherence, i.e. perturbations of the physical system (e.g. two energy levels of an atom) used to implement the qubit. Those perturbations are caused by its interactions with the environment. The main goal of the work presented in this thesis is to identify and engineer materials in which decoherence is suppressed and the lifetime of energy levels is enhanced. Specifically, we concentrate on the case of rare-earth-ion (REI) doped solid state materials (see chapter 1.2 and 6) and silicon vacancy centers in diamond (chapter 5.8).

Two different approaches are pursued. The first approach, presented in chapter 5, is to modify the properties of impurity-doped solid-state materials using nano-structuring. The target is to inhibit detrimental vibrations in the material that reduce coherence times and cause relaxation between energy levels. The development of the required nano-fabrication methods (chapter 5.2 and 5.9) together with our in-depth investigations of nano-scale structures and their properties using many different methods such as electron microscopes, x-ray diffraction and spectroscopic methods, presented in chapter 5.3.1, also directly benefits future on-chip implementation of possible quantum devices.

The second approach is to study to what extent disordered materials such as glass fibers can be employed for applications such as quantum memories or processors for quantum states; it is presented in chapter 6. Disordered materials should reduce the interaction between the doped impurities, which, in turn, will slow down relaxation rates compared to crystalline materials. We employ several spectroscopic tools (see chapter 3) to directly measure the relevant properties such as coherence lifetimes and relaxation rates and to benchmark the various materials.

New materials that show improved performance in terms of reduced decoherence rates and increased lifetimes of energy levels are beneficial for a plethora of applications. In this thesis we will focus on the fabrication and characterization of the mentioned materials and determine to what degree they can be used to implement an efficient quantum memory (chapter 1.3), one of the integral building blocks of a quantum repeater, based on impurity doped solid state materials. For nano-structured REI-

doped materials we find some signatures of the desired suppression of vibrational modes. Our detailed investigations of the transition from bulk to nano structures also showed that new, detrimental processes can arise during the fabrication and prevent the use of our materials in applications. However, the characterization of these effects, presented in this thesis, will facilitate future material development and lay the foundation for applications based on nano-structured REI materials. On the other hand, our results with impurity doped fibers present a first step to develop a material that can store quantum information at telecom wavelengths, i.e. around 1550 nm. Enabling such a material and implementing a quantum memory with it would have the distinct advantage that quantum networks could be directly implemented with fiber infrastructure that is already in place and currently used for classical communication.

1.2. Rare-earth-ions and their applications

REI-doped crystals have been studied for decades because of their unique spectroscopic properties [16, 4, 17]. For REI, the lifetimes T_1 of the excited states of the optical transitions within the $4f$ orbital are generally long ($> \mu s$) since those transitions are forbidden by selection rules that are only slightly broken by imperfect crystal symmetries. Furthermore, many properties derive benefit from the shielding of $4f$ -electrons by electrons occupying the $5s$ and $5p$ shells, as shown in Fig. 1.1. This results in typically narrow homogeneous linewidths that can reach the order of Hz for certain ion:host combinations such as $\text{Er}^{3+}:\text{Y}_2\text{SiO}_5$ [18] and $\text{Eu}^{3+}:\text{Y}_2\text{SiO}_5$ [19] at cryogenic temperatures. In general, the homogeneous linewidth is limited by

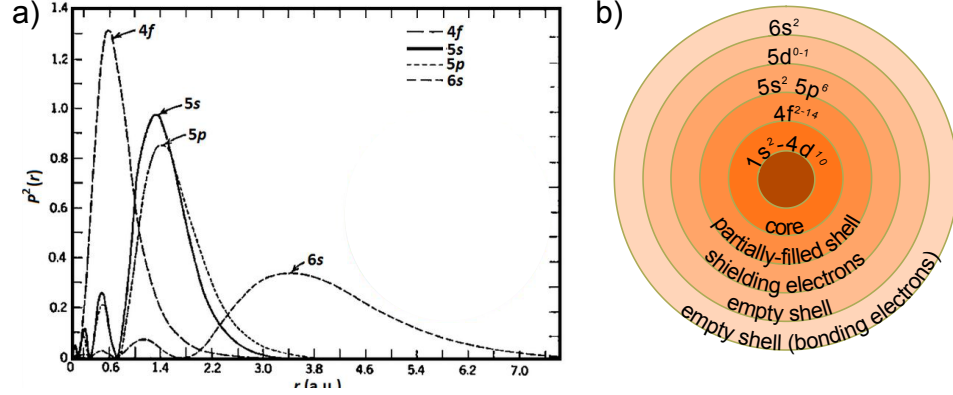


Figure 1.1.: a) Radial probability for the electronic wavefunction for the example of Gd^+ , reproduced from [1]. The electrons of the 4f shell are shielded from the environment by the electrons of the 5s/p shells. b) Illustration of the various shells and their filling in case of REIs.

dynamic processes that perturb the optical transition frequency between the ground- and excited state. Such processes happen even at very low temperatures. Due to their shielding, REI are less sensitive to these fluctuations in their environment, however, e.g. fluctuating strain fields caused by lattice vibrations, and magnetic coupling to neighboring spins still contribute to the homogeneous broadening. For REIs, the homogeneous linewidth Γ_h can approach its ultimate limit $\Gamma_h \geq 1/2\pi T_1$, which is determined by the excited state lifetime T_1 as required by the uncertainty relation.

Since every REI experiences a slightly different local environment in its host in terms of defects as well as stress, the crystal field interaction and thus the position of the homogeneously broadened optical transition is slightly different for each ion, as shown in Fig. 1.2.

The values of the various energy levels of a REI are governed by the following Hamil-

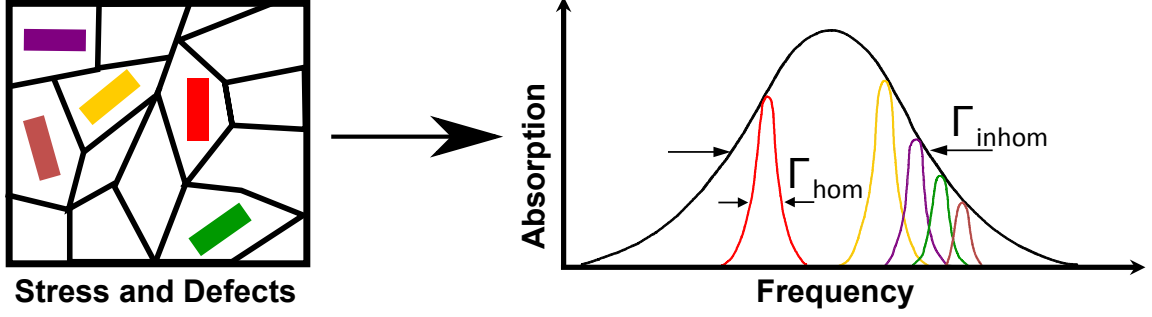


Figure 1.2.: Inhomogeneously broadened absorption line Γ_{inhom} composed of homogeneously broadened absorption lines Γ_{hom} of individual ions in a different crystal environment. Figure reproduced from [2].

tonian:

$$H = H_C + H_{SO} + H_{CF} + H_Q + H_{ZE} + H_{NZ} + H_{HF} + H_{SHF} \quad (1.1)$$

where H_C is the central field Hamiltonian and H_{SO} corresponds to the spin orbit coupling. These two terms make up the description of the free ion. H_{CF} is the crystal field Hamiltonian followed by the quadrupole interaction H_Q . The Zeeman interaction with an external magnetic field is given by H_{ZE} (electronic Zeeman interaction) and H_{ZN} (nuclear Zeeman interaction). Finally, the last two terms of Eq. 1.1 describe the hyperfine (H_{HF}) interaction caused by coupling of nuclear spins to spin and orbital angular momentum of the electrons and the superhyperfine interaction H_{SHF} that arises due to coupling of the REI to other nuclear spins in the host matrix. The individual energy levels of erbium in a solid state host are shown in Fig. 1.3. Each energy level is identified using a set of quantum nubers $^{2S+1}L_J$ with S the spin-, L the orbital angular momentum- and J the total angular momentum quantum number. From left to right, the interactions decrease in magnitude.

The ensemble of homogeneous absorption lines of all ions doped into the crystal

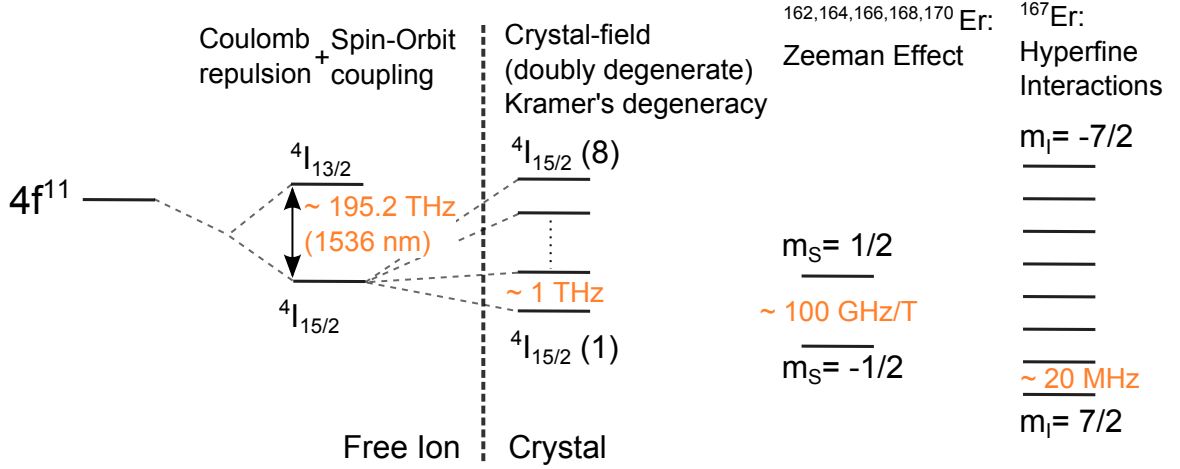


Figure 1.3.: Energy levels of the Er^{3+} isotopes in a solid. Quantum numbers as described in the main text with m_S the electron spin projection and m_I the nuclear spin projection.

create the so-called inhomogeneous broadening (see Fig. 1.2). Its width strongly depends on the specific crystal and can range from tens of MHz in chloride crystals [20] to hundreds of GHz in the case of lithium niobate [21]. The narrow homogeneous linewidths of REI and the possibility to spectrally modify their broad inhomogeneous absorption lines via optical pumping [4] have led to many applications, including signal processing [22], laser stabilization [23], ultra-precise radio frequency spectrum analyzers [24] and optical quantum memories [25].

1.3. Spectral tailoring and the atomic frequency comb quantum memory

The atomic frequency comb (AFC) quantum memory protocol [26] theoretically allows quantum storage with unity efficiency and is particularly suited for REI-doped crystals. In addition, the protocol makes it possible to store quantum information

encoded in multiple modes without requiring more resources in terms of the storage material. Multimode storage together with the existing ability to transmit multiple modes through fiber networks directly increases the maximum rate of communication in a repeater-based quantum network. All other quantum memory protocols require more resources, specifically more absorbers, to increase the number of modes that can be stored.

The AFC- and many other quantum memory protocols, e.g. CRIB, reviewed in [27], rely on the ability to spectrally tailor the inhomogeneously broadened optical absorption line via frequency selective hole burning as described in section 3.1. In case of the AFC protocol, it is shaped into a comb-like sequence of peaks and troughs as shown in Fig. 1.4.

The incoming photon, which must have a spectral width smaller than the extent of

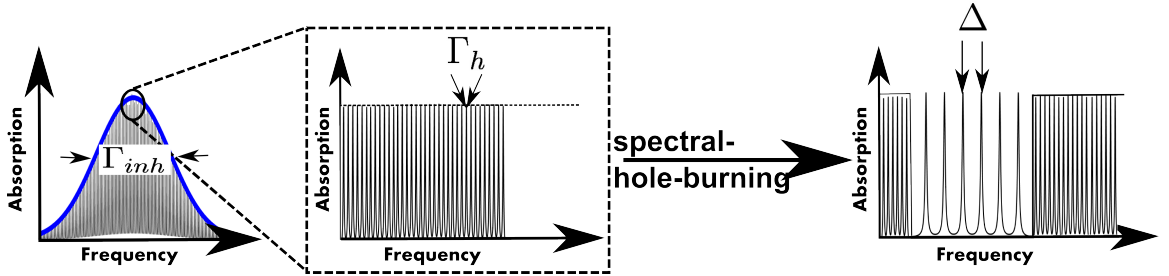


Figure 1.4.: Generation of an atomic frequency comb with splitting Δ via frequency selective spectral hole burning on the inhomogeneously broadened absorption line Γ_{inh} .

the prepared pattern, and much larger than the tooth spacing Δ , is absorbed by the

medium resulting in a collective excitation

$$|\Psi\rangle = \sum_{j=1}^N c_j e^{i\delta_j t} e^{-ikz_j} |g_1 \dots e_j \dots g_N\rangle, \quad (1.2)$$

a so called Dicke state [28]. The index j labels the corresponding ion within the comb, δ_j is the frequency detuning of the atom compared to the center frequency of the absorbed photon, and c_j are the amplitudes corresponding to atom j . k is the wavenumber of the light field. After absorption of the photon, each term of the sum accumulates a phase depending on its frequency detuning $\delta_j = n_j \cdot \Delta$ with Δ being the spacing between the individual teeth and n_j integer numbers. After a time $T = 2\pi/\Delta$ the ensemble re-phases and the photon is re-emitted. In this form, the quantum memory's storage time is pre-determined by the spacing between the teeth. However, on-demand retrieval can be achieved by transferring the excitation (Eq. 1.2) to an auxiliary energy level, usually a long lived spin level, and returning it after the desired storage time.

The quality of the comb pattern directly influences the maximum achievable efficiency for quantum storage. In case the photon is re-emitted in backwards direction and the peaks have Gaussian shape, the efficiency η is given by

$$\eta = \left(1 - e^{-(\alpha/F)}\right)^2 e^{-(7/F^2)} e^{-\alpha_0}. \quad (1.3)$$

Here α is the peak absorption of the medium, $F = \Delta/\gamma$ the finesse of the comb with

γ the width of the individual teeth and α_0 the residual absorption in the troughs of the comb. We note that whereas the efficiency in case of Eq. 1.3 can reach unity, it is limited to 54 % due to re-absorption in case the photon is re-emitted in forwards direction.

From Eq. 1.3 one can see that the efficiency directly scales with the finesse of the comb, which is ultimately limited by the minimum achievable peak width γ . The minimum peak width is given by the homogeneous linewidth of the material that is used. In many cases, and specifically in Erbium doped materials that are interesting due to their transitions within the telecom wavelength range around 1550 nm, this linewidth is broadened by phonons. Furthermore, if there is residual absorption in the troughs of the comb, i.e. ions that have not been optically transferred to the auxiliary energy level or that relaxed back into the ground state, system loss exponentially reduces the memory efficiency (see Eq. 1.3). Depending on the chosen material and the chosen auxiliary energy level, phonons can cause rapid relaxation from the auxiliary level back in the ground state and degrade memory efficiency. This phonon-driven relaxation is fastest at high magnetic fields where coherence properties usually are optimal. At low magnetic fields, interactions between neighboring ions often make high-quality spectral tailoring difficult. Paper 5.1 discusses these processes for the specific case of erbium doped materials.

Thus, in order to improve the performance of quantum memories based on spectral tailoring in REI, it would be beneficial to either inhibit phonons present in the host material that cause relaxation and line broadening, or to reduce interactions between

neighboring ions. This thesis investigates methods to achieve both of the above mentioned goals: Inhibit phonons in the host material through nano-structuring (chapter 5) and inhibit erbium-erbium interactions through the use of disordered, amorphous materials (chapter 6).

We note that inhibiting phonon-driven relaxation and line broadening, and reducing ion-ion interactions in solid state hosts is not just useful to improve the performance of the AFC quantum memory protocol but also benefits other protocols such as CRIB [29] and all applications mentioned in section 1.2 that are based on spectral tailoring.

2. Light-matter interaction

All quantum memory protocols and all the spectroscopic investigations that are described in this thesis rely on the interaction of light with matter, in this case REI doped solid state hosts. Therefore, this chapter will provide a brief introduction to light-matter interactions and derive (following the methods presented in [30, 31, 32]) the essential equations required to describe it.

2.1. Rabi oscillations

In the most simple case, the system of interest consists of one atom featuring two energy levels — the ground state g and the excited state e — and a plane wave electric field \mathbf{E} . In the interaction picture, the state of the atom, already including the time evolution of the atom, can be written as

$$|\Psi(t)\rangle = g(t)e^{-iE_g t/\hbar} |g\rangle + e(t)e^{-iE_e t/\hbar} |e\rangle = \begin{pmatrix} g(t)e^{-iE_g t/\hbar} \\ e(t)e^{-iE_e t/\hbar} \end{pmatrix} \quad (2.1)$$

with E_g and E_e the energy of the ground and excited state, respectively, \hbar the reduced Planck constant and $e(t)$, $g(t)$ the time dependent amplitudes for the respective states. The electric field \mathbf{E} is given by:

$$\mathbf{E}(x, t) = \frac{1}{2} (\mathbf{E}^+(x)e^{i\omega t} + \mathbf{E}^-(x)e^{-i\omega t}) \quad (2.2)$$

with ω the frequency of the electric field. The electric field interacts with the atom through the dipole interaction $-\boldsymbol{\mu}\mathbf{E}(x, t)$ with the dipole moment $\boldsymbol{\mu} = -e\mathbf{x}$ where e is the charge of the electron and \mathbf{x} the position. Assuming the electric field varies on a much larger scale than the extent of the atom (dipole approximation), the expectation values for this observable can be computed as $\mathbf{E}(x, t) \langle \Psi(t) | \boldsymbol{\mu} | \Psi(t) \rangle$. Furthermore assuming an inversion symmetric medium results in vanishing diagonal elements such that the total energy of the interaction can be written as

$$H(t) = -\boldsymbol{\mu} \cdot \mathbf{E}(t) = \begin{pmatrix} 0 & \mathbf{M}^* \mathbf{E}(x, t) \\ \mathbf{M} \mathbf{E}(x, t) & 0 \end{pmatrix} \quad (2.3)$$

where $M = e \langle g | \mathbf{x} | e \rangle$ is the matrix element of the dipole operator. Solving the Schrödinger equation

$$i\hbar \partial_t \Psi(t) = H(t) \Psi(t) \quad (2.4)$$

with this Hamiltonian results in the time varying amplitudes $g(t)$ and $e(t)$ that describe the state the atom is in. Assuming the so-called rotating wave approximation is valid, i.e. terms rotating with frequencies $\omega + (E_e - E_g)/\hbar = \omega + \omega_{eg}$ can be

neglected and assuming the frequency of the electric field is on resonance with the atomic transition $\omega = \omega_{eg}$ one finds

$$g(t) = \cos\left(\frac{\Omega_R t}{2}\right) \quad \text{and} \quad e(t) = -i \sin\left(\frac{\Omega_R t}{2}\right) \quad (2.5)$$

with Ω_R the Rabi frequency given by $\Omega_R = \left|\frac{\mathbf{M}\mathbf{E}}{\hbar}\right|$. These time-varying amplitudes reflect that the atom is oscillating between its two states when interacting with a resonant field, i.e. the atomic population can be transferred from one state to another using an electric field.

2.2. Maxwell-Bloch equations

This semi-classical treatment can be extended by including a phenomenological spontaneous emission term in the interaction operator H . One can write the state of the atom in form of a density matrix

$$\rho = |\Psi(t)\rangle \langle \Psi(t)| = \begin{pmatrix} e(t)e(t)^* & e(t)g(t)^* \\ g(t)e(t)^* & g(t)g(t)^* \end{pmatrix} = \begin{pmatrix} \rho_{ee} & \rho_{eg} \\ \rho_{ge} & \rho_{gg} \end{pmatrix}.$$

Assuming $|\Psi(t)\rangle$ is a pure state and the rotating wave approximation holds, this leads to the well known Bloch equations [33]:

$$\frac{d}{dt}\rho_{ge} = -\left(\frac{1}{2T_1} - i\omega_{eg}\right)\rho_{ge} + \frac{1}{2i\hbar}\mathbf{M}\mathbf{E}^+(\rho_{ee} - \rho_{gg}) \quad (2.6)$$

$$\frac{d}{dt}(\rho_{ee} - \rho_{gg}) = -\frac{(\rho_{ee} - \rho_{gg}) - N_0}{T_1} + \frac{1}{i\hbar}(\mathbf{M}^* \mathbf{E}^- \rho_{ge} - \mathbf{M} \mathbf{E}^+ \rho_{ge}^*) \quad (2.7)$$

with the equilibrium population inversion $N_0 = -\tanh(\hbar\omega_{eg}/2kT)$, k the Boltzman constant and T the temperature of the medium. T_1 is the population lifetime of the excited energy level $|e\rangle$ and $T_2 = 2T_1$ the dephasing time. Note that in general the dephasing time T_2 is shorter than twice the population lifetime due to dephasing processes.

2.3. Jaynes Cumings model

The semi-classical treatment presented in the previous sections 2.1 and 2.2 of this chapter make it possible to describe most aspects of light-matter interaction. However, their limits are obvious since, for example spontaneous emission had to be included in a phenomenological way to derive the Bloch equations. A full quantum description makes it possible to describe this phenomenon in a rigorous way. The derivation is similar to the one presented in the previous sections but with the electromagnetic field quantized in terms of occupation of modes labeled by the wave vector \mathbf{k} and polarization l :

$$\hat{\mathbf{E}}(\mathbf{x}, t) = \sum_l \sum_{\mathbf{k}} \sqrt{\frac{\hbar}{2\omega V \epsilon_0}} \left(\mathbf{e}_l \hat{a}_{\mathbf{k},l} e^{i\mathbf{k}\mathbf{x}} e^{i\omega t} + \mathbf{e}_l^* \hat{a}_{\mathbf{k},l}^\dagger e^{-i\mathbf{k}\mathbf{x}} e^{-i\omega t} \right) \quad (2.8)$$

with ϵ_0 the vacuum permittivity, \mathbf{e} the polarization vector, $\hat{a}_{\mathbf{k},l}$, $\hat{a}_{\mathbf{k},l}^\dagger$ the creation and annihilation operators of the electric field in a particular mode. V is the mode volume that can be tailored in wave guides or cavities [34], which, as shown below, can lead

to faster Rabi frequencies. This quantization leads to the Hamiltonian describing the System:

$$\hat{H} = \hat{H}_{atom} + \hat{H}_{field} + \hat{H}_I = \frac{1}{2}\hbar\omega_{eg}\sigma_z + \sum_{\mathbf{k}} \sum_l \hbar\omega_l \hat{a}_{\mathbf{k},l}^\dagger \hat{a}_{\mathbf{k},l} + \sum_{\mathbf{k}} \sum_l \hbar\tilde{\Omega}_R^{l,\mathbf{k}} (\hat{a}_{\mathbf{k},l}\sigma_+ + \hat{a}_{\mathbf{k},l}^\dagger\sigma_-) \quad (2.9)$$

with the same definitions as in the previous sections and σ_i operators for the atom defined as

$$\sigma_z = \begin{pmatrix} 1 & 0 \\ 0 & -1 \end{pmatrix} \quad \sigma_+ = \begin{pmatrix} 0 & 1 \\ 0 & 0 \end{pmatrix} \quad \sigma_- = \begin{pmatrix} 0 & 0 \\ 1 & 0 \end{pmatrix}. \quad (2.10)$$

The Rabi frequency for $\omega = \omega_{eg}$

$$\tilde{\Omega}_R^{k,l} = M\mathbf{e}_{\mathbf{k},l} \sqrt{\frac{\hbar\omega(n_{\mathbf{k},l} + 1)}{2\epsilon_0 V}}$$

is similar to the classical one but the electric field has to be replaced with the quantized version and $\hat{n}_{\mathbf{k},l} = \hat{a}_{\mathbf{k},l}^\dagger \hat{a}_{\mathbf{k},l}$ is the occupation number operator of a specific mode. This Hamiltonian allows for oscillations, even if the electric field is in the vacuum state, i.e. it describes spontaneous emission assuming the atom starts in the excited state. This manifests itself since the Rabi frequency is not zero for $n=0$. For the simplest case of one two-level system interacting with one mode of the electromagnetic field Eq. 2.9 is called the Jaynes Cummings Hamiltonian [35].

3. Spectroscopic tools and spectral tailoring

The previous chapter described the interaction between light and matter. Due to this interaction, light provides us with a unique tool to investigate the properties of matter and to understand the underlying mechanisms that lead to them. This chapter will discuss various spectroscopic methods and their ability to measure different material properties. The main goal is to provide a set of measurements that allows one to quantify the ability to perform spectral tailoring as described in chapter 1.3. By performing the mentioned measurements for a broad range of environmental parameters such as temperature and magnetic fields, it is then possible to determine the nature of the underlying processes leading to the observed properties.

3.1. Spectral hole burning

As described in section 1.3, many applications of REI-doped materials depend on the ability to move atomic population to a shelving level in a frequency-selective way, a

process known as spectral tailoring. The simplest possible case is to only remove the population from one single frequency bin within the inhomogeneous line and store it in a metastable state; a process called spectral hole burning, first described in 1975 by Szabo [36]. The spectral hole is created using a narrowband laser that is resonant with the transition of interest and transfers the atomic population from the ground to the excited state (see Fig. 3.1). From the excited state the population may decay into a metastable (e.g. hyperfine) state within the order of μs to ms for many common REI materials. After the spectral hole has been created, it can be probed after a

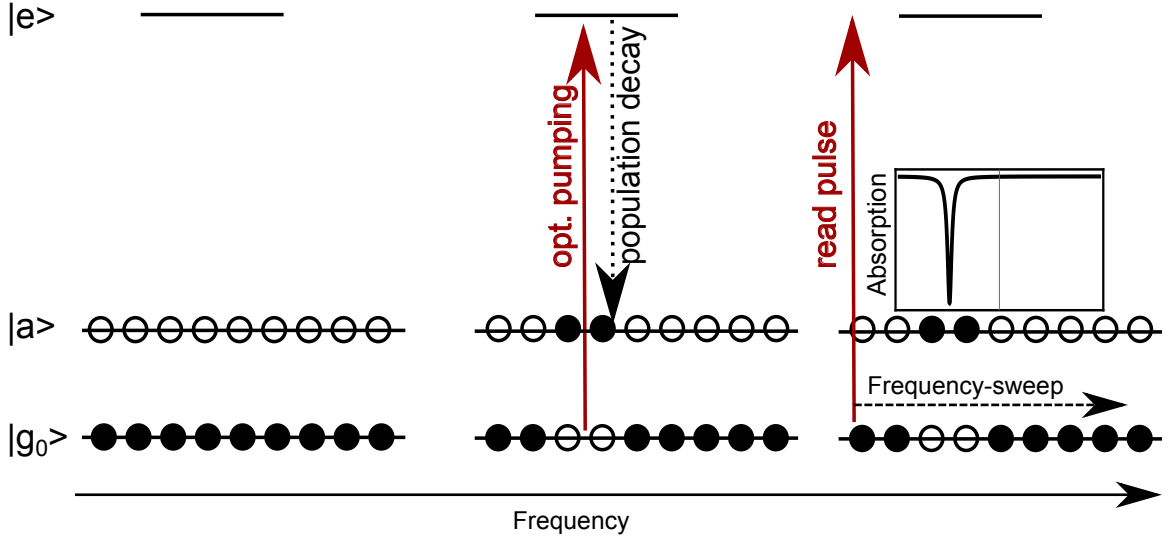


Figure 3.1.: Experimental hole burning sequence, frequency-selective optical pumping moves population from $|g_0\rangle$ to $|a\rangle$. When the hole is read by a laser pulse that is swept in frequency over the extent of the hole this manifests itself in decreased absorption.

certain time τ using a second, narrowband laser whose frequency is swept over the extent of the created hole. In this way both, the width and the area of the spectral hole can be measured in a time resolved manner. In this thesis, if the spectral hole vanishes after a relatively short time τ , typically on the sub millisecond scale, which

may correspond to population lifetimes in excited electronic states, it is referred to as a transient hole. If the hole is long lived ($> \text{ms}$), as is the case of most Zeeman or hyperfine states, it is referred-to as a persistent hole. By burning multiple spectral holes within the inhomogeneously broadened line and storing the population in an auxiliary level, more complicated spectral patterns such as atomic frequency combs can be created. The maximum time during which the created spectral features exist is a key figure of merit for all applications mentioned in section 1.2.

Often spectral hole burning is used to extract the lifetimes of the various levels that lie between the excited state $|e\rangle$ and the ground state $|g_0\rangle$. This is done by measuring the area of the spectral hole, which is directly proportional to the amount of population absent from $|g_0\rangle$, with varying τ . In case only two levels $|g_0\rangle$ and $|e\rangle$ are involved, the area of the spectral hole will decay exponentially with time. Additional levels will produce a multi- exponential decay. The decay times of the individual exponential functions directly correspond to the population lifetimes of the involved energy levels. Furthermore, in case of 3 or more involved levels, the analysis of the decay allows one to determine the branching ratio β , i.e. the fractions of the population in $|e\rangle$ that decay into the various levels between $|e\rangle$ and $|g_0\rangle$. As an example, for a 3 level system as depicted in Fig. 3.1, the decay of the spectral hole area can be fit to [37]

$$A(\tau) = e^{-\tau/T_e} + \frac{\beta}{2} \frac{T_a}{T_a - T_e} (e^{-\tau/T_a} - e^{-\tau/T_e}) \quad (3.1)$$

and the lifetimes T_a , T_e and the branching ratio β can be obtained.

Furthermore, it is possible to measure the width Γ_{hole} of the spectral hole. Extrapolated to zero burn power and zero time delay $\tau = 0$, the measured hole width is a convolution between the line width of the laser that was used to burn the spectral hole and twice the homogeneous linewidth [38]. For increasing laser intensity I , the measured hole width Γ_{meas} will increase as $\Gamma_{meas} = \Gamma_{hole}(1 + \sqrt{1 + \Omega^2 T_1 T_2})$ [39] with $\Omega^2 = M^2 I / \hbar^2$ the square of the Rabi frequency, T_1 the lifetime of the excited state and T_2 its coherence lifetime. This so-called power broadening arises since with more laser power, ions that are slightly off resonant with the laser can be excited and take part in the spectral hole.

Depending on the exact level structure of the ion under investigation, additional features besides one central hole can appear when the spectral hole is scanned. Assuming an excited state and ground state that each split into two states as in Fig. 3.2, and that the hole is created on the $|g\rangle_1 \rightarrow |e\rangle_1$ transition, one side-hole will appear as the transition $|g\rangle_1 \rightarrow |e\rangle_2$ is also depleted. Since the population after the pumping process will be stored in $|g\rangle_2$, two anti-holes will appear since the transitions $|g\rangle_2 \rightarrow |e\rangle_1$ and $|g\rangle_2 \rightarrow |e\rangle_2$ obtain increased absorption. Due to the inhomogeneous broadening, each transition $|g\rangle_i \rightarrow |e\rangle_i$ with $i = 1, 2$ will be on resonance with the pump laser for a certain subset of ions. The amount of side- and anti holes is thus increased accordingly (see Fig. 3.2). The splitting between the additional holes- and anti holes allows one to determine the energy splittings of the involved levels and, in case of Zeeman levels, the extraction of g-tensors as was done in the paper included in chapter 5.6.

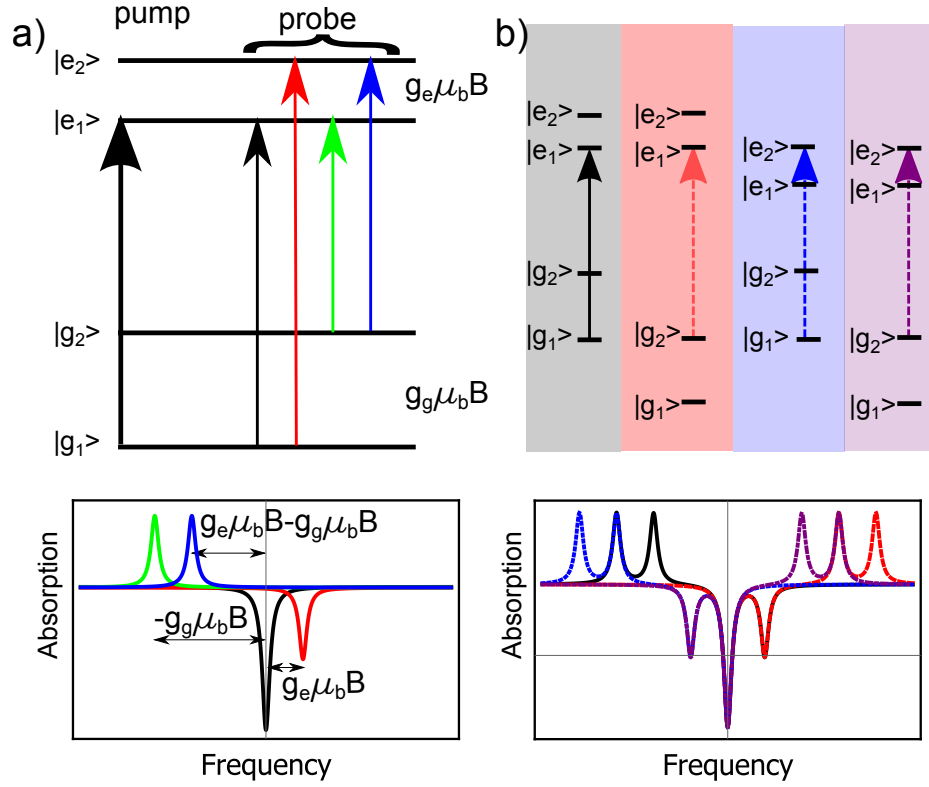


Figure 3.2.: a) Holeburning on an ensemble without inhomogeneous broadening. Two antiholes arise since population is transferred into the upper ground-state. A sidehole arises since the other transition originating from the same level as the pump is also depleted. b) Due to the inhomogeneous broadening the pump (vertical arrows) is simultaneously resonant with various transitions resulting in a symmetric hole-spectrum. Figure reproduced from [3].

Spectral hole burning, as described above, does not provide a reliable way to measure homogeneous line-widths since the result depends on many experimental factors. The following section will thus concentrate on different measurements of the homogeneous line-widths. However, for some applications such as the AFC quantum memory protocol it is of great interest to measure spectral holes in terms of width and depth including all the mentioned experimental contributions since these quantities ultimately determine the memory's performance.

3.2. Coherence measurements

As stated previously in chapter 1.3, the homogeneous linewidth Γ_h , which is inversely proportional to the coherence time $T_2 = 1/\pi\Gamma_h$, is another key performance indicator for applications based on REI-doped materials. For example, in case of the atomic frequency comb protocol, it limits the achievable efficiency. This section will thus be discussing methods to reliably measure coherence times in various materials. Since much of the work presented in this thesis consists of the study of powder materials, we will also discuss methods, such as free-induction decay, that are not very common but well suited to investigate strongly scattering materials.

3.2.1. Two-pulse photon echo

Today the most commonly used method to measure the coherence time of optical transitions in REI-doped materials is the so-called two-pulse photon echo, which has been first observed 1964 by Kurnit et.al [40] in ruby. The advantage of this technique is that the measurement result is independent of the laser line width and detector bandwidth (as long as it is large enough to resolve the specific pulses in time). The sequence consists of two laser pulses (see Fig. 3.3) interacting with the medium. The first pulse, ideally a $\pi/2$ pulse, excites a set of ions to a superposition between the two states that span the transition of interest. Following the first pulse, the ions contributing to the superposition will dephase since each ion has a slightly different resonance frequency. After a certain time τ a second pulse is applied, ideally a π pulse that reverts the phase angle. Therefore, after a time $2\tau + t_\pi$ (see Fig. 3.3), all ions

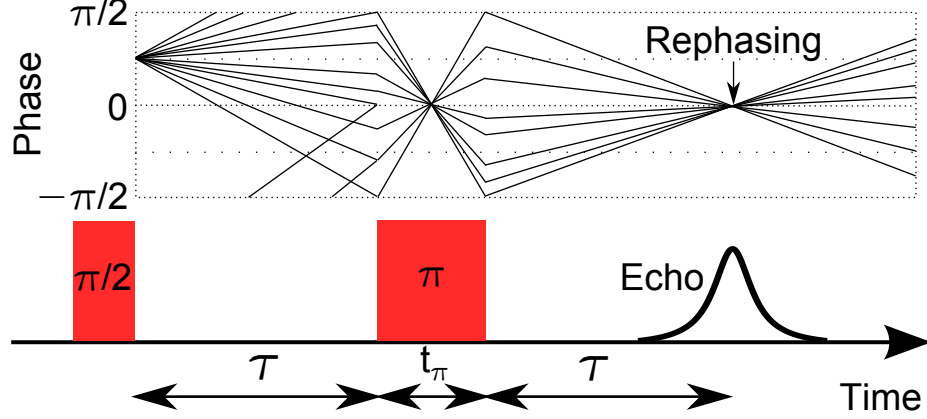


Figure 3.3.: Pulse sequence and phase evolution in a two-pulse photon echo. Diverging lines in the phase evolution correspond to ions affected by a decoherence inducing process. The more ions are affected by such processes, the smaller the echo becomes. Reproduced from [4].

will be in phase again and the photon echo is emitted. Ideally, without any processes limiting the coherence, the intensity of the echo would be independent of the time τ . However, the coherent phase evolution is perturbed by many processes, such as phonons, electric fluctuations in the environment and ultimately spontaneous decay of population. This causes the intensity of the echo to decay with increasing τ . If spectral diffusion (see chapter 3.2.2) is not present, or much slower than the timescale of the two-pulse echo, the resulting decay of the echo's intensity can be fitted using an exponential

$$I_{echo} = I_0 \exp \left\{ -2 \left(\frac{2\tau}{T_2} \right) \right\} \quad (3.2)$$

and the coherence time T_2 can be extracted.

3.2.2. Spectral diffusion and three- pulse photon echo

Spectral diffusion describes the time-dependent random change of an ion's transition frequency. It is caused by dynamic processes in the ion's environment such as lattice vibrations, two-level systems (see chapter 6.3.1) or flipping of neighboring spins. The timescales of those processes can be vastly different. Since all ions in the material are affected by spectral diffusion, the homogeneous linewidth of a subset of ions, i.e. the ones probed by the measurement, appears to increase over time. For example the width of a spectral hole seems to broaden with time since the transition frequencies of the ions contributing to the hole are perturbed by spectral diffusion.

Because processes contributing to spectral diffusion occur at different rates, spectral diffusion can perturb the phases of ions in a superposition in a time-dependent way. This effect manifests itself in two-pulse echo decays as a non exponential shape. In the presence of spectral diffusion, the two-pulse photon echo decays are usually fitted using a generalized version of Eq. 3.2, also known as Mims [41] decay:

$$I_{echo} = I_0 \exp \left\{ -2 \left(\frac{2\tau}{T_M} \right)^m \right\} \quad (3.3)$$

with T_M the so called effective phase memory time of the system, i.e. the time over which the coherence decays to $1/e^2$ of its initial intensity [42], and m is the so-called Mims exponent that describes the non-exponential decay caused by spectral diffusion.

Since spectral diffusion occurs over various timescales, it is impossible to fully charac-

terize it using a measurement like the two-pulse photon echo or spectral holeburning. The former addresses the shortest timescales and the latter rather long timescales. A measurement that can access the homogeneous linewidth after arbitrary timescales T_W is needed. The three-pulse photon echo measurement has those capabilities. It is very similar to the two-pulse photon echo, however, the π pulse is split into two $\pi/2$ pulses (see Fig. 3.4). The first pulse prepares the coherence, the second pulse, occurring after a wait time t_{12} , transfers the coherence into a population difference between ground- and excited state, thus effectively creating a comb like structure in frequency. The third pulse, after a wait time T_W , then probes the grating and is re-emitted after a time t_{12} due to a rephasing process very similar to the AFC quantum memory protocol (see chapter 1.3). A different way to view this is that the third pulse transfers the population difference back into a superposition, which then rephases and causes a photon echo to be emitted. During $T_W + 2t_{12}$ spectral diffusion occurs and affects the efficiency of the reemission, i.e. decreases the intensity of the echo as

$$I(t_{12}, T_W) = I_0 \exp \{-2T_W/T_1\} \exp \left\{ -2 \left(\frac{2t_{12}}{T_M} \right)^m \right\} \quad (3.4)$$

with T_1 the lifetime of the excited state and all other variables as defined before.

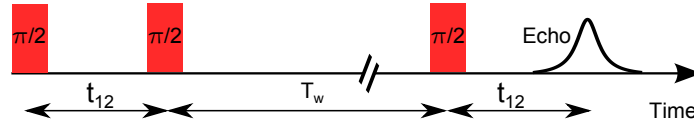


Figure 3.4.: Pulse sequence in a three-pulse photon echo. See main text for a detailed description.

The different decay shapes can be modeled and information about the different pro-

cesses contributing to spectral diffusion, their rate and relative importance can be obtained. For the specific example of an erbium doped silica glass fiber, the paper included in chapter 6.3 describes this procedure in detail.

3.2.3. Free-induction decay

Whereas the two-pulse photon echo is generally the most reliable way to measure coherence times, this method proved to be challenging to perform for small, strongly scattering powder materials with short coherence times. In practice, it was sometimes easier to measure the coherence time by observing the free-induction decay (FID) using heterodyne detection. Compared to hole burning, FID measurements make it possible to measure the homogeneous linewidth on shorter timescales and also reveals the evolution of decoherence processes over the timescale of the measurement similar to the decays measured in a two-pulse echo measurement. However, FID measurements are limited by the laser linewidth. There are different version of FID measurements. Here we will describe the so called delayed FID technique [16], which we used in Paper 5.4.

In a delayed FID measurement (see Fig. 3.5), an initial narrowband laser creates a spectral hole whose width, as in a spectral hole burning measurement, depends on the homogeneous linewidth of the material and the laser linewidth. After a waiting time T_W , an excitation pulse at the same frequency but much shorter puts ions in a coherent superposition between the ground- and excited state. Subsequently, the

excited ions coherently emit radiation that

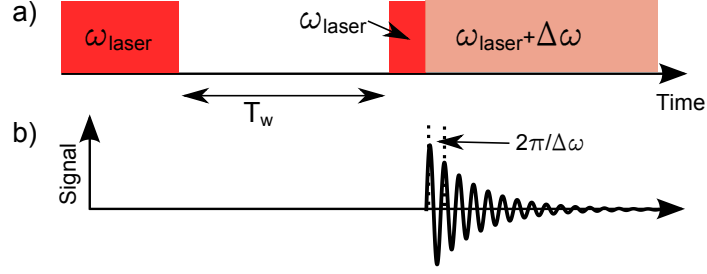


Figure 3.5.: a) Pulse sequence for a delayed FID measurement together with the signal observed on the Photodiode b).

can be heterodyned with a local oscillator (a laser detuned in frequency) to amplify the signal. Since the excitation pulse has a very large bandwidth due to its short duration, excitation at any individual frequency is minimized and the pulse does not create a spectral hole. Thus, the FID decay is determined by the spectral hole prepared by the first laser and the decay of the decay of the beat signal with time t provides information about the hole width broadened by spectral diffusion on the timescale of T_W :

$$I_{FID}(t, T_W) = I_0 \exp \left\{ - \left(\frac{t}{T_M(T_W)} \right)^m \right\} \quad (3.5)$$

Note that there is no factor of two in the exponent since, in a heterodyne measurement, the electric field is probed rather than the intensity of the signal. This provides more dynamic range for the measurement since the signal decays half as fast and is especially useful to measure short coherence times.

4. Spin lattice relaxation

One of the approaches to develop materials that allow for better spectral tailoring in terms of persistence and spectral feature width is to prevent undesired spin-lattice relaxation, i.e. relaxation of population from spin levels through interaction with lattice phonons. Since for many applications, population that is moved to create spectral features is stored in low-lying spin states $|g_1\rangle$, avoiding spin-lattice relaxation caused by phonons resonant with the $|g_0\rangle \leftrightarrow |g_1\rangle$ transition would improve spectral tailoring in two ways. First, without this relaxation, spin lifetimes will increase if no other limiting processes are present. Second, since spin-lattice relaxation can contribute significantly to spectral diffusion, narrower spectral features can be achieved without it. As described in chapter 5.1, specifically for the desirable erbium-doped materials at high magnetic fields, spin-lattice relaxation is limiting both persistence and line width.

The next section will provide the background to understand how phonons interact with impurities doped into host materials, and derive the dependence of the spin-lattice interaction on magnetic field and temperature. The derivations follow mainly

the original work presented by Orbach in 1961 [43].

4.1. Orbach theory

The first theoretical treatment of spin-lattice relaxation goes back more than 80 years. Early theories were developed by Waller (1932) [44], Heitler and Teller (1936) [45] and Fierz (1938) [46]. However, all of those theories failed to correctly reproduce early experimental results obtained by Gorter (1936) [47]. The later work of Kronig (1939) [48] and Van Vleck (1939 and 1940) [49, 50] succeeded to explain spin-lattice relaxation around 77 K. Although valid at elevated temperatures, their explanation failed to produce correct results at liquid helium temperatures, the temperature range which is of interest today since all applications mentioned in chapter 1.2 are implemented at temperatures lower than 4 K.

A theory for spin lattice relaxation at low temperatures, e.g. at or below liquid helium temperatures, was developed by Orbach in 1961 [43]. The treatment is based on the assumption that relaxation is facilitated by fluctuations in the crystal's electric field, described by the potential V_{ol} , that are caused by phonons.

Orbach's treatment distinguishes between Kramers ions (REI with an odd number of electrons such as erbium³⁺) and non-Kramers ions (REI with an even number of electrons such as thulium³⁺). An additional distinction between direct phonon processes, resonant two phonon processes (Orbach processes) and off-resonant two phonon processes (Raman processes) is made (see Fig. 4.1). Each process is described

in detail in the following.

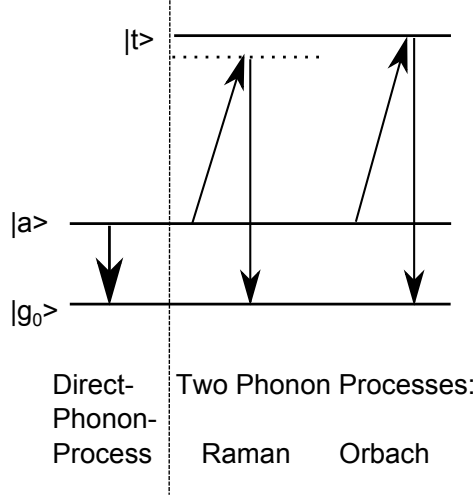


Figure 4.1.: Different phonon processes facilitating transitions between $|a\rangle$ and $|g_0\rangle$, each described in detail in the main text.

4.1.1. Direct-phonon process

A transition between two levels $|a\rangle$ and $|g_0\rangle$ can be caused via the interaction of a REI with a single phonon of the lattice, the so called direct-phonon process. Known as Fermi's golden rule, in first order perturbation theory, the probability of making such a transition is given by

$$W_{a \rightarrow g_0} = \frac{2\pi}{\hbar} |\langle g_0 | \sum_i V_{ol} | a \rangle|^2 \rho(E). \quad (4.1)$$

Here $|a\rangle$ is the initial state, $\langle g_0 |$ is the final state; the sum covers all ions that are in the initial state $|a\rangle$ and $\rho(E)$ is the density of states. Using Elliott's and Stevens' expansion of the spin lattice potential $V_{ol} = \sum_{m,n} V_n^m \epsilon_{nm}$ with ϵ_{nm} the average crystal strain and the corresponding expansion coefficients V_{nm} [51], one can express V_{ol} in

terms of the average strain in the crystal lattice at a certain point in the crystal. These matrix elements have been computed by Ziman 1960 [52] and depend on the phonon occupation number N given by the Bose-Einstein distribution. Using Eq. 4.1 one can then compute the total transition rate

$$1/T_1 = \frac{3\delta_{g_0a}^3}{2\pi\hbar\rho c_s^5} | \langle g_0 | \sum_{m,n} V_n^m | a \rangle |^2 \coth \left(\frac{\hbar\delta_{g_0a}}{2k_bT} \right). \quad (4.2)$$

Here T_1 is the spin state lifetime, δ_{g_0a} is the energy difference between the initial and final state, k_b is the Boltzman constant, ρ the material's density and c_s the speed of sound in the material. The inverse proportionality of the transition rate to the fifth power of the sound velocity shows that phonons couple strongest in soft materials in which c_s is small. Up to this point the treatment is still valid for both classes of REIs, Kramers and non-Kramers. The distinction arises from differences in the matrix element $\langle g_0 | \sum_{m,n} V_n^m | a \rangle$, it vanishes if initial and final state are time reversed states of half-integer quantum numbers, i.e. electron spin 1/2 leading to degenerate crystal field levels for a Kramers ion without an external magnetic field. For Non-Kramers ions this is not the case and consequently, the above mentioned matrix element does not vanish.

Since for most applications, the crystal field levels are not used, we here consider the special case in which the levels $|g_0\rangle$ and $|a\rangle$ are Zeeman states. The rate of direct

phonon processes for non-Kramers ions Eq. 4.2 is then given by [53]

$$1/T_1 \propto H^2 T \quad \text{for } g\mu_B H \ll k_B T \quad (4.3)$$

and

$$1/T_1 \propto H^3 \coth\left(\frac{g\mu_B H}{2k_B T}\right) \quad \text{otherwise} \quad (4.4)$$

with H the magnetic field, g the g-factor, μ_B the Bohr magneton and T the temperature.

Kramers ions, ions with an odd number of electrons, are the second important subclass of the REI. The unpaired electron in general makes them more susceptible to interactions with the environment. This leads to different phonon coupling strengths and different dependencies of the relaxation rates on external factors such as the magnetic field. However, the processes themselves are the same. In the case of Kramers ions and $|g_0\rangle$, $|a\rangle$ again being Zeeman states, Eq. 4.2 transforms to [53, 42]

$$1/T_1 \propto H^4 T \quad \text{for } g\mu_B H \ll k_B T \quad (4.5)$$

and

$$1/T_1 \propto H^5 \coth\left(\frac{g\mu_B H}{2k_B T}\right) \quad \text{otherwise} \quad (4.6)$$

These temperature- and magnetic field dependencies of the direct phonon process (Eq. 4.4 and 4.6) are characteristic and can serve to identify it. Note however, that

only observing the linear temperature dependence can be misleading since, for example, interactions with paramagnetic impurities in the environment also give rise of a linear temperature dependence of the decay rate [54].

Generally the direct-phonon process is dominant at lowest temperatures. At higher temperatures, phonons with higher energy are available and multi-phonon processes become important. The specific temperature at which higher order processes dominate relaxation strongly depends on the material.

4.1.2. Two-phonon processes

Two-phonon processes are explained by second order perturbation theory. Here the spin lattice potential acts twice upon the involved states and two phonons induce a transition between the initial and final state. Therefore an intermediate level $|t\rangle$ via which the transition takes place must be involved. Using the same approach as in Eq. 4.1 the transition probability is now given by

$$W_{a \rightarrow g_0} = \frac{2\pi}{\hbar} |\langle g_0 | \sum_{i,t} \frac{V_{ol} |t\rangle \langle t| V_{ol}}{E_i - E_t} |a\rangle|^2 \rho(E). \quad (4.7)$$

Here, $E_a - E_t$ is the energy difference between the initial and intermediate state and the sum i again counts all ions that are in the initial state $|a\rangle$ whereas the sum t sums over all possible intermediate states $|t\rangle$. Using the same expansion of the spin lattice potential as for the single phonon process, the relaxation rate for two phonon

processes is given by

$$\begin{aligned}
1/T_1 = & \frac{9}{16\pi^3 \rho^2 c_s^{10}} \cosh\left(\frac{\delta_{g_0 a}}{2k_b T}\right) \int \sum_{t, m, n, m', n'} \\
& \left\{ \left| \frac{\langle g_0 | V_n^m | t \rangle \langle t | V_{n'}^{m'} | a \rangle}{\hbar \omega_{n', m'} + 1/2 \delta_{g_0 a} - \Delta_t} \right|^2 \omega_{n', m'}^3 (\omega_{n', m'} - \delta_{g_0 a} / \hbar)^3 \right. \\
& \left. \operatorname{cosech}\left(\frac{\hbar \omega_{n', m'}}{2k_b T}\right) \operatorname{cosech}\left(\frac{\hbar \omega_{n', m'} - \delta_{g_0 a}}{2k_b T}\right) \right\} d\omega_{n', m'}
\end{aligned} \tag{4.8}$$

with all variables defined as before and Δ_t the energy difference between the initial state $|a\rangle$ and the intermediate state $|t\rangle$. This expression can be simplified under the assumption that only the intermediate state $|t\rangle$ closest to the initial state takes part in the relaxation process.

There are two fundamentally different two-phonon processes, distinguished by whether the intermediate level can be populated (Orbach process), which is mostly the case if $k_b T_D > \Delta_t$, or the intermediate level is not populated (Raman process), and the transitions occurs via a virtual level. This process is dominant if $k_b T_D < \Delta_t$. T_D is the Debye temperature and $\omega_{max} = k_b T / \hbar$ the largest available phonon frequency in the material. For non-Kramers-ions, the two-phonon Orbach process scales as

$$1/T_1 \propto \exp\left\{-\frac{\Delta_t}{k_b T}\right\} \tag{4.9}$$

and the Raman process scales as

$$1/T_1 \propto T^7. \tag{4.10}$$

It is important to note that both two-phonon processes are independent of the magnetic field and can be distinguished using their temperature dependence.

For Kramers ions, the same processes exist. However, the dependence of the Raman process on temperature and field is different:

$$1/T_1 = c_R T^9 + \tilde{c}_R H T^7. \quad (4.11)$$

with c_R , \tilde{c}_R the respective proportionality constants. The Orbach process scales in the same way as for non-Kramers ions (see Eq. 4.9).

Multi-phonon processes that include the interaction with more than two phonons can be treated in the same way as in the derivation of the one- and two-phonon processes. However, in this thesis, we will not consider those cases since we restrict ourselves to applications implemented at and below liquid helium temperatures at which they play an insignificant role.

All derivations of the different phonon processes above are based on the assumption that the phonon density of states is continuous and increases with the phonon frequency squared (Debye model). Thus, if one can modify the phonon density of states in a material, one can directly influence phonon processes. Specifically, if one succeeds to create gaps within the density of states at frequencies resonant with the phonons that cause direct relaxation between levels, one can avoid the contribution of the direct phonon process. The paper included in the next chapter discusses this

possibility in detail.

5. Phonon suppression in engineered materials

As described in the introduction, phonons are often detrimental for applications that require spectral tailoring of REI-doped materials. In many materials, phonons shorten the persistence time and limit the minimum spectral width of spectral features. As a consequence, for example in case of the AFC quantum memory protocol, both the efficiency and the storage time are affected. This chapter and the papers included in it will describe in detail how phonon suppression can be achieved in either small powder materials or nano-structured host materials, i.e. phononic crystals.

Since all the approaches that are mentioned in the following involve a transition from bulk to nano-scale structures, we also investigate how material properties change if this transition is made. Furthermore, we will identify and characterize other detrimental processes related to fabrication methods that can limit the application of nano-scale materials. The latter is of great importance since nano-fabricated devices become more and more popular in fields like optomechanics, cavity quantum electro-

dynamics, on-chip implementation of optical devices and luminescent materials due to the broad availability of nano-fabrication tools.

5.1. Paper 1: Modification of phonon processes in nanostructured rare-earth-ion-doped crystals

Physical Review A, **94**, 013801, 1 July 2016

5.1.1. Summary

Paper one presents a detailed investigation of how nano-materials in form of small powders as well as nano-structured materials, i.e. phononic crystals that are designed in a way that does not allow phonons at a certain frequency (phononic band gap), can be used to suppress phonons that are detrimental to various applications. The manuscript focuses on applications based on erbium-doped materials since they are appealing due to their transitions at telecom wavelengths around 1550 nm. As an example $\text{Er}^{3+}:\text{Y}_2\text{SiO}_5$ is discussed. Numerical simulations that compute the required dimensions for small powder materials as well as a complete design for a phononic crystal are presented. *My contribution to this work involved co-development of the original idea of suppressing phonons in nano-crystals. Furthermore, I performed all numerical simulations, both on small powder materials as well as the phononic crystals. The discussion of how those ideas can be applied to $\text{Er}^{3+}:\text{Y}_2\text{SiO}_5$ is the result of a joint effort by the co-authors Lucile Veissier, Charles Thiel and myself.*

Modification of phonon processes in nanostructured rare-earth-ion-doped crystals

Thomas Lutz¹, Lucile Veissier^{1†}, Charles W. Thiel², Rufus L. Cone², Paul E.

Barclay¹ and Wolfgang Tittel¹

¹*Institute for Quantum Science and Technology, and Department of Physics & Astronomy, University of Calgary, Calgary Alberta T2N 1N4, Canada*

²*Department of Physics, Montana State University, Bozeman, MT 59717 USA*

[†] *Present address: Laboratoire Aimé Cotton, CNRS-UPR 3321, Univ. Paris-Sud, Bât. 505, F-91405 Orsay Cedex, France*

**Corresponding author: thomasl@ucalgary.ca*

Abstract: Nano-structuring impurity-doped crystals affects the phonon density of states and thereby modifies the atomic dynamics induced by interaction with phonons. We propose the use of nano-structured materials in the form of powders or phononic bandgap crystals to enable or improve persistent spectral hole-burning and coherence for inhomogeneously broadened absorption lines in rare-earth-ion-doped crystals. This is crucial for applications such as ultra-precise radio-frequency spectrum analyzers and optical quantum memories. As an example, we discuss how phonon engineering can enable spectral hole burning in erbium-doped materials operating in the convenient telecommunication band, and present simulations for density of states of nano-sized powders and phononic crystals for the case of Y_2SiO_5 , a widely-used material in current quantum memory research.

5.1.2. Introduction

Rare-earth-ion-doped crystals have been studied for decades because of their unique spectroscopic properties [1, 2, 3] that arise since their $4f$ -electrons do not participate in chemical bonding. At cryogenic temperatures they can offer narrow linewidths [4, 5, 6] together with the possibility to spectrally tailor their broad inhomogeneous absorption lines [2]. These properties have led to many applications, including optical quantum memories [7, 8, 9], signal processing [10, 11], laser stabilization [12, 13, 14], as well as ultra-precise radio frequency spectrum analyzers [15, 16]. Quantum memory implementations in rare-earth-ion-doped (REI-doped) crystals, such as those based on electromagnetically-induced transparency [17]), atomic frequency comb [18], or controlled reversible inhomogeneous broadening [19], crucially rely on long coherence and spin-state lifetimes to achieve high efficiency and long storage time.

Operating REI-doped crystals at low temperatures generally improves material properties. Yet, even at temperatures below 2 K, spin-lattice relaxation, i.e. thermalization of spins via interaction with phonons, still restricts lifetimes of spin states, reducing the ability to spectrally tailor the material. Furthermore, by contributing to spectral diffusion [20, 21] and two-phonon elastic scattering processes [22], lattice vibrations limit coherence times. We propose the use of nano-structured materials to overcome these limitations. This is achieved by tailoring the phonon density of states [23] to restrict phonon processes, an approach not limited to REI-doped materials but also applicable to other impurity-doped materials such as color centers

in diamond [24]. The result is an improved performance for all applications based on spectral hole burning, or that require long coherence times, by providing long-lived spin states while simultaneously suppressing phonon-driven decoherence. We note that the modification of population dynamics between REI crystal field levels in small powders, possibly related to phonon restriction, has been observed in the context of understanding luminescence dynamics [25, 26] - but not yet to improve spectral hole burning or optical coherence properties.

In this paper, we propose a general procedure to identify the frequency range of detrimental lattice vibrations and restrict the relevant phonon processes in impurity-doped solids. As an example, we apply this approach to erbium-doped materials. First, we recall the mechanisms causing detrimental electronic spin flips and discuss how the suppression of the direct phonon process influences spin-state lifetimes and spectral diffusion. Then, two methods for nano-structuring REI-doped crystals to suppress the direct phonon process affecting electronic spin states in $\text{Er}^{3+}:\text{Y}_2\text{SiO}_5$ are analyzed: powder materials, which introduce a cutoff frequency in the phonon density of states, and phononic band gap crystals with a structure optimized for the targeted material and application. Numerical simulations for $\text{Er}^{3+}:\text{Y}_2\text{SiO}_5$ are presented.

Relaxation of optically pumped spin populations back to thermal equilibrium by spin flips is caused by phonons primarily via three different processes [27, 28]: the direct process where phonons resonant with the spin transition induce a spin flip, the Orbach process where two resonant phonons produce a spin flip via excitation to, and

relaxation from, excited crystal field levels, and the off-resonant Raman process where two phonons lead to a spin flip via inelastic scattering. Levels involved in spectral hole burning, typically hyperfine or Zeeman levels, are mostly separated by MHz to GHz. The rates of phonon processes are proportional to the phonon density of states in the material as discussed in [27]. Interestingly, the Debye approximation for the density of states

$$\rho(\omega) \propto V\omega^2 \quad (5.1)$$

with V the volume of the particle and ω the frequency, breaks down for small structures. In this regime, the density of states becomes discrete [29] and acquires a cutoff frequency below which no vibrational modes are possible and thus no phonons can exist [23]. We predict that an ensemble of sufficiently small REI-doped crystals, or an appropriate REI phononic band gap material, will allow suppression of the direct phonon process responsible for relaxation between the spin states.

5.1.3. Phonon restriction in Er:Y₂SiO₅

As an example, we consider extending lifetimes of the ground-state Zeeman levels for persistent spectral hole burning and reducing spectral diffusion in erbium-doped crystals, particularly appealing for quantum memory applications due to the $^4I_{15/2} \leftrightarrow ^4I_{13/2}$ transition of Er³⁺ ions around 1530 nm and long coherence times. Three important cases are Er³⁺:Y₂SiO₅, for which optical coherence lifetimes of up to 4.4 ms have been observed [30], Er³⁺:LiNbO₃, exhibiting a large oscillator strength ac-

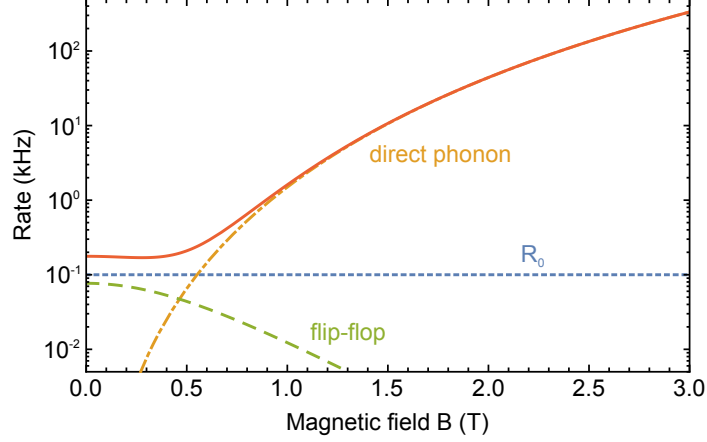


Figure 5.1.: Magnetic field dependence of the spin-flip rate. As described by Equation 5.2, the total rate R (solid red line) is composed of a constant term R_0 (dotted blue line), a spin flip-flop term (green dashed line) and a direct phonon term (orange dash-dotted line), dominant above 1 T. We assume $T = 3$ K, $g = 14$, $R_0 = 0.1$ kHz, $\alpha_D = 5 \times 10^{-4}$ kHz/T⁵ and $\alpha_{ff} = 2$ kHz.

accompanied by a very broad inhomogeneous linewidth [31], and $\text{Er}^{3+}:\text{KTiOPO}_4$, which has shown narrow homogeneous linewidths down to 1.6 kHz [32]. All Er-doped crystals so far eluded efficient quantum-state storage [33, 34, 35, 31] since no efficient persistent hole burning involving electronic Zeeman levels [36] has been achieved. The only material that has shown long spin-state lifetimes is an Er-doped glass fiber [37], in which disorder broadens the spin transition and effectively weakens the coupling between Er^{3+} ions. This reduces the relaxation rate at low magnetic field. Introducing controlled disorder in crystals is potentially an alternative approach to improve spin lifetimes however, disorder can be extremely detrimental for the coherence properties, as it is the case in impurity-doped glasses. Indeed, the latter are restricted in their applications since coherence times are intrinsically limited to a few μs or less by low frequency disorder mode dynamics that are present in any amorphous material [38]. The goal of our study is to propose a method to simultaneously

achieve long coherence and spin lifetimes, which excludes, e.g., Er-doped fibers - at least given current knowledge.

Phonons can limit the lifetime of persistent spectral holes, but other processes can also contribute, for example paramagnetic interactions of REI with neighbouring ions or with other impurities in the host. For erbium-doped materials such as $\text{Er}^{3+}:\text{Y}_2\text{SiO}_5$, $\text{Er}^{3+}:\text{LiNbO}_3$ or $\text{Er}^{3+}:\text{KTiOPO}_4$, the total spin-flip rate at temperatures below 4 K can be approximated by [20, 31, 32]

$$R(B, T) = R_0 + \alpha_{\text{ff}} g^4 \text{sech}^2 \left(\frac{g\mu_B B}{2kT} \right) + \alpha_{\text{D}} g^3 B^5 \coth \left(\frac{g\mu_B B}{2kT} \right). \quad (5.2)$$

The second term represents the average rate of mutual spin flip-flops, i.e. exchange of spin states between two Er ions, with α_{ff} a constant, g the g -factor of the ions, μ_B the Bohr magneton and k the Boltzmann constant. The last term corresponds to the direct phonon process and is proportional to $B^4 T$ for $g\mu_B B < 2kT$, where the parameter α_{D} characterizes the strength of the phonon coupling [27]. The constant R_0 includes all residual relaxation processes. The Raman and Orbach rates are not considered here since they are strongly suppressed at low temperature [28], particularly when the crystal-field splitting is much larger than kT as is the case for the materials considered here. The magnetic field dependence of the spin-lattice relaxation is illustrated in Figure 5.1, which shows the total rate and its different components. Values of the parameters vary for the three materials cited above. The R_0 term is negligible

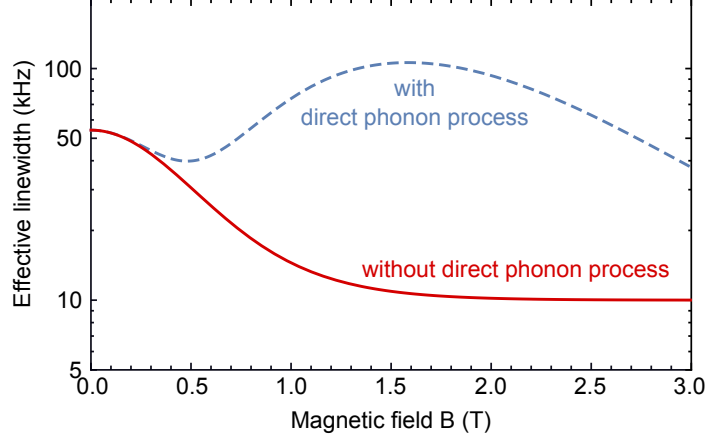


Figure 5.2.: Effect of the direct phonon process suppression on the effective homogeneous linewidth. As described by Equation 5.4, Γ_{eff} after $t = 10 \mu\text{s}$ is shown as a function of the magnetic field strength in the presence (blue dashed line) and in the absence (red solid line) of the direct phonon process. We assume the same parameters as in Fig. 5.1 and, in addition, $\Gamma_{\text{max}} = 5 \times 10^{10} \text{ Hz}$, $\Gamma_0 = 10 \text{ kHz}$.

in Er:LiNbO_3 [31], whereas the spin flip-flop rate is very small for $\text{Er:Y}_2\text{SiO}_5$ [20]. Er:KTiOPO_4 has unusually small R_0 and weak spin flip-flop process, so that only the direct phonon process significantly contributes to the field-dependent spectral diffusion, even at low field strengths [32]. However, in all cases the direct phonon process becomes dominant for magnetic field strengths of 1 T and higher.

From the above discussion, the optimum operating point would seem to be at magnetic fields below 0.5 T; however, to reduce spectral diffusion and improve coherence properties, erbium-ion-doped-crystals often require magnetic fields of a few Tesla. It has been shown that the maximum linewidth due to spectral diffusion can be described by [20]

$$\Gamma_{\text{SD}}(B, T) = \Gamma_{\text{max}} \text{sech}^2 \left(\frac{g\mu_B B}{2kT} \right), \quad (5.3)$$

with Γ_{max} the full-width at half-maximum frequency broadening caused by magnetic dipole-dipole interactions between Er ions. One can see that Γ_{SD} decreases with magnetic field and spectral diffusion can thus be suppressed at high fields due to the increased magnetic order in the system. This leads to narrow homogeneous linewidths at high fields. However, high fields lead to increased spin-lattice relaxation (see Figure 5.1). In addition to being detrimental to persistent spectral hole burning, this results in faster broadening of the spectral line to its maximum value, as shown in the effective linewidth after a time delay t [20]

$$\Gamma_{\text{eff}}(t) = \Gamma_0 + \frac{1}{2}\Gamma_{\text{SD}} (1 - e^{-Rt}), \quad (5.4)$$

with Γ_0 the homogeneous linewidth without spectral diffusion. Therefore, removing the direct phonon process will not only improve persistent spectral hole burning, but also inhibit spectral diffusion, especially at magnetic fields around 1 T (see Figure 5.2).

We now identify the range of frequencies at which phonons must be suppressed. In our example of erbium-doped materials, the goal is to eliminate phonons below the frequency corresponding to the maximum Zeeman splitting under an external magnetic field of around 1 T. In $\text{Er}^{3+}:\text{Y}_2\text{SiO}_5$ the g -factor along the b -axis is 13.6 [39], leading to a splitting of 190 GHz/T. As we will describe next, inhibiting phonons at such high frequency requires small structures. For other types of paramagnetic centers or nuclear hyperfine states, the energy splitting of the spin states is usually smaller, so that larger structures can inhibit the detrimental phonon processes. Furthermore, it

is possible to suppress phonons resonant with transitions between crystal-field levels, depending on the energy level splitting. In consequence, two-phonon processes such as Raman or Orbach processes can be suppressed. This would also lead to improved coherence lifetimes for materials in which two-phonon elastic scattering is responsible for dephasing [22]. More generally, suppressing phonons will enable to increase the range of working temperatures for all impurity-doped materials that have properties limited by phonon processes.

5.1.3.1. Restriction in small powder materials

We first discuss the case of small crystals. To suppress phonon processes we use the fact that the density of states of a particle features a cutoff at

$$\nu_{min} = \eta_{min} \frac{c}{\pi d}, \quad (5.5)$$

with c the sound velocity, d the diameter of the crystal, and η_{min} a numerical constant that is 2.05 for a spherical particle [40]. Below this cutoff no phonons are allowed. In the region above the cutoff, the phonon density of states exhibits gaps before it transitions into a continuous function described by Equation 5.1.

To simulate the phonon density of states for a spherical particle, the eigenmodes must first be calculated. They can be separated into spheroidal-transverse, spheroidal-longitudinal, and torsional modes. The characteristic equations needed to calculate

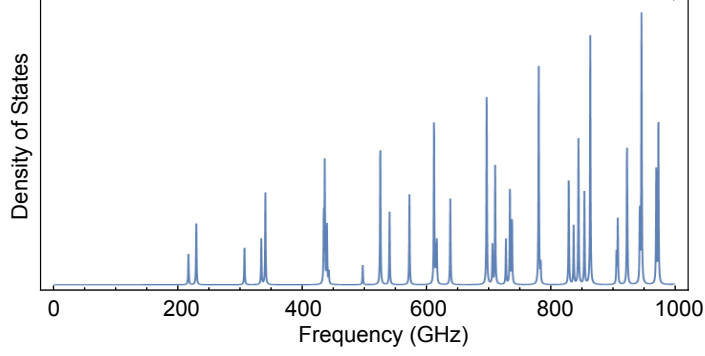


Figure 5.3.: Simulated phonon density of states in a Y_2SiO_5 nanoparticle with a diameter of 12 nm. Each eigenmode of the spherical particle is represented by a Lorentzian with a width of 1 GHz.

their frequencies have been described in a quantized form by Takagahara [41]. Each eigenmode is identified using three quantum numbers: the radial quantum number j , the angular momentum l , and σ , which specifies the type of mode. Using those eigenmodes, the phonon density of states can be written as [42]

$$\rho(\omega) = \sum_{j,l,\sigma} (2l+1) \frac{\Delta\omega}{(2\pi)^2} \left[(\omega - \omega_{l,j}^\sigma)^2 + \frac{\Delta\omega^2}{2} \right]^{-1}. \quad (5.6)$$

Each eigenmode is $2l+1$ times degenerate. We assume that the density of states is composed of Lorentzian shaped lines at the frequency of the respective eigenmode $\omega_{l,j}^\sigma$ and linewidth $\Delta\omega$. In the work of Meltzer and Hong [42], the Lorentzian width was assumed to increase with the frequency squared, an empirical assumption that described their particular experimental data adequately. However, since there is no theoretical framework to support that assumption, the width is assumed to be constant here.

In the case of $\text{Er}^{3+}:\text{Y}_2\text{SiO}_5$ around 1 T, we estimated from Eq. 5.28 that nanoparticles

of 12 nm diameter are suitable to suppress the direct phonon process. The phonon density of states for a Y_2SiO_5 nanoparticle of 12 nm diameter, calculated according to Equation 5.6, is shown in Figure 5.3. Phonon processes at frequencies below 200 GHz are fully restricted. This assumes that there is no phonon propagation between the particles. Simulating the effect of touching particles on phonon propagation is not trivial and subject further theoretical and experimental research. However, for a lightly packed powder immersed in cold helium gas we expect properties approaching those of single, isolated particles. Note that particles separated by electrostatic interaction can be obtained by coating the powder with the appropriate surfactant or by specific syntheses [43].

In powders, averaging of anisotropic properties over the random distribution of crystallite orientations generally causes issues in applications such as quantum memories and spectroscopy. However, if the material has a dielectric or magnetic anisotropy, the crystals can be preferentially oriented using external fields [44, 45]. This allows the control of parameters, such as Zeeman splittings and the direction of the ion's transition dipole moment. Scattering of laser light by powder samples can be reduced or even eliminated if the size of the crystals is smaller than the wavelength of the interacting light, since the powder can be treated as a bulk material with an effective (average) refractive index.

Crystal powders can be produced using several approaches and spectroscopic properties comparable to bulk crystals have been observed in some cases [46]. A thor-

ough review of different growth methods can be found in [47] and references therein. Growing nano/microcrystals has the advantage of being relatively inexpensive. An alternative way to produce nanocrystals is to grind a bulk crystal into powder using techniques such as ball milling. With this approach, sizes on the order of 10 nm are achievable by using very small grinding balls [48, 49]. However, reducing dimensions below around 10 nm may result in additional (detrimental) decoherence [50, 42] and lifetime limiting effects [51].

5.1.3.2. Restriction in phononic crystals

A second possibility to avoid detrimental phonons is to create a phononic band gap material [52, 53, 54] engineered to produce a gap in the density of states around the undesired frequencies. Such structures are employed in the field of optomechanics [55, 56], and are also used for thermal phonon engineering i.e. for thermal metamaterials and thermocrystals [57]. By changing the geometry and overall size of phononic crystal structures, it is possible to optimize the band gaps for a specific application [58].

Phononic crystal materials have the advantage of employing an oriented single crystal. In addition, the problem of contact between nanoparticles would be avoided. The fabrication of phononic band gap materials has already been explored for materials such as silicon or gallium arsenide [60] and phononic structures with a bandgap at 33 GHz and dimensions around 100 nm have been demonstrated [61]. To create

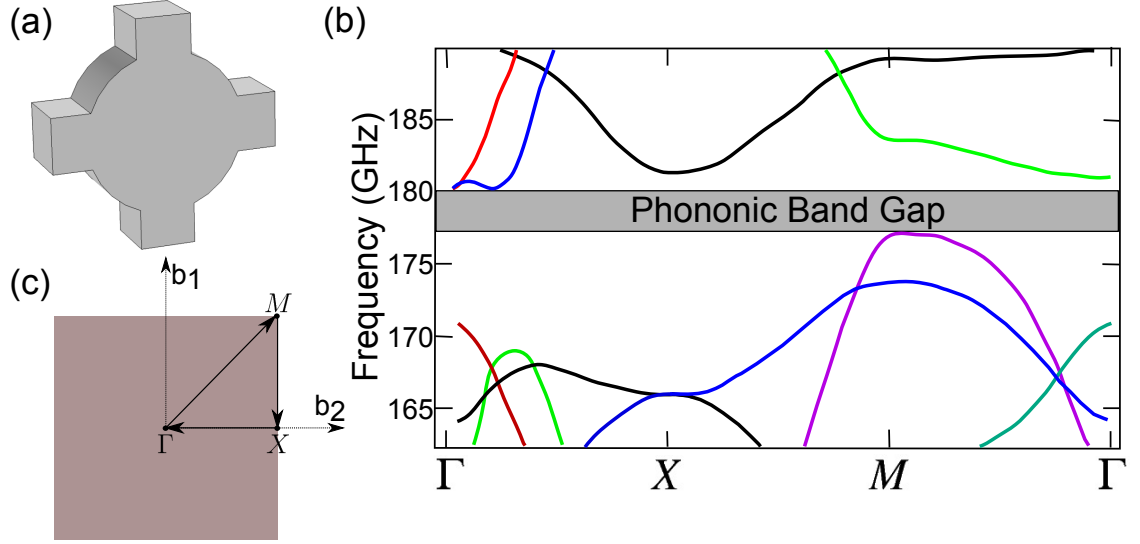


Figure 5.4.: (a) Unit cell of the proposed phononic crystal structure. The radius of the island is 9.5 nm, the width of the arms is 5 nm, and their length 5 nm. This structure is 7 nm thick. (b) Band structure of the phononic crystal in (a). The band gap (shaded grey) around the center frequency of 178 GHz is clearly visible. (c) Reciprocal lattice [59] showing the points traversed in the band structure.

phononic crystal structures in currently-used host materials such as Y_2SiO_5 , $\text{Y}_3\text{Al}_5\text{O}_{12}$ or LiNbO_3 , thin films of those materials would be a prerequisite. Thin films of LiNbO_3 are commercially available and there have been demonstrations of thin single-crystal film fabrication for other REI host materials [62, 63]. Finally, structuring these materials with nanometer precision has been shown to be feasible using focused ion beam milling [64, 65].

To illustrate this approach for our example of Er:YSiO , we designed and optimized a phononic structure using finite element simulations (COMSOL). The structure is inspired by designs of Safavi-Naeini et al. [66]. We engineered our structure such that it produces a band gap around 178 GHz with a width of 3.5 GHz. Figure 5.4 shows the

proposed geometry of the phononic crystal unit cell together with its band structure. Even though it is still challenging, the rapid progress in the field of nano-fabrication together with the discovery of helium focused ion beam milling allows structures with these dimensions to be fabricated out of a thin film [67, 68]. Through additional etching it is possible to remove part of the substrate below the phononic crystal such that the structure is suspended and only connected to the substrate at its borders. This ensures complete phonon suppression.

5.1.4. Conclusion

In summary, we propose to restrict phonon processes in REI-doped materials through nano-tailoring in order to improve persistent spectral hole burning and reduce spectral diffusion. We briefly discussed two methods towards this end – the use of nano-crystals and engineered phononic band gap structures – and described how our concept can be applied to well-studied Er-doped crystals. In turn, this would allow realizing optical quantum memories operating at convenient telecommunication wavelengths and increase the performance of other applications that are based on persistent spectral hole burning or that rely on narrow homogeneous line widths.

Acknowledgements: The authors acknowledge support from Alberta Innovates Technology Futures (ATIF), the Natural Sciences and Engineering Council of Canada (NSERC), the Canadian Institute for Advanced Research (CIFAR) of which W.T. is

a Senior Fellow, and the National Science Foundation of the United States (NSF) under Award No. PHY-1212462, No. PHY-1415628, and No. CHE-1416454.

Bibliography

- [1] R. M. Macfarlane and R. M. Shelby, in *Modern Problems in Condensed Matter Sciences*, vol. 21 of *Spectroscopy of Solids Containing Rare Earth Ions*, A. A. K. a. R. M. Macfarlane, ed. (Elsevier, 1987), pp. 51–184.
- [2] G. Liu and B. Jacquier, *Spectroscopic Properties of Rare Earths in Optical Materials* (Springer Berlin Heidelberg, 2005).
- [3] Y. Sun, C. Thiel, R. Cone, R. Equall, and R. Hutcheson, *Journal of Luminescence* **98**, 281 (2002).
- [4] T. Böttger, Y. Sun, C. W. Thiel, and R. L. Cone, *Phys. Rev. B* **74**, 075107 (2006).
- [5] C. W. Thiel, T. Böttger, and R. L. Cone, *Journal of Luminescence* **131**, 353 (2011).
- [6] C. Thiel, N. Sinclair, W. Tittel, and R. Cone, *Physical Review Letters* **113**, 160501 (2014).
- [7] A. I. Lvovsky, B. C. Sanders, and W. Tittel, *Nature of Photonics* **3**, 706 (2009).

- [8] N. Sangouard, C. Simon, H. de Riedmatten, and N. Gisin, *Rev. Mod. Phys.* **83**, 33 (2011).
- [9] F. Bussi eres, N. Sangouard, M. Afzelius, H. de Riedmatten, C. Simon, and W. Tittel, *Journal of Modern Optics* **60**, 1519 (2013).
- [10] W. R. Babbitt, Z. W. Barber, S. H. Bekker, M. D. Chase, C. Harrington, K. D. Merkel, R. K. Mohan, T. Sharpe, C. R. Stiffler, A. S. Traxinger, and A. J. Woidtke, *Laser Physics* **24**, 094002 (2014).
- [11] E. Saglamyurek, N. Sinclair, J. A. Slater, K. Heshami, D. Oblak, and W. Tittel, *New Journal of Physics* **16**, 065019 (2014).
- [12] P. B. Sellin, N. M. Strickland, J. L. Carlsten, and R. L. Cone, *Opt. Lett.* **24**, 1038 (1999).
- [13] M. J. Thorpe, L. Rippe, T. M. Fortier, M. S. Kirchner, and T. Rosenband, *Nature Photonics* **5**, 688 (2011).
- [14] C. W. Thiel, R. L. Cone, and T. B ottger, *Journal of Luminescence* **152**, 84 (2014).
- [15] V. Lavielle, I. Lorg er , J.-L. Le Gou  t, S. Tonda, and D. Dolfi, *Optics Letters* **28**, 384 (2003).
- [16] F. Schlottau, M. Colice, K. H. Wagner, and W. R. Babbitt, *Opt. Lett.* **30**, 3003 (2005).
- [17] M. Fleischhauer and M. D. Lukin, *Physical Review Letters* **84**, 5094 (2000).

- [18] H. de Riedmatten, M. Afzelius, M. U. Staudt, C. Simon, and N. Gisin, *Nature* **456**, 773 (2008).
- [19] B. Kraus, W. Tittel, N. Gisin, M. Nilsson, S. Kröll, and J. I. Cirac, *Physical Review A* **73**, 020302 (2006).
- [20] T. Böttger, C. W. Thiel, Y. Sun, and R. L. Cone, *Phys. Rev. B* **73**, 075101 (2006).
- [21] N. Sinclair, E. Saglamyurek, M. George, R. Ricken, C. L. Mela, W. Sohler, and W. Tittel, *Journal of Luminescence* **130**, 1586 (2010). Special Issue based on the Proceedings of the Tenth International Meeting on Hole Burning, Single Molecule, and Related Spectroscopies: Science and Applications (HBSM 2009) - Issue dedicated to Ivan Lorgere and Oliver Guillot-Noel.
- [22] Y. Sun, C. W. Thiel, and R. L. Cone, *Phys. Rev. B* **85**, 165106 (2012).
- [23] G. Liu and X. Chen, in *Handbook on the Physics and Chemistry of Rare Earths*, vol. Volume 37, J.-C. B. a. V. K. P. Karl A. Gschneidner, ed. (Elsevier, 2007), pp. 99–169.
- [24] K. D. Jahnke, A. Sipahigil, J. M. Binder, M. W. Doherty, M. Metsch, L. J. Rogers, N. B. Manson, M. D. Lukin, and F. Jelezko, *New Journal of Physics* **17**, 043011 (2015).
- [25] H.-S. Yang, S. P. Feofilov, D. K. Williams, J. C. Milora, B. M. Tissue, R. S. Meltzer, and W. M. Dennis, *Physica B: Condensed Matter* **263264**, 476 (1999).

- [26] G. K. Liu, H. Z. Zhuang, and X. Y. Chen, Nano Letters **2**, 535 (2002).
- [27] R. Orbach, Proceedings of the Royal Society of London. Series A. Mathematical and Physical Sciences **264**, 458 (1961).
- [28] I. N. Kurkin and K. P. Chernov, Physica B+C **101**, 233 (1980).
- [29] K. Gschneider, J. Buezli, and V. Pecharsky, eds., *Handbook on the Physics and Chemistry of Rare Earths Volume 37 Chapter 4.3* (North-Holland, 2007).
- [30] T. Böttger, C. W. Thiel, R. L. Cone, and Y. Sun, Physical Review B **79**, 115104 (2009).
- [31] C. W. Thiel, R. M. Macfarlane, T. Böttger, Y. Sun, R. L. Cone, and W. R. Babbitt, Journal of Luminescence **130**, 1603 (2010).
- [32] T. Böttger, C. W. Thiel, Y. Sun, R. M. Macfarlane, and R. L. Cone, Journal of Luminescence **169**, 466-471 (2015).
- [33] S. R. Hastings-Simon, B. Lauritzen, M. U. Staudt, J. L. M. van Mechelen, C. Simon, H. de Riedmatten, M. Afzelius, and N. Gisin, Phys. Rev. B **78**, 085410 (2008).
- [34] B. Lauritzen, S. R. Hastings-Simon, H. de Riedmatten, M. Afzelius, and N. Gisin, Phys. Rev. A **78**, 043402 (2008).
- [35] B. Lauritzen, J. c. v. Minář, H. de Riedmatten, M. Afzelius, and N. Gisin, Phys. Rev. A **83**, 012318 (2011).

- [36] R. M. Macfarlane and J. C. Vial, Physical Review B **36**, 3511 (1987).
- [37] E. Saglamyurek, T. Lutz, L. Veissier, M. P. Hedges, C. W. Thiel, R. L. Cone and W. Tittel, Physical Review B **92**, 241111(R) (2015)
- [38] R. M. Macfarlane, Y. Sun, P. B. Sellin, and R. L. Cone, Physical Review Letters **96**, 033602 (2006).
- [39] T. Böttger, “Laser frequency stabilization to spectral hole burning frequency references in erbium-doped crystals: Material and device optimization”, Ph.D. thesis, Montana State University (2002).
- [40] H. Lamb, Proceedings of the London Mathematical Society **s1-13**, 189 (1881).
- [41] T. Takagahara, Journal of Luminescence **70**, 129 (1996).
- [42] R. S. Meltzer and K. S. Hong, Phys. Rev. B **61**, 3396 (2000).
- [43] J. Park, K. An, Y. Hwang, J.-G. Park, H.-J. Noh, J.-Y. Kim, J.-H. Park, N.-M. Hwang, and T. Hyeon, Nat Mater **3**, 891 (2004).
- [44] D. Schütze, B. Knabe, M. Ackermann, and K. Buse, Applied Physics Letters **97**, 242908 (2010).
- [45] J. Akiyama, Y. Sato, and T. Taira, Optics Letters **35**, 3598 (2010).
- [46] A. Perrot, P. Goldner, D. Giaume, M. Lovri, C. Andriamiadamanana, R. R. Goncalves, and A. Ferrier, Physical Review Letters **111**, 203601 (2013).
- [47] B. M. Tissue, Chemistry of Materials **10**, 2837 (1998).

- [48] D. Bork and P. Heitjans, The Journal of Physical Chemistry B **102**, 7303 (1998).
- [49] H. J. Song, J. H. Noh, H.-S. Roh, J. S. Kim, D.-W. Kim, and K. S. Hong, Current Applied Physics **13**, **Supplement 2**, S69 (2013).
- [50] F. T. H. den Hartog, C. van Papendrecht, R. J. Silbey, and S. Völker, The Journal of Chemical Physics **110**, 1010 (1999).
- [51] L. Aminov, I. Kurkin, and D. Lukoyanov, Applied Magnetic Resonance **14**, 447 (1998).
- [52] F. R. Montero de Espinosa, E. Jiménez, and M. Torres, Phys. Rev. Lett. **80**, 1208 (1998).
- [53] J. V. Sánchez-Pérez, D. Caballero, R. Martínez-Sala, C. Rubio, J. Sánchez-Dehesa, F. Meseguer, J. Llinares, and F. Gálvez, Phys. Rev. Lett. **80**, 5325 (1998).
- [54] W. M. Robertson and J. F. Rudy, The Journal of the Acoustical Society of America **104**, 694 (1998).
- [55] T. P. M. Alegre, A. Safavi-Naeini, M. Winger, and O. Painter, Opt. Express **19**, 5658 (2011).
- [56] J. Chan, A. H. Safavi-Naeini, J. T. Hill, S. Meenehan, and O. Painter, Applied Physics Letters **101**, 081115 (2012).
- [57] M. Maldovan, Nature **503**, 209 (2013). Review.

- [58] O. R. Bilal and M. I. Hussein, Phys. Rev. E **84**, 065701 (2011).
- [59] C. Kittel, *Introduction to solid state physics* (Wiley, 2004).
- [60] J. Petrus, R. Mathew, and J. Stotz, Ultrasonics, Ferroelectrics, and Frequency Control, IEEE Transactions on **61**, 364 (2014).
- [61] D. F. Goettler, M. F. Su, C. M. Reinke, S. Alaie, P. E. Hopkins, R. H. Olsson, I. El-Kady, and Z. C. Leseman, AIP Advances **1**, 042001 (2011).
- [62] G. R. Bai, H. L. M. Chang, and C. M. Foster, Applied Physics Letters **64**, 1777 (1994).
- [63] O. Gaathon, J. D. Adam, S. V. Krishnaswamy, J. W. Kysar, S. Bakhru, H. Bakhru, D. O. Welch, and R. M. Osgood Jr., Optical Materials **35**, 25 (2012).
- [64] F. Lacour, N. Courjal, M.-P. Bernal, A. Sabac, C. Bainier, and M. Spajer, Optical Materials **27**, 1421 (2005).
- [65] T. Zhong, J. M. Kindem, E. Miyazono, and A. Faraon, Nature Communications, **6**, 8206 (2015).
- [66] A. H. Safavi-Naeini and O. Painter, Opt. Express **18**, 14926 (2010).
- [67] O. Scholder, K. Jefimovs, I. Shorubalko, C. Hafner, U. Sennhauser, and G.-L. Bona, Nanotechnology **24**, 395301 (2013).
- [68] N. Kalhor, S. A. Boden, and H. Mizuta, Microelectronic Engineering **114**, 70 (2014).

5.2. Powder fabrication methods

All the experimental work towards the restriction of phonons in REI-doped materials that is presented here has been performed on powder materials. This section will describe approaches that can be used to fabricate these powders. Since the main focus of this thesis is on the understanding and modification of spectroscopic properties of structured materials, the following is meant to provide a working understanding of the different methods rather than an in-depth knowledge of the involved chemical processes. The references to the specific methods used can be found in the respective papers (sections 5.3 and 5.4).

5.2.1. Mechanical processing

Powders can be fabricated using the so-called top-down approach through various crushing techniques. In most cases, the original bulk crystal is pre-crushed with a mortar and pestle or a jaw-crusher. The size of the crystallites can then be further reduced down to the nanometer range using various types of ball mills such as high-energy planetary mills or low-energy tumbling mills as described in chapters 5.3 and 5.4. The container of a ball mill is usually filled with spheres made from a material that is much harder than the powder to be crushed, e.g. zirconia or aluminum oxide, the pre-crushed powder itself, and a solvent such as ethanol or water. The impacts between the powder and the balls then reduce the powder's size; the final size can reach a few nanometers and depends on the balls that are used and the milling time.

This kind of mechanical processing usually creates a large amount of crystal strain and defects due to the high-energy impacts. This is true even for low-energy tumbling mills. Therefore, in many cases it is favorable to fabricate powders using chemical syntheses as described in the following.

5.2.2. Chemical synthesis

Fabricating powders using a bottom-up approach, i.e. via chemical synthesis, is appealing since it promises avoiding detrimental strain and defects that are inevitably caused by mechanical processing. Furthermore, using chemical synthesis makes the need for a good-quality bulk crystal, which is only available for a relatively small subset of materials, obsolete. Often, there are many different ways to synthesize a given material. Powders mentioned in this thesis were fabricated using sol-gel synthesis, coprecipitation or solid-state synthesis. Each of these techniques is briefly described hereafter:

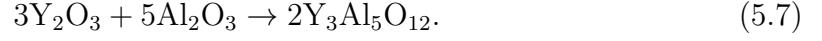
Sol-gel synthesis: Sol-gel synthesis is a very versatile and relatively simple way to produce powders. Most of the synthesized powders mentioned in the subsequent papers (chapters 5.3, 5.4 and 5.7) were created using this method. The name of the process "sol-gel" partially describes the method. First, various precursors are put into solution (sol) in which the individual particles are suspended by Brownian motion. Note that the desired REI impurities are also introduced in this step, and since they also dissolve, they are distributed in a uniform way in the resulting powder. Then,

the various solutions are mixed together, and after time, a gel containing a liquid and a solid phase of either discrete particles or polymer networks is formed. In case of host materials such as $\text{Y}_3\text{Al}_5\text{O}_{12}$ (YAG) , Y_2SiO_5 and LiNbO_3 , the different metal centers are cross-linked during the formation of the gel and the solid state structure evolves at an atomic level [55].

During the mixing of the solutions, various surfactants can be introduced to partially control the powder size and morphology after calcination, as described in paper 5.3. However, due to the high calcination temperatures required for our host materials, no surfactant was found to be able to produce non-agglomerated, small particles. After the gel has formed, it is usually dried, i.e. all solvents are evaporated. We found that the drying step can be critical for the morphology of the powder that is obtained after calcination. In most cases, fast drying at elevated temperatures between 80 and 100 C produced dense, strongly agglomerated powders. Freeze-drying at cold temperatures below -40 C and under vacuum produced less agglomeration.

During the calcination step the individual crystal grains grow and the bulk crystal structure forms. Different materials have different calcination temperatures. All materials mentioned in this thesis were calcined around 1000 C. Lower calcination temperatures favor smaller particles but usually produce poorer crystal quality in terms of residual strain and lattice defects. Higher temperatures create larger particles with generally better crystal quality. The detailed reactions for the different materials mentioned in this thesis are all different and can be found in the corresponding references listed in the respective papers. As an example, we synthesized $\text{Y}_3\text{Al}_5\text{O}_{12}$ using the sol-gel method. As precursors, yttrium oxide powder and aluminum oxide were

used, both of which were dissolved in water. At calcination temperatures > 900 C the desired $Y_3Al_5O_{12}$ is formed [56]



Note that depending on the specific calcination temperature, different, unwanted, crystal phases such as $YAlO_3$ may be created.

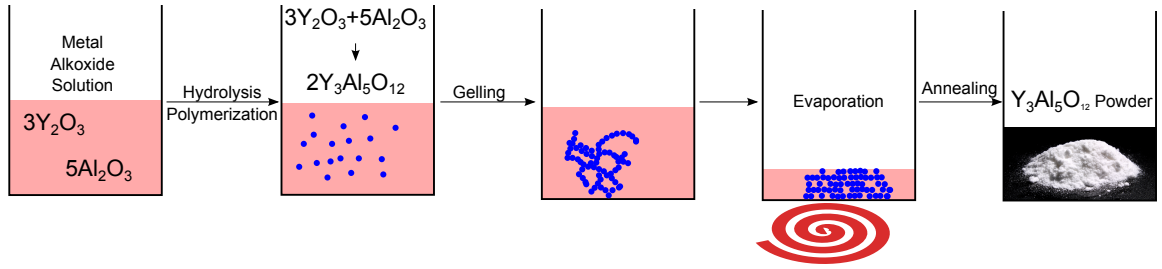


Figure 5.5.: Flow diagram of the sol-gel synthesis used to produce YAG powders. For a detailed description see main text.

Coprecipitation: Coprecipitation is another wet chemistry method to synthesize powder materials; it is similar to the sol-gel method in many ways. As for the sol-gel method, the precursors are put in solution and mixed together. For coprecipitation this solution is usually acidic. However, as opposed to the sol-gel method, there is no formation of a solid phase at this step. Precipitation, the process during which the desired material forms from the dissolved precursors and then sinks to the bottom of the solution is usually induced by the slow addition of a base. Following the precipitation, the precipitate is washed to remove all solvents and other undesired chemicals that are still in the solution. The washing is carried out by repeatedly adding a solvent, e.g. water or ethanol, and then removing it again through filtration

or centrifugation. After each washing step a secondary solvent such as ethanol or water is added. After the final filtration/centrifugation step the precipitate is dried. Again, as for the sol-gel method, the detailed way this step is carried out influences the final powder's morphology and agglomeration. Finally, the powder formation is concluded by a calcination step.

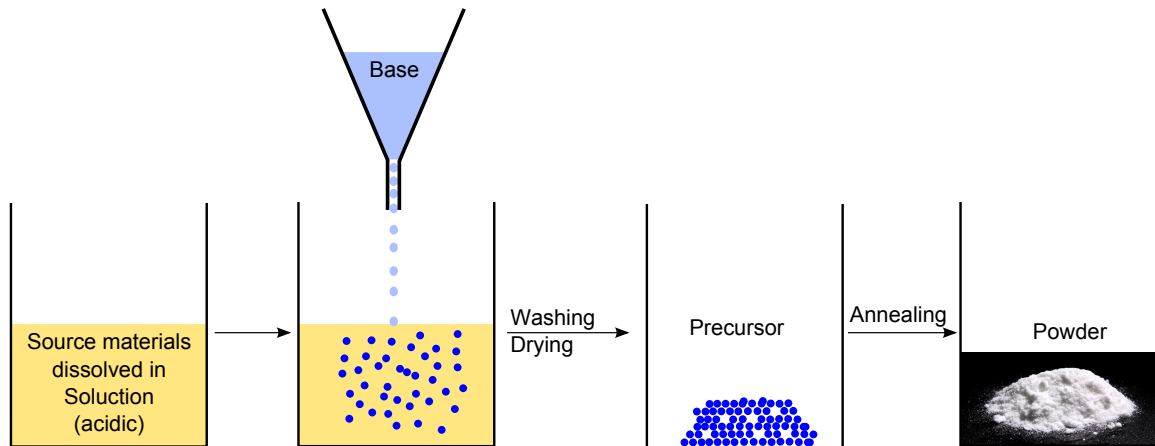


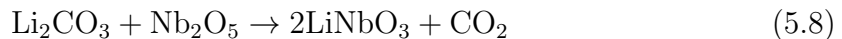
Figure 5.6.: Schematic of a typical coprecipitation synthesis. The target material forms in the solution of source materials after addition of a base.

Solid-state synthesis: Solid-state synthesis is a method that is even simpler to perform than the wet chemistry methods mentioned above. Here the precursors are present in form of solids. In order to facilitate reaction between the precursors, they are usually ground into very small powders using a mortar and pestle or even mixed together in ball mills. This grinding and mixing creates large areas of contact at which the desired reaction and the formation of the new material can take place.

At the interface between two different precursors, the two materials can diffuse into each other, react and thereby form a layer of the desired material. The efficiency of the process is determined by the efficiency of this diffusion process. The latter can

be enhanced by increasing the sample temperature or by using materials that decompose easily during reaction. Common precursors are nitrates or carbonates [57]. Sometimes the reaction between the precursors is accelerated by adding fuel such as urea [58], a process then referred-to as combustion synthesis. The rate at which the final material is formed can also be enhanced by selecting precursors that have similar crystal structure as the outcome. As in the other synthesis approaches, the resulting particle size and crystal quality is dependent on the temperature at which the solid-state reaction is carried out.

As an example, we employed solid-state synthesis to fabricate LiNbO_3 powders (see paper 5.4). As precursors, lithium carbonate (Li_2CO_3) and niobium pentoxide (Nb_2O_5) were used and mixed together using a mortar and pestle. During the calcination (mostly below 800 C) LiNbO_3 forms through the following reaction:



Due to its piezoelectric effect LiNbO_3 is a very widely used material and thus many routes to synthesize it are known. In general, however, due to the high reactivity of lithium and possible out-diffusion of oxygen at high temperatures it is challenging to perform these reactions. The specific details are mentioned in paper 5.4.

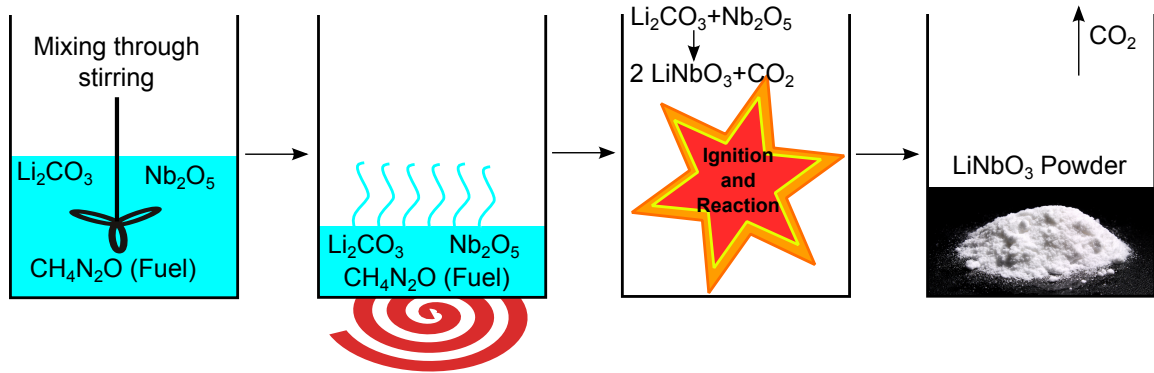


Figure 5.7.: Schematic illustrating the process of combustion synthesis with the example of LiNbO_3 . The process is described in detail in the main text.

5.3. Paper 2: Effects of fabrication methods on spin relaxation and crystallite quality in rare-earth-ion doped powders studied using spectral hole burning

Science and Technology of Advanced Materials, **17**, 63, 16 Mar 2016

5.3.1. Summary

In Paper 2, we study the change of population lifetimes of nuclear spin states during the transition from a high-quality bulk $\text{Y}_3\text{Al}_5\text{O}_{12}$ crystals to nano powders. Since our ultimate goal was to extend population lifetimes through phonon restriction, it was important to ensure that the fabrication of nano powders does not introduce detrimental effects that prevent one from observing the desired improvement of properties. We employed spectral hole burning as a method to quantify the properties of each

powder. The results showed that spectral hole burning is more sensitive in detecting certain crystal imperfections than techniques like X-ray diffraction.

Powders with various sizes were fabricated from the same bulk material using mechanical processing, i.e. crushing using a mortar and pestle and ball mills. Despite the assumption that the lifetimes of nuclear spin states would be rather insensitive to the crystal environment, it was discovered that population lifetimes decrease when the sizes of the powders were reduced, regardless of the specific method. In the manuscript we also investigate to what degree thermal annealing can restore bulk properties and show that in some cases where only limited processing is performed, the original properties can be achieved through annealing. However, for the smallest powders, as required to suppress phonons, this was not possible and residual crystal strain and induced defects decrease population lifetimes by orders of magnitude.

Together with the co-author Lucile Veissier, I performed all experiments that were required to obtain the data and conclusions listed in the paper. The experiments were performed in the laboratory of Charles Thiel and Rufus Cone. I analyzed most of the experimental data and wrote the initial draft of the manuscript.

**Effects of fabrication methods on spin relaxation and crystallite quality
in Tm-doped $\text{Y}_2\text{Al}_5\text{O}_{12}$ powders studied using spectral hole burning**

Thomas Lutz¹, Lucile Veissier^{1†}, Charles W. Thiel², Philip J. T. Woodburn², Rufus

L. Cone², Paul E. Barclay¹ and Wolfgang Tittel¹

¹*Institute for Quantum Science and Technology, and Department of Physics &
Astronomy, University of Calgary, Calgary Alberta T2N 1N4, Canada*

²*Department of Physics, Montana State University, Bozeman, MT 59717 USA*

[†] *Present address: Laboratoire Aimé Cotton, CNRS-UPR 3321, Univ. Paris-Sud,
Bât. 505, F-91405 Orsay Cedex, France*

**Corresponding author: thomasl@ucalgary.ca*

Abstract: High-quality rare-earth-ion (REI) doped materials are a prerequisite for many applications such as quantum memories, ultra-high-resolution optical spectrum analyzers and information processing. Compared to bulk materials, REI doped powders offer low-cost fabrication and a greater range of accessible material systems. Here we show that crystal properties, such as nuclear spin lifetime, are strongly affected by mechanical treatment, and that spectral hole burning can serve as a sensitive method to characterize the quality of REI doped powders. We focus on the specific case of thulium doped $\text{Y}_2\text{Al}_5\text{O}_{12}$ (Tm:YAG). Different methods for obtaining the powders are compared and the influence of annealing on the spectroscopic quality of powders is investigated on a few examples. We conclude that annealing can reverse some detrimental effects of powder fabrication and, in certain cases, the properties of the bulk material can be reached. Our results may be applicable to other impurities and

other crystals, including color centers in nano-structured diamond.

5.3.2. Introduction

Rare-earth-ion (REI) doped bulk crystals cooled to cryogenic temperatures are used for a multitude of applications. Examples are quantum memories [1], quantum information processing [2], and ultra-high-resolution optical spectrum analyzers [3]. In contrast to REI doped bulk materials, powders offer low cost and rapid prototyping. Furthermore, the understanding of powders constitutes a first step towards nanofabrication of devices from these materials [4, 5, 6, 7]. However, despite much effort [8, 9, 10, 11], producing monodisperse powders with properties comparable to those of bulk materials remains challenging.

Fabrication or manipulation of REI doped powders can induce stress, especially during grinding or milling, that creates strain in the crystal lattice [12, 13]. In addition, impurities can contaminate the host matrix during synthesis. Strain and impurities often significantly impact the performance of the powders in both signal processing and more general luminescence applications. The goal of this work is to study REI doped powders at temperatures near 1.6 K and improve their properties to reach those of bulk materials. Towards that goal, we compared properties of powders that were synthesized chemically or milled down from larger crystals using either high-energy planetary ball mills or low-energy tumbling mills. We used scanning electron microscope (SEM) to determine the shape and size of the particles, x-ray diffraction (XRD) to analyze the composition and phase of the crystalline structure, and we

employed sensitive spectral hole burning (SHB) methods to probe variations in the optical decoherence dynamics, deduced from the spectral hole width, and the ^{169}Tm nuclear spin relaxation dynamics, deduced from the spectral hole lifetime. We find that induced damage and strain in the crystal lattice, which does not affect XRD or SEM measurements, can produce large variations in the measured low-temperature dynamics of the powders that are observed using SHB techniques. Thus, SHB can serve as a quantitative characterization tool, complementing traditional techniques such as XRD, SEM or Raman scattering. Our results also demonstrate that mechanical and thermal treatment of REI doped crystals influences properties, such as the lifetime of nuclear spins, in a surprisingly strong way. Consequently, SHB is a well-suited technique to reveal the presence of residual damage in powders due to fabrication and to evaluate the effectiveness of methods used to reduce strain and improve material quality, such as thermal annealing.

5.3.3. Experiment

5.3.3.1. Tm:YAG

Our investigations employ crystalline $\text{Y}_3\text{Al}_5\text{O}_{12}$ doped with thulium impurities (Tm:YAG), whose relevant electronic level structure is shown in Figure 5.8. Under an external magnetic field, both the 3H_6 ground state and the 3H_4 excited state split into two non-degenerate states through the hyperfine interaction with the ^{169}Tm nuclear spin ($I = 1/2$), allowing persistent atomic population storage with lifetimes as long as hours in bulk crystals at liquid helium temperatures through optical pumping of the

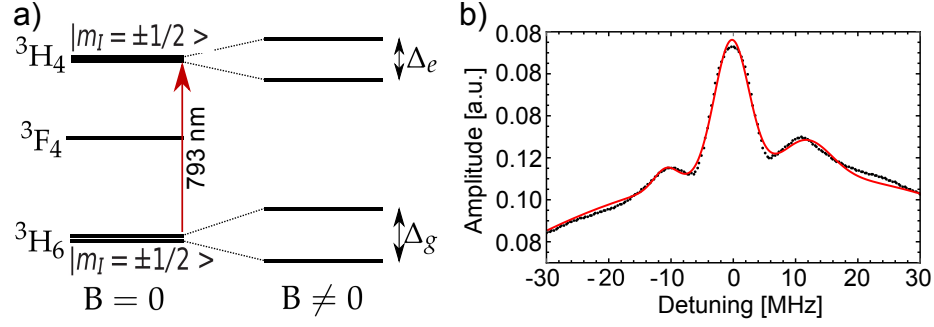


Figure 5.8.: a) Level structure of Tm:YAG without and with an applied magnetic field. b) Hole burning spectrum of the 1% Tm:YAG bulk crystal together with a fit (red line).

nuclear spin states.

The 20 GHz wide inhomogeneously broadened line of the $^3H_6 \leftrightarrow ^3H_4$ transition in Tm:YAG is centered at 793.156 nm [14]. The samples were mounted in an Oxford Instruments Spectromag cryostat and all powders were held in unsealed glass cuvettes. All samples were 0.5 mm thick, and, for the nominal Tm concentration of 1%, featured an optical depth of ≈ 1 . This allowed for direct transmission detection of spectral holes while keeping optical scattering at an acceptable level. To prevent scattered light from reaching the detector, the cuvette was placed inside a copper box with two pinholes to allow light to enter and exit. For all measurements, the samples were cooled in helium vapor to 1.6 K and the applied magnetic field was set to 1 T.

5.3.3.2. Spectral hole burning

To assess the quality of different powders, we used persistent spectral holes. We extracted the lifetime of the spin states from the hole decay, and the magnitude of optical decoherence from the width of the hole [15]. As we describe later, we found that both quantities strongly depend on the crystal quality in terms of strain as well

as impurities. In this approach, a spectral hole is burnt into the inhomogeneously broadened absorption line by using a laser to optically pump population between the nuclear spin states. After a certain waiting time, the absorption line is scanned using a tunable laser and the area of the spectral hole is measured. From the exponential decay of the hole area with waiting time, the spin lifetime is extracted. Note that the width of the spectral hole ideally corresponds to twice the homogeneous linewidth; however, the measured width is generally larger due to laser frequency jitter, spectral diffusion, and power broadening.

We used a Coherent 899-21 Ti:sapphire laser emitting at a wavelength of 793.38 nm and with a linewidth of less than 1 MHz. For the bulk single crystal measurement that served as a reference for the best material properties, the laser power was set to 5 μ W. For the powder samples, more power was necessary to overcome loss due to scattering and achieve a sufficiently high signal-to-noise ratio. Otherwise, the experimental conditions were kept the same for all materials. The burn and read pulses were generated from the CW laser beam using two acousto-optic modulators (AOMs) in series. This arrangement gave an extinction ratio of >90 dB, ensuring that no unintentionally leaked light reached the sample. During the reading pulse, the laser sweep was implemented using a double-passed AOM scanned in frequency. A New Focus model 2051 photo-receiver was used to detect the transmitted light.

5.3.3.3. Bulk single crystal reference

First, as a reference against which we compare the properties of our Tm:YAG powders (the different methods used to create these powders are described below), we assessed

the properties of a 1% doped Tm:YAG crystal from Scientific Materials Corporation (SMC) (growth number 3-8). The crystal is 0.5 cm thick and features an optical depth of about 0.5. Depending on the crystal orientation, we found spin lifetimes between 5 and 16 hours [16]. Furthermore, as shown in Figure 5.8 b), the observed spectral hole width was limited to 6 MHz – much wider than the intrinsic kHz-wide homogeneous linewidth of Tm:YAG [17] under these conditions – primarily due to power broadening effects. The figure also shows clear side holes, split by 10 MHz/T and caused by super-hyperfine coupling between the thulium ions and the nuclear spin of the ^{27}Al present in the host matrix [15, 18]. Because powders are composed of randomly oriented crystallites, measurements of powders probe all possible orientations at once and we expect to observe lifetimes that span the range of those observed in the bulk material.

5.3.4. Results

In the following, we study the impact of fabrication and annealing methods on nuclear spin lifetimes T_a as well as on hole linewidths Γ . Due to the strong scattering caused by the powders, higher laser power was required for these measurements, leading to additional power broadening. As a consequence, hole linewidths were measurable only down to approximately 10 MHz. A summary of the properties of all investigated materials is shown in Table 5.1.

In addition, we performed SEM imaging and powder XRD analysis to further characterize each sample. Example powder XRD spectra are shown in Figure 5.9 for a selected subset of our samples. The spectra were obtained with a Scintag Inc X-1, Ad-

Material	size [μm]	Γ [MHz]	T_a [min]
SMC Bulk		6	300-960
SMC thermal crushing:	500	\lesssim 10	60
annealed:	500	\lesssim 10	420
SMC low energy BM*:	< 0.1	28.6	20
annealed:	< 1	17.2	60
Crytur:	30-50	\lesssim 10	60
annealed:	30-50	\lesssim 10	60
Crytur low energy BM:	< 0.1	23	15
annealed:	< 1	\lesssim 10	20
Crytur high energy BM:	< 2	\lesssim 10	10
Chemical synthesis:	< 0.1	26.6	2

Table 5.1.: Hole widths (Γ) (bold fonts indicate visible side holes), and lifetimes (T_a) of all measured materials at 1.6 K and $B = 1$ T. *ball milled

vanced Diffraction System. We find that all the analyzed samples formed the expected crystalline structure of YAG. Small deviations from the reference spectrum (JCPDS # 30-0040) can be observed for some samples. Differences in peak heights can be assigned mostly to sample preparation issues, while additional peaks correspond to the presence of residual amounts of impurity phases [19].

5.3.4.1. Crushing and ball milling

Our first approach to obtain small powders was “top-down” fabrication starting from a 1% doped Tm:YAG bulk single crystal originating from the same growth as the one studied above. To pre-crush the crystal, we heated the bulk crystal to ≈ 500 °C and then immersed the hot crystal in water (21 °C) to thermally shock the crystal, causing it to crack into millimeter and larger sized pieces. This procedure was repeated on all pieces with sizes greater than ≈ 5 mm until all were in the few millimeter or smaller size range. We then ground the small pieces in a mortar and pestle to

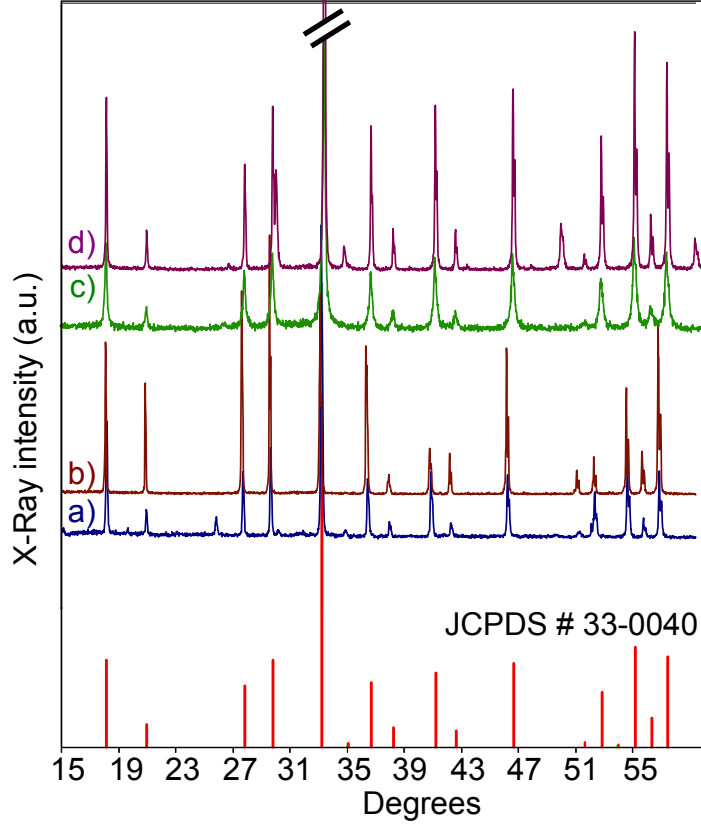


Figure 5.9.: XRD spectra of selected powders together with the reference spectrum (JCPDS # 30-0040) of YAG. a) Chemical synthesis, b) Crytur non-annealed, c) SMC low energy ball milled, d) SMC low energy ball milled and annealed.

produce a powder composed of crystallites with sizes of less than 0.5 μm . With spectral hole burning spectroscopy, we measured a hole width of $\lesssim 10$ MHz, limited by power broadening. Side holes due to superhyperfine coupling with ^{27}Al nuclear spins were still resolvable, as in the bulk material. The spin lifetime was on the order of 1 hour – significantly shorter than the values obtained in the bulk material at the same temperature and magnetic field. Since this powder originated from a bulk crystal whose properties were well characterized, and was composed of relatively large particles of ≈ 0.5 μm size that had been ground only for a short time, it is unlikely that any change in chemical composition or in-diffusion of impurities could have

occurred (as might be a factor for much smaller particles when processed using high-energy methods). The only explanation for the significant reduction in lifetime was residual strain induced in the crystallites due to the thermal shocking and grinding used to produce the powder.

With the < 0.5 mm sized crushed powder as a starting material, we produced a smaller powder using a low-speed tumbling mill. The Tm:YAG powder was dispersed in ethanol and milled for 48 hours using a mix of zirconia balls with sizes ranging from 1 mm to 1 cm. Figure 5.10 a) shows an SEM image of the obtained powder. The average size of the irregular particles was below 100 nm. The XRD spectrum, shown in Figure 5.9 c), displays the expected YAG structure with no observable peak broadening or amorphous background. A spectral hole burning trace, shown in Figure 5.10 c), revealed a hole width of 28.6 MHz. The hole was about 5 times larger than that observed in the bulk, which could not solely be attributed to additional power broadening and reveals a significant difference in the material not detectable from our XRD measurement. No sideholes were visible, which was expected since their splitting (10 MHz at $B = 1$ T) is less than the spectral hole width. Moreover, we found a further reduction of the spin lifetime to 20 minutes. Overall, as opposed to the XRD analysis, the SHB results suggest that a significant amount of damage (strain) was induced in the crystallites during the 2 days of milling.

The surprisingly strong effect of mechanical strain on coherence and spin relaxation dynamics may be understood within the framework of the two-level system (TLS) model first developed to describe dynamic disorder modes in amorphous materials

[20, 21]. These very low-frequency modes are enabled by the disordered structure and involve groups of atoms tunneling between local configurations with nearly equivalent energies. It has been proposed that low densities of TLS may also be enabled in crystalline materials by large inhomogeneous lattice strains [22], and optical decoherence of rare-earth ions due to interactions with TLS has been observed in both bulk crystals [23, 24] and powders [25]. Furthermore, it is known that TLS can also be effective in causing rapid electron and nuclear spin relaxation [26, 27, 28]. Here, both the increase in spectral hole widths and the decrease in nuclear spin lifetimes that we observe in powders are likely to result from the creation of TLS from strain induced during the mechanical fabrication process. This interpretation is also consistent with past observations of increased electronic spin-lattice relaxation rates of Nd^{3+} doped into bulk YAG crystals with greater densities of structural defects in the lattice [29].

5.3.4.2. Effects of annealing

Next, we investigated to what degree annealing of the powders can repair the induced damage. After we confirmed that low annealing temperatures around 600 °C were unable to improve material properties, and since higher temperatures generally lead to better properties [30], we annealed both the 0.5 mm and the 100 nm powders at our highest accessible temperature of 1400 °C. The annealing was performed for 4 hours in an oxygen atmosphere (using a tube furnace) to minimize the outdiffusion of oxygen from the YAG matrix. The 0.5 mm annealed crystals appeared unchanged under the SEM. The spin-state lifetime improved significantly to 7 hours and became comparable to that extracted from measurements on the bulk. This suggests that

annealing can mostly repair the damages induced by stress during the grinding via mortar and pestle.

The SEM image of the annealed 100 nm powder, shown in Figure 5.10 b), reveals that the size of the particles increased to around 1 μm . The particles were almost spherical, with close to uniform size distribution, and appeared to be agglomerated. Compared to the same powder before annealing (panel a)) this is a major improvement. The XRD spectrum, shown in Figure 5.9 d), shows no significant change compared to the non-annealed powder. The signal-to-noise ratio in this spectrum is better than the one in the spectrum for the non-annealed powder since more material was available for analysis. This indicates that, in contrary to the SHB measurement, the current XRD analysis is not sensitive enough to detect the changes caused by annealing for this powder. Indeed, the hole burning spectrum in Figure 5.10 d) shows a hole width of 17.2 MHz, which is 30% smaller than the value measured before annealing. Furthermore, the spin lifetime increased by a factor of three to 1 hour. Hence, our method of annealing also improved the properties of the ball-milled powder, but it was not sufficient to completely re-establish the properties of the bulk. We anticipate that optimized annealing procedures, in particular involving temperatures closer to the melting point, will lead to further improvements.

5.3.4.3. Comparison of high- and low-energy ball-milling methods

The above results indicated that the grinding methods used here, namely mortar and pestle and ball-milling, caused damage to the host material. To better understand this surprisingly large effect, and to determine the degree to which damage can be

repaired through annealing, we continued studying ball-milling methods starting with a powder from a commercial supplier (Crytur). The powder was created from outer fragments of a large crystal, grown from 99.999% pure starting materials using the Czochralski method. Those fragments were then pre-crushed using a mechanical jaw crusher and finally milled down to a size of 30-50 μm in a tumbling mill. The resulting powder was cleaned using mineral acids.

First, we characterized the “as purchased” micrometer-sized Crytur powder using SEM, XRD, and SHB, as shown in Figures 5.11 a), b), and 5.9 b). The SEM image reveals that the powder has sharp edges and few particles with dimensions below 30 μm . The XRD spectrum shows good YAG crystalline structure. From the hole burning trace we extracted a hole width of $\lesssim 10$ MHz; however, the lifetimes were only on the order of one hour and comparable to the thermally crushed bulk crystal. This indicates that the crushing method employed by Crytur also induced a comparable amount of strain that is not detected in the XRD spectrum.

Since our annealing procedure was successful for the 0.5 mm-sized powder made from the SMC bulk crystal, we annealed the Crytur powder using the same method. The SEM image taken after annealing resembles that of the powder before annealing (see Figure 5.11 a)), and the hole width as well as the spin lifetime also remained comparable to those of the powder before annealing. Hence, in contrast to the powder created from the SMC crystal, besides an improvement in signal strength (see Figure 5.11 c)), our annealing method did not succeed in improving the properties of the powder. A possible explanation for this observation is the different way of creating the bulk crystal from which the powders were made. While both crystals were grown

in a Czochralski process using starting materials of similar purity (99.999% in the case of Crytur, and 99.995% for SMC), the original bulk crystal from SMC has been cut from the center of a boule and annealed before shipping. In contrast, the starting material at Crytur was outer fragments of a large crystal that were not annealed before crushing. These differences in the procedures employed in the growth process and sample preparation may affect the density of intrinsic defects and strain in the initial bulk crystal, potentially explaining the differences between the samples that are observed here.

In addition to jaw crushing and low-energy ball milling, we also used a high-energy planetary ball mill to obtain small powders. This technique requires shorter milling times compared to the low energy approach, but the energy of the impacts during milling is higher. For a direct comparison between high-energy and low-energy ball milling, we used the same starting material, i.e. the non-annealed, 30-50 μm -size crystals from Crytur, and milled the powder for 4 hours using 1 cm-diameter balls in a high-energy ball-mill. The SEM image in Figure 5.12 showed that the particles were not agglomerated and on average about 2 μm large. This is the smallest average size we could achieve using this mill with balls of that size. Figure 5.12 also reveals the sharp, irregular surfaces of the particles, suggesting significant strain, as well as a broad size distribution. For this powder, we measured a spectral hole width $\lesssim 10$ MHz (no side holes are visible) and a lifetime of around 10 min – considerably shorter than any other milled material. We conclude that despite the reduced milling time, the crystallites contained an even greater amount of strain and defects due to the high-energy impacts during milling.

Finally, we employed a low-energy tumbling mill for 48 hours to reduce the size of the original Crytur powder. The SEM image reveals agglomerated particles on the order of 100 nm. Furthermore, we found a spectral hole width of 23 MHz (no side holes are visible) and spin lifetimes of around 15 min. This new powder was very similar in all its properties to the one obtained from the SMC bulk crystal after the same ball-milling procedure (see Figures 5.10 a) and c)). The same annealing procedure as described before was then applied to the low-energy ball-milled powder. As observed in the case of the powders originating from the SMC bulk crystal, the particles grew from 100 nm to 1 μm , exhibiting clear garnet dodecahedral habit. Improvements in terms of spectral hole burning were more pronounced, with a measurement limited hole width of less than 10 MHz and visible side holes. However, the obtained lifetimes were still only around 20 min (as opposed to 1 h in the case of the SMC powder), which might be explained by a larger number of defects or impurities in the original bulk crystal from which the Crytur powder was obtained.

5.3.4.4. Direct chemical synthesis

Apart from milling larger crystals, small-sized powders can also be obtained using “bottom-up” chemical synthesis. In addition to not requiring initial growth of a high-quality crystal – a substantial advantage for fast prototyping – this method does not suffer from potential damage induced during grinding. We therefore examined the performance of a 1% Tm doped YAG powder that was prepared using a co-precipitation method [31, 32, 33]. This 1% Tm:YAG powder was synthesized from starting materials with at least 99.9% purity. An aqueous nitrate solution was

prepared by dissolving $\text{Tm}(\text{NO}_3)_3 \cdot 5\text{H}_2\text{O}$, $\text{Y}(\text{NO}_3)_3 \cdot 6\text{H}_2\text{O}$, and $\text{Al}(\text{NO}_3)_3 \cdot 9\text{H}_2\text{O}$ with a molar ratio of 0.03:2.97:5 in HPLC-grade water. The precipitant solution was prepared with a 1 M concentration of aqueous ammonium bicarbonate and ≈ 1 mM concentrations of sodium dodecyl sulfate and polyethylene glycol 400 added as anionic and nonionic surfactants, respectively. The solutions were mixed by stirring for 1 hour and then the nitrate solution was added drop-wise to an excess of the precipitant solution while stirring at room temperature to form the precipitate. The resulting suspension was aged for several hours while stirring to allow the solutions to fully react, and the resulting gelatinous precipitate was centrifugally separated from the solution. The precipitate was then washed by vortex mixing and sonication using deionized water, ethanol, and finally n-butanol, and it was then allowed to dry overnight in a vacuum desiccator. A YAG precursor powder was obtained by subsequently drying the precipitate at 300 °C for 4 hours and then grinding in a mortar to obtain a fine powder. The precursor was then mixed with 5% Li_2CO_3 by weight as a flux to promote growth of large crystallites, placed in a covered alumina crucible, and then crystallized in a tube furnace at a temperature of 1300 °C for 8 hours in air. Analysis of the resulting powder using XRD, shown in Figure 5.9 a), revealed complete formation of single-phase crystalline YAG. The quality of the XRD spectrum, in terms of signal-to-noise ratio and peak widths, is comparable to the spectrum of the purchased Crytur powder (see Figure 5.9 b)). An SEM image of the synthesized 1% Tm:YAG powder is shown in Figure 5.13, revealing that it consisted of uniform, non-agglomerated crystallites with diameters of 500 nm to 2 μm that exhibited the characteristic dodecahedral crystal habit of the garnets.

Although the XRD and SEM results for the synthesized powders appeared promising, spectral hole burning measurements revealed the poor quality of the material. We observed a very broad hole width of 26.6 MHz with no visible side holes. Furthermore, the measured nuclear spin lifetime was limited to values of at most 2 minutes. Hence, the properties of the synthesized powder were significantly worse than the properties of all of the powders obtained using the top-down ball-milling approach. We expect that the poor performance of the synthesized crystallites may result from residual chemical impurities that can cause lattice strain from incorporation of the defects as well as the presence of paramagnetic impurities such as iron that can couple to the Tm^{3+} ions and induce nuclear spin relaxation and optical decoherence. Consequently, further studies are required on powders synthesized from higher-purity starting materials to investigate whether the properties show improvement and how they compare to powders of similar purity obtained from top-down fabrication.

5.3.5. Discussion of different characterization methods

The three methods used in this work, SEM, XRD and SHB, complement each other as they provide information about different aspects of the nanocrystal properties. We found that SHB was the most sensitive method to detect effects of crushing as well as annealing on the powder quality in our measurements.

SEM images constitute the most convenient method to assess the size of the particles, and also observe their shape, which can be an indication of the crystalline quality, provided one knows the crystal's habit. For instance, the powder obtained

by chemical synthesis exhibits the characteristic dodecahedral crystal habit of YAG (see Figure 5.13). However, the SEM results do not allow one to identify the chemical composition, and thus cannot detect impurities present in the particles.

XRD analysis is the most reliable method to assess the composition and the phase of the nanocrystals. If the concentration of impurities is high enough, they can also be detected by this method. Potential amorphous character of the particles should also be visible as a broad background on the XRD spectrum. However, we were not able to observe the amorphous components or crystal strain that was clearly observed in our SHB measurements. In principle, by analyzing the peak widths in the spectrum, XRD can also give access to the particle size, but this requires a resolution beyond that of our instrument.

The SHB measurement gives access to the population lifetime of the nuclear spin states of $\text{Tm}^{3+}:\text{YAG}$, as well as to the homogeneous linewidth of the optical transition if the hole width is not broadened by laser power, which limited our resolution to 10 MHz. Both quantities are very sensitive to the crystal quality in terms of both strain and impurities. This sensitivity originates from the coupling between the ion's nuclear spin and the environment. In some cases, the SHB measurements reveal differences in the materials that are not observed in the SEM or XRD results. For example, the chemically synthesized nanocrystals exhibited very short spin lifetimes despite promising SEM and XRD results. The SHB measurement gives a quantitative, and sensitive method to determine the overall quality of the nanocrystals, even though it does not directly determine the nature of the limiting factors.

5.3.6. Conclusions and Outlook

In summary, we studied properties of 1% Tm:YAG powders produced by different methods via SEM imaging, XRD analysis, and spectral hole burning. We found that SHB is a very sensitive and well suited method to assess the quality of REI doped crystals in a quantitative way.

We found that any grinding or milling technique degraded the performance of the REI doped material in terms of homogeneous linewidth and especially spin-state lifetimes, most likely due to induced stress and deformation to the host matrix. Annealing is crucial and allowed us to recover the bulk spin-state lifetimes in the case of a soft-grinding method. In the case of more severe damage caused by ball-milling, bulk properties were partly recovered in powders originating from high-quality, annealed bulk crystals, whereas it remained poor in the case of powders obtained from non-annealed crystal fragments. This shows the importance of starting with high-quality crystals and the need for annealing. Finally, we found that the performance of the synthesized powder studied here was likely limited by the quality of the starting materials.

We anticipate our findings to be generalizable to other impurities and other hosts, in particular to color centers in nano-structured diamond, and to provide valuable insight towards nano-structuring REI doped crystals. Furthermore, SHB is a way to reveal variations in terms of quality and uniformity of powders that could have consequences for traditional applications where low levels of lattice defects can affect performance, such as luminescence efficiency and thermal quenching of phosphors.

Acknowledgements: The authors acknowledge support from Alberta Innovates Technology Futures (ATIF), the National Engineering and Research Council of Canada (NSERC), and the National Science Foundation of the USA (NSF) under award nos. PHY-1212462, PHY-1415628, and CHE-1416454. W. T. is a Senior Fellow of the Canadian Institute for Advanced Research (CIFAR). This work is based upon research conducted in part at the Montana State University Imaging and Chemical Analysis Laboratory.

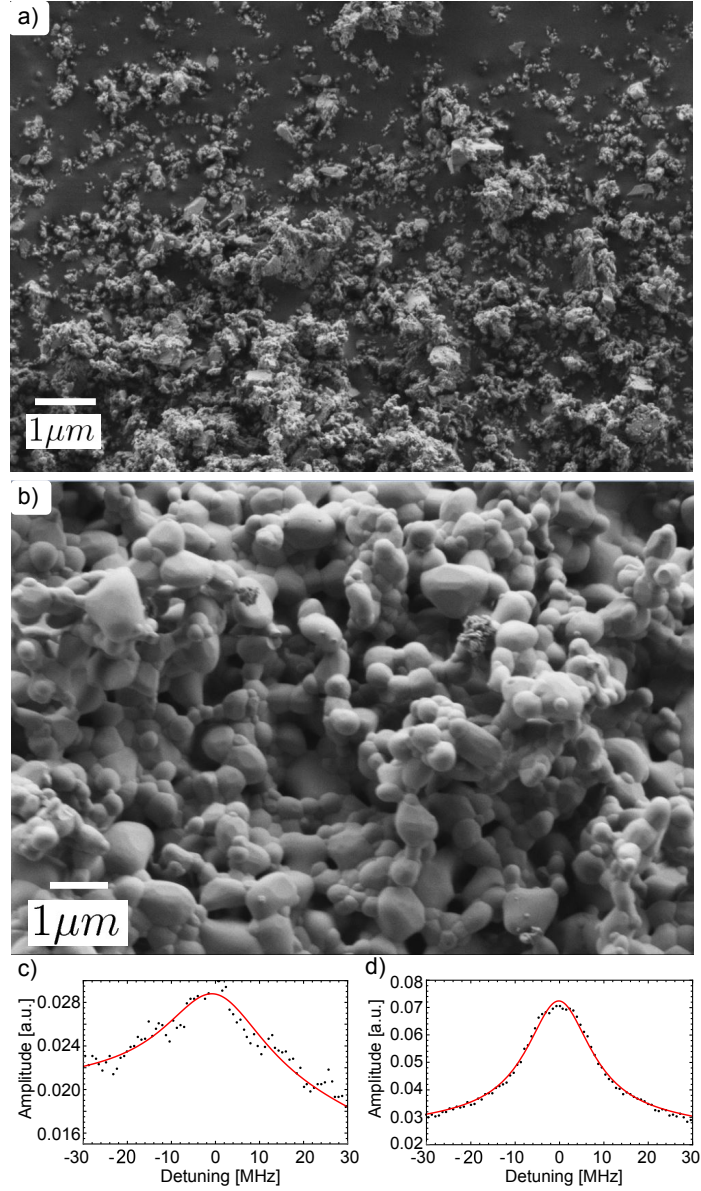


Figure 5.10.: SEM images and typical hole burning spectra of the powder obtained after ball-milling the bulk crystal from SMC for two days. a), c) before, and b), d) after annealing at 1400 °C for 4 hours.

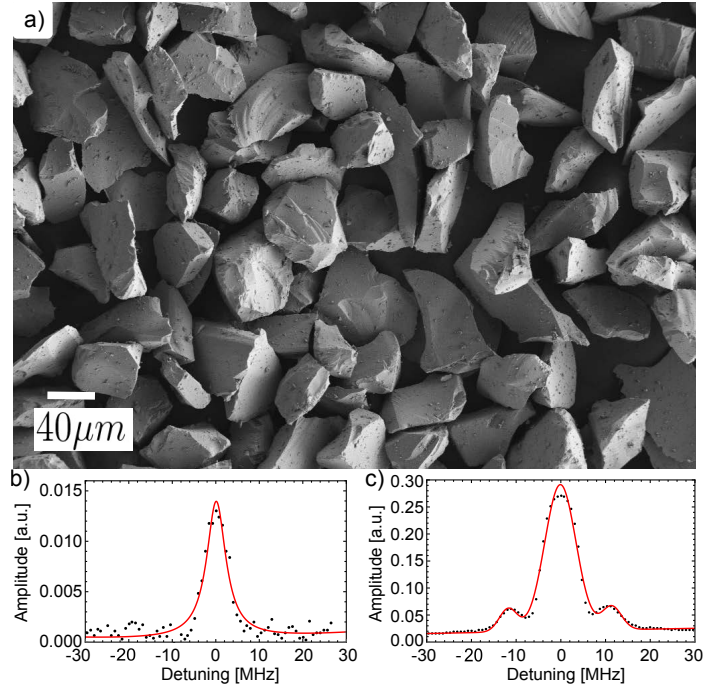


Figure 5.11.: a) SEM image of the 1% Tm:YAG powder provided by Crytur, and typical hole burning spectrum b) before and c) after annealing.

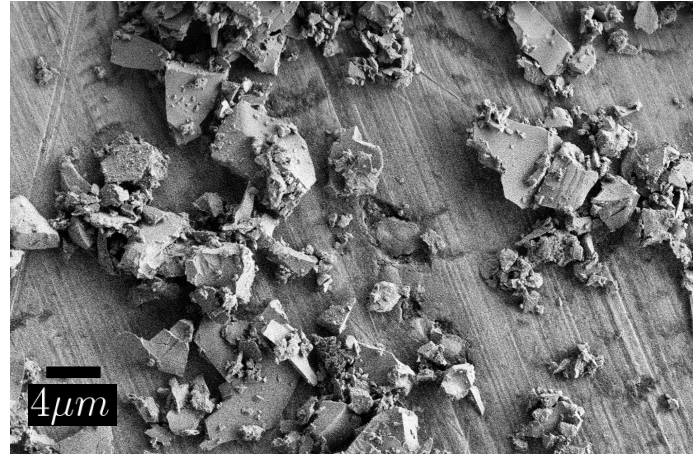


Figure 5.12.: SEM image of the 1% Tm:YAG powder after 4 hours of high-energy planetary ball-milling.

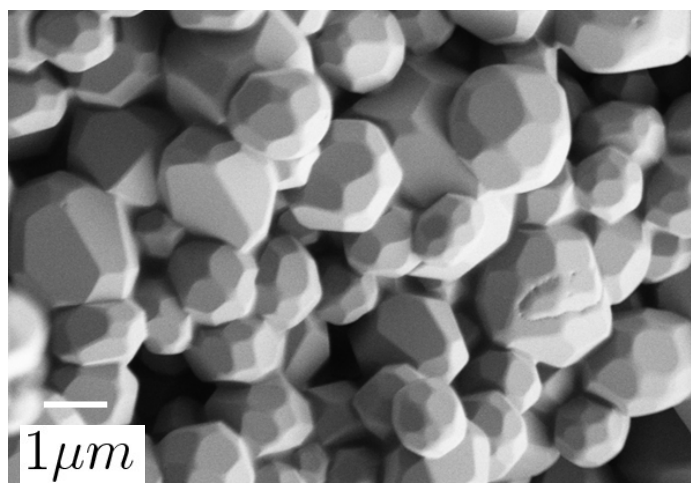


Figure 5.13.: SEM image of the synthesized 1% Tm:YAG powder.

Bibliography

- [1] H. de Riedmatten and M. Afzelius, “Quantum light storage in solid state atomic ensembles”, ArXiv:1502.00307 (2015).
- [2] E. Saglamyurek, N. Sinclair, J. A. Slater, K. Heshami, D. Oblak, and W. Tittel, New Journal of Physics **16**, 065019 (2014).
- [3] L. Ménager, I. Lorgeré, J.-L. L. Gouët, D. Dolfi, and J.-P. Huignard, Optics Letters **26**, 1245 (2001).
- [4] D. L. McAuslan, J. J. Longdell, and M. J. Sellars, Physical Review A **80**, 062307 (2009).
- [5] C. O'Brien, N. Lauk, S. Blum, G. Morigi, and M. Fleischhauer, Physical Review Letters **113**, 063603 (2014).
- [6] A. Walther, L. Rippe, Y. Yan, J. Karlsson, D. Serrano, A. N. Nilsson, S. Bengtsson, and S. Kröll, ArXiv:1503.08447 (2015).
- [7] T. Lutz, L. Veissier, C. W. Thiel, R. L. Cone, P. E. Barclay, and W. Tittel, Phys. Rev. A **94**, 013801 (2016). .

- [8] K. Hong, R. Meltzer, B. Bihari, D. Williams, and B. Tissue, *Journal of Luminescence* **7677**, 234 (1998). Proceedings of the Eleventh International Conference on Dynamical Processes in Excited States of Solids.
- [9] Y. V. Malyukin, A. A. Masalov, and P. N. Zhmurin, *Physics Letters A* **316**, 147 (2003).
- [10] R. M. Macfarlane and M. J. Dejneka, *Optics Letters* **26**, 429 (2001).
- [11] A. Perrot, P. Goldner, D. Giaume, M. Lovrić, C. Andriamiadamanana, R. R. Gonçalves, and A. Ferrier, *Physical Review Letters* **111**, 203601 (2013).
- [12] P. Heitjans, M. Masoud, A. Feldhoff, and M. Wilkening, *Faraday Discussions* **134**, 67 (2007).
- [13] G. Scholz, R. Stösser, J. Klein, G. Silly, J. Y. Buzar, Y. Laligant, and B. Ziemer, *Journal of Physics: Condensed Matter* **14**, 2101 (2002).
- [14] Y. Sun, G. M. Wang, R. L. Cone, R. W. Equall, and M. J. M. Leask, *Physical Review B* **62**, 15443 (2000).
- [15] R. M. Macfarlane and R. M. Shelby, in *Modern Problems in Condensed Matter Sciences*, vol. 21 of *Spectroscopy of Solids Containing Rare Earth Ions*, A. A. Kaplyanskii and R. M. Macfarlane, eds. (Elsevier, 1987), pp. 51–184.
- [16] L. Veissier, C. W. Thiel, T. Lutz, P. E. Barclay, W. Tittel and R. L. Cone, *Physical Review B* **94**, 205133 (2016).

- [17] G. Liu and B. Jacquier, *Spectroscopic Properties of Rare Earths in Optical Materials* (Springer Berlin Heidelberg, 2005).
- [18] M. Bonarota, J. Ruggiero, J. L. L. Gouët, and T. Chanelière, *Physical Review A* **81**, 033803 (2010).
- [19] A. Kareiva, *Materials Science* **17**, 1392-1320 (2011).
- [20] P. W. Anderson, B. I. Halperin, and C. M. Varma, *Philosophical Magazine* **25**, 1 (1972).
- [21] W. Phillips, *Journal of Low Temperature Physics* **7**, 351 (1972).
- [22] S. K. Watson, *Physical Review Letters* **75**, 1965 (1995).
- [23] G. P. Flinn, K. W. Jang, J. Ganem, M. L. Jones, R. S. Meltzer, and R. M. Macfarlane, *Physical Review B* **49**, 5821 (1994).
- [24] R. M. Macfarlane, Y. Sun, R. L. Cone, C. W. Thiel, and R. W. Equall, *Journal of Luminescence* **107**, 310 (2004). *Proceedings of the 8th International Meeting on Hole Burning, Single Molecule, and Related Spectroscopies: Science and Applications.*
- [25] R. Meltzer, K. Jang, K. Hong, Y. Sun, and S. Feofilov, *Journal of Alloys and Compounds* **250**, 279 (1997).
- [26] J. Szeftel and H. Alloul, *Journal of Non-Crystalline Solids* **29**, 253 (1978).
- [27] T. R. Askew, H. J. Stapleton, and K. L. Brower, *Physical Review B* **33**, 4455 (1986).

- [28] G. Balzer-Jöllenbeck, O. Kanert, J. Steinert, and H. Jain, Solid State Communications **65**, 303 (1988).
- [29] L. Aminov, I. Kurkin, and D. Lukoyanov, Applied Magnetic Resonance **14**, 447 (1998).
- [30] S. Georgescu, S. Constantinescu, A. Chinie, A. Stefan, O. Toma, and I. Bibicu, in *ROMOPTO 2006: Eighth Conference on Optics* (International Society for Optics and Photonics, 2007), pp. 67850A–67850A.
- [31] X. Li, H. Liu, J. Wang, H. Cui, X. Zhang, and F. Han, Materials Science and Engineering: A **379**, 347 (2004).
- [32] A. Pradhan, K. Zhang, and G. Loutts, Materials Research Bulletin **39**, 1291 (2004).
- [33] G. Xu, X. Zhang, W. He, H. Liu, H. Li, and R. I. Boughton, Materials Letters **60**, 962 (2006).

5.4. Paper 3: Effects of mechanical processing and annealing on optical coherence properties of $\text{Er}^{3+}:\text{LiNbO}_3$ powders

Journal of Luminescence, **191**, 2, 28 Mar 2017

5.4.1. Summary

In Paper 2, we established that, in certain cases, the bulk properties in terms of spin population lifetimes can be restored in a powder that is treated using thermal annealing. The same had to be ensured for optical coherence properties, especially since we expect a positive impact from phonon suppression in small powders on the latter as well. Paper 3 investigates how mechanical processing influences coherence properties in powder materials. Since our final goal was to develop material in which phonons are suppressed and thus the AFC quantum memory protocol can be performed more efficiently, and since the optical transition of erbium lies within the convenient telecom range, we chose $\text{Er}^{3+}:\text{LiNbO}_3$ as a material.

We found that coherence properties vary widely depending on the specific kind of processing a powder underwent. Furthermore, small powder materials make spectroscopic investigations difficult since they strongly scatter any probe light. Nevertheless, in the paper we show that various spectroscopic techniques such as hole burning, two-pulse photon echo and free-induction decay can be successfully employed to measure

optical coherence times and spectral diffusion over a broad range of values. We also present a model that predicts the decay shape of a two-pulse photon echo in a randomly oriented powder from known bulk crystal values.

Overall, we show that homogeneous linewidths are broadened in powders that underwent mechanical processing, which indicates the presence of crystal strain and amorphous phases. Even relatively gentle grinding methods that result in large powder sizes cause significant broadening. Thermal annealing is rather difficult to perform with LiNbO_3 since in many cases lithium and oxygen can out-diffuse from the crystal lattice. In the manuscript we identify annealing temperatures and atmospheres with which annealing can still be performed and we find that it can partially reverse the detrimental effects caused by our fabrication methods.

After we determined that REI are that sensitive to any kind of mechanical processing and that thermal annealing can often only partially restore bulk crystal properties in a small powder, we decided to produce small powders via chemical synthesis rather than mechanical crushing, in order to avoid damage to the crystal lattice caused by mechanical grinding.

The first draft of this manuscript was written by myself. All experiments were performed by the first four authors of the manuscript in the lab of Rufus Cone. The data analysis and interpretation was done by Lucile Veissier and myself.

**Effects of mechanical processing and annealing on optical coherence
properties of $\text{Er}^{3+}:\text{LiNbO}_3$ powders**

Thomas Lutz¹, Lucile Veissier^{1†}, Charles W. Thiel², Philip J. T. Woodburn², Rufus

L. Cone², Paul E. Barclay¹ and Wolfgang Tittel¹

¹*Institute for Quantum Science and Technology, and Department of Physics &
Astronomy, University of Calgary, Calgary Alberta T2N 1N4, Canada*

²*Department of Physics, Montana State University, Bozeman, MT 59717 USA*

[†] *Present address: Laboratoire Aimé Cotton, CNRS-UPR 3321, Univ. Paris-Sud,
Bât. 505, F-91405 Orsay Cedex, France*

**Corresponding author: thomasl@ucalgary.ca*

Abstract: Optical coherence lifetimes and decoherence processes in erbium-doped lithium niobate ($\text{Er}^{3+}:\text{LiNbO}_3$) crystalline powders are investigated for materials that underwent different mechanical and thermal treatments. Several complimentary methods are used to assess the coherence lifetimes for these highly scattering media. Direct intensity or heterodyne detection of two-pulse photon echo techniques was employed for samples with longer coherence lifetimes and larger signal strengths, while time-delayed optical free induction decays were found to work well for shorter coherence lifetimes and weaker signal strengths. Spectral hole burning techniques were also used to characterize samples with very rapid dephasing processes. The results on powders are compared to the properties of a bulk crystal, with observed differences explained by the random orientation of the particles in the powders combined with new decoherence mechanisms introduced by the powder fabrication. Modeling of the

coherence decay shows that paramagnetic materials such as $\text{Er}^{3+}:\text{LiNbO}_3$ that have highly anisotropic interactions with an applied magnetic field can still exhibit long coherence lifetimes and relatively simple decay shapes even for a powder of randomly oriented particles. We find that coherence properties degrade rapidly from mechanical treatment when grinding powders from bulk samples, leading to the appearance of amorphous-like behavior and a broadening of up to three orders of magnitude for the homogeneous linewidth even when low-energy grinding methods are employed. Annealing at high temperatures can improve the properties in some samples, with homogeneous linewidths reduced to less than 10 kHz, approaching the bulk crystal linewidth of 3 kHz under the same experimental conditions.

5.4.2. Introduction

Rare-earth-ion (REI) doped solid-state materials have received much attention for their properties such as long optical coherence lifetimes, broad inhomogeneous linewidths and long population lifetimes that are appealing for a multitude of applications [1, 2, 3, 4, 5, 6, 7]. Erbium-doped lithium niobate ($\text{Er}^{3+}:\text{LiNbO}_3$) features a wide, inhomogeneously broadened transition within the C-band of the current telecommunication infrastructure [8]. This is desirable for high-bandwidth applications such as quantum memories [9] or classical information processing devices, e.g. pulse ordering that would seamlessly integrate with today's technology. Furthermore, lithium niobate is of particular interest due to its strong electro-optic effects [10] that enable amplitude and phase modulation of light, as well as its high refractive index that can

be readily modified to enable optical waveguide applications [11, 12, 13]. The optical coherence properties of the 1.5 micron transition of bulk $\text{Er}^{3+}:\text{LiNbO}_3$ crystals have also been studied for optical signal processing and quantum information applications [1, 14, 15, 7, 16, 17], providing a knowledge base for comparing with any changes in the properties of micro- and nano-structured materials.

For many photonic applications, there is a strong trend towards miniaturization of devices with the ultimate goal of on-chip implementation and integration of many optical components. Nanofabrication tools such as chemical etching [18, 19] and focused ion beam milling [20] are already available and numerous nano-scale devices have been fabricated specifically from LiNbO_3 . Furthermore, employing LiNbO_3 crystalline films with thicknesses of only a few microns can provide advantages for the design of next generation high-speed, broadband electro-optic modulators [21, 22] as well as providing a platform for integration of heterogeneous photonic structures and components [23]. As fabrication techniques are refined further, additional improvements may be achieved by employing micron-sized ridge waveguide structures, such as for enhanced optical frequency conversion [24]. Nanostructured LiNbO_3 is of interest for diverse applications such as nanocrystals for in situ biological imaging [25] or nano-wires for directional optical second-harmonic generation [26] and enhanced pyroelectric sensors [27]. These materials are also promising for nanoscale ferroelectric capacitors that can enable high-density non-volatile data storage [28].

While much progress has been made in recent years on nanofabrication of optical materials [29, 30], little is known about how fabrication processes affect the spectroscopic properties of resonant impurities in the host, such as rare-earth ions. Many

properties, such as optical coherence lifetimes that are studied here, can be sensitive to the quality of the host crystal and even modest variations can critically affect applications that rely on those properties. Consequently, it is important to find ways to maintain those properties in nanoscale structures.

In the specific area of REI-doped powders and nanocrystals, there have been very few optical coherence studies. The initial work in this field focused on the specific case of Eu^{3+} -doped into sesquioxide host crystals, where fluorescence detection of spectral hole burning revealed rapid decoherence relative to the bulk crystals due to the introduction of glass-like two-level system (TLS) dynamics in the powders [31, 32, 33, 34]. Beyond the sesquioxide powders, nano-crystallites in glass ceramics have also suffered from rapid decoherence processes due primarily to interactions with the surrounding amorphous host matrix [35, 36, 37]. Following the pioneering demonstrations of photon echo measurements on highly scattering powders [38], optical coherence properties approaching those of bulk crystals have recently been demonstrated in $\text{Eu}:\text{Y}_2\text{O}_3$ nano powders, confirming that there is significant potential to improve these and other nano-materials [39]. In addition, long optical coherence times have been reported for micro-fabricated structures in $\text{Nd}:\text{Y}_2\text{SiO}_5$ crystals, again suggesting that at least some systems and fabrication methods can produce properties suitable for practical applications [40]. Nevertheless, beyond these cases, little is known about optical coherence in nano- and micro-structured crystals or powders.

With this motivation, the focus of the work reported here is to employ high-resolution optical characterization methods, namely two-pulse photon echo (2PE), spectral hole burning (SHB), and free induction decay (FID) techniques, to assess optical coher-

ence lifetimes in micro- and nano-sized powders of Er^{3+} -doped lithium niobate. The greatest challenges in carrying out these studies involve detecting optically coherent signals in highly scattering media and the complexity in behavior introduced by the random orientation of crystallites in the powder relative to both the external magnetic field and light polarization, which crucially influence the spectroscopic properties. In addition, we find that the bulk crystal properties degrade significantly with any mechanical processing used to obtain micro/nanocrystals. Therefore, techniques with a very large measurement dynamic range are necessary.

As a primary goal, our study seeks to probe the thresholds where low-energy mechanical processing methods begin to degrade the optical coherence properties and to what extent the effects might be reversed by high-temperature annealing. Investigating micron-sized crystals allowed us to probe this threshold region and get a better understanding of the mechanisms responsible for degraded properties when the particle size is reduced, down to the nanoscale. In addition to the direct relevance to nano- and micro-fabrication, these results can also reveal insights into potential surface damage introduced by cutting, grinding, and polishing as well as what processing steps may be successful in reducing the resulting surface strain and defects. Another important goal is to demonstrate that powders of highly anisotropic materials may be quantitatively analyzed within the framework of decoherence models developed for bulk single crystals. Finally, this work demonstrates how combinations of 2PE, SHB, and FID measurement techniques allow optical coherence properties to be studied and compared across a range of samples with very different behaviors as described in the following.

The following subsection of this paper describes the fabrication of our powder samples. We then discuss and compare the results of the different experimental methods to probe the optical coherence lifetimes. The properties of the fabricated powders are then compared with the ones of a bulk crystal, including quantitative modeling of the effects due to the random orientation of crystallites in the powder. We identify the factors limiting the optical coherence lifetimes in small crystals and show that high-temperature annealing to relieve strain induced by the fabrication process can improve those properties; however, in the majority of samples, the bulk crystal properties could not be preserved or fully recovered.

5.4.3. Sample preparation

Mechanical grinding is a very general, simple, rapid, and flexible approach for fabricating nano-powders from bulk crystalline materials. In particular, high-energy planetary ball milling has been extensively used to produce monodisperse nano-powders with crystallite sizes down to less than 10 nm [41, 42]. However, it is known that high-energy ball milling can cause significant damage to the crystal structure, with the resulting disorder leading to amorphous-like behavior or even transformations to different crystal phases after extended milling [42, 43]. Since very large internal electric fields can be produced through the piezoelectric and pyroelectric effects in LiNbO_3 [10], which are also known to contribute to optical damage processes in the bulk crystals [44], we might expect even greater potential for crystal damage from high-energy milling of this material. High-energy ball milling has been used

by a number of groups to produce LiNbO_3 nanopowders, mostly undoped, and the resulting materials have been extensively characterized [45, 46, 47, 48, 49, 50]. A range of techniques including nuclear magnetic resonance spectroscopy, extended X-ray absorption fine structure spectroscopy, impedance spectroscopy, X-ray diffraction, transmission electron microscopy, differential scanning calorimetry, thermogravimetric analysis, infrared absorption spectroscopy, and Raman spectroscopy have all indicated a significant increase in amorphous behavior in the LiNbO_3 crystallites when they are reduced to sizes below 100 nm by high-energy ball milling [45, 46, 47, 48, 49].

Very little is known regarding how the extent of crystal damage caused by mechanical fabrication or processing relates to the energy, processing time, and specific method used. While it is clear that the extended high-energy milling required to produce nanocrystalline powders produces significant damage, it is unknown if the damage is intrinsically linked to the size reduction or whether lower energy grinding methods might better preserve the properties of the bulk crystal. For LiNbO_3 , some of the same measurements that reveal the large degradation in nanocrystals indicate that microcrystals have nearly the same properties as the bulk crystal [49]. In our previous SHB studies of Tm^{3+} -doped yttrium aluminum garnet powders, we found that high-energy planetary ball milling dramatically affected $^{169}\text{Tm}^{3+}$ nuclear hyperfine state lifetimes; however, we also found that the lifetimes were still significantly reduced in relatively large microcrystals produced by low-energy ball milling [51]. Since we expect crystal defects introduced by grinding to affect optical coherence properties more strongly than nuclear spin lifetimes due to the stronger coupling of the electronic states to the crystal lattice, optical coherence measurements should provide a uniquely

sensitive method for probing even very low levels of crystal damage. For the same reasons, we expect mechanical fabrication methods to be particularly detrimental to material performance in applications that rely on long coherence lifetimes and narrow optical homogeneous linewidths. Consequently, in this work we only used very slow and low-energy grinding methods, resulting in micron-sized powders, in an attempt to minimize the accumulated mechanical strain in the crystallites and also to probe the threshold at which measurable damage is induced to the crystal structure.

As a single crystal reference to compare with powder samples prepared in different ways, we chose a bulk single crystal of 0.1% $\text{Er}^{3+}:\text{LiNbO}_3$ with congruent composition, grown by Scientific Materials Corp. (SMC) using the Czochralski method. This crystal has been previously studied by Thiel et al. [16, 17] and showed good coherence properties with homogeneous linewidths as narrow as 3 kHz with applied magnetic fields along the crystal's c -axis. The choice of doping concentration is a trade-off between the absorption needed to obtain a reasonable signal-to-noise ratio in powder samples and the additional decoherence created by increased doping due to Er^{3+} - Er^{3+} interactions. Starting from a bulk crystal, we fabricated several powder samples, as detailed below. The procedures used to fabricate each of the samples are outlined in Tab. 5.2. In order to analyze the size and shape distribution of the resulting powders, we performed scanning electron microscope (SEM) imaging, as presented in Fig. 5.14 and 5.15.

An initial reference powder (powder #1 in Tab. 5.2) was first fabricated by relatively gentle mechanical crushing and grinding using an alumina ceramic mortar and pestle. This resulted in monocrystalline particles with a wide distribution of sizes ranging

Sample	Method
bulk	0.1 % $\text{Er}^{3+}:\text{LiNbO}_3$ (SMC)
1 (ref)	bulk crushed via mortar and pestle
2	sample 1 re-crushed with mortar and pestle ball milled, 0.5 Hz mill, 30 min
3	sample 1 ball milled, 0.5 Hz mill, 2 hr annealed (1 hr at 900 C and 4 hr at 600 C)
4	sample 1 ball milled, 0.5 Hz mill, 2 hr annealed (4 hr at 1100 C)
5	sample 1 ball milled, 5 Hz mill, 10 hr annealed (4 hr at 950 C and then 4 hr at 1100 C)
6	indiffusion of Er^{3+} into commercial LiNbO_3 powder: $\text{LiNbO}_3 + \text{ErCl}_3$ ball milled, 5 Hz mill, 3 hr annealed (4 hr at 1100 C)

Table 5.2.: Powders characterized in the manuscript and their fabrication methods.

from 1 to 100 μm , as shown in Fig. 5.14(a). However, we believe that when we later optically probed the samples the signal mainly originated from the largest particles. To further reduce the crystallite size of the crushed LiNbO_3 powder, we employed two different horizontal tumbling-type low-energy ball mills: a ball mill with a 4-inch diameter HDPE-jar rotating at a relatively slow rate of approximately 5 Hz, and an even slower ball mill rotating at a rate of only approximately 0.5 Hz. Both mills were loaded with a mix of ceramic yttria-stabilized zirconia balls with diameters ranging from 0.3 mm to 1 cm. The reference powder samples were mixed with ethanol to produce a slurry and then ground in a mill under the conditions listed in Tab. 5.2. This method was chosen to minimize both the mechanical and thermal energy involved in the grinding. From the powder sample #1, we produced another sample (powder #2) by ball-milling for only 30 min at 0.5 Hz. The corresponding SEM image (Fig. 5.14(b)), shows very little decrease in particle size demonstrating that our low-energy ball milling method only reduces the particles very slowly by gradual

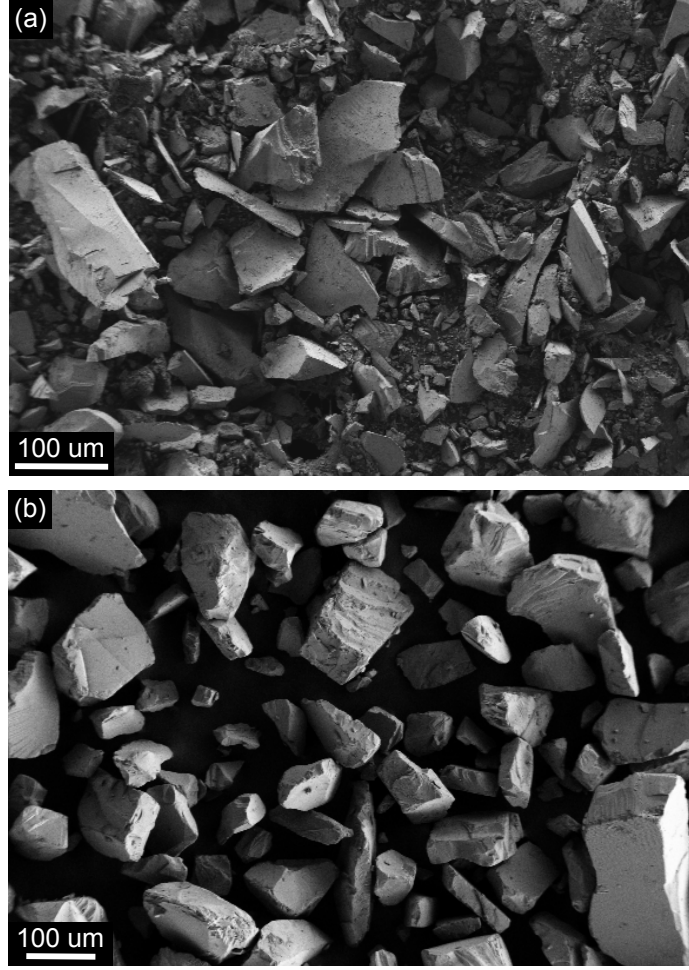


Figure 5.14.: Scanning electron microscope images of (a) powder #1 made from a 0.1% $\text{Er}^{3+}:\text{LiNbO}_3$ bulk crystal (SMC) by grinding with a mortar and pestle, (b) powder #2 ball-milled for only 30 min.

attrition. Nevertheless, even short periods of milling may potentially introduce measurable lattice strain that can be characterized. The next sample fabricated, powder #3, was produced by ball-milling powder #1 for 2 hours at 0.5 Hz, resulting in a significant reduction in average particle size. As shown in Fig 5.15(a), this sample has particle sizes roughly on the order of $1\ \mu\text{m}$ after annealing in the furnace.

To investigate the effect of post fabrication thermal treatment, some powders were annealed in alumina crucibles in a tube furnace using a mullite tube providing peak

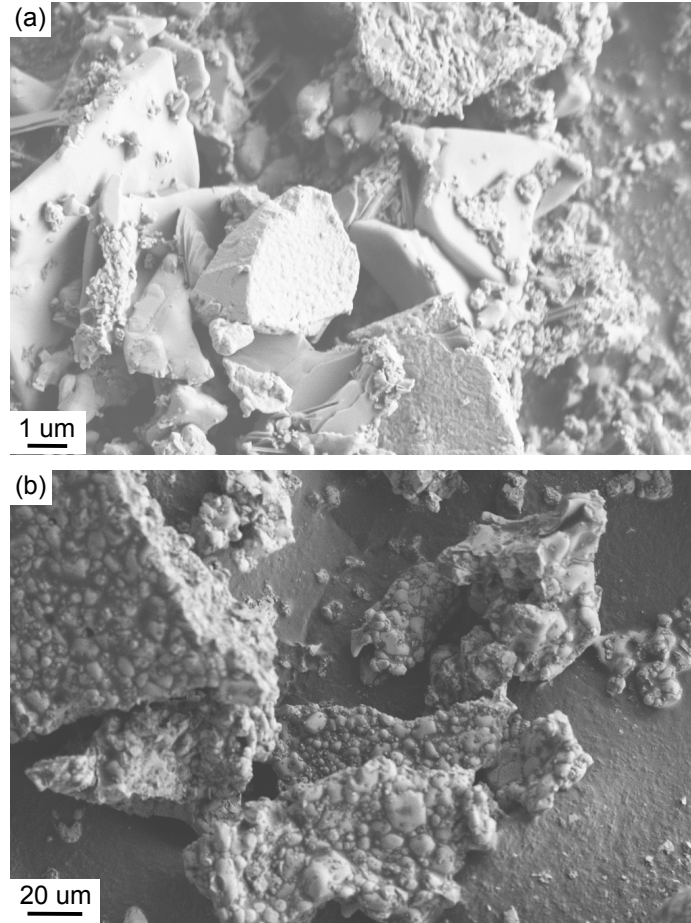


Figure 5.15.: Scanning electron microscope images (a) powder #3 ball-milled and annealed at 900 C, and (b) powder #6 annealed up to 1100 C.

temperatures of up to 1400 C. While thermal annealing can increase defect mobility and relieve crystal strain, LiNbO_3 can also be detrimentally affected by annealing at high temperatures due to the potential for out-diffusion of both lithium and oxygen, affecting the optical and electrical properties of the crystal. Past studies have found that thin crystalline films of LiNbO_3 are particularly sensitive to high annealing temperatures [52, 53], suggesting that similar effects might be observed for powders. Furthermore, while bulk crystals generally require reducing atmospheres [54] or vacuum [55] for significant oxygen to diffuse out of the crystal matrix during annealing,

we found that in small crystallites the out diffusion occurs even when annealed in an ambient atmosphere, resulting in black powders. To prevent the loss of oxygen from the material, we annealed the powders under a continuous flow of oxygen (ultra-high purity grade), a method that has been shown to inhibit the reduction process for bulk crystals [55], although for thin films there have been some indications that excess oxygen may potentially be absorbed and produce defects [56]. To inhibit the out-diffusion of lithium, we employed the well-known technique used for LiNbO_3 wafer processing of introducing small amounts of water vapor into the oxygen by bubbling the gas through a column of deionized water [57, 58].

The effects of several different annealing procedures were examined. Powder #3 was annealed at a low-temperature of around 900 C, which resulted in a growth in particle size of only a factor of two at most for the micron- and sub-micron-sized particles and only produced weak agglomeration of the powder. The resulting maximum particle size of 2 μm or less constitutes the finest powder examined in this study as shown in Fig. 5.15(a). We also performed higher temperature annealing at 1100 C that tended to produce significant crystallite growth as well as hard agglomeration and fusing of the particles. Samples #4, #5 and #6 had initial particle sizes of less than 2 μm after ball-milling but fused into much larger masses around 100 μm after annealing at 1000 C, as shown in Fig. 5.15(b). Powder #5 also underwent an initial pre-annealing step at 950 C. Better crystal quality, and therefore improved coherence properties should in principle come with this increase in size.

Finally, we fabricated an $\text{Er}^{3+}:\text{LiNbO}_3$ powder (sample # 6) via in-diffusion of Er^{3+} ions into a commercial congruent LiNbO_3 powder (Sigma Aldrich, 99.9% purity) with

initial crystallite sizes of less than 70 μm . The LiNbO_3 powder was mixed with a 5% molar concentration of anhydrous ErCl_3 powder (ProChem Inc., > 99.9% purity) and ethanol to produce a slurry, and the mixture was ball milled for 3 hours. The powder was then allowed to dry in a desiccator, after which it was heated in the tube furnace for 4 hours at 1100 C while under a continuous flow (3 SCFM) of oxygen. The resulting powder was then crushed with a mortar and pestle and washed with deionized water followed by ethanol. Optical spectroscopy of the 1532 nm absorption line verified that significant Er^{3+} had diffused into the LiNbO_3 powder. While the amount of Er^{3+} incorporated into the LiNbO_3 powder is unknown, the magnitude of the optical absorption and the effective homogeneous linewidth were comparable to our other 0.1% Er powders (see Tab. 5.4). Not accounting for possible broadening of the inhomogeneous line, which would have to be very large, this suggests a similar effective doping level in the indiffused powder and our other powders.

5.4.4. Optical coherence lifetime measurements

Key requirements for many applications of REI-doped materials in classical and quantum signal processing are long optical and spin coherence lifetimes. To investigate the effect of powder fabrication on the optical coherence lifetime of the 1.5 μm telecom-compatible transition of Er^{3+} , we used several different measurement techniques. One issue that must be overcome for powders is a much weaker signal strength. Powders with particle sizes below 10 μm scatter light very strongly, especially for our samples, since LiNbO_3 has a relatively high refractive index of approximately 2.2 at 1.5 μm

wavelengths [59, 60] and most of our particles have sizes larger than the wavelength of the probing light. The latter causes light to be scattered at every surface of the micro/nano-crystals, randomizing the direction, path length, and polarization of the light, making the transmitted or emitted light difficult to collect. Therefore, the usual characterization methods employed for REI-doped crystals such as 2PE, SHB, or FID are difficult to perform with powders. Previous measurements on powders have mostly employed detection of fluorescence emission to observe SHB [31, 61, 33], with direct transmission detection of SHB [51] and 2PE [38, 39] only recently being successfully applied to powders. In particular, FID measurements on powders have not been previously reported to our knowledge.

Another consideration is the random orientation of individual crystallites in the powder relative to applied external fields. It is known that Er^{3+} coherence lifetimes strongly depend on the magnetic field orientation due to the anisotropy of the g tensors in both the ground and excited states [62]. As a consequence, the coherence lifetimes measured in a randomly orientated powder sample correspond to an average of the bulk lifetime over all possible orientations, complicating the interpretation of the results.

Finally, the degradation of coherence properties in micro/nano-crystals due to new decoherence mechanisms introduced by the powder fabrication process can limit the range of materials that can be studied using a single technique. In some cases, the optical coherence lifetime is drastically reduced, making a direct measurement via 2PEs difficult with standard techniques.

In the work reported here, we employed a combination of three techniques, SHB,

2PE, and FID, to study optical coherence over the wide range behavior encountered in different powder samples. Also, SHB signals were detected in transmission rather than emission to allow information about absorption depths to be determined. For all of these measurements, unless mentioned otherwise, the powder samples were loaded into a 0.4 mm thick space within an unsealed glass cuvette and then cooled to a temperature of 1.6 K in an Oxford Spectromag cryostat using helium exchange gas. A superconducting solenoid provided magnetic fields of up to 6 T for these measurements. Since most of the incident laser light was diffusely scattered in all directions, it was critical to minimize stray light from reaching the detector and producing a large background signal. For this purpose, the glass cuvette containing the powder was mounted against a mask with a small hole that only allowed light at the center of the cuvette to be transmitted and with extensive light baffles on all sides to direct any scattered light away from the detector.

5.4.4.1. Two pulse photon echoes

The most precise method to characterize long coherence lifetimes, as observed in $\text{Er}^{3+}:\text{LiNbO}_3$ bulk crystals, is the 2PE technique since it is not limited by the linewidth of the excitation laser. For these measurements, a homemade Littman-Metcalf extended-cavity diode laser emitting at 1532 nm was amplified using an erbium-doped fiber amplifier (IPG Photonics Corp EAD-1-C). Two short pulses, separated by a time t_{12} , with duration ranging from 30 to 100 ns, optimized for each sample, were generated using an acousto-optic modulator (Crystal Technology Inc. 3165). The light was then focused on the front face of the sample and the transmitted light was detected using

an amplified high-speed InGaAs photodetector (New Focus 1811) with no optical gate used between the photodetector and the powder samples.

In addition to direct detection of the echo intensity, we also performed heterodyne measurements of the echo. For those measurements, after the second excitation pulse, a weak optical local oscillator pulse detuned by 10 MHz was sent through the sample to the detector to ensure it undergoes the same scattering path and to provide better spatial mode matching of the local oscillator and the excitation beam. The envelope of the beat signal between the emitted echo and the local oscillator corresponds to the emitted temporal shape of the photon echo electric field strength. Because of the need to limit the local oscillator pulse intensity to avoid undesired hole burning or heating effects and attenuation due to scattering, the heterodyne signal strength was not significantly larger than the intensity detection. Nevertheless, the factor of two slower echo decay rate of the electric field observed in the heterodyne measurement, compared to the decay rate of the intensity observed in a regular 2PE, allows shorter coherence lifetimes to be characterized with the heterodyne technique.

5.4.4.2. Echo decays in powders of randomly orientated crystallites

In the simplest 2PE decay measurement, the area of the echo emitted at a time $2t_{12}$ after the first excitation pulse follows an exponential decay determined by the coherence lifetime. In $\text{Er}^{3+}:\text{LiNbO}_3$, as for many other Er^{3+} materials, spectral diffusion broadens the homogeneous linewidth during the measurement timescale [16] leading to a non-exponential echo decay often described by the empirical formula proposed

by Mims [63, 64]

$$I(t_{12}) = I_0 \exp \left[-2 \left(\frac{2 t_{12}}{T_M} \right)^x \right] , \quad (5.9)$$

where the exponent $x \geq 1$ determines the decay shape and T_M is the phase memory lifetime, usually related to the effective homogeneous linewidth as $\Gamma_{\text{eff}} = 1/\pi T_M$ [16]. In heterodyne detection, the electric field of the emitted photon echo is detected rather than the intensity so that the decay of the echo heterodyne envelope area is slower by a factor of two and is given by

$$E(t_{12}) = E_0 \exp \left[- \left(\frac{2 t_{12}}{T_M} \right)^x \right] . \quad (5.10)$$

In general, the effective homogeneous linewidth can strongly depend on the orientation of the applied magnetic field \mathbf{B} as well as the specific ion sites addressed in the crystal by the resonant optical excitation [62]. For amorphous media, there can be a wide range of local environments and a corresponding need to average over a complex distribution of sites and orientations [65]. In contrast, it should be possible to predict the behavior for a powder of randomly oriented crystallites from the measured orientation dependence of the bulk single crystal. In LiNbO_3 , Er^{3+} ions substitute for Li^+ with a local environment that nominally maintains an axial point symmetry with respect to the c -axis described by the C_3 point group [66, 67]. Assuming that the sites maintain perfect axial symmetry, the orientation-dependent properties depend only on the angle θ between the magnetic field \mathbf{B} and the c -axis. Fig. 5.16(a) shows the effective linewidth as a function of θ in a 0.1% $\text{Er}^{3+}:\text{LiNbO}_3$ bulk crystal at $T = 1.6$

K and $B = 2$ T. The minimum homogeneous linewidth is observed for \mathbf{B} along the c -axis, i.e. $\theta = 0$, with a measured value of 3 kHz, agreeing with the linewidth previously reported for these conditions in a 0.06% $\text{Er}^{3+}:\text{LiNbO}_3$ crystal [16]. The values of Γ_{eff} were extracted from 2PE intensity decays fitted by Eq. 5.9, as shown in the inset for \mathbf{B} along the c -axis. The measured angular dependence $\Gamma_{\text{eff}}(\theta)$ was fit well using an empirical eighth order polynomial containing only even powers. To simulate the observed echo intensity I_{tot} , we averaged the echo intensities over all possible random crystallite orientations as follows

$$I_{\text{tot}}(t_{12}) = I_0 \int_0^{\pi/2} \exp[-4\pi\Gamma_{\text{eff}}(\theta)t_{12}] \sin\theta d\theta. \quad (5.11)$$

This model assumes a uniform distribution of particle orientations and that all particles contribute equally to the averaged decay. Fig. 5.16(b) shows the measured echo intensity as a function of waiting time t_{12} in powder #1 under the same conditions as for the bulk measurements, i.e. $B = 2$ T and $T = 1.6$ K, as well as the decay simulated using Eq. 5.11 with the measured bulk crystal parameters. The simulated and measured decays agree very well, indicating that the observed echo signals in this case do represent a simple average over all possible particle orientations. This conclusion is important for interpreting the later results since it suggests that the probe light interacts uniformly with different particles and that there is no preferential alignment of the crystallites in the powder.

From both the simulations and the measurements, we observed echo decays for the $\text{Er}^{3+}:\text{LiNbO}_3$ powders that could be approximately described by a double-exponential

shape. Using simulations to investigate the contributions of different particle orientations to the echo signal, we found that, for the conditions studied in this work, the slow component of the decay corresponds to the subset of crystallites in the powder that have their c -axis oriented almost parallel to the applied magnetic field direction while the fast component of the decay corresponds to all crystallites with other orientations. For example, under the conditions in Fig. 5.16(a), fitting the powder decay with a double exponential gives effective homogeneous linewidths of 7.6 and 45 kHz for the two components, roughly corresponding to that of the bulk crystal with \mathbf{B} along the c -axis (3.5 kHz), and an average over the behavior for other orientations (up to 300 kHz for \mathbf{B} orthogonal to the c -axis), respectively. Note that the excited state population lifetime in Er:LiNbO₃ bulk crystals was measured to be 2 ms [16], which leads to an absolute lower limit for the optical homogeneous linewidth of 80 Hz.

Because the slower decay component probes the subset of particles with their c -axis approximately aligned with the external field, as confirmed by the analytical model described by Eq. 5.11, we can quantitatively analyze the decoherence mechanisms by directly comparing this component of the decay to the bulk crystal behavior for $\mathbf{B} \parallel c$. Consequently, in all of the following analysis, we focus on the slower component of the double exponential decay observed for the powder samples. In the spectral hole burning and free induction decay measurements described later, only single exponential decays are observed since at the timescales of these measurements, additional decoherence effects dominate the decay behavior and are more important than the orientation effect observed in the 2PE measurements.

5.4.4.3. Magnetic field dependence of coherence lifetimes

In this subsection we discuss the observed magnetic field dependence of the coherence lifetimes in the different samples and investigate additional decoherence processes resulting from the powder fabrication methods. Fig. 5.17 shows the magnetic field dependence of the effective linewidth at $T = 3$ K for the bulk crystal, powder #1 (the reference), and powder #2. No heterodyne technique was needed here, but we verified that the heterodyne measurement of the decay fitted by Eq. 5.10 gave the same characteristic lifetime. For all other powder samples listed in Tab. 5.2, the signal was either too weak or exhibited a decay too rapid to extract a lifetime corresponding to the slow component with a reasonable uncertainty. The experimental points $\Gamma_{\text{eff}}(B)$ are fitted by the spectral diffusion model from Ref. [16], where the effective linewidth is given by

$$\Gamma_{\text{eff}}(B, T) = \frac{\Gamma_{\text{SD}} R}{-2\Gamma_0 + 2\sqrt{\Gamma_0^2 + \frac{\Gamma_{\text{SD}} R}{\pi}}} , \quad (5.12)$$

where Γ_0 is the linewidth without spectral diffusion, Γ_{SD} is the broadening caused by interactions between the Er^{3+} electronic spins, and R is the rate of spectral diffusion. The spectral diffusion broadening has a full width at half maximum described by

$$\Gamma_{\text{SD}}(B, T) = \Gamma_{\text{max}} \text{sech}^2 \left(\frac{g_{\text{env}} \mu_B B}{2k_B T} \right) , \quad (5.13)$$

where Γ_{max} is the maximum broadening due to magnetic dipole-dipole interactions, $g_{\text{env}} \mu_B B$ is the splitting of the Er^{3+} spin states, and the hyperbolic secant function in Eq. 5.13 describes the suppression of spectral diffusion at high magnetic fields due to

sample	g	$\alpha_{\text{ff}}(\text{kHz})$	$\alpha_{\text{D}}(\text{kHz/T}^5)$
bulk	15.7	11	69
1	14	12	240
2	14	9	200

Table 5.3.: Parameters from fitting the experimental data shown in Fig. 5.17 by Eq. 5.12. For all samples, the value of Γ_{max} was fixed to 1 MHz and the parameter Γ_0 was constrained to be larger or equal than minimum bulk value ($\Gamma_0 = 3$ kHz at 6 T), which lead to $\Gamma_0 = 3$ kHz.

the increased magnetic ordering of the spins. Spectral diffusion occurs at a rate R characterizing the flip rate of the perturbing Er^{3+} spins; that is approximately given by

$$R(B, T) = \alpha_{\text{ff}} \text{sech}^2 \left(\frac{g_{\text{env}} \mu_{\text{B}} B}{2k_{\text{B}} T} \right) + \alpha_{\text{D}} g_{\text{env}}^3 B^5 \coth \left(\frac{g_{\text{env}} \mu_{\text{B}} B}{2k_{\text{B}} T} \right). \quad (5.14)$$

This expression assumes that only the mutual Er^{3+} - Er^{3+} spin flip-flop process with coefficient α_{ff} and the direct phonon process with coefficient α_{D} drive Er^{3+} spin flips, as expected for temperatures below 4 K.

Fitting Eq. 5.12 to the three sets of data (bulk crystal and powders #1 and #2) gives very similar spectral diffusion parameters except for the coefficient α_{D} that is 4 times larger for powder #1 and 3 times larger for powder #2 as compared to the bulk crystal (see Tab. 5.6). This suggests that additional spin relaxation processes that increase with magnetic field are introduced through powder fabrication by crushing or ball-milling. Such processes may be understood within the framework of the two-level system (TLS) model developed to describe dynamics in amorphous materials [68, 69]. In this model, very low-frequency modes that involve groups of atoms tunneling

between local configurations with nearly equivalent energies are enabled by defects and disorder in the crystal structure. It has been proposed that low densities of TLS can be present in some crystalline materials with large inhomogeneous lattice strains [70]. Decoherence attributed to TLS has been previously observed in both bulk crystals [31, 61] and powders [32], and it has also been suggested that TLS can cause rapid electron spin relaxation [71]. This interpretation is also consistent with past observations of increased electronic spin-lattice relaxation rates of Nd^{3+} in YAG single crystals with a high density of structural defects in the lattice [72] as well as increased nuclear spin relaxation rates of $^{169}\text{Tm}^{3+}$ in YAG powders fabricated by ball milling [51]. While it is known that high-energy ball milling of nanocrystals can produce significant disorder in the crystal structure and introduce some amorphous behavior [45, 46, 47, 48, 49], our results suggest that even very low-energy grinding methods applied to much larger microcrystals still cause substantial damage that produce TLS. Since the powders examined all have sizes larger than $1\text{ }\mu\text{m}$ we assume that contamination of the crystal surface or surface effects in general do not play a role in this case.

Because 2PE techniques did not allow us to extract the long component of the decay corresponding to the longer coherence lifetime in the bulk, we also used SHB and FID techniques in all of the powder samples to probe the effects of faster decoherence processes. These measurements are described in the following subsections.

5.4.4.4. Spectral hole burning

We employed spectral hole burning to measure Γ_{eff} as well as the effective absorption depth α_{eff} of our samples. We use the latter to qualitatively estimate the amount of scattering and the quality of the micro/nano-crystals. In this measurement, a 500 μs long burn pulse excited the resonant Er^{3+} ions into the $^4\text{I}_{13/2}$ excited state and created a corresponding transparency window in the inhomogeneously broadened absorption line. After a 25 μs delay, a subsequent 50 μs long read pulse with lower power was frequency swept across the spectral hole to measure the absorption spectrum.

A typical hole burning trace is shown in Fig. 5.18 for powder #1 at a temperature of 1.6 K and a magnetic field of 2 T. In addition to the main hole in the center of the spectrum, we observed additional sideholes originating from the superhyperfine coupling between the Er^{3+} electronic spins and the nuclear spins of the host ions, with ^{93}Nb producing a superhyperfine splitting of 9 MHz/T and ^7Li producing a splitting of 14.8 MHz/T [17].

Spectral hole burning measurements provide information about the optical coherence lifetime via the width of the spectral hole. In the absence of power broadening, the spectral hole width is twice the effective homogeneous linewidth convolved with the laser linewidth [73]. To estimate the effect of power broadening and the laser linewidth, we carried out a series of hole burning measurements on the bulk crystal using different laser powers. This measurement allowed us to extrapolate to the hole width at zero burning power. From a power broadening measurement performed on powder #3, we estimated that our measured hole widths exhibited 1.93 MHz of power

sample	α_{eff} (cm ⁻¹)	$\Gamma_{\text{eff}}^{\text{HB}}$ (kHz)	$\Gamma_{\text{eff}}^{2\text{PE}}$ (kHz)	$\Gamma_{\text{eff}}^{\text{FID}}$ (kHz)
bulk	3.9	< 10	3.2	<10
1 (ref)	13.5	60	4.5/40	32
3	9.4	< 10	12/45	38
4	1.4	1050	30	30
5	0.71	990	38	29
6	2.96	150	37	42

Table 5.4.: Maximum effective absorption coefficient α_{eff} extracted from SHB measurements, as well as effective linewidths Γ_{eff} extracted from SHB (after a $T_w = 25 \mu\text{s}$), 2PE (heterodyne measurement for samples #3 to #6) and FID (after a $T_w = 5 \mu\text{s}$) measurements at $T = 1.6 \text{ K}$ and $B = 2 \text{ T}$ for different samples. When a double exponential decay was observed, as described in the main text, both decay values are listed. For the bulk crystal, the magnetic field and light polarization were parallel to the c -axis ($\mathbf{B} \parallel \mathbf{E} \parallel c$).

broadening, and we then assumed that the power broadening was the same for each powder under the same excitation conditions. This gives a large uncertainty that we estimated to be 10 kHz on the extracted values of the effective linewidth, but still allows us to compare the effects of the different treatments applied to the powders. A comparison between SHB and 2PE measurements for the bulk crystal resulted in an estimated contribution of the laser linewidth to the hole width of 420 kHz. Using these values, the effective homogeneous linewidths were computed from the hole burning measurements by subtracting the power broadening and laser linewidth contributions, with the outcome summarized in Tab. 5.4.

Tab. 5.4 contains a summary of effective homogeneous linewidths measured using different techniques. Note that the values obtained using holeburning and FID are influenced by spectral diffusion (on the timescale of $25 \mu\text{s}$ and $5 \mu\text{s}$ respectively) and laser jitter. We see that powder #1, which was crushed using only a mortar and pestle, shows broader hole widths than the bulk crystal, meaning that additional

spectral diffusion processes occur in this powder. Remarkably, the effective homogeneous linewidth of powder #3, which was ball-milled and then annealed, is narrower, and on the same order of magnitude as that of the bulk crystal. This indicates that crystal damage (strain and defects) caused by mechanical processing, in this case crushing using a mortar and pestle and slow ball milling, could be mostly removed by annealing the powder with the smallest particle sizes studied of roughly $2\text{ }\mu\text{m}$ and lower. On the other hand, powder #4 shows much broader spectral holes with the same mechanical processing as powder #3 but annealing at a higher temperature. To further explore the effect of temperature, powder #5 was ball milled at a higher speed and for a longer time than powders #3 and #4, but was then annealed at the same upper temperature as powder #4, resulting in very large spectral hole widths – nearly the same as for powder #4. These results suggest that the much broader linewidths observed in powders #4 and #5 arise from the higher annealing temperatures. Consequently, it appears that temperatures above 1000 C are detrimental to the material properties rather than beneficial, likely due to additional disorder caused by loss of either lithium or oxygen from the crystal matrix. This hypothesis is consistent with past observations of substantial lithium out-diffusion from the surface of bulk crystals when annealed in a wet oxygen atmosphere at temperatures above approximately 1100 C [58]. Moreover, changes in material properties due to lithium out-diffusion have been observed at temperatures as low as 600 C for LiNbO_3 thin films [52, 53], suggesting that even lower annealing temperatures than used here may be optimal for micro/nano-powders.

Finally, we examined powder #6 that was fabricated through in-diffusion of erbium

into commercial LiNbO_3 powder. This powder was processed using similar mechanical and thermal treatments as for powders #4 and #5, although noticeably narrower linewidths than those of powders #4 and #5 were observed. Further study is required to determine whether the difference in linewidth is a result of the different starting materials, the presence of ErCl_3 mixed with the powder, or other factors.

From the hole burning spectra, we also extracted effective absorption depths for each powder sample. Since scattering in the powder increases the optical path length traveled by the light as it passes through the sample, we should observe a larger absorption depth for samples with more scattering, as well as the expected increase in the overall frequency-independent scattering loss. On the other hand, scattering of light between and around loosely packed particles will reduce the absorption compared to a bulk crystal. In particular, any small gap in the 0.4 mm thick loose powder can result in a weakly scattered background signal that does not strongly probe the powder. Furthermore, when the individual crystallites have anisotropic absorption, the transmitted light in general will not follow the usual Beer-Lambert-Bouguer exponential decay law. Nevertheless, if we assume that the incident light polarization is randomized many times during the scattering process, as we observe experimentally from the transmitted light, then we can approximate the propagation through the powder using the absorption coefficient averaged over all polarizations states. Thus, while it is difficult to extract real absorption coefficients or effective path lengths from the measured transmission spectrum, we do expect the observed effective absorption to provide some qualitative information about the relative scattering path lengths in the powder samples.

For the 1532 nm transition of $\text{Er}^{3+}:\text{LiNbO}_3$, the absorption coefficient is dependent on both the polarization and the propagation direction of the light since the transition has comparable electric and magnetic transition dipole strengths [17]. The maximum absorption coefficients are known for light propagating orthogonally to the crystal's c -axis with π polarization, i.e. $\mathbf{E} \parallel c$ (4.1 cm^{-1}), and σ polarization, i.e. $\mathbf{E} \perp c$ (6.8 cm^{-1}), as well as for the light propagating along the crystal's c -axis with the two circular polarization states (11.1 cm^{-1} averaged over left and right handed polarizations). Consequently, averaging over all possible random crystal orientations and polarizations, we would expect an effective absorption coefficient α_{eff} of 7.3 cm^{-1} for a powder in the limit of many scattering events.

To estimate the effective absorption coefficient α_{eff} for each powder sample, we used high-power (resonant) optical excitation to burn a very deep spectral hole for which we assumed complete transparency since further increasing the burning power did not produce any additional increase in the transmission. Using this approach, α_{eff} was calculated from the transmitted intensity I_t at the center of the hole and the intensity I_0 with the laser tuned away from the hole (where it experiences the full absorption) through the relation

$$\alpha_{\text{eff}} = -\ln\left(\frac{I_t}{I_0}\right)/L, \quad (5.15)$$

where $L = 0.4 \text{ mm}$ is the powder thickness. The resulting effective absorption values are listed in Tab. 5.4 for each sample.

For powders #1 and #3 we measured absorption coefficients (see Tab. 5.4) higher than the bulk average increased by a factor of 1.8 and 1.3 respectively. This is consistent

with the transmitted light experiencing a longer path in the powder sample. However, for the other powder samples, the measured absorption coefficient is significantly lower compared to the bulk. We note that all powders with small optical depth (#4 to #6) underwent the same annealing procedure, with maximum temperatures of around 1100 C, which might have introduced modifications in the host matrix that potentially could cause broadening of the inhomogeneous linewidth or other effects responsible for decreased absorption. This explanation would also be consistent with our observation of larger effective homogeneous linewidths in those same samples. Nevertheless, to conclusively identify the cause of the weaker observed spectral hole depths in these samples requires further study.

The experiment described above shows that SHB measurements in direct transmission could be successfully conducted in powder samples and that the effective linewidths were successfully extracted in samples for which 2PE measurements did not allow a good estimation of the coherence lifetime. Overall, we observed that coherence properties degraded in powders that underwent mechanical processing. This suggests the presence of two-level systems in these samples. To further verify these results, we also used FID techniques to probe the coherence properties over an intermediate range that overlaps those accessible through SHB and 2PE measurements.

5.4.4.5. Free induction decay and spectral diffusion

SHB measurements may be used to probe powders with broad homogeneous linewidths that cannot be accessed by 2PE techniques. However, in cases where rapid spectral diffusion or complex spectral structure such as spin-flip sidebands are present, op-

tical coherent transient FID measurements can serve as a better method to extract the effective homogeneous linewidth [73]. While FID measurements that probe a single spectral hole are still limited by the laser linewidth, FID may be employed immediately following the hole preparation without the need for laser chirping, allowing the broadening to be probed over shorter timescales than frequency domain SHB measurements. Furthermore, FIDs are more amenable to heterodyne detection techniques, allowing for improved signal discrimination and dynamic range relative to SHB. The shape of the FID curve also reveals the evolution of decoherence processes over the timescale of the measurement in a manner similar to 2PE techniques [16], unlike direct SHB that requires an extensive series of measurements to extract similar information.

Motivated by the ability of FID measurements to probe rapid decoherence processes contributing to the homogeneous linewidth (i.e. processes faster than the shortest timescales observable using 2PEs), we employed FID measurements to study all of our powder samples. Specifically, we applied a variation of the FID technique sometimes referred to as a delayed FID that is analogous to a stimulated photon echo measurement [73]. For this approach, a laser pulse first burnt a hole in the inhomogeneously broadened absorption line of the sample: in our case we used a 50 μ s long burn pulse to provide an approximately 20 kHz Fourier-limited spectral resolution. After a waiting time T_w , a second brief excitation pulse was applied to induce an optical coherence across the frequency window of the burnt hole. The decay of the coherent emission after the brief pulse provides information about the effective width of the spectral hole resulting from the convolution of the effective homogeneous

linewidth and the laser linewidth, as well as any spectral diffusion that occurs over the waiting time T_w . In our case, we employed heterodyne detection to measure the coherence decay by beating it with a third laser pulse shifted in frequency by 10 MHz. The decay of the resulting 10 MHz beat signal is given by

$$E(t) = E_0 \exp \left[- \left(\frac{t}{T_M^{T_w}} \right)^x \right] . \quad (5.16)$$

By fitting this equation to the experimentally measured decay, we extracted the effective homogeneous linewidth $\Gamma_{\text{eff}} = 1/\pi T_M^{T_w}$ after a waiting time T_w . An exemplary FID decay signal for powder #1 (reference) at $B = 3.9$ T, $T = 1.6$ K and waiting time $T_w = 5 \mu\text{s}$ is shown in Fig. 5.19, where the steady-state transmitted intensity has been subtracted from the signal. The fit of the FID is shown by the solid line, revealing an exponential decay envelope (i.e. $x = 1$ in Eq. 5.16) that corresponds to an effective linewidth of $\Gamma_{\text{eff}} = 147$ kHz.

By changing the waiting time T_w between the burn and excitation pulses, the delayed FID technique was used to determine the effective homogeneous linewidth at different timescales and thus study time-dependent decoherence processes, i.e. spectral diffusion. The effective homogeneous linewidth over a range of waiting times for different powders is shown in Fig. 5.20. From a comparison of the obtained effective homogeneous linewidths using FID at $T_w = 5 \mu\text{s}$ and the local slope of the two pulse photon echo decay around $t_{12} = 5 \mu\text{s}$ for each powder, we estimated the experimental contribution to each FID measurement due to laser linewidth, power broadening and shot-to-shot laser jitter.

As shown in Fig. 5.20, we observed a rapid time-dependent broadening of the linewidth due to spectral diffusion occurring at timescales of less than 500 μ s, and then a saturation of the broadening at longer timescales, indicating that those waiting times were longer than the inverse of the spectral diffusion rate. Comparing the behaviors at $B = 2$ T and $B = 3.9$ T (see Fig. 5.20(a) and (b)) indicates that spectral diffusion is faster at 2 T, whereas the final linewidth at long T_w is similar at both magnetic fields. Overall, the bulk crystal shows the narrowest linewidths, although powder #1 (the reference powder) that underwent minimal grinding using only a mortar and pestle exhibits similar spectral diffusion broadening as the bulk crystal at the longest time delays. All ball-milled powders show significantly larger effective linewidths. For powders #3 and #4 that underwent the same mechanical treatment, the data points at short T_w suggest that the higher annealing temperature of 1100 C for powder #4 was detrimental. Furthermore, we could not observe a clear saturation of the effective homogeneous linewidth with waiting time for powder #4, unlike all of the other powders. Powder #5 that experienced more severe mechanical treatment (fast ball milling for 10 hours) but the same annealing process as #4, shows comparable broadening as #4, further suggesting that the high annealing temperature was the limiting factor for these samples. This observation is consistent with the SHB results discussed earlier and again points toward defects and disorder in the crystal caused by out-diffusion of lithium at high temperatures [58, 52, 53]. Since the dynamic TLS modes enabled by the disorder typically exhibit a broad distribution of relaxation rates, they are expected to cause significant spectral diffusion that often produces a logarithmic increase in the homogeneous linewidth over time [74, 75].

The commercial powder with large crystallites that were diffusion-doped with Er^{3+} (powder #6) exhibited better coherence properties at long timescales compared to all of the ball-milled powders, although still significantly worse than the bulk crystal and the crushed reference powder #1. This again suggests that higher processing temperatures are a key factor in producing spectral diffusion, although at a lower level for larger particles as might be expected if lithium out-diffusion is the cause.

5.4.5. Conclusion

We demonstrated that spectroscopic properties such as optical coherence lifetimes in $\text{Er}^{3+}:\text{LiNbO}_3$ powders that experienced various mechanical and thermal treatments could be measured despite strong scattering, random orientations, and shorter coherence lifetimes. The 2PE measurements were optimal to access long coherence lifetimes whereas SHB and FID techniques were well suited to quantify fast dephasing processes. Furthermore, we described how the powder properties could be predicted and understood by averaging the orientation dependent properties of the bulk single crystal.

We observed that mechanical grinding of the powders resulted in a broadening of their effective homogeneous linewidths, indicating the presence of dynamic TLS modes characteristic of amorphous phases. This conclusion was also supported by observations of corresponding decreases in the maximum absorption as well as a broader distribution of spectral diffusion rates as compared to the bulk crystal. Surprisingly, we found that even crushing and grinding with mortar and pestle to produce large

microcrystals resulted in significant damage as indicated by an order-of-magnitude increase in the homogeneous linewidth. In the powders that experienced less processing, spectral diffusion broadening at longer timescales approached the values observed in the bulk, suggesting that grinding primarily accelerates existing spectral diffusion mechanisms (such as Er^{3+} electronic spin flips) rather than introducing new sources of broadening. This conclusion is also consistent with the increase in the magnetic-field-dependent spectral diffusion rates extracted from analysis of the 2PE coherence measurements (summarized in Tab. 5.6). We found that the broadening could be partially reversed by high-temperature annealing in oxygen atmospheres for some powders; however, treatment at temperatures above 1000 C was detrimental for the coherence properties. The powders annealed at temperatures above 1000 C exhibited a large increase in the magnitude of spectral diffusion, suggesting that additional broadening mechanisms were introduced, possibly due to out-diffusion of lithium and oxygen from the crystallites.

Together, our results demonstrate that even minimal low-energy mechanical processing significantly degrades the material properties of interest for classical and quantum signal-processing applications. Chemical fabrication methods, such as chemical synthesis or etching may minimize the amount of amorphous-like behavior introduced when fabricating micro- and nano-materials and lead to better optical coherence properties. This hypothesis is consistent with past structural and spectroscopic studies of nanocrystalline LiNbO_3 where powders produced by sol-gel methods had significantly better properties than those produced by high-energy ball milling [46, 48], although still not reaching the bulk crystal properties [49]. The detrimental effects of high an-

nealing temperatures also suggest that lower temperature bottom-up synthesis may be preferred. The demonstration of long coherence lifetimes in $\text{Eu:Y}_2\text{O}_3$ nanopowders produced using solvothermal methods confirms that at least some materials can be fabricated with optical coherence properties approaching those of the bulk crystal [39]. Based on the recent work on $\text{Nd:Y}_2\text{SiO}_5$ [40], we expect that focused-ion-beam milling may also be successful in preserving the coherence properties of REI-doped LiNbO_3 , potentially providing a suitable tool to fabricate micro- and nano-structures for optical signal-processing applications. Nevertheless, further studies are required to determine whether there are other fundamental limitations of material performance when the crystal size is reduced to the nanoscale.

5.4.6. Acknowledgments

The authors wish to thank Ph. Goldner and A. Ferrier for valuable discussions on optical coherence measurements in powders. The work reported here was supported by Alberta Innovates Technology Futures (ATIF), the National Engineering and Research Council of Canada (NSERC), and the National Science Foundation of the USA (NSF) under award nos. PHY-1212462, PHY-1415628, and CHE-1416454. W. T. is a senior fellow of the Canadian Institute for Advance Research (CIFAR).

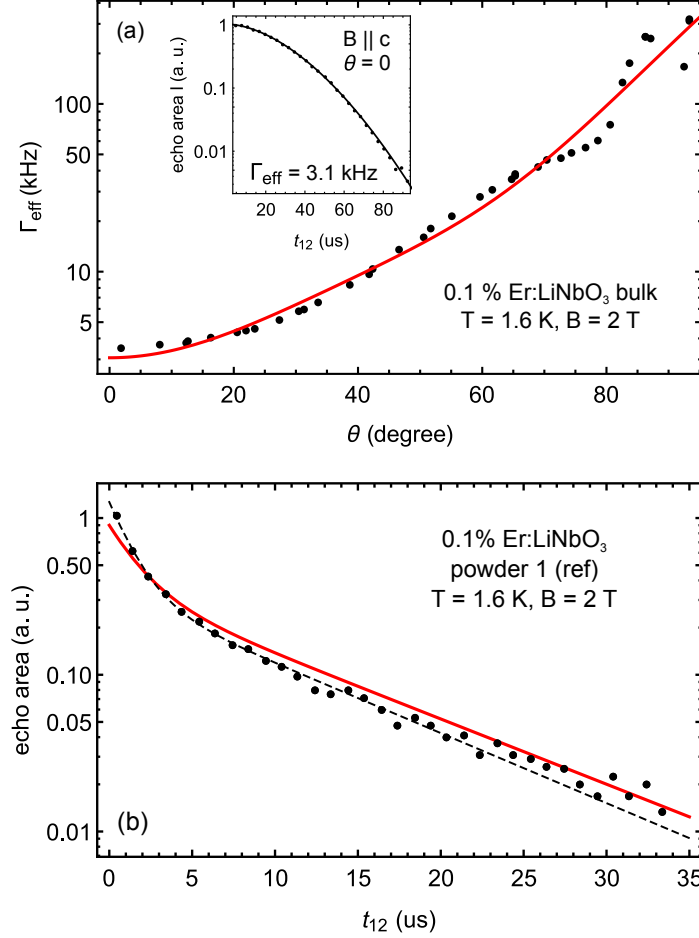


Figure 5.16.: (a) Orientation dependence of the effective linewidth Γ_{eff} in a 0.1% $\text{Er}^{3+}:\text{LiNbO}_3$ bulk crystal measured at $T = 1.6$ K and $B = 2$ T. The magnetic field orientation is rotated by an angle θ from the c -axis of the crystal. The inset shows an example echo intensity decay at $\theta = 0$ i.e. $\mathbf{B} \parallel c$, where the fit of Eq. 5.9 gives $\Gamma_{\text{eff}} = 1/\pi T_M = 3.1$ kHz. The red solid line is an empirical polynomial fit to the experimental $\Gamma_{\text{eff}}(\theta)$ data. (b) Decay of the echo area for the 0.1% $\text{Er}^{3+}:\text{LiNbO}_3$ reference powder. The dashed line corresponds to a fit of a sum of two exponential decays to the experimental data (black dots). The red solid line corresponds to a calculation of the expected decay in the powder due to the orientation dependence of Γ_{eff} in the bulk crystal.

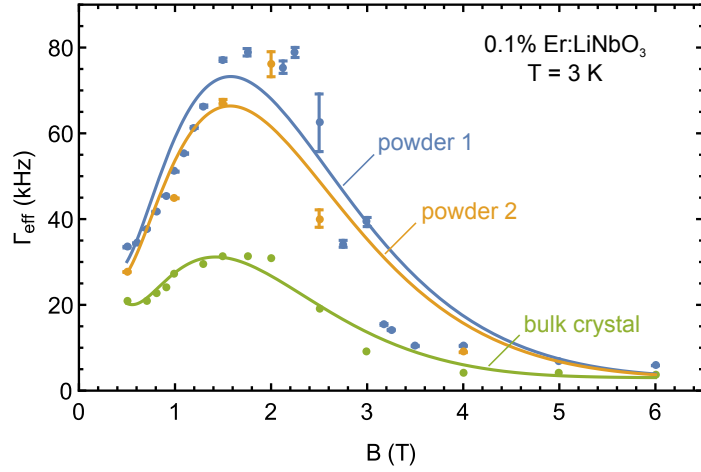


Figure 5.17.: Magnetic field dependence of the effective homogeneous linewidth in 0.1% $\text{Er}^{3+}:\text{LiNbO}_3$ at $T = 3$ K for the bulk crystal (for $\mathbf{B} \parallel c$), the reference powder #1, and a powder ball-milled for 30 min. (powder #2).

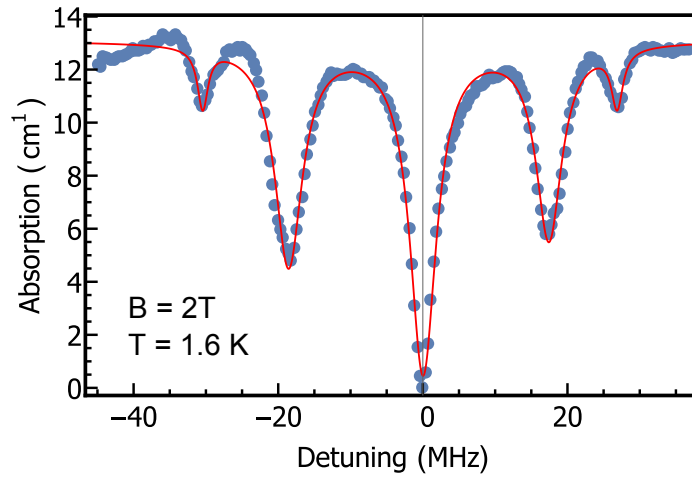


Figure 5.18.: Hole burning spectrum in 0.1% $\text{Er}^{3+}:\text{LiNbO}_3$ (powder #1) at $T = 1.6$ K and $B = 2$ T. Zero detuning corresponds to 1531.882 nm in vacuum.

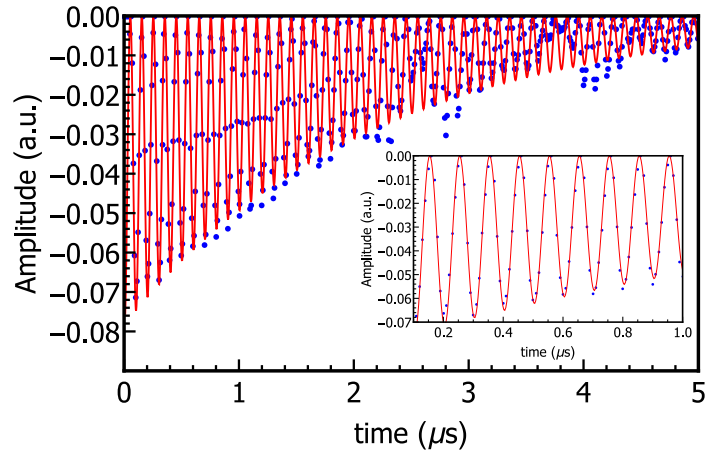


Figure 5.19.: Typical background-subtracted FID decay of the reference powder #1 at $B = 3.9$ T, $T = 1.6$ K and waiting time $t_w = 5$ μ s. Solid points are measured values and the solid line is a fit of the FID signal. The inset shows a magnification of the first 1 μ s of the decay.

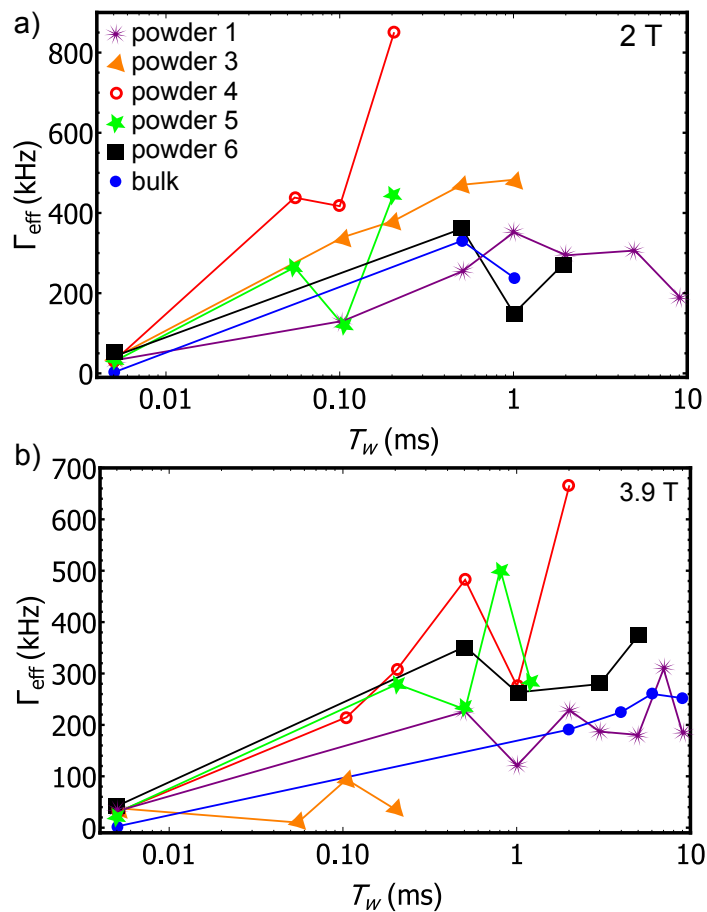


Figure 5.20.: Effective homogeneous linewidths at a) $B = 2$ T and b) $B = 3.9$ T at $T = 1.6$ K as a function of the waiting time T_w measured using the delayed FID technique for powders #1, # 3 through #6 and for the bulk crystal. The solid lines are guides to the eye.

Bibliography

- [1] Y. C. Sun, in *Spectroscopic Properties of Rare Earths in Optical Materials*, P. R. Hull, P. J. Parisi, P. R. M. O. Jr, P. H. Warlimont, D. G. Liu, and P. B. Jacquier, eds. (Springer Berlin Heidelberg, 2005), no. 83 in Springer Series in Materials Science, pp. 379–429.
- [2] L. Ménager, I. Lorgeré, J.-L. Le Gouët, D. Dolfi, and J.-P. Huignard, *Optics Letters* **26**, 1245 (2001).
- [3] B. Lauritzen, J. Minář, H. de Riedmatten, M. Afzelius, and N. Gisin, *Physical Review A* **83**, 012318 (2011).
- [4] R. Lauro, J. Ruggiero, A. Louchet, A. Alexander, T. Chanelière, I. Lorgeré, F. Bretenaker, F. Goldfarb, and J. L. Le Gouët, *Journal of Luminescence* **129**, 1951 (2009).
- [5] M. Afzelius, C. Simon, H. de Riedmatten, and N. Gisin, *Physical Review A* **79**, 052329 (2009).

- [6] E. Saglamyurek, N. Sinclair, J. A. Slater, K. Heshami, D. Oblak, and W. Tittel, New Journal of Physics **16**, 065019 (2014).
- [7] C. W. Thiel, T. Böttger, and R. L. Cone, Journal of Luminescence **131**, 353 (2011).
- [8] J. Amin, B. Dussardier, T. Schweizer, and M. Hempstead, Journal of Luminescence **69**, 17 (1996).
- [9] E. Saglamyurek, N. Sinclair, J. Jin, J. A. Slater, D. Oblak, F. Bussi eres, M. George, R. Ricken, W. Sohler, and W. Tittel, Nature **469**, 512 (2011).
- [10] R. S. Weis and T. K. Gaylord, Applied Physics A **37**, 191 (1985).
- [11] C. E. R uter, S. Suntsov, D. Kip, G. Stone, V. Dierolf, H. Hu, and W. Sohler (2014), vol. 8982, pp. 89821G–89821G–8.
- [12] M. N. Armenise, IEE Proceedings J - Optoelectronics **135**, 85 (1988).
- [13] W. Sohler and H. Suche, *Integrated optical circuits and components Design and applications* (Marcel Dekker, 1999).
- [14] Y. Sun, C. W. Thiel, R. L. Cone, R. W. Equall, and R. L. Hutcheson, Journal of Luminescence **98**, 281 (2002).
- [15] S. R. Hastings-Simon, M. U. Staudt, M. Afzelius, P. Baldi, D. Jaccard, W. Tittel, and N. Gisin, Optics Communications **266**, 716 (2006).
- [16] C. W. Thiel, R. M. Macfarlane, T. B ttger, Y. Sun, R. L. Cone, and W. R. Babbitt, Journal of Luminescence **130**, 1603 (2010).

- [17] C. W. Thiel, Y. Sun, R. M. Macfarlane, T. Böttger, and R. L. Cone, *Journal of Physics B: Atomic, Molecular and Optical Physics* **45**, 124013 (2012).
- [18] S. Benchabane, L. Robert, J.-Y. Rauch, A. Khelif, and V. Laude, *Journal of Applied Physics* **105**, 094109 (2009).
- [19] N. Courjal, S. Benchabane, J. Dahdah, G. Ulliac, Y. Gruson, and V. Laude, *Applied Physics Letters* **96**, 131103 (2010).
- [20] F. Lacour, N. Courjal, M. P. Bernal, A. Sabac, C. Bainier, and M. Spajer, *Optical Materials* **27**, 1421 (2005).
- [21] I. L. Gheorma, P. Savi, and R. M. Osgood, *IEEE Photonics Technology Letters* **12**, 1618 (2000).
- [22] T. A. Ramadan, M. Levy, and R. M. Osgood, *Applied Physics Letters* **76**, 1407 (2000).
- [23] H. Robinson, C. W. Pitt, and R. A. Gibson, *Applied Optics* **32**, 3981 (1993).
- [24] H. Hu, R. Ricken, W. Sohler, and R. B. Wehrspohn, *IEEE Photonics Technology Letters* **19**, 417 (2007).
- [25] B. Knabe, K. Buse, W. Assenmacher, and W. Mader, *Physical Review B* **86**, 195428 (2012).
- [26] R. Grange, J.-W. Choi, C.-L. Hsieh, Y. Pu, A. Magrez, R. Smajda, L. Forró, and D. Psaltis, *Applied Physics Letters* **95**, 143105 (2009).

- [27] A. N. Morozovska, E. A. Eliseev, G. S. Svechnikov, and S. V. Kalinin, Journal of Applied Physics **108**, 042009 (2010).
- [28] A. Rüdiger, T. Schneller, A. Roelofs, S. Tiedke, T. Schmitz, and R. Waser, Applied Physics A **80**, 1247 (2005).
- [29] N. Kunkel, J. Bartholomew, S. Welinski, A. Ferrier, A. Ikesue, and P. Goldner, Phys. Rev. B **94**, 184301 (2016).
- [30] J. G. Bartholomew, K. de Oliveira Lima, A. Ferrier, and P. Goldner, Nano Letters **17**, 778 (2017).
- [31] G. P. Flinn, K. W. Jang, J. Ganem, M. L. Jones, R. S. Meltzer, and R. M. Macfarlane, Phys. Rev. B **49**, 5821 (1994).
- [32] R. Meltzer, K. Jang, K. Hong, Y. Sun, and S. Feofilov, Journal of Alloys and Compounds **250**, 279 (1997).
- [33] K. S. Hong, R. S. Meltzer, B. Bihari, D. K. Williams, and B. M. Tissue, Journal of Luminescence **76**, 234 (1998).
- [34] S. P. Feofilov, Physics of the Solid State **44**, 1407 (2002).
- [35] R. M. Macfarlane and M. J. Dejneka, Optics Letters **26**, 429 (2001).
- [36] H. Zheng, X.-j. Wang, S.-X. Qu, M. J. Dejneka, and R. S. Meltzer, Journal of Luminescence **119**, 153 (2006).
- [37] R. S. Meltzer, H. Zheng, and M. J. Dejneka, Journal of Luminescence **107**, 166 (2004).

- [38] F. Beaudoux, A. Ferrier, O. Guillot-Noël, T. Chanelière, J.-L. Le Gouët, and P. Goldner, *Optics Express* **19**, 15236 (2011).
- [39] A. Perrot, P. Goldner, D. Giaume, M. Lovrić, C. Andriamiadamanana, R. R. Gonçalves, and A. Ferrier, *Physical Review Letters* **111**, 203601 (2013).
- [40] T. Zhong, J. M. Kindem, E. Miyazono, and A. Faraon, *Nature Communications* **6**, 8206 (2015).
- [41] C. C. Koch, *Nanostructured Materials* **2**, 109 (1993).
- [42] V. Šepelák, S. Bégin-Colin, and G. L. Caër, *Dalton Transactions* **41**, 11927 (2012).
- [43] D. Michel, L. Mazerolles, P. Berthet, and E. Gaffet, *European Journal of Solid State and Inorganic Chemistry* **32**, 673 (1995).
- [44] S. L. Bravina, A. N. Morozovska, N. V. Morozovsky, and Y. A. Skryshevsky, *Ferroelectrics* **298**, 31 (2004).
- [45] D. Bork and P. Heitjans, *The Journal of Physical Chemistry B* **102**, 7303 (1998).
- [46] M. J. Pooley and A. V. Chadwick, *Radiation Effects and Defects in Solids* **158**, 197 (2003).
- [47] P. Heitjans and S. Indris, *Journal of Materials Science* **39**, 5091 (2004).
- [48] A. V. Chadwick, M. J. Pooley, and S. L. P. Savin, *Physica Status Solidi (C)* **2**, 302 (2005).

- [49] P. Heitjans, M. Masoud, A. Feldhoff, and M. Wilkening, *NMR and Impedance Studies of Nanocrystalline and Amorphous Ion Conductors: Lithium Niobate as a Model System*, vol. 134 (2007).
- [50] S. Kar, S. Logad, O. P. Choudhary, C. Debnath, S. Verma, and K. S. Bartwal, *Universal Journal of Materials Science* **1**, 18 (2013).
- [51] T. Lutz, L. Veissier, C. W. Thiel, P. J. T. Woodburn, R. L. Cone, P. E. Barclay, and W. Tittel, *Science and Technology of Advanced Materials* **17**, 63 (2016).
- [52] X. Wang, Z. Ye, G. Li, and B. Zhao, *Journal of Crystal Growth* **306**, 62 (2007).
- [53] G. C. Budakoti and R. S. Rawat, *Journal of Crystal Growth* **310**, 4205 (2008).
- [54] H. Jhans, J. M. Honig, and C. N. R. Rao, *Journal of Physics C: Solid State Physics* **19**, 3649 (1986).
- [55] A. Dhar and A. Mansingh, *Journal of Applied Physics* **68**, 5804 (1990).
- [56] A. Z. Simões, M. A. Zaghete, B. D. Stojanovic, A. H. Gonzalez, C. S. Riccardi, M. Cantoni, and J. A. Varela, *Journal of the European Ceramic Society* **24**, 1607 (2004).
- [57] J. L. Jackel, V. Ramaswamy, and S. P. Lyman, *Applied Physics Letters* **38**, 509 (1981).
- [58] S. Forouhar, G. E. Betts, and W. S. C. Chang, *Applied Physics Letters* **45**, 207 (1984).

- [59] U. Schlarb and K. Betzler, *Physical Review B* **48**, 15613 (1993).
- [60] D. E. Zelmon, D. L. Small, and D. Jundt, *JOSA B* **14**, 3319 (1997).
- [61] R. Macfarlane, Y. Sun, R. Cone, C. Thiel, and R. Equall, *Journal of Luminescence* **107**, 310 (2004). Proceedings of the 8th International Meeting on Hole Burning, Single Molecule, and Related Spectroscopies: Science and Applications.
- [62] T. Böttger, C. W. Thiel, R. L. Cone, and Y. Sun, *Physical Review B* **79**, 115104 (2009).
- [63] W. B. Mims, *Physical Review* **168**, 370 (1968).
- [64] T. Böttger, C. W. Thiel, Y. Sun, and R. L. Cone, *Physical Review B* **73**, 075101 (2006).
- [65] L. Veissier, M. Falamarzi, T. Lutz, E. Saglamyurek, C. W. Thiel, R. L. Cone, and W. Tittel, *Physical Review B* **94**, 195138 (2016).
- [66] T. Gog, M. Griebenow, and G. Materlik, *Physics Letters A* **181**, 417 (1993).
- [67] J. García Solé, L. E. Bausá, D. Jaque, E. Montoya, H. Murrieta, and F. Jaque, *Spectrochimica Acta Part A: Molecular and Biomolecular Spectroscopy* **54**, 1571 (1998).
- [68] P. W. Anderson, B. I. Halperin, and c. M. Varma, *Philosophical Magazine* **25**, 1 (1972).
- [69] W. Phillips, *Journal of Low Temperature Physics* **7**, 351 (1972).

- [70] S. K. Watson, Phys. Rev. Lett. **75**, 1965 (1995).
- [71] T. R. Askew, H. J. Stapleton, and K. L. Brower, Phys. Rev. B **33**, 4455 (1986).
- [72] L. Aminov, I. Kurkin, and D. Lukoyanov, Applied Magnetic Resonance **14**, 447 (1998).
- [73] R. M. Macfarlane, *Coherent transient and holeburning spectroscopy of rare earth ions in solids, in Spectroscopy of Solids Containing Rare Earth Ions* (North-Holland, 1987).
- [74] J. L. Black and B. I. Halperin, Physical Review B **16**, 2879 (1977).
- [75] R. J. Silbey, J. M. A. Koedijk, and S. Völker, The Journal of Chemical Physics **105**, 901 (1996).

5.5. Identification and suppression of the direct-phonon process

After identifying methods that allowed us to fabricate small crystalline powders with similar spectroscopic properties as a bulk material, we had to find materials that are suitable for proof-of-principle experiments that show that phonon suppression is indeed achievable in small structures and can lead to enhanced population lifetimes, for both spin- and crystal field levels. As shown in chapter 4, for spin levels, the direct phonon process can be easily identified by its magnetic field dependence. In the case of crystal field levels this is not possible. However, if relaxation can be inhibited in small materials, it must have been caused by the direct phonon process. The following subsections will report on the observation of phonon-driven relaxation between spin states in $\text{Tm}^{3+}:\text{Y}_3\text{Al}_5\text{O}_{12}$ and on the observation of suppression of spin lattice relaxation between crystal field levels in small $\text{Tb}^{3+}:\text{Y}_3\text{Al}_5\text{O}_{12}$ powders.

5.6. Paper 4: Quadratic Zeeman effect and spin-lattice relaxation of $\text{Tm}^{3+}:\text{Y}_3\text{Al}_5\text{O}_{12}$ at high magnetic fields

Physical Review B, **94**, 205133, 22 Nov, 2016

5.6.1. Summary

In Paper 4 we characterized the magnetic field and temperature dependence of spin lifetimes in $\text{Tm}^{3+}:\text{Y}_3\text{Al}_5\text{O}_{12}$. A model that is in good agreement with the experimental data and explains the different relaxation processes involved is presented. For the first time, we observe the contribution of direct phonon process to the relaxation between Zeeman states in $\text{Tm}^{3+}:\text{Y}_3\text{Al}_5\text{O}_{12}$. The rate of the process increases, as expected, with the magnetic field to the fourth power and dominates relaxation at fields above 3.5 T and temperatures below 2 K.

Furthermore, the paper characterizes the frequency shift of the optical transition around 793 nm due to the quadratic Zeeman effect. The measurements were performed for the different crystallographic sites that are occupied by the thulium ions in the YAG matrix and for various orientations of the magnetic field. The results are in good agreement with theoretical predictions that are also presented in the manuscript. Knowledge about the orientation and site dependence of the optical transition is of particular importance for any subsequent work on powders of that material since any measurement will average over all possible field orientations and all crystallographic sites in a randomly oriented powder material. We show that the site dependent frequency shift provides a tool to spectrally select ions of different crystallographic sites. In a randomly oriented powder, strong scattering also randomizes the polarization of the probe light and each crystallite has its own orientation compared to the external field. Thus the spectral selection is the only way to perform

site selective spectroscopy in such a material.

The first measurements towards the identification of the direct phonon-driven relaxation in $Tm^{3+}:Y_3Al_5O_{12}$ were performed by myself. Later measurements, including the measurement of the site- and orientation-dependent shift of the optical transition and measurements at high magnetic field ($> 2T$) were performed by the first authors with equal contribution. Lucile Veissier performed the data analysis for the orientation- and site dependent measurements whereas I did the analysis of the spin relaxation measurements. The first draft of the manuscript was written by Lucile Veissier.

**Quadratic Zeeman effect and spin-lattice relaxation of $\text{Tm}^{3+}:\text{YAG}$
at high magnetic fields**

Lucile Veissier^{1*†}, Charles W. Thiel², Thomas Lutz¹, Paul E. Barclay¹ Wolfgang
Tittel¹ and Rufus L. Cone²

¹*Institute for Quantum Science and Technology, and Department of Physics &
Astronomy, University of Calgary, Calgary Alberta T2N 1N4, Canada*

²*Department of Physics, Montana State University, Bozeman, MT 59717 USA*

[†] *Present address: Laboratoire Aimé Cotton, CNRS-UPR 3321, Univ. Paris-Sud,
Bât. 505, F-91405 Orsay Cedex, France*

**Corresponding author: lucile.veissier@u-psud.fr*

Abstract: Anisotropy of the quadratic Zeeman effect for the $^3\text{H}_6 \rightarrow ^3\text{H}_4$ transition at 793 nm wavelength in $^{169}\text{Tm}^{3+}$ -doped $\text{Y}_3\text{Al}_5\text{O}_{12}$ is studied, revealing shifts ranging from near zero up to + 4.69 GHz/T² for ions in magnetically inequivalent sites. This large range of shifts is used to spectrally resolve different subsets of ions and study nuclear spin relaxation as a function of temperature, magnetic field strength, and orientation in a site-selective manner. A rapid decrease in spin lifetime is found at large magnetic fields, revealing the weak contribution of direct-phonon absorption and emission to the nuclear spin-lattice relaxation rate. We furthermore confirm theoretical predictions for the phonon coupling strength, finding much smaller values than those estimated in the limited number of past studies of thulium in similar crystals. Finally, we observe a significant – and unexpected – magnetic field dependence of the two-phonon Orbach spin relaxation process at higher field strengths, which

we explain through changes in the electronic energy-level splitting arising from the quadratic Zeeman effect.

5.6.2. Introduction

$\text{Tm}^{3+}:\text{Y}_3\text{Al}_5\text{O}_{12}$ (YAG) has been intensely studied and widely used for applications ranging from photonic signal processing [1, 2] and laser frequency stabilization [3] to solid-state quantum memories [4, 5]. Indeed, the optical $^3\text{H}_6 \rightarrow ^3\text{H}_4$ transition of this material exhibits desired properties, such as long coherence lifetimes of up to $105\ \mu\text{s}$ in zero field [6] and $300\ \mu\text{s}$ in a small magnetic field [7]. Furthermore, its wavelength of 793 nm is easily accessible with commercial laser technologies. Another advantage is the absence of hyperfine structure (and corresponding spin-flip sidebands) in zero magnetic field for the single thulium isotope ^{169}Tm , which has a nuclear spin of $1/2$ and therefore no nuclear quadrupole structure; the absence of sidebands enhances resolution in optical-microwave frequency spectrum analysis applications. An external magnetic field lifts the degeneracy of spin states through the enhanced effective nuclear Zeeman interaction [8], and optical pumping of those nuclear hyperfine states provides long population storage lifetimes and enables many spectral hole burning applications [9, 10, 11, 12].

In order to find optimal operation parameters for applications, characterization of the orientation and site dependent properties such as spin-state lifetimes and magnitude of the quadratic Zeeman shift is required. This is particularly important in the case of $\text{Tm}:\text{YAG}$, since due to the cubic symmetry of the YAG crystal structure, the

lattice contains six classes of thulium sites that have the same point symmetry but different local orientations relative to externally applied electric and magnetic fields [13] (see Fig. 5.21). Because of a large anisotropy in the magnetic properties of the thulium ions, many spectroscopic properties depend strongly on the orientation of the applied magnetic field and, as a result, different behavior can be observed for ions at each of the six magnetically-inequivalent sites. In particular, this site dependence has been observed for the thulium nuclear spin-state lifetimes [12]. In addition, the quadratic Zeeman effect, caused by the mixing of the crystal field levels due to the applied magnetic field, shifts the energy levels in both the ground and excited states, leading to a shift of the optical transition that is expected to be strongly orientation and site dependent. Finally, by observing the properties at higher magnetic field strengths, physical mechanisms with different field sensitivities may be separated and unambiguously identified, improving the general understanding of material properties. This paper is arranged as follows. After outlining the theoretical background, the orientation dependence of the optical transition frequency is experimentally characterized and compared to the theoretical prediction. We also measure the spin-lattice relaxation of the thulium sites with the longest hyperfine lifetime as a function of the magnetic field strength and temperature. We identify the contribution from the direct phonon process, finding that it only becomes larger than the two-phonon Orbach relaxation process for fields greater than 4 T - this holds even at temperatures below 2 K. These results reveal that the phonon coupling strength in Tm:YAG is much smaller than what has been previously estimated for thulium in other hard oxide crystals, suggesting that past measurements [16, 17, 18] were limited by other

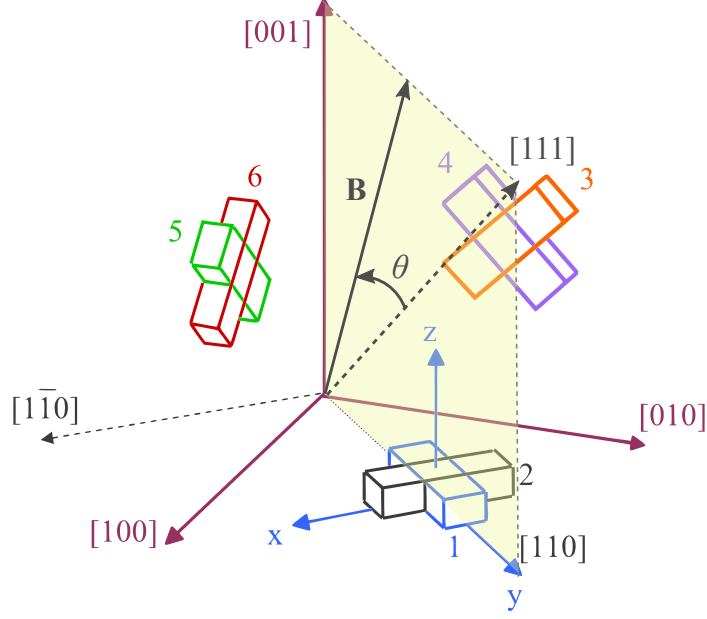


Figure 5.21.: Orientation of the six different sites of Tm^{3+} ions in the YAG crystal lattice [14, 15]. Each parallelepiped represents the orientation of the local D_2 point symmetry for a subset of sites. The specific set of x , y , and z axes labeled in the diagram correspond to the local frame of site 1. In our experiment, the light propagates along $[1\bar{1}0]$ and the magnetic field is applied in the plane defined by $[110]$ and $[001]$, forming an angle θ with the $[111]$ axis. Because of the D_2 point symmetry of the sites, the electric transition dipole moment for the specific ground and excited states involved in the 793 nm optical transition is aligned along the local y axis. The gyromagnetic tensor γ_J orientation is also determined by the local frame.

relaxation mechanisms such as paramagnetic impurities.

5.6.3. Quadratic Zeeman shift

5.6.3.1. Theoretical background

When studying properties of rare-earth transitions at higher external magnetic field strengths (generally $B > 1$ T), one must consider the second-order mixing of crystal-field wavefunctions due to the quadratic Zeeman effect. Here we study this effect in order to be able to predict the position of energy levels and transition frequencies at

different magnetic fields up to 6 T. Furthermore, as we will show later, in the case of Tm:YAG the anisotropy of the quadratic Zeeman effect allows us to spectrally resolve different subsets of ions.

For a Tm^{3+} ion in a crystal matrix, the Hamiltonian is given by

$$H = H_{\text{FI}} + H_{\text{CF}} + H_{\text{HF}} + H_{\text{Q}} + H_{\text{eZ}} + H_{\text{nZ}}, \quad (5.17)$$

where the first two terms are the largest, corresponding to the free ion and the crystal field coupling. Consequently, the wavefunctions of the system can be expressed by the eigenstates of these two terms together, and the other terms, namely the hyperfine, nuclear quadrupole, electronic and nuclear Zeeman interaction, are treated as perturbations [19]. The Tm^{3+} ion is a non-Kramers ion that sits at a site with D_2 point symmetry in the YAG lattice, resulting in a singlet electronic ground state. Consequently, the electronic angular momentum J is effectively quenched to first order and the hyperfine structure is given by second-order terms [20]. Taking into account the ^{169}Tm nuclear spin of 1/2, the effective Hamiltonian corresponding to the last four terms in Eq. 5.17, is

$$H_{\text{eff}} = -2A_J g_J \mu_{\text{B}} \mathbf{B} \cdot \mathbf{\Lambda} \cdot \mathbf{I} - \gamma_{\text{n}} \mathbf{B} \cdot \mathbf{I} - g_J^2 \mu_{\text{B}}^2 \mathbf{B} \cdot \mathbf{\Lambda} \cdot \mathbf{B}, \quad (5.18)$$

where A_J is the magnetic hyperfine constant, g_J is the Landé factor of the electron, μ_{B} is the Bohr magneton, \mathbf{B} the applied magnetic field, \mathbf{I} the nuclear spin, and γ_{n} the nuclear gyromagnetic ratio. The tensor $\mathbf{\Lambda}$, expressed in second-order perturbation

theory is

$$\Lambda_{\alpha\beta} = \sum_{n \neq 0} \frac{\langle 0 | J_\alpha | n \rangle \langle n | J_\beta | 0 \rangle}{E_n - E_0}. \quad (5.19)$$

The sum is performed over the crystal field levels, which have energy E_n .

The first term of Eq. 5.18 describes the second order coupling between the hyperfine interaction and the electronic Zeeman effect. Together with the second term, the nuclear Zeeman interaction, they form the so-called enhanced nuclear Zeeman interaction, which can be re-written as [21]

$$H_{\text{enZ}} = -\hbar (\gamma_{J,x} B_x I_x + \gamma_{J,y} B_y I_y + \gamma_{J,z} B_z I_z) \quad (5.20)$$

with $\gamma_{J,\alpha} = \gamma_n + \frac{2A_J g_J \mu_B \Lambda_{\alpha\alpha}}{\hbar},$

where $\alpha = x, y$ or z . In case of the D_2 symmetry of the yttrium ion sites in YAG, the Λ -tensor is diagonal in each local frame $(\mathbf{x}, \mathbf{y}, \mathbf{z})$. This interaction leads to the splitting of the crystal field levels into spin states that are involved in persistent hole burning [10]. The effective gyromagnetic tensors γ_J have been estimated theoretically for the ground and excited states of the optical ${}^3\text{H}_6 \rightarrow {}^3\text{H}_4$ transition [21], and their components have been measured experimentally [22, 23]. These γ_J components are approximately 10 times larger in the ground state than in the excited state, which leads to much larger hyperfine splittings in the ground state.

The last term of Eq. 5.18 corresponds to the second-order, or quadratic, electronic Zeeman interaction that results from the magnetic-field-induced mixing of the electronic crystal field wavefunctions. As the third crystal field level of the ground state is far from the lowest two levels, with an energy of 216 cm^{-1} or 4.63 THz , its con-

tribution is negligible, so that this effect can be viewed as simple mixing between the lowest two crystal field levels. Because of this interaction, the applied magnetic field induces a weak magnetic moment, called Van Vleck paramagnetism, [26] that shifts the energy of each crystal field level in both the ground and excited states, as illustrated in Fig. 5.22. This then leads to a frequency shift of the optical transition that is proportional to B^2 in the regime where the shifts are much smaller than the crystal field splittings.

Because a large enhancement of the effective nuclear moment arises from the coupling of the nuclear spin to the induced electronic paramagnetism [8], the quadratic Zeeman interaction can be directly related to the resulting hyperfine splittings [20]. Thus, the energy displacement can be written in terms of the effective gyromagnetic tensor of the enhanced nuclear Zeeman interaction γ_J

$$D_J = \frac{g_J \mu_B}{2A_J} [(\gamma_{J,x} - \gamma_n) B_x^2 + (\gamma_{J,y} - \gamma_n) B_y^2 + (\gamma_{J,z} - \gamma_n) B_z^2] . \quad (5.21)$$

Finally, the frequency shift on the optical transition is given by $\Delta = (D_g - D_e)/h$ where g and e denote the ground and excited state, respectively. Because of the relation between excited and ground state hyperfine splittings and quadratic Zeeman effects, the observed hyperfine splittings can be used to infer the relative magnitude of the ground and excited state quadratic Zeeman effects. Moreover, since the component $\gamma_{J,y}$ is much larger in the ground state than in the excited state while the two other components of γ_J are of the same order of magnitude [21], the quadratic

Zeeman effect in the ground state is the largest contribution to the shift Δ of the optical transition. With this approximation, one should observe $\Delta(B) \sim \Delta_{\text{CF}}(B)/2$, with $\Delta_{\text{CF}}(B)$ the crystal field transition frequency (see Fig. 5.22).

5.6.3.2. Measurements of the inhomogeneous line

All measurements were performed on $\text{Tm}^{3+}:\text{YAG}$ bulk crystals from Scientific Materials, with doping concentrations of either 0.1 or 1 %. The sample was cooled in an Oxford Instruments Spectromag cryostat through helium exchange gas. Our setup provided magnetic-field strengths of up to 6 T and sample temperatures T down to 1.6 K.

5.6.3.3. Magnetic field strength dependence

We first studied the properties of the inhomogeneously broadened $^3\text{H}_6 \rightarrow ^3\text{H}_4$ absorption line (see Fig 5.22) as we varied the magnetic field strength for a specific orientation of the magnetic field relative to the crystal. We initially chose to apply the magnetic field \mathbf{B} along the $[111]$ crystallographic axis (see Fig. 5.21). In this case, the sites 1, 3, and 5 are magnetically equivalent, and the sites 2, 4, and 6 are magnetically equivalent. The light probing the medium with the \mathbf{k} vector along $[1\bar{1}0]$ was linearly polarized with the electric field vector \mathbf{E} parallel to the $[111]$ axis. In this case, the electric transition dipoles μ of site 2, 4, and 6 ions are orthogonal to the light polarization and thus only ions of sites 1, 3, and 5 are addressed (all featuring identical Rabi frequencies).

High resolution measurements of the inhomogeneous line were performed by scanning

a New Focus Vortex laser with ~ 1 MHz linewidth over the $^3\text{H}_6 \rightarrow ^3\text{H}_4$ transition. The scans were calibrated via a Fabry Perot cavity with a free spectral range of 97 MHz. At zero magnetic field, the inhomogeneous line, shown in Fig. 5.23 (a), exhibits a Lorentzian shape with a full width at half maximum of 17 GHz, a center frequency of $\nu_0 = 377868$ GHz (793.3788 nm) and a peak absorption coefficient of 2.3 cm^{-1} . When we applied a magnetic field along the [111] axis, the inhomogeneous line was shifted by Δ , as shown in Fig. 5.23 (b) where $B = 3$ T and $\Delta = 42.7$ GHz. We then quantified the shift of the inhomogeneous line center frequency as the magnetic field strength B was varied, as shown in Fig. 5.24. The experimental data were fitted by the quadratic function $\Delta(B) = \gamma_2 B^2$, yielding a coefficient $\gamma_2 = 4.69 \pm 0.03$ GHz/T². From Eq. 5.21, the energy displacements of the ground and excited states were calculated, using the known values of A_J for $^{169}\text{Tm}^{3+}$ [21] and the experimentally measured components of γ_J [22]. This leads to an expected value of 4.2 GHz/T², which is in agreement with the experimental one, supporting the validity of our model. In addition to a shift in the transition energy due to the Zeeman effect, we also observed a nonlinear increase in the inhomogeneous linewidth Γ_{inh} . A quadratic increase in Γ_{inh} is expected due to the inhomogeneous broadening at zero field and the resulting spread of energy splittings in Eq. 5.19. It is straightforward to show that if Γ_{CF} is the inhomogeneous broadening of the energy level splitting Δ_{CF} between the two crystal field levels mixed by the quadratic Zeeman effect with a magnitude of γ_{CF} , then the contribution to the optical inhomogeneous broadening will simply be

$$\Delta\Gamma_{\text{inh}} = \frac{\gamma_{\text{CF}}\Gamma_{\text{CF}}}{\Delta_{\text{CF}}} B^2. \quad (5.22)$$

Using our values of γ_{CF} and Δ_{CF} , obtained from measurements described in subsequent subsections, we found that the observed coefficient of 0.28 GHz/T^2 would result entirely from the quadratic Zeeman effect assuming an inhomogeneous broadening of the crystal field energy level splitting of 27 GHz , which is within the range expected for this parameter, suggesting that this mechanism could explain the broadening.

Finally, a significant decrease in the integrated linestrength k of the absorption was observed at higher fields. This effect likely results from a change in transition strength caused by the mixing of crystal field wavefunctions through the quadratic Zeeman effect. Consequently, we fit the measurements to a B^2 dependence, giving a coefficient of $-1.3 \text{ GHz cm}^{-1} \text{ T}^{-2}$.

5.6.3.4. Orientation dependence

Transmission spectra were obtained by probing the optical ${}^3\text{H}_6 \rightarrow {}^3\text{H}_4$ transition at 793 nm with broadband light from a tungsten-halogen lamp, and analyzing the transmitted light with an Advantest Q8347 optical spectrum analyzer with 900 MHz frequency resolution. A constant magnetic field of 6 T was applied, and the crystal was rotated to vary the orientation of the magnetic field by 90° within a plane defined by the $[111]$ and $[\bar{1}\bar{1}2]$ crystal axes; the axis $[001]$ is also contained in the plane (see Fig. 5.21). The angle θ denotes the angle between \mathbf{B} and the $[111]$ axis. The light propagated along $[\bar{1}\bar{1}0]$, with polarization either along $[111]$ or $[\bar{1}\bar{1}2]$. With $\mathbf{E} \parallel [111]$, the electric transition dipoles μ of site 2, 4, and 6 ions are orthogonal to the light polarization and thus only ions of sites 1, 3, and 5 were addressed with identical Rabi frequencies. With $\mathbf{E} \parallel [\bar{1}\bar{1}2]$, the electric transition dipole of site 2 is orthogonal to

the light polarization, and the ratio $\boldsymbol{\mu} \cdot \mathbf{E}/(\mu E)$, which is a measure of the interaction strength, is $\sqrt{3}/2 \approx 0.87$ for sites 4 and 6, $1/\sqrt{3} \approx 0.58$ for site 1, and $1/(2\sqrt{3}) \approx 0.29$ for sites 3 and 5.

Fig. 5.25 shows the obtained spectra, where zero frequency detuning was defined as $\nu_0 = 377868$ GHz. The individual spectra were fit to extract the frequency shift Δ . For panel (a), the spectra were recorded with the probe light polarized along $[111]$, exciting only the ions of sites 1, 3, and 5. These three sites are magnetically equivalent for $\mathbf{B} \parallel [111]$, and the first spectrum shows that they experience a large shift of about 150 GHz for $\theta = 0$. As the magnetic field moved away from the $[111]$ axis, two different lines were observed, one corresponding to site 3- and 5-, the other to site 1-ions. For panel (b), the spectra were recorded with the polarization of the probe light along $[\bar{1}\bar{1}2]$, i.e. addressing mainly the ions of sites 4 and 6. The ions of those two sites are magnetically equivalent as long as the magnetic field is applied in the plane defined by the $[111]$ and $[\bar{1}\bar{1}2]$. Thus, they experience the same frequency shift, which is zero for $\mathbf{B} \parallel [111]$ and reaches its maximum of around 160 GHz for $\mathbf{B} \parallel [\bar{1}\bar{1}2]$. With this polarization, the interaction with sites 1, 3, and 5 is significantly reduced so that their absorption lines are only weakly visible in the spectra.

All frequency shifts obtained for the different configurations are shown in Fig. 5.26 as a function of the angle of the magnetic field θ . Due to the limited precision of the mechanical rotation mount used to hold the crystal, the uncertainty in the magnetic field angle was $\pm 2^\circ$. For each site, the energy displacements of the ground and excited states were determined from Eq. 5.21 using the known values of A_J for $^{169}\text{Tm}^{3+}$ ions [21] and the experimentally measured components of γ_J [22]. The theoretical

orientation dependence of the shift is also plotted in Fig. 5.26. Experimental and semi-theoretical values are in relatively good agreement.

Our study revealed that at magnetic field strengths of a few Tesla and for certain orientations of the field, site-selectivity by tuning the laser frequency to follow the corresponding quadratic Zeeman shifts is possible e.g. by tuning the laser by 160 GHz from ν_0 mainly ions at sites 4 and 6 will be selected at a field of 6 Tesla. Due to its independence of polarization, this method to select different ions is beneficial if one has random polarization, for example when working with powders that scramble polarization through scattering [27].

5.6.4. Nuclear spin-state lifetimes

The above characterization of the quadratic Zeeman shift was employed to study the lifetimes of the spin states in a high magnetic field. Using persistent spectral hole burning methods, we monitored the relaxation of optically pumped non-equilibrium spin populations [19]. Light from a Coherent 899-21 Ti:Sapphire laser was sent to the sample for 100 ms to burn a spectral hole. After a variable wait time, the laser was scanned across 180 MHz in 250 μ s via a double-passed 200 MHz acousto-optic modulator to probe the spectral hole. The power of the laser beam focused into the crystal was $\sim 10 \mu$ W. After the sample, the transmitted pulse was measured with a New Focus 2051 detector. The decay of the spectral hole area as a function of the waiting time enables one to obtain the lifetime of the spin states, which can be as long as hours for Tm^{3+} :YAG at 1.6 K.

5.6.4.1. Orientation dependence

The spin-state lifetime T_1 at $B = 6$ T and $T = 1.6$ K was first measured in a 1% Tm:YAG crystal for different orientations of the magnetic field and light polarization relative to the crystal. The frequency of the laser was tuned to follow the inhomogeneous line of the investigated transitions, according to each line's different quadratic Zeeman shift. The polarization direction of the light was kept either along the magnetic field or perpendicular to it. Table 5.5 shows the spin-state lifetimes T_1 for the different configurations of laser frequencies, magnetic field orientations, and polarizations.

We observed that the spin-state lifetime significantly changes as a function of the magnetic field orientation and depends on which subset of sites are addressed. The longest T_1 were found for the subset of ions at sites 1, 3, and 5, in the configuration in which they are magnetically and optically equivalent and experience a large shift of the optical transition due to the quadratic Zeeman effect, i.e. $\mathbf{B} \parallel \mathbf{E} \parallel [111]$. In this case the spin-state lifetime is $\sim 1/2$ hour, whereas it is only 20 s for sites 4 and 6 with the same magnetic field strength and orientation. This suggests that different processes dominate the spin-relaxation depending on the site. In the E configuration (see Table 5.5), the projection of the g -tensor of sites 4 and 6 on the magnetic field direction is small [22]. In this case, the process responsible for spin-relaxation could be mutual spin flips caused by the magnetic dipole-dipole interaction between Tm^{3+} ions and other nuclear spins in the lattice [28], or relaxation induced by trace paramagnetic impurities in the crystal [29, 30, 31]. In the following, we focused on

label	sites	B and E	shift	T_1
A	1, 3, 5	B \parallel E \parallel [111]	153 GHz	32 ± 2 min.
B	3, 5	30° from [111]	160 GHz	17 ± 1 min.
C	3, 5	B \parallel E \parallel [001]	120 GHz	7 ± 0.5 min.
D	4, 6	B \parallel E \parallel $[\bar{1}\bar{1}2]$	165 GHz	23 ± 3 min.
E	4, 6	B \parallel [111], E \parallel $[\bar{1}\bar{1}2]$	0 GHz	20 ± 1 s

Table 5.5.: Nuclear spin-state lifetimes for ions at different sites in a magnetic field of 6 T and at 1.6 K in 1 % Tm³⁺:YAG. Each measurement is labeled and displayed in Fig. 5.26.

the subset of ions at sites 1, 3, and 5 in order to understand the spin-relaxation mechanisms that limit the longest nuclear spin-state lifetimes.

5.6.4.2. Spin-lattice relaxation

Next, the nuclear spin-state lifetime was studied for ions at sites 1, 3, and 5, which offer the longest relaxation time (see above). We used the configuration in which they are optically and magnetically equivalent, i.e. with the magnetic field and the light polarization along [111]. For this experiment we chose a lower concentration 0.1% Tm³⁺:YAG crystal. The frequency of the laser was adjusted to follow the shift of the optical transition due to the quadratic Zeeman effect as B was increased. We investigated the temperature and magnetic field dependences of the nuclear spin-state lifetime for $1.6 \text{ K} \leq T \leq 4.5 \text{ K}$ and $0 \text{ T} \leq B \leq 6 \text{ T}$, as shown in Fig. 5.27, 5.28 and 5.29. For this range of parameters, we identified two processes limiting the spin-state lifetime: the direct single-phonon process, and the two-phonon Orbach process. As we will describe below, the direct phonon process, which results from the absorption or emission of a phonon resonant with the hyperfine splitting in the ground state, is dominant at low temperature and high magnetic field. The Orbach process, in which

two higher energy phonons induce relaxation by driving transitions to and from other electronic crystal field levels, is dominant at higher temperature.

5.6.4.3. Temperature dependence

Two regimes of relaxation are easily visible in Fig. 5.27, which depicts the temperature dependence of the spin-relaxation rate R , i.e. the inverse of the nuclear spin-state lifetime T_1 , at a magnetic field of 3 T. For temperatures above 2 K, the relaxation rate increases very rapidly, which is characteristic for a relaxation mechanism involving two phonons. Indeed, the rate of the Orbach process varies as $\sim e^{-h\Delta_{\text{CF}}/k_{\text{B}}T}$, where Δ_{CF} is the transition frequency between the two lowest crystal field levels, h is the Planck constant and k_{B} is the Boltzmann constant [32]. Below $T = 2$ K, the spin relaxation rate increases linearly with temperature, characteristic of the direct phonon process. However, the temperature dependence of the spin-relaxation rate is not sufficient to identify the direct phonon process since other mechanisms, such as the magnetic dipole-dipole interaction between rare-earth ions that leads to mutual spin flips, can also have a linear temperature dependence [33]. More generally, interactions with paramagnetic impurities in the host matrix can also give rise to a linear temperature dependence of the spin relaxation rate [29, 30, 31]. However, the magnetic field dependence of the nuclear spin-state lifetime allowed us to unambiguously identify the direct process, as detailed below.

5.6.4.4. Magnetic field dependence at 1.6 K

To identify the direct phonon process, we studied the nuclear spin-state lifetime as a function of the magnetic field strength B at low temperatures, i.e. below 2 K. When the thermal energy is much larger than the level splittings, as in the case considered here, the magnetic field dependence of the direct phonon process is B^2 for non-Kramers ions and B^4 for Kramers ions [32]. Since the enhanced nuclear Zeeman splitting of the spin 1/2 states of $^{169}\text{Tm}^{3+}$ arises from the induced electronic paramagnetism [8], the spin-lattice relaxation is thus expected to be proportional to B^4 . Fig. 5.28 shows the spin relaxation rate at $T = 1.6$ K, which increases with the magnetic field strength as B^4 . We can thus confirm that the direct phonon process dominates the spin relaxation of Tm:YAG at 1.6 K and magnetic field above 3 T.

5.6.4.5. Magnetic field dependence at 4 K

We also investigated the spin relaxation rate at $T = 4$ K, a temperature at which the Orbach process is dominant. The rate of this process is generally expected to be independent of magnetic field because it depends only on the energy spacing between the crystal field levels. The experimental points are shown in Fig. 5.29, and exhibit a slight increase between 1 and 3 T, followed by a decrease. As we describe below in more detail, this behavior can be explained by taking into account the increase in the energy splitting of the two lowest crystal field levels due to the quadratic Zeeman effect, as shown in Fig. 5.22. At magnetic fields below 0.03 T, the spin relaxation seems to slow down with decreasing field, which may indicate a modification of the

Orbach mechanism at small magnetic fields. However, further investigations in this region of weak magnetic fields would be required for a better understanding of this behavior, and we model in the following the relaxation rate observed for magnetic fields above 0.03 T.

5.6.4.6. Model

Following the conclusions from the above discussion, we assume that for our range of parameters ($1.6 \text{ K} \leq T \leq 4.5 \text{ K}$ and $0 \text{ T} \leq B \leq 6 \text{ T}$), the spin relaxation rate can be written as

$$R(B, T) = R_0 + \alpha_D \gamma^2 B^4 T + \frac{\alpha_O(B)}{e^{h\Delta_{\text{CF}}(B)/k_B T} - 1}, \quad (5.23)$$

with $\alpha_O(B) = \alpha + \beta B^2$ and $\Delta_{\text{CF}}(B) = \Delta_{\text{CF}}^0 + \gamma_{\text{CF}} B^2$. The first term corresponds to the residual relaxation at zero magnetic field and temperature. The second term describes the direct phonon process [32], with the coefficient α_D depending on the properties of the host material such as the speed of sound and crystal density, and γ represents the effective nuclear gyromagnetic ratio (in frequency units) along the magnetic field direction for the ground state hyperfine levels, equal to 329 MHz/T in this orientation [22]. This term is valid for $\gamma B \ll k_B T$, which is the case for our measurements. The last term corresponds to the Orbach process, with a coupling coefficient α_O that depends on the splitting Δ_{CF} [32]. To take into account the shift of the transition between the crystal field levels arising from the quadratic Zeeman effect, we include the corresponding B^2 dependence in the coupling coefficient α_O and in the energy difference Δ_{CF} .

R_0	$9.5 \times 10^{-5} \text{ Hz}$
α_D	$1.8 \times 10^{-24} (\text{Hz K T}^2)^{-1}$
α	$3.0 \times 10^4 \text{ Hz}$
β	$1.3 \times 10^4 \text{ Hz T}^{-2}$
Δ_{CF}^0	$8.3 \times 10^{11} \text{ Hz}$
γ_{CF}	$8.0 \times 10^9 \text{ Hz T}^{-2}$

Table 5.6.: Parameters obtained from the 2-dimensional fit of the experimental spin relaxation rate data by Eq. 5.23.

We simultaneously fit the three experimental data sets shown in Figures 5.27, 5.28 and 5.29 using a two dimensional fit, with the magnetic field and temperature as variables, to our model (5.23) describing the relaxation. We obtained the set of parameters given in Table 5.6, which describes all of the observed behavior well. From this fit we find a direct phonon coefficient of $\alpha_D = (1.8 \pm 0.4) \times 10^{-24} (\text{Hz K T}^2)^{-1}$. We compare this result to theoretical estimates using the method of Bleaney et al [30]. In their approach, the electron-phonon coupling matrix elements are approximated by order-of-magnitude estimates, giving the simple analytical relation

$$\alpha_D \sim \frac{24\pi^2 k_B \gamma^2}{\rho v^5}, \quad (5.24)$$

where ρ is the crystal density, and v is the average acoustic phonon velocity. For YAG, the density is $\rho = 4564 \text{ kg/m}^3$ [34] and the longitudinal and transverse acoustic velocities are $v_l = 8600 \text{ m/s}$ and $v_t = 5000 \text{ m/s}$ [35]. If we approximate v by the acoustic velocity averaged over the single longitudinal mode and the two transverse modes, then, for our field orientation where $\gamma = 329 \text{ MHz/T}$, Bleaney's approach predicts a direct phonon coefficient on the order of $10^{-26} (\text{Hz K T}^2)^{-1}$, somewhat smaller than our observed value but within the range expected considering the approximations

involved in the theoretical estimate.

The only cases that we are aware of in which direct phonon relaxation has been suggested for $^{169}\text{Tm}^{3+}$ have been related to studies of TmPO_4 and TmVO_4 materials for nuclear cooling applications [16, 17, 18]. In these works, the observed relaxation rates require exceedingly large phonon coupling coefficients of $6 \times 10^{-11} (\text{Hz K T}^2)^{-1}$ in TmPO_4 [17] and $4 \times 10^{-8} (\text{Hz K T}^2)^{-1}$ in TmVO_4 [17]. It was subsequently proposed that the observed relaxation was due to paramagnetic impurities rather than phonon interactions [30, 31], although explanations in terms of phonon bottleneck effects were also proposed [18]. Considering the small value of α_D observed in our work and the reasonable agreement of this value with theoretical predictions, our results support this conclusion. Thus, to the best of our knowledge, there have been no other unambiguous observations of direct phonon relaxation of the nuclear hyperfine states of $^{169}\text{Tm}^{3+}$ other than the ones presented here for $\text{Tm}^{3+}:\text{YAG}$.

Our fit of Eq. 5.24 results in a value of 0.83 THz for the crystal field level transition frequency Δ_{CF} , in agreement with the value of 0.81 THz usually cited in the literature from direct spectroscopic measurements [36]. Furthermore, we found $\gamma_{\text{CF}} = 8.0 \text{ GHz/T}^2$ for the coefficient of the quadratic Zeeman shift of the splitting between the first two crystal field levels in the $^3\text{H}_6$ ground state. As discussed in the theoretical subsection, it is likely that the shift of the optical transition would be mainly due to the splitting between the crystal field levels in the ground state, and so that the coefficients would be approximated by $\gamma_{\text{CF}} \sim 2\gamma_2 \sim 9 \text{ GHz/T}^2$. The value given by our fit is very close to this limit, supporting our analysis.

5.6.5. Conclusion

In summary, we characterized the shifts of the optical ${}^3\text{H}_6 \rightarrow {}^3\text{H}_4$ transition in $\text{Tm}^{3+}:\text{YAG}$ resulting from the quadratic Zeeman effect for the ground and excited states in large magnetic fields. The orientation dependence of the shifts is in agreement with the theoretical predictions. A coefficient of 4.69 GHz/T^2 is measured in the case where the sites 1, 3, and 5 are optically and magnetically equivalent. This shift provides a tool to spectrally select ions at different sites.

We furthermore measured the spin lifetimes for different sites and orientations of the magnetic field, with a maximum value observed for sites 1, 3, and 5 when they are optically and magnetically equivalent. In that configuration, the spin lifetime was investigated as a function of magnetic field strength and temperature, enabling us to identify the processes responsible for spin relaxation, i.e. the direct phonon process at low temperature ($T \leq 2 \text{ K}$) and high magnetic field ($B \geq 3 \text{ T}$), and the Orbach process at higher temperature ($T \geq 2 \text{ K}$) and fields up to 6 T . We also found that the small increase in the energy splitting of the electronic crystal field levels due to the quadratic Zeeman effect can result in a significant decrease in the two-phonon Orbach process rate at low temperatures, introducing a magnetic field dependence into the otherwise field-independent relaxation process. Consequently, it is essential to consider this additional effect when analyzing spin-lattice relaxation of this and other rare-earth ions at higher magnetic field strengths. This finding potentially also affects the interpretation of past spin relaxation studies at low temperatures.

5.6.6. Acknowledgments

The authors acknowledge support from Alberta Innovates Technology Futures (ATIF), the National Engineering and Research Council of Canada (NSERC), and the National Science Foundation of the USA (NSF) under award nos. PHY-1212462, PHY-1415628, and CHE-1416454. W. T. is a senior fellow of the Canadian Institute for Advance Research (CIFAR).

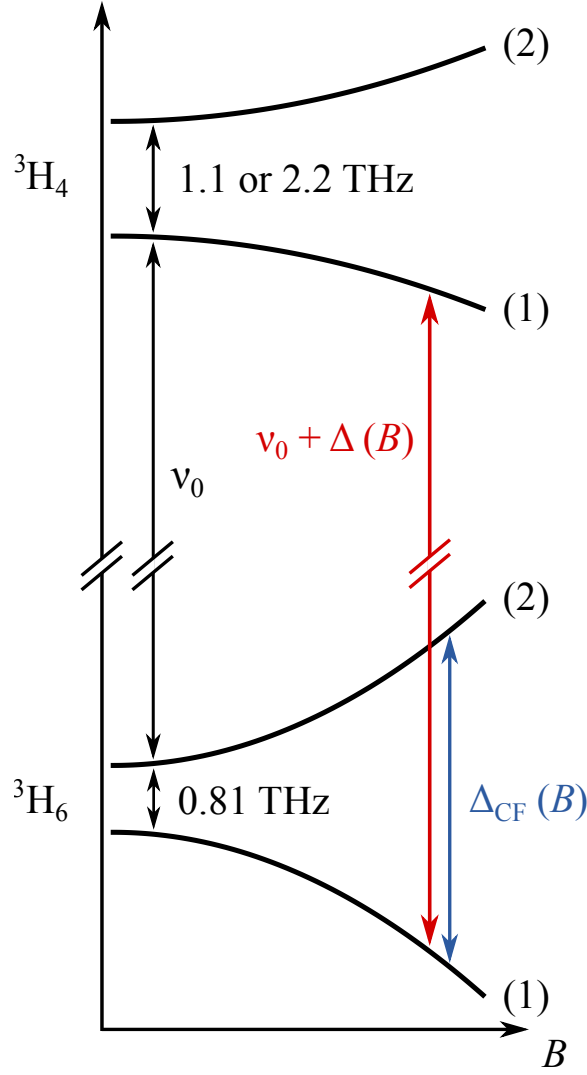


Figure 5.22.: Simplified energy level structure of $\text{Tm}^{3+}:\text{YAG}$, relevant for our study. Represented are the two lowest crystal field levels of the ${}^3\text{H}_6$ and ${}^3\text{H}_4$ multiplets [24, 25]. In an external magnetic field, the crystal field level energies vary as B^2 due to the quadratic Zeeman effect, with different coefficients for each level. As a consequence, the optical transition ${}^3\text{H}_6(1) \rightarrow {}^3\text{H}_4(1)$, which has a zero-field frequency of ν_0 , is shifted by $\Delta(B)$. The frequency Δ_{CF} , corresponding to the transition between the two crystal field levels in the ground state, also varies as B^2 .

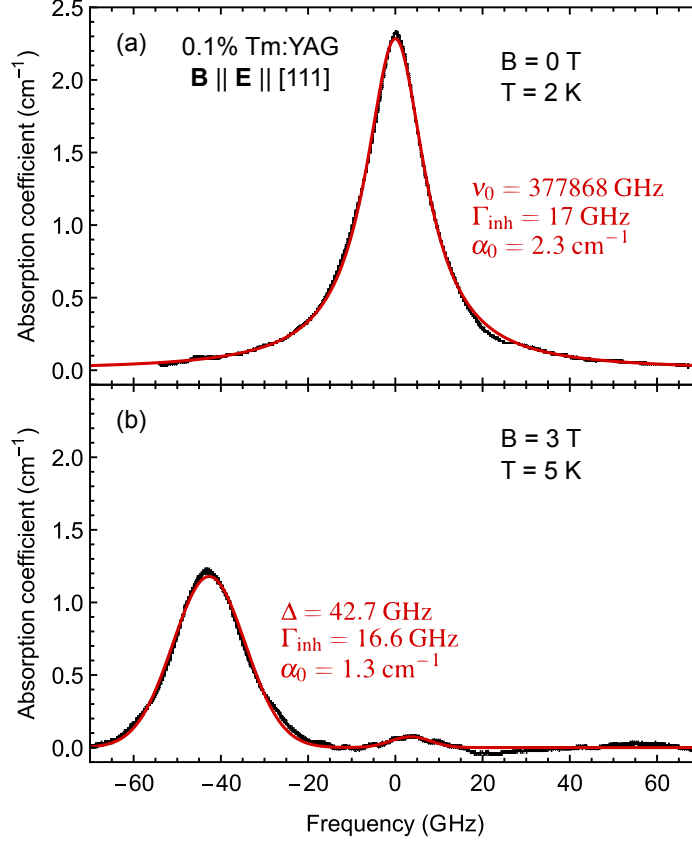


Figure 5.23.: Inhomogeneous line of a 0.1 % Tm³⁺:YAG crystal (a) at zero magnetic field and $T = 2$ K, and (b) with a 3 T magnetic field along [111] and at $T = 5$ K. A narrowband laser probed the medium with $\mathbf{k} \parallel [1\bar{1}0]$ and $\mathbf{E} \parallel [111]$ (see main text for definitions). The experimental points were fit by a Lorentzian function with a full width at half maximum $\Gamma_{\text{inh}} = 17$ GHz at zero magnetic field. The center frequency is $\nu_0 = 377868$ GHz, and the absorption coefficient is $\alpha_0 = 2.3 \text{ cm}^{-1}$. Because of polarization imperfections, the probe light slightly interacted with ions at sites 2, 4, and 6 that do not experience any shift for $\mathbf{B} \parallel [111]$. In consequence, the model includes two Lorentzian functions for $B = 3$ T. The shift Δ of the strongest line corresponding to ions at sites 1, 3, and 5 is 42.7 GHz.

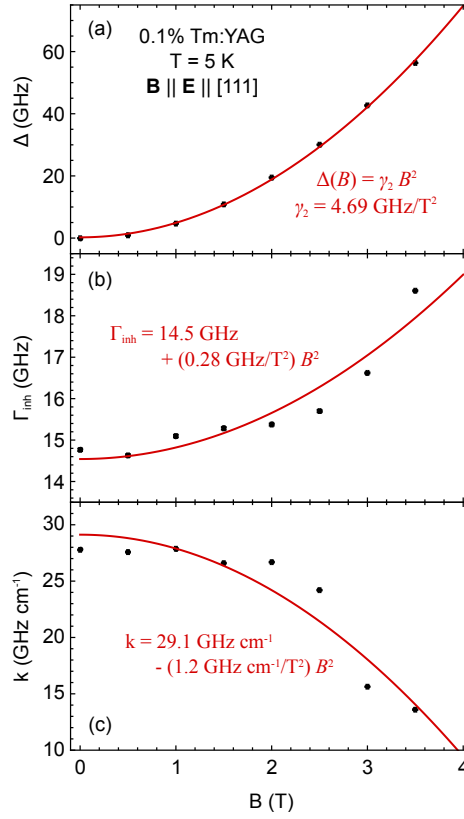


Figure 5.24.: Magnetic field dependence of several inhomogeneous line properties of a 0.1 % Tm³⁺:YAG crystal at $T = 5 \text{ K}$ and with $\mathbf{B} \parallel \mathbf{E} \parallel [111]$. (a) Frequency shift Δ as a function of the magnetic field strength B . The experimental points were fit by a quadratic function, giving a coefficient $\gamma_2 = 4.69 \pm 0.03 \text{ GHz/T}^2$. (b) Observed nonlinear increase in the inhomogeneous linewidth Γ_{inh} as a function of the magnetic field strength B . The experimental points were fit by a B^2 dependence, giving a broadening coefficient of 0.28 GHz/T^2 . (c) Observed nonlinear decrease in the integrated transition linestrength k as a function of the magnetic field strength B . The experimental points were fit by a B^2 dependence, giving a coefficient of $-1.3 \text{ GHz cm}^{-1} \text{ T}^{-2}$.

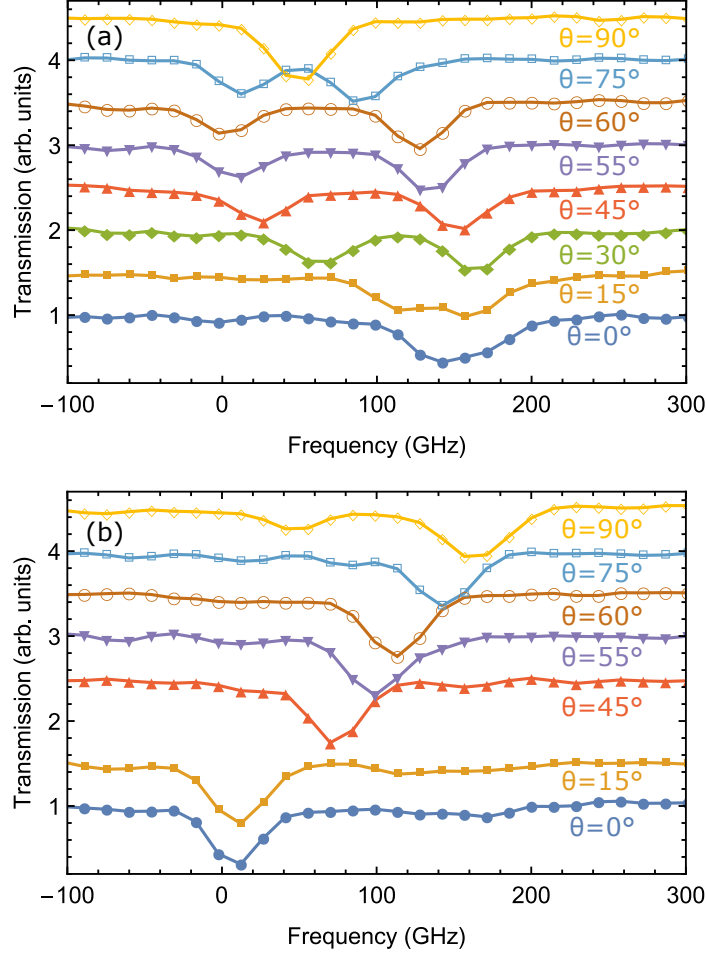


Figure 5.25.: Transmission spectra for various angles θ of magnetic field with respect to the $[111]$ crystal axis in the plane defined by the $[111]$ and $[\bar{1}\bar{1}2]$, of a 1% $\text{Tm}^{3+}:\text{YAG}$ crystal at 1.6 K. The strength of the applied magnetic field was 6 T. The polarization of the probing light was (a) along $[111]$, leading to interaction with ions of sites 1, 3, and 5, and (b) along $[\bar{1}\bar{1}2]$ leading to interaction with ions of sites 4 and 6.

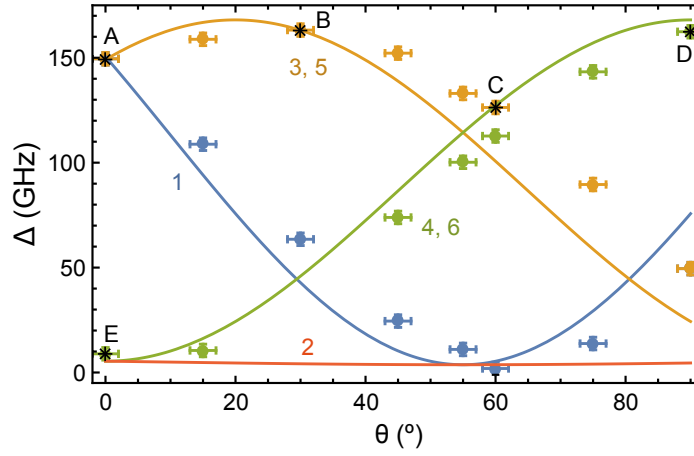


Figure 5.26.: Frequency shift Δ as a function of the magnetic field angle θ at $B = 6$ T for ions of the site 1 (blue), sites 3 and 5 (yellow), and sites 4 and 6 (green), extracted from the transmission spectra shown in Fig. 5.25. The experimental points are presented together with the expected values (solid lines). The points labeled by letters (A-E) identify configurations for which the spin-state lifetime was measured (see Table 5.5)

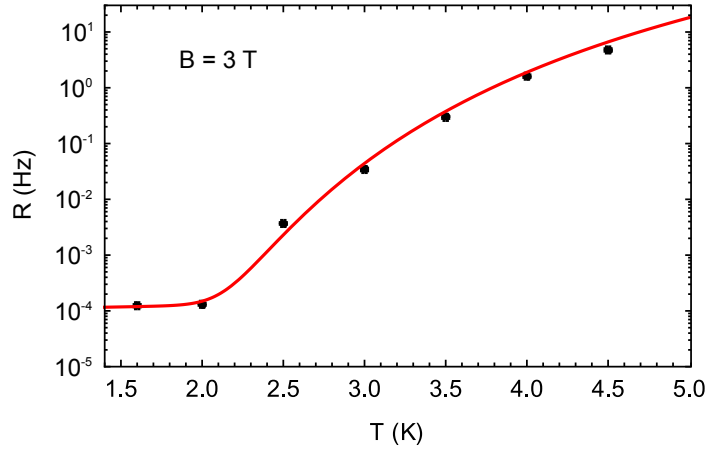


Figure 5.27.: Spin-lattice relaxation rate as a function of the temperature T for $B = 3$ T in 0.1% Tm:YAG for ions of sites 1, 3, and 5. The magnetic field and the light polarization were along [111], and ions of sites 1, 3, and 5 were thus optically and magnetically equivalent. The experimental points were fit by Eq. 5.23 with the parameters given in Table 5.6.

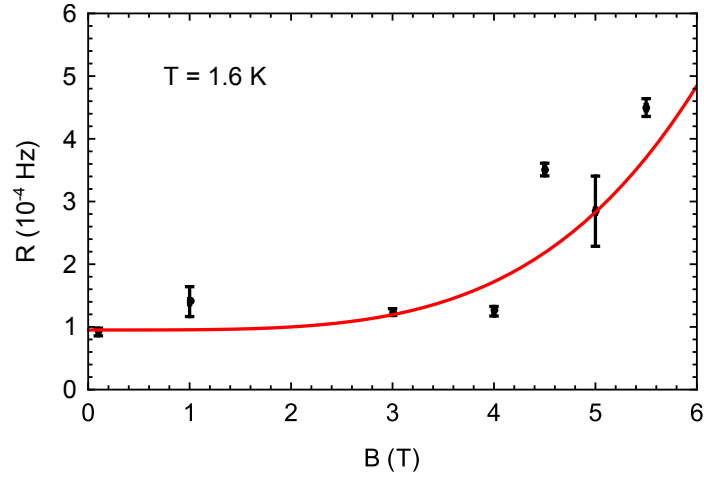


Figure 5.28.: Spin-lattice relaxation rate as a function of the magnetic field strength B at $T = 1.6$ K in 0.1% Tm:YAG for ions of sites 1, 3, and 5. The magnetic field and the light polarization were along [111]. Ions of sites 1, 3, and 5 were optically and magnetically equivalent. The experimental points were fit by Eq. 5.23 with the parameters given in Table 5.6.

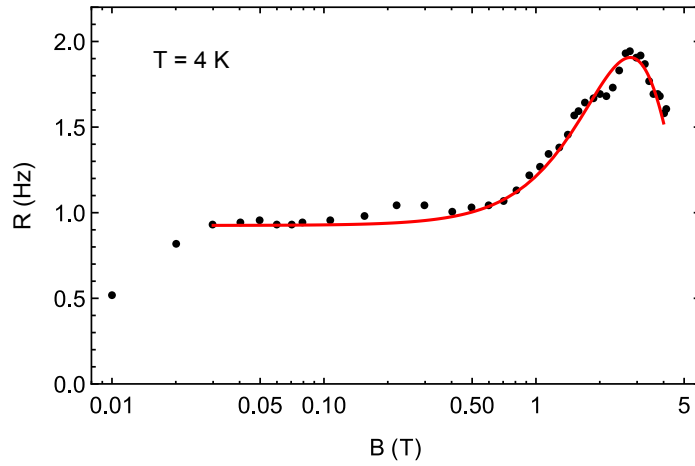


Figure 5.29.: Spin-lattice relaxation rate as a function of the magnetic field strength B at $T = 4$ K in 0.1% Tm:YAG for ions of sites 1, 3, and 5. The magnetic field and the light polarization were along [111], so ions of sites 1, 3, and 5 were optically and magnetically equivalent. The experimental points were fit by Eq. 5.23 with the parameters given in Table 5.6.

Bibliography

- [1] Z. Cole, T. Böttger, R. K. Mohan, R. Reibel, W. R. Babbitt, R. L. Cone, and K. D. Merkel, Applied Physics Letters **81**, 3525 (2002).
- [2] V. Lavielle, I. Lorgère, J.-L. Le Gouët, S. Tonda, and D. Dolfi, Optics Letters **28**, 384 (2003).
- [3] N. M. Strickland, P. B. Sellin, Y. Sun, J. L. Carlsten, and R. L. Cone, Physical Review B **62**, 1473 (2000).
- [4] R. Lauro, T. Chanelière, and J. L. Le Gouët, Physical Review A **79**, 063844 (2009).
- [5] M. Bonarota, J. Ruggiero, J. L. Le Gouët, and T. Chanelière, Physical Review A **81**, 033803 (2010).
- [6] R. M. Macfarlane, Optics Letters **18**, 1958 (1993).
- [7] C. W. Thiel, R. M. Macfarlane, Y. Sun, T. Böttger, N. Sinclair, W. Tittel, and R. L. Cone, Laser Physics **24**, 106002 (2014).

- [8] A. Abragam and B. Bleaney, Proceedings of the Royal Society of London. Series A, Mathematical and Physical Sciences **387**, 221 (1983).
- [9] R. M. Macfarlane and J. C. Vial, Physical Review B **36**, 3511 (1987).
- [10] N. Ohlsson, M. Nilsson, S. Kröll, and R. K. Mohan, Optics Letters **28**, 450 (2003).
- [11] P. Goldner, O. Guillot-Noël, A. Louchet, F. de Sèze, V. Crozatier, I. Lorgeré, F. Bretenaker, and J. L. Le Gouët, Optical Materials **28**, 649 (2006).
- [12] A. Louchet, J. S. Habib, V. Crozatier, I. Lorgeré, F. Goldfarb, F. Bretenaker, J.-L. Le Gouët, O. Guillot-Noël, and P. Goldner, Physical Review B **75**, 035131 (2007).
- [13] Y. Sun, G. M. Wang, R. L. Cone, R. W. Equall, and M. J. M. Leask, Physical Review B **62**, 15443 (2000).
- [14] J. F. Dillon and L. R. Walker, Physical Review **124**, 1401 (1961).
- [15] R.-C. Tongning, Ph.D. thesis, Université Paris Sud - Paris XI (2014).
- [16] H. Suzuki, Y. Higashino, and T. Ohtsuka, Journal of Low Temperature Physics **41**, 449 (1980).
- [17] H. Suzuki, T. Inoue, and T. Ohtsuka, North-Holland Publishing Company **Physics**, 563 (1981).
- [18] Y. Roinel, V. Bouffard, J.-F. Jacquinot, C. Fermon, and G. Fournier, Journal de Physique **46**, 1699 (1985).

- [19] R. M. Macfarlane and R. M. Shelby, in *Modern Problems in Condensed Matter Sciences*, vol. 21 of *Spectroscopy of Solids Containing Rare Earth Ions*, A. A. Kaplyanskii and R. M. Macfarlane, eds. (Elsevier, 1987), pp. 51–184.
- [20] M. A. Teplov, Soviet Physics, JETP **26**, 872 (1968).
- [21] O. Guillot-Noël, P. Goldner, E. Antic-Fidancev, and J. L. Le Gouët, Physical Review B **71**, 174409 (2005).
- [22] F. de Sèze, A. Louchet, V. Crozatier, I. Lorgeré, F. Bretenaker, J.-L. Le Gouët, O. Guillot-Noël, and P. Goldner, Physical Review B **73**, 085112 (2006).
- [23] I. Zafarullah, “Thulium Ions in a Yttrium Aluminum Garnet Host for Quantum Computing Applications: Material Analysis and Single Qubit Operations”, Ph.D. thesis, Montana State University, Bozeman, Montana (2008).
- [24] J. B. Gruber, M. E. Hills, R. M. Macfarlane, C. A. Morrison, G. A. Turner, G. J. Quarles, G. J. Kintz, and L. Esterowitz, Physical Review B **40**, 9464 (1989).
- [25] C. Tiseanu, A. Lupei, and V. Lupei, Journal of Physics: Condensed Matter **7**, 8477 (1995).
- [26] J. H. V. Vleck, *The theory of electric and magnetic susceptibilities* (Oxford University Press, 1932).
- [27] T. Lutz, L. Veissier, C. W. Thiel, P. J. T. Woodburn, R. L. Cone, P. E. Barclay, and W. Tittel, Science and Technology of Advanced Materials **17**, 63 (2016).

- [28] R. L. Ahlefeldt, M. F. Pascual-Winter, A. Louchet-Chauvet, T. Chanelière, and J.-L. Le Gouët, *Physical Review B* **92**, 094305 (2015).
- [29] A. Abragam, *The principles of nuclear magnetism* (Oxford University Press, 1961).
- [30] B. Bleaney, J. H. T. Pasman, and M. R. Wells, *Proceedings of the Royal Society of London. Series A, Mathematical and Physical Sciences* **387**, 75 (1983).
- [31] L. K. Aminov and M. A. Teplov, *Soviet Physics Uspekhi* **28**, 762 (1985).
- [32] R. Orbach, *Proceedings of the Royal Society of London. Series A. Mathematical and Physical Sciences* **264**, 458 (1961).
- [33] T. Böttger, C. W. Thiel, Y. Sun, and R. L. Cone, *Phys. Rev. B* **73**, 075101 (2006).
- [34] P. R. Stoddart, P. E. Ngoepe, P. M. Mjwara, J. D. Comins, and G. A. Saunders, *Journal of Applied Physics* **73**, 7298 (1993).
- [35] E. G. Spencer, R. T. Denton, T. B. Bateman, W. B. Snow, and L. G. V. Uitert, *Journal of Applied Physics* **34**, 3059 (1963).
- [36] R. M. Macfarlane, *Journal of Luminescence* **85**, 181 (2000).

5.7. Paper 5: Modification of relaxation dynamics in

$\text{Tb}^{3+}:\text{Y}_3\text{Al}_5\text{O}_{12}$ nanopowders

submitted to Physical Review B November 2017

5.7.1. Summary

In Paper 5 we demonstrate that population dynamics can indeed be modified in small powder materials in a way that is consistent with phonon suppression. Modifications of population dynamics in REI-doped nanocrystals have previously been reported by Meltzer *et al.* [59, 60], Liu *et al.* [61] and Mercier *et al.* [62], and it was suggested that they may be due to phonon suppression. However, the used particles were not always sufficiently small to suppress phonons at the desired frequencies, and some observations are consistent with explanations based on locally elevated temperatures caused by the optical excitation of the powder materials. Furthermore, most of these manuscripts do not include details on powder characterization measurements. Thus the demonstration of phonon suppression in small particles remains an open challenge. In this manuscript, we address each of these points in an attempt to show phonon suppression in powder materials.

For our measurements, we chose to investigate relaxation between closely spaced crystal field levels in the excited state of $\text{Tb}^{3+}:\text{Y}_3\text{Al}_5\text{O}_{12}$. Firstly, the transition between such levels is expected to be driven predominantly by the direct phonon process and thus there is no need for high magnetic fields as in $\text{Tm}^{3+}:\text{Y}_3\text{Al}_5\text{O}_{12}$. In addition, the

small splitting of ~ 35 GHz between the crystal field levels together with the high speed of sound in $\text{Y}_3\text{Al}_5\text{O}_{12}$ (6400 m/s) allows one to suppress resonant phonons with relatively large particles of ~ 100 nm diameter. Finally, crystal field levels are more robust than spin states with respect to perturbations in the host matrix that are caused by fabrication methods.

We fabricated $\text{Tb}^{3+}:\text{Y}_3\text{Al}_5\text{O}_{12}$ powders with different crystal sizes ranging from ~ 40 nm to > 500 nm. The powders were obtained through various chemical syntheses in order to achieve fine size control and avoid crystal damage caused by mechanical processing. In addition, we employed thermal annealing methods to further improve the quality of the synthesized powders. The resulting powders were then carefully characterized using a scanning electron microscope, transmission electron microscope and x-ray diffraction techniques. These techniques showed that the powders have the correct crystal phase and that the particle size can indeed be controlled as we expected. However, spectroscopic measurements showed an increased inhomogeneous linewidth in the smallest powders that might lead to phenomena that can be wrongly interpreted as signatures of phonon suppression. We analyzed this effect and show that in our case we can nevertheless observe signatures of phonon suppression. In addition, we directly obtained the local sample temperature through absorption measurements and ensured that none of our findings can be explained by sample heating.

Through time-resolved fluorescence measurements we showed that the contribution of fast non-radiative relaxation from the upper into the lower crystal field level decreases with decreasing particle size as expected since phonons driving non-radiative

transitions should be suppressed in the smallest particles. To assess whether or not phonon-driven transitions between the crystal field levels are completely forbidden, we performed a second measurement and recorded the temperature dependence of the relative populations in the upper and lower crystal field level after optical pumping. If transitions between the levels are absent, the ratio of populations should be independent of temperature. However, our measurements show a temperature dependence that is identical to that of the bulk crystal for all our powders. Thus, even though phonons are potentially suppressed, a different non-radiative process must facilitate transitions between the levels. This process could arise from crystal defects or surface imperfections, even though significant effort was dedicated to achieve the best possible nanocrystal quality.

The manuscript concludes that it is imperative to carefully characterize the fabricated powders and to directly measure the sample temperature to unambiguously demonstrate phonon suppression. Furthermore, powder fabrication and annealing methods must be improved to avoid additional relaxation processes and increased inhomogeneous broadening related to imperfect host materials. As described in the manuscript, there are many technical difficulties that are related to measurements of powder materials and, furthermore, REIs are very sensitive to imperfections in their host materials. Therefore, for future investigations, we decided to use different materials that allow measurements on single emitters, which would avoid the problem of ambiguities due to inhomogeneous broadening, and that can be fabricated using modern nanofabrication tools. Initial experiments with individual silicon vacancy

centers in diamond are presented in the next section.

The experiments presented in this manuscript were performed by the first two authors with equal contributions. Simulations of phonon suppression in small powder materials were performed by myself. Absorption and thermalization measurements were analyzed by myself whereas the time-resolved fluorescence data was analyzed together with Lucile Veissier. The first draft was jointly written by the first two authors.

Modification of relaxation dynamics in $\text{Tb}^{3+}:\text{Y}_3\text{Al}_5\text{O}_{12}$ nanopowders

Thomas Lutz¹, Lucile Veissier^{1†}, Philip J. T. Woodburn², Rufus L. Cone², Paul E.

Barclay¹, W. Tittel¹, Charles W. Thiel²

¹*Institute for Quantum Science and Technology, and Department of Physics &*

Astronomy, University of Calgary, Calgary Alberta T2N 1N4, Canada

²*Department of Physics, Montana State University, Bozeman, MT 59717 USA*

[†]*Present address: Laboratoire Aimé Cotton, CNRS-UPR 3321, Univ. Paris-Sud,*

Bât. 505, F-91405 Orsay Cedex, France

Abstract: Nanostructured rare-earth-ion doped materials are increasingly being investigated for on-chip implementations of quantum information processing protocols as well as commercial applications such as fluorescent lighting. However, achieving high-quality and optimized materials at the nanoscale is still challenging. Here we present a detailed study of the restriction of phonon processes in the transition from bulk crystals to small (≤ 40 nm) nanocrystals by observing the relaxation dynamics between crystal-field levels of $\text{Tb}^{3+}:\text{Y}_3\text{Al}_5\text{O}_{12}$. We find that the dynamics are modified as the particle size is reduced, consistent with our simulations of inhibited relaxation through a modified vibrational density of states and hence modified phonon emission. On the other hand, we were not able to observe a change in the thermal population distribution among the crystal-field levels in the powders, indicating that non-radiative processes other than phonons are present, causing transitions and rapid thermalization between the levels on a timescale of <100 ns.

5.7.2. Introduction

Crystalline materials doped with impurities such as rare-earth-ions (REI), or diamond silicon-vacancy (SiV) and nitrogen-vacancy (NV) centers, have found many applications in fields as diverse as quantum information processing [1, 2, 3, 4], quantum memories [5, 6, 7], sensing [8], lasers [9], and phosphors [10, 11]. Nanometer-sized structures fabricated from these materials have begun to be investigated for on-chip implementations of these applications. In addition, small-sized nano-phosphors are desired for high-quality window materials used in lamps as well as for state-of-the-art displays [12, 13]. Finally, nano-powders have also been proposed for optical refrigeration applications where their modified phonon spectrum and particle morphology could enhance the cooling efficiency [14].

Nano-materials can be obtained through different routes: nano-structures can be milled or etched from high-quality bulk materials, and nanocrystals can be obtained through chemical synthesis, mechanical crushing, or ablation techniques. The transition to nano-sized structures generally introduces detrimental effects such as poor crystal quality, surface effects, and amorphous behavior that can severely restrict practical applications [15, 16]. While some of these effects, such as the increasing surface-to-volume ratio, are fundamental, others can be minimized by optimizing the fabrication process [15]. Indeed, in some cases, both chemical synthesis as well as fabrication methods starting with bulk materials produced high-quality materials [17, 18]. However, none of those structures have allowed studying the effects of decreasing dimensions on phonon-mediated population dynamics. Furthermore, a

general procedure for achieving consistently high-quality nano-materials is still unknown and many open questions remain regarding the transition to smaller sizes, requiring further systematic studies.

During the transition from a bulk material to nano-structures, many material properties change. One interesting effect is the predicted modification of the vibrational density of states (VDOS) in small structures. Whereas a bulk crystal has a Debye VDOS (a continuous function that increases with the square of the vibrational frequency), the distribution becomes discrete in small crystallites, exhibiting gaps and even a cut-off below which no phonons are supported. Furthermore, phononic crystals—nanomachined, periodic structures—can feature engineered frequency band-gaps where vibrations are forbidden [19]. These approaches to phonon engineering could potentially benefit applications in the field of quantum information, in particular quantum memories, since the absence of phonons could enhance spin-population lifetimes as well as optical coherence times. Modifications of population dynamics in REI-doped nanocrystals have been previously reported by Meltzer *et al.* [20, 21], Liu *et al.* [22] and Mercier *et al.* [23], and it was suggested that the changes were due to phonon suppression in the nanocrystals. However, the particles employed in some of those studies were not sufficiently small to suppress phonons at the desired frequencies, and locally elevated temperatures caused by the optical excitation of the powder materials might explain some of the observed effects. Thus, unambiguous confirmation of the suppression of phonon-mediated relaxation in optical centers through VDOS-engineering remains an open challenge.

In this manuscript we examine the effect of the transition from bulk crystals to ≤ 40

nm particles (see Fig. 5.30) on the population dynamics between excited-state crystal-field levels in Tb^{3+} -doped $\text{Y}_3\text{Al}_5\text{O}_{12}$ (YAG). Specifically, we study the influence of size restriction on relaxation dynamics and equilibrium population distribution between the crystal-field levels, i.e. thermalization. We observe that the population dynamics are strongly modified for smaller particles, which can be explained by a modified density of states. However, we also find that the thermal population distribution exhibited by the nano-powders is the same as in the bulk material. From the latter observation we conclude that, in addition to possible phonon suppression, other non-phononic processes—e.g. related to surface defects or energy transfer [24]—are introduced, enabling rapid thermalization of population between the closely-spaced energy levels.

5.7.3. Experimental Details

We chose Tb^{3+} doped $\text{Y}_3\text{Al}_5\text{O}_{12}$ (YAG) since the combination of its energy level structure and its high acoustic velocity is well suited to investigate the effects of size on the direct phonon process. More precisely, the small excited-state splitting $\Delta_e = 35$ GHz between the Tb^{3+} crystal-field levels $^5\text{D}_4 a/b$ (see Fig. 5.30), together with the acoustic velocity of 6400 m/s [25], results in an expected suppression of the direct phonon process for relatively large particles of ~ 100 nm diameter. In addition, in the bulk crystal, the inhomogeneous broadening of about 20 GHz allows one to selectively address each of the $^5\text{D}_4 a/b$ crystal-field levels. Furthermore, the ground state splitting $\Delta_g = 83$ GHz is large enough that resonant phonons are not expected

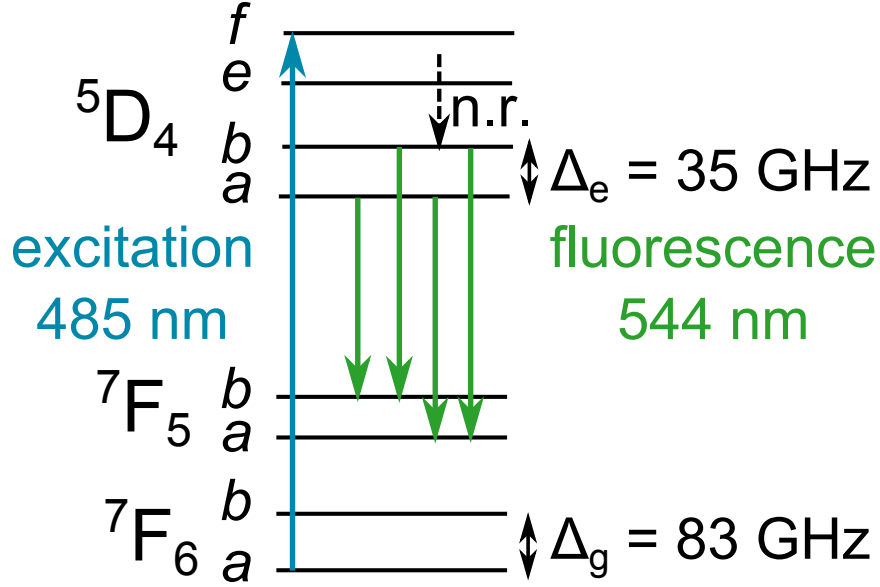


Figure 5.30.: Relevant energy levels of $\text{Tb}^{3+}:\text{Y}_3\text{Al}_5\text{O}_{12}$ (vertical axis not to scale) for the measurement of population relaxation between the first two crystal-field levels within the $^5\text{D}_4$ excited-state manifold. A pulsed laser excites the ions from the $^7\text{F}_6 a$ ground state to the $^5\text{D}_4 f$ excited state, from where they decay rapidly into $^5\text{D}_4 a$ and b . The resulting fluorescence due to the four $^5\text{D}_4 a/b \rightarrow ^7\text{F}_5 a/b$ transitions are collected, spectrally resolved, and then analyzed.

to be inhibited in the > 40 nm diameter nanocrystals, and we can therefore directly measure the internal sample temperature through the ratio of population in the two levels $^7\text{F}_6 a/b$.

We created our powders using a sol-gel synthesis (method 1 [26]) and a modified sol-gel synthesis with a freeze drying step under vacuum and at temperatures below -20 C to restrict agglomeration (method 2 [27]). Each method leads to slightly different particle morphologies and size distributions. Additional size control can be achieved by changing the annealing duration and temperature. In this way we were able to vary the nanocrystal diameter d between 40 and 500 nm, and 40 and 70 nm using method 1 and 2, respectively. We evaluated the crystal quality of our powders using

a scanning electron microscope, a transmission electron microscope, x-ray diffraction, and optical spectroscopy methods (APPENDIX A and B). From these measurements we conclude that the bulk crystal quality can be maintained for crystallites with diameters down to ~ 80 nm. For smaller sizes, we observe a slight decrease in crystal quality that manifests itself in an increase of the inhomogeneous broadening. Measurements of the radiative lifetime as a function of particle size (APPENDIX A) confirm that we can approximately treat the powders as individual particles rather than large agglomerates, with method 2 producing less agglomeration than method 1.

All powders were mounted in an unsealed glass cuvette within an Oxford Instruments cryostat. The samples were held at temperatures from ~ 1 K up to 10 K; for temperatures below 2.17 K, the samples were immersed in superfluid liquid helium, whereas for higher temperatures, the samples were cooled by a continuous flow of helium vapor. A pulsed Hänsch-style nitrogen-laser-pumped dye laser [28] with peak powers of up to 10 kW, a pulse duration of 6 ns and a repetition rate of 6 Hz was used with Coumarin 481 dye to provide excitation light at 485 nm. As shown in Fig. 5.30, we resonantly excited Tb ions from the ground state $^7F_6 a$ to the $^5D_4 f$ level, a transition that provides strong absorption. From the $^5D_4 f$ level, the population rapidly decays ($< \text{ns}$) non-radiatively by emission of high-frequency acoustic phonons into the two levels $^5D_4 a$ and b . Using a SPEX 1401 monochromator (< 3 GHz resolution), we selectively collected fluorescence from each of the four $^5D_4 a/b \rightarrow ^7F_5 a/b$ transitions. The collection was at an angle of 90° relative to the excitation laser, and the fluorescence was measured using a photomultiplier tube (Hamamatsu R928) terminated

with a variable resistance that allowed for time resolutions as fast as 100 ns.

For all powders and experimental configurations described below, we directly measured the local temperature through the relative population in the two levels ${}^7F_6 a$ and b , as detailed in APPENDIX C. We found no local heating, thus confirming that observed changes in relaxation dynamics were not due to elevated sample temperatures.

5.7.4. Time Resolved Fluorescence Measurements

Before studying the population dynamics of the ${}^5D_4 a/b$ levels, we first ensured that we could selectively collect fluorescence from the two excited levels ${}^5D_4 a/b$ for each of our samples. We recorded fluorescence spectra by scanning the monochromator over the four lines connecting ${}^5D_4 a/b \rightarrow {}^7F_5 a/b$, with typical fluorescence spectra shown in Fig. 5.31. We observed that the smallest nanocrystals feature an increased inhomogeneous broadening compared to the bulk (for details see APPENDIX B). As a consequence, some overlap in emission from the neighboring transition is present. Since this overlap can lead to observations that could wrongfully be interpreted as modifications in relaxation dynamics, it must be considered in the analysis of any obtained data.

Following this initial characterization, we recorded fluorescence decays from the two crystal-field levels ${}^5D_4 a/b$ at a temperature of 1.5 K. The individual decays were collected by sequentially tuning the monochromator on resonance with each of the four transitions ${}^5D_4 a/b \rightarrow {}^7F_5 a/b$. The specific frequencies of these transitions

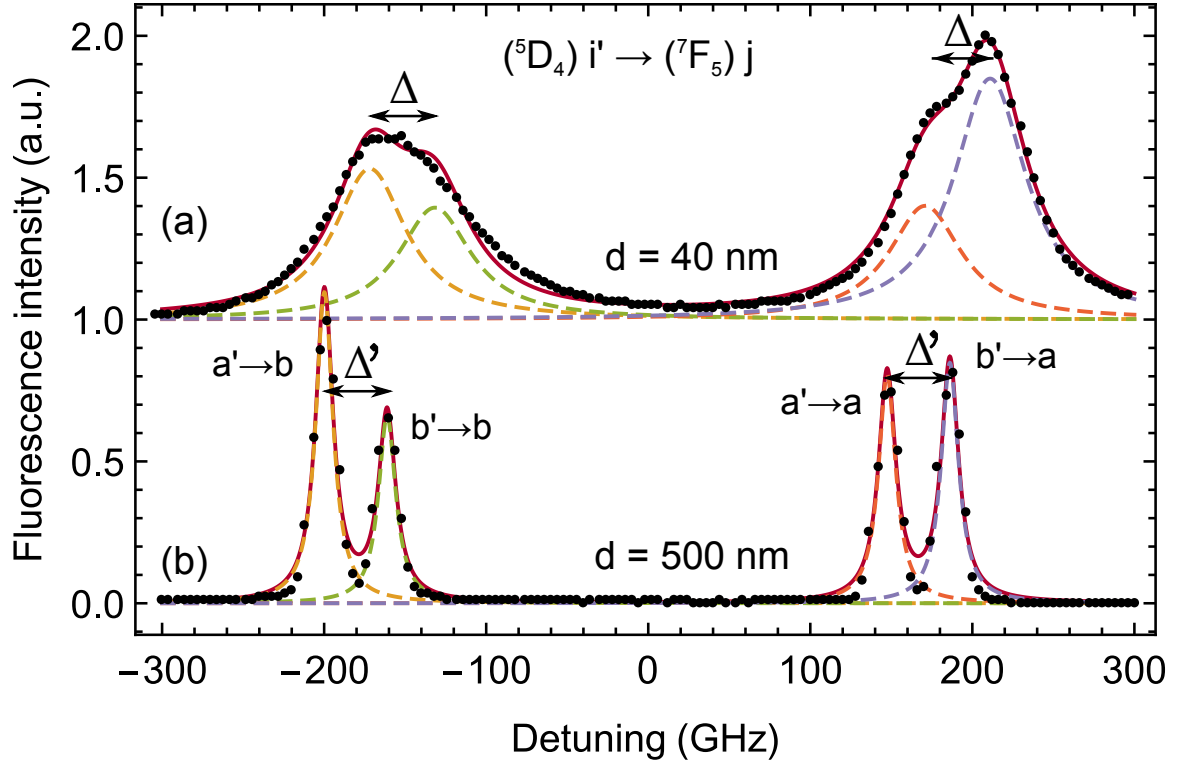


Figure 5.31.: Fluorescence spectra at 5 K of (a) a 40 nm diameter powder and (b) a 500 nm diameter powder (synthesized via method 1). Each spectrum (black dots) is fit with the sum of four identical Lorentzian lines with the same pairwise energy splitting Δ (Δ'). For $d = 40$ nm the width is 53 GHz and Δ is 40 GHz, and for $d = 500$ nm the width is 13 GHz and Δ' is 39 GHz.

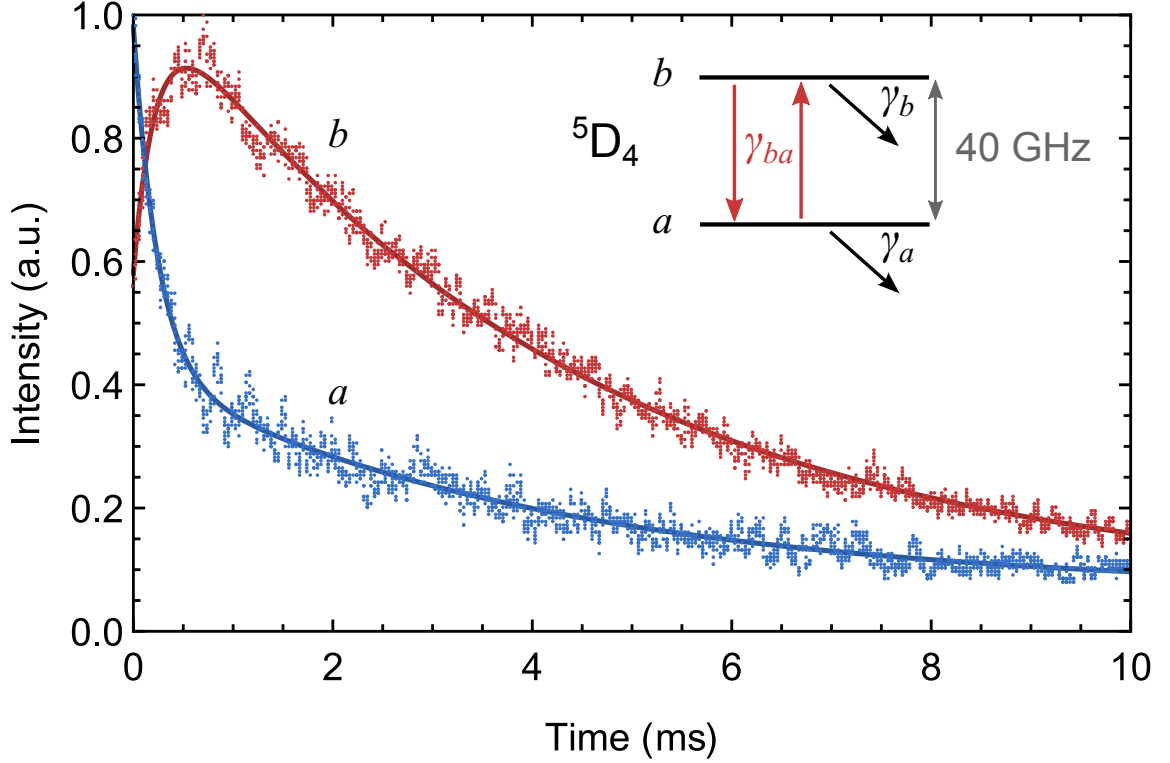


Figure 5.32.: Fluorescence decays ${}^5\text{D}_4 a \rightarrow {}^7\text{F}_5 a$ (red dots) and ${}^5\text{D}_4 b \rightarrow {}^7\text{F}_5 a$ (blue dots) at 1.5 K in large crystallites ($d = 500$ nm). The experimental points are fit with Eq. 5.27 (solid lines), resulting in $T_\alpha = 235 \mu\text{s}$ and $T_\beta = 4$ ms. Inset: relevant level structure and rates associated with the fluorescence decays (see definitions in the main text).

were obtained from the fluorescence spectra measured for each sample as described above. After excitation of the ${}^5\text{D}_4 f$ level, 2 THz above ${}^5\text{D}_4 a$, the population first decays rapidly and equally into ${}^5\text{D}_4 a/b$, and from there into ${}^7\text{F}_5 a/b$. The dynamics are captured by the following rate equations:

$$\dot{n}_a(t) = \gamma_{ba} [n_b(t) - n_a(t)] - \gamma_a n_a(t) \quad (5.25)$$

$$\dot{n}_b(t) = -\gamma_{ba} [n_b(t) - n_a(t)] - \gamma_b n_b(t) \quad (5.26)$$

where $n_{a/b}(t)$ denote the populations in the levels ${}^5\text{D}_4 a/b$ at a time t after excitation, $\gamma_{a/b}$ are the rates of the radiative decay from each level into the ${}^7\text{F}_5$ multiplet, and γ_{ba} is the rate of the nonradiative process coupling the levels ${}^5\text{D}_4 a/b$. Note that relaxation into the ground state multiplet is ignored (experimentally and in Eq. 5.26) due to the transitions' comparably small rates.

For all four transitions (see Fig. 5.32 for two examples), we observed fluorescence decays composed of two components. The first component corresponds to the non-radiative decay of population from ${}^5\text{D}_4 b$ to ${}^5\text{D}_4 a$ and manifests in the fluorescence decays from ${}^5\text{D}_4 a$ to ${}^7\text{F}_5 a/b$ as a fill-in, i.e. an increase of the fluorescence intensity with time, and in the fluorescence from ${}^5\text{D}_4 b$ to ${}^7\text{F}_5 a/b$ as an initial, fast decay, both with the same characteristic time of about 0.2 ms. The second, long component corresponds to the radiative decay. Thus, we fit the recorded, time-dependent fluorescence intensities $I_{a,b}(t)$ from the levels ${}^5\text{D}_4 a, b$ using

$$I_{a,b}(t) = \tilde{\alpha}_{a,b}e^{-t/T_\alpha} + \beta_{a,b}e^{-t/T_\beta}, \quad (5.27)$$

where T_α and T_β are the time constants of the fast (non-radiative) and slow (radiative) components with corresponding amplitudes $\tilde{\alpha}_{a,b}$ and $\beta_{a,b}$. As discussed before, due to increased inhomogeneous broadening in the small powders, the fluorescence signals collected from transitions starting in either ${}^5\text{D}_4 a$ or b contain a certain amount of emission, characterized by a line overlap δ , from the other transition. This affects the recorded signal since the fill-in and the fast decay originating from ${}^5\text{D}_4 a$ and b , respectively, compensate each other to a certain degree. However, the time constants

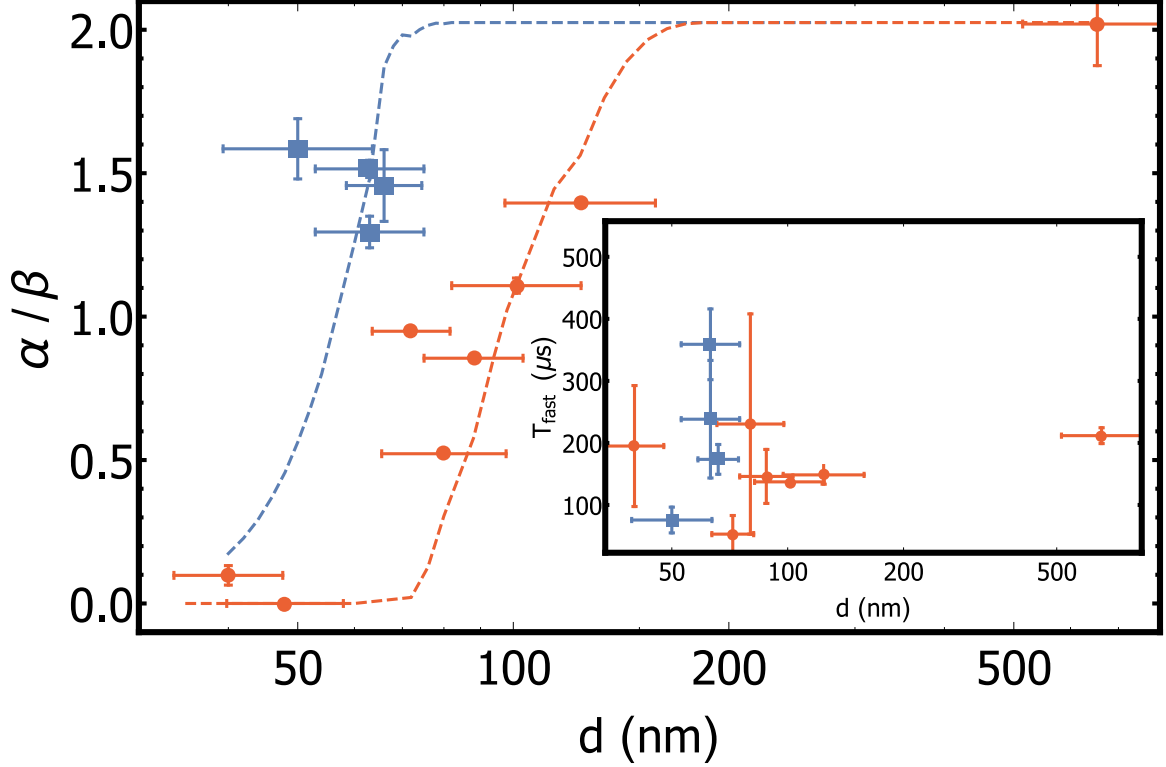


Figure 5.33.: Amplitude ratio α/β obtained from an average of the fits of Eq. 5.27 to the four decays ${}^5\text{D}_4 a, b \rightarrow {}^7\text{F}_5 a, b$ as a function of average nanocrystal diameter d for powder 1 (red circles) and powder 2 (blue squares) at 1.5 K. Simulations are depicted using dashed lines. Note that the amplitude of the fast decay has been corrected for the partially overlapping lines as described in the main text. Inset: Characteristic time of the fast decay component as a function of nanocrystal diameter d

and the amplitudes of the slow decays are not affected. We determined the value of δ from fits to our measured fluorescence spectra and subsequently compute the corrected amplitudes $\alpha_{a,b} = \tilde{\alpha}_{a,b}/(1 - 2\delta)$. Since we obtained similar results from decays to the levels ${}^7\text{F}_5 a$ and b , the following observations correspond to averages over all four transitions unless otherwise stated.

By reducing the size of the particles, we expect to introduce a frequency cutoff in the VDOS below which phonons are not allowed. Consequently, we expect to observe a change in the non-radiative relaxation between the two closely spaced crystal-field

levels ${}^5\text{D}_4 a$ and b , described by the first term in Eq. 5.27. The cutoff frequency is given by

$$\nu_{\min} = \eta \frac{c}{\pi d}, \quad (5.28)$$

where c is the sound velocity, d is the diameter of the crystal, and η is a numerical constant that equals 2.05 for a spherical particle [29]. According to this formula, YAG particles (where $c = 6400$ m/s [25]) with diameters below 100 nm should not be able to support phonons at $\Delta = 35$ GHz, corresponding to the splitting between the two crystal-field levels ${}^5\text{D}_4 a/b$. Because our powder samples inevitably exhibit some distribution of particle sizes, the non-radiative relaxation should be suppressed in more and more particles as the mean of the size distribution is reduced below ~ 100 nm. This should lead to a gradual decrease in the amplitude of the fast component α of the fluorescence decays. Note that increased inhomogeneous broadening causing partial overlap of the levels ${}^5\text{D}_4 a$ and b could also lead to similar observations. In our case, we account for this effect by computing the actual amplitude α from the measured one $\tilde{\alpha}$ as described above. As shown in Fig. 5.33, we find that for particles created using method 1, the decay ratio begins to decrease at around 130 nm diameter, whereas the onset for particles created via method 2 starts at sizes of ~ 70 nm.

We modeled this effect by calculating the VDOS [19] for 10^5 particles with different mean particle diameter and a standard deviation that we determined from the SEM images of our samples. We assumed that a nanocrystal with diameter d contributes only to the fast decay if its VDOS at $\Delta = 35$ GHz is greater than zero. The only free parameter in the simulations is the width $\Delta\nu$ of the individual vibrational modes,

which we obtain through a fit to the experimental data. The results of the simulations are presented in Fig. 5.33.

For large crystal diameters d , the simulated amplitude ratios (for crystals created via either method) are around 2, which corresponds to the bulk value at 1.5 K. When we reduce d , the amplitude ratios start decreasing at two distinct diameters (130 nm for method 1 and 70 nm for method 2 crystals). This can be explained by different mode widths ($\Delta\nu = 0.5$ and 6 GHz for powders of methods 1 and 2, respectively) obtained from the simulations. If phonon modes are broad, as in powders from method 2, it is more likely that they overlap with the transition between the $^5D_4 a/b$ levels, even for small crystals. However, for sharp modes (powders from method 1), overlap becomes significant only for larger particles in which more modes exist. Note that the width of the phonon modes is related to the powder quality. In particular, crystallites with reduced surface roughness should feature narrower phonon modes. This leads us to conclude that powder 1 should be of higher quality, which, however, cannot be verified given the insufficient resolution of our SEM pictures. Note that the optical inhomogeneous linewidths suggest that method 2 produces powders with less internal strain; however, it is not known if there is a relationship between particle surface morphology and internal strain.

Overall, the simulated values are in good agreement with the experimental data for powders produced by either method, consistent with suppression of phonon-induced relaxation in sufficiently small powders. In particular, we observed the complete transition from large particles, where the relevant phonon processes are fully allowed, to the smallest particles, where we could not measure any contribution of the phonon-

induced component to population relaxation.

In addition to a change in the amplitude of the fast decay, we also expect a change in its characteristic decay time T_α . For the fraction of particles with $\nu_{\min} \simeq \Delta_e$, the phonon density of states at Δ_e should be equal to an intermediate value between zero and the maximum value exhibited by the bulk crystal. Thus, because the rate of the non-radiative relaxation is proportional to the VDOS, the phonon induced decay rate for these nanocrystals should be slower than the one for the bulk, i.e. T_α should increase with decreasing particle size. Experimentally (see inset Fig. 5.33), we do not observe the expected increase for particles from method 1. This is consistent with the conjecture of having sharp phonon modes (resulting from the fit of the decay ratios in Fig. 5.33), in which case the phonon cutoff occurs abruptly as the size is reduced so that the particles either experience the bulk phonon rate or no phonon decay at all. Hence, the experimental data should only show the bulk decay, which is the case for our powder created via method 1 at $d = 48$ nm. For powders from method 2, the fit of the decay ratios predicts broader phonon modes, and we thus expect that more particles experience decay times longer than the bulk before the decay is suppressed completely. Indeed, except for the smallest powder created using method 2, we see signatures of such an increase in T_α , consistent with the predictions of our model.

5.7.5. Measurement of temperature dependent population

re-distribution

Another indication of the restriction of phonon modes is the inhibition of thermalization (population re-distribution) between the two crystal-field levels ${}^5D_4 a/b$ after their initial population through decay from ${}^5D_4 f$. While the decay from the upper crystal-field level produces equal population in both levels so that $n_b/n_a = 1$, the ratio will subsequently change and approach thermal equilibrium due to nonradiative transitions between ${}^5D_4 a/b$. For $t > T_\alpha$, the population ratio is described by

$$n_b/n_a = (1 - N_0) e^{-\Delta/k_B T} + N_0 \quad (5.29)$$

i.e. the Boltzmann distribution that assumes thermalization through nonradiative processes, with an additional offset N_0 included. The population ratio n_b/n_a for $t > T_\alpha$ is directly related to the ratio of the amplitudes β_b and β_a of the long fluorescence decay components (see Eq. 5.27): $\beta_b/\beta_a \propto n_b(t)/n_a(t)$. This allows us to extract the actual population distribution for different temperatures.

The measured temperature dependence of n_b/n_a , calculated by averaging β_a (and β_b) over both transitions starting in ${}^5D_4 a$ (and ${}^5D_4 b$), is shown in Fig. 5.34 for the bulk crystal as well as for two nanocrystal samples ($d = 40$ and 72 nm) created via method 1. We fit the experimental points using Eq. 5.29 after fixing the energy separation Δ_e to the bulk value of 35 GHz and leaving N_0 as a free variable. For both powders we observe a non-zero offset N_0 . The fit gave $N_0 = 0.21 \pm 0.1$ and 0.14 ± 0.07 for the two powders with $d = 72$ nm and 40 nm, respectively, and for the bulk crystal it resulted

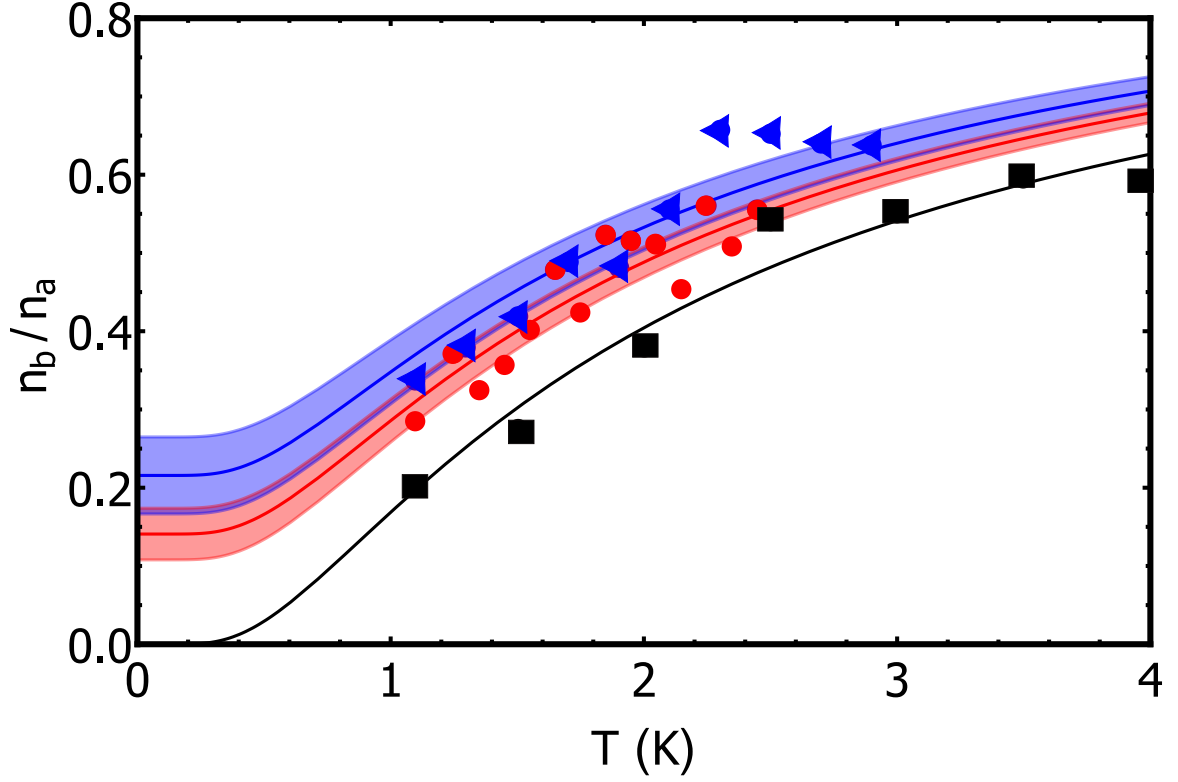


Figure 5.34.: Ratio of population n_b/n_a as a function of temperature in the bulk crystal (black squares) and in nanocrystals from method 1 of average diameter $d = 72$ nm (blue triangles) and 40 nm (red dots). Solid lines are best fits using Eq. 5.29, and shaded areas represent uncertainties.

in $N_0=0$, suggesting that there is the expected difference in thermalization in the powders. However, this offset can be fully explained by the emission line overlap δ with the neighboring transition due to the increased inhomogeneous broadening as discussed above. Indeed, calculating N_0 by taking only line overlap into account, we find $N_0 = 0.3 \pm 0.02$ and 0.26 ± 0.02 for $d = 72$ nm and 40 nm, respectively. This seems to be at odds with the observed reduction of the nanocrystal's fast decay amplitude (Fig. 5.33), which is also supported by VDOS simulations. Thus, the observation of thermalization indicates that other processes, happening on time scales smaller than the 100 ns resolution of our detector, are responsible for population re-distribution

in our smallest nanocrystals. Such fast relaxation could be caused by coupling of the Tb^{3+} ions to tunneling modes characteristic of amorphous materials [30, 31] (note that the increase of amorphous character as the particle size is reduced is supported by the observation of larger inhomogeneous broadening). Other explanations are relaxations driven by energy transfer [24] or interactions between ions and surface states.

5.7.6. Conclusion

In conclusion, we observed modifications in relaxation dynamics between crystal field levels of $\text{Tb}^{3+}:\text{Y}_3\text{Al}_5\text{O}_{12}$ crystals as the particle size is varied from bulk to 40 nm, and confirmed via absorption measurements that this effect is not due to local heating. One possible explanation is a modification of the VDOS in the nanocrystals, which restricts phonon processes between the two first crystal-field levels in the $^5\text{D}_4$ excited state that are separated by 35 GHz.

However, other measurements suggest a different explanation: population redistribution is still observed within the two closely-spaced levels, meaning that other, fast, non-radiative processes must enable this transition. These processes may arise from a partially amorphous character of the nanocrystals, even though significant effort was dedicated to achieving good crystal quality by exploring various synthesis methods and modifying different important parameters in each of them, such as the addition of surfactants or the annealing temperature. We note that the case of YAG is particularly difficult because of the high annealing temperature—which favors particle

growth— required to crystallize the particles.

Improving the nanocrystal quality by optimizing fabrication methods, as well as switching to a different material with a lower annealing temperature, such as fluoride crystals, may enable one to observe the full phonon restriction. However, there may exist a fundamental limit to how small a particle can become while still preserving the spectroscopic properties of a large crystal – this limit is frequently estimated to be around 10 nm [32]. Our results suggest that, for YAG, it may be around 100 nm. Measurements of crystal structure may shed more light on this important question.

5.7.7. Acknowledgements

The authors acknowledge support from Alberta Innovates Technology Futures (ATIF), the National Engineering and Research Council of Canada (NSERC), and the National Science Foundation of the USA (NSF) under award nos. PHY-1415628 and CHE-1416454, and the Montana Research and Economic Development Initiative. W. T. is a Senior Fellow of the Canadian Institute for Advanced Research (CIFAR).

5.7.8. APPENDIX A: Powder characterization

For all investigations of population dynamics presented in the main text, information about the morphology and size distribution of the various powders is needed to interpret the results. We obtained this information for powders from method 1 and 2 using a scanning electron microscope (SEM), with example images shown in

Fig. 5.35. The images indicate that method 2 produces slightly less agglomerated powders compared to method 1. In addition, we confirmed that we obtained good single-phase crystalline YAG particles using powder x-ray diffraction (XRD) analysis. Figures 5.35 (e,f) show the perfect overlap between the XRD spectrum of the $\text{Tb}^{3+}:\text{Y}_3\text{Al}_5\text{O}_{12}$ powders produced by method 1 and 2 with the reference spectrum for YAG (JCPDS # 30-0040). For selected powder samples, we also directly probed the quality of the crystal structure using a transmission electron microscope (TEM), as shown in Fig. 5.35 (d). The TEM analysis revealed that the crystallite orientations in agglomerated nanocrystals can remain nearly aligned throughout multiple grains when they are fused together. Since it is possible that phonon modes extend across several crystallites in these cases, we considered the effective particle size in agglomerated samples to be equal to the larger size of the approximately aligned agglomerations rather than the individual grain size. The effect of agglomeration on phonon propagation dynamics cannot be quantified at this stage.

In addition to using the TEM measurements, we also investigated the degree to which the crystallites within the powder act as isolated particles versus being part of a larger agglomerated mass by observing the increase in radiative lifetime as the particle sizes are reduced. As known from relations such as the Strickler-Berg equation [33], the radiative lifetime T_{rad} of an electric dipole transition depends on the average index of refraction, n , of the material. Because of this, when the size of a fluorescing particle becomes comparable to the wavelength of the emitted light, the index of the medium surrounding the particle can have a significant effect on the

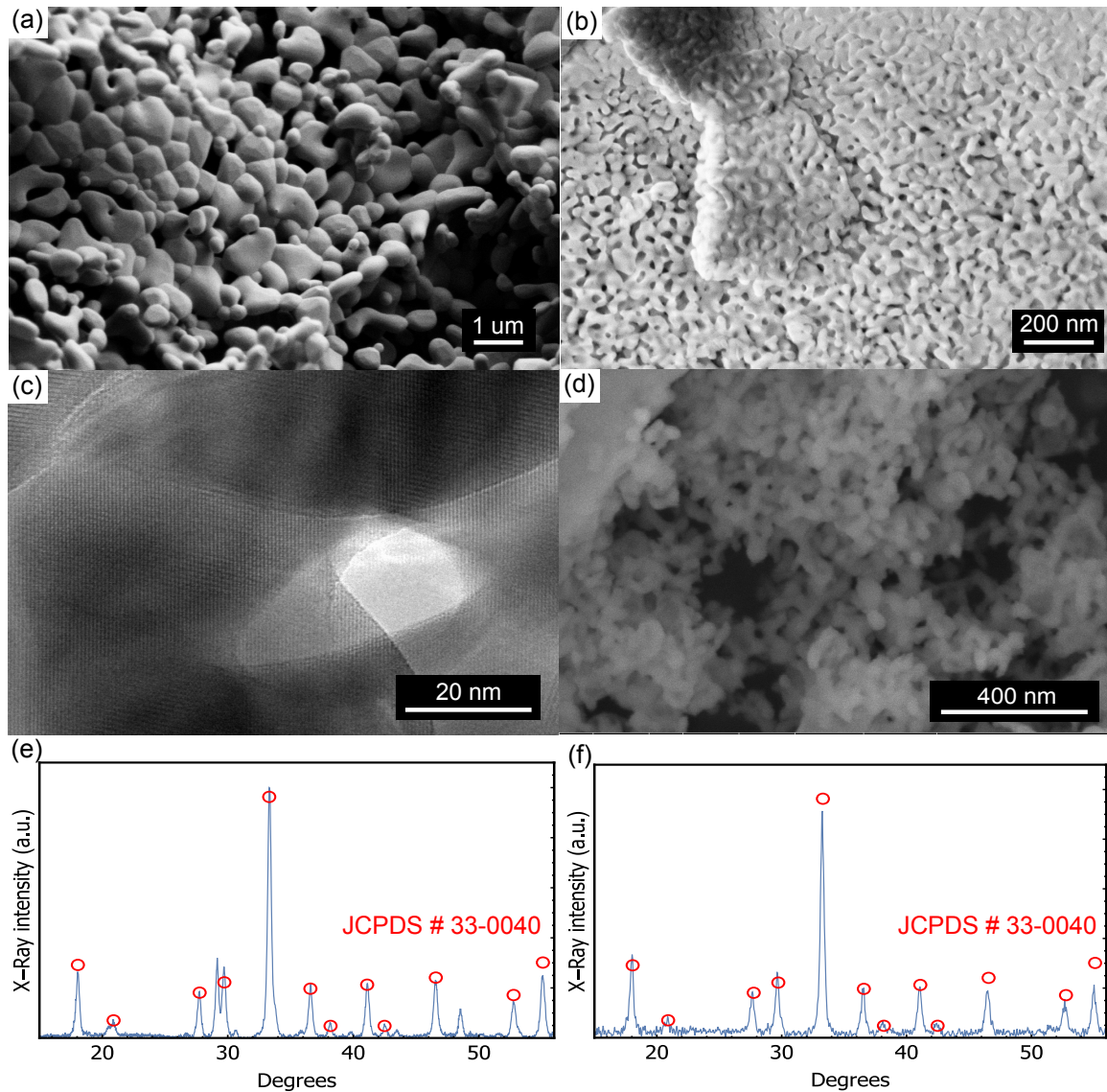


Figure 5.35.: Microscope images of 1% $\text{Tb}^{3+}:\text{Y}_3\text{Al}_5\text{O}_{12}$ created using method 1 and annealed at 1400 C (a), or 900 C (b,c), and from method 2 annealed at 900 C (d). Panels (a,b,d) are SEM images, showing the size distribution of the nanocrystals. Panels (e) and (f) show XRD spectra of powders produced by method 1 and 2, respectively (solid blue lines), and the corresponding reference spectrum (JCPDS # 30-0040; red circles) for YAG. Panel (c) is a high-resolution TEM image showing the crystalline structure (narrow white lines), which can extend over several particles if they are agglomerated.

radiative lifetime[20, 34, 35]. Consequently, we expect to observe an increase in the fluorescence lifetime as the average particle size in our powders is reduced. Note that strongly agglomerated particles would effectively act as a single, larger particle in this case.

We employ a simple analytical model to estimate the size dependence of the fluorescence lifetime for perfectly isolated particles. More precisely, we used the form of the Lorentz local field, sometimes referred-to as the virtual cavity model [36], where the radiative lifetime in the medium T_{rad} is related to the lifetime in vacuum T_0 according to $1/T_{\text{rad}} = (1/T_0) n_{\text{eff}}(n_{\text{eff}}^2 + 2)^2/9$, with n_{eff} being an effective index of refraction averaged over the surrounding medium within a distance on the order of the wavelength of light from the ion.

For particles smaller than the wavelength of light, the electric field extends beyond the particle. To evaluate n_{eff} for such particles, we assumed that the electric field of the emitted light experiences the bulk crystal dielectric constant within the particle, and the vacuum dielectric constant outside the particle. We furthermore assumed that the electric field outside the particle decays as $E(r) = E_0 e^{-r/l}$ over the decay length l , which is equal to the evanescent field decay length outside of a bulk dielectric given by $l = \lambda_0/2\pi\sqrt{n^2 - 1}$ [37]. Here n is the refractive index of the bulk material and λ_0 the wavelength of the transition. The value of n_{eff} experienced by the emitting ion, and the resulting change in radiative lifetime, was then estimated by calculating the field-strength-weighted average dielectric constant over the area of non-zero electric field.

By using this simple model, we estimated the change in lifetime with particle size using only the known bulk crystal index, transition wavelength, and lifetime with no free parameters, resulting in the solid line in Fig. 5.36. We find that the measured lifetimes in our samples agree reasonably well with the calculated dependence (Fig. 5.36). For method 1, the radiative lifetime increases up to 7 ms, as the crystallite size decreases, but powders smaller than 50 nm show lifetimes similar to the bulk crystal, indicating that some degree of agglomeration is present. For method 2, the radiative lifetime increases up to 13 ms, indicating that the particles in powders synthesized with this method indeed behave as individual particles with sizes approximately equal to the values estimated from the SEM and TEM analysis.

5.7.9. APPENDIX B: Spectroscopic investigations of powder quality

To ensure that we can selectively collect fluorescence from the two excited levels $^5D_4 a/b$ for each of our samples, we recorded fluorescence spectra by scanning the monochromator over the four lines connecting $^5D_4 a/b \rightarrow ^7F_5 a/b$. As shown in Fig. 5.37, we observed that for both fabrication methods, the smallest nanocrystals feature an increased inhomogeneous broadening compared to the bulk. This increase, which was expected due to an increased amount of strain, was not observable in the XRD spectra due to the limited resolution of our XRD diffractometer (Rigaku Multiflex). The observation of increased inhomogeneous broadening is consistent

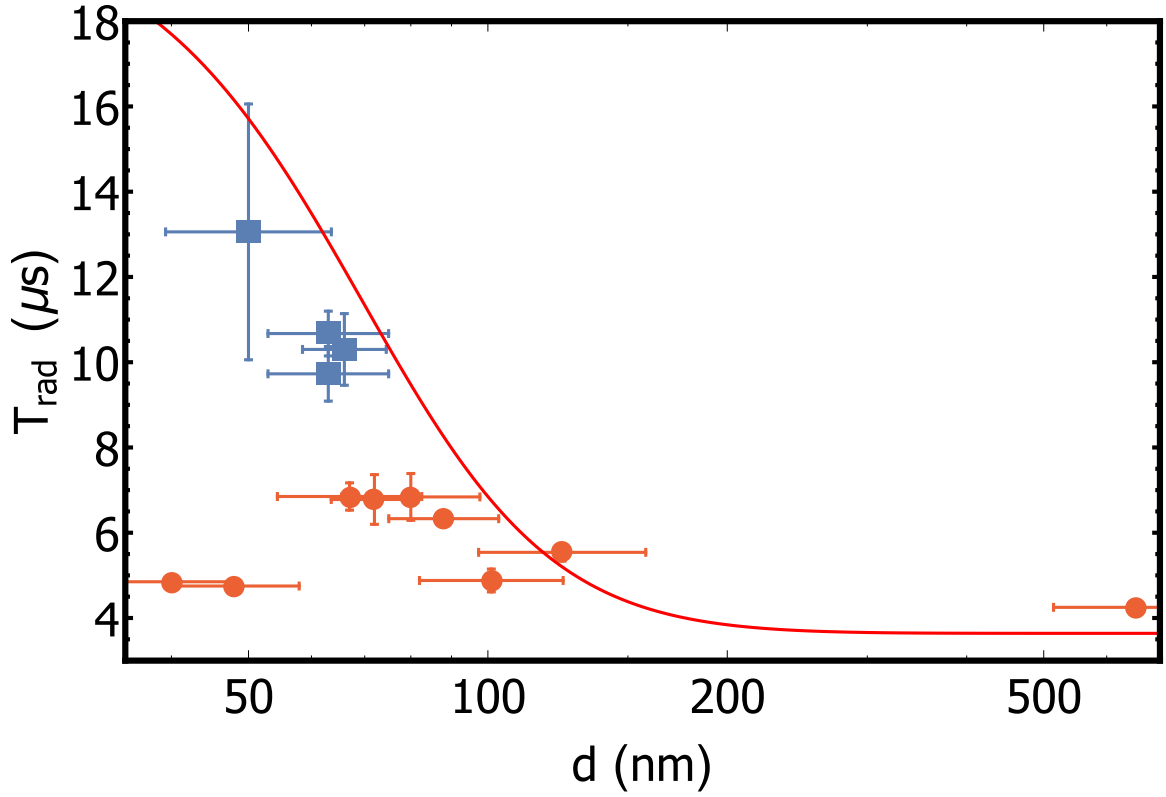


Figure 5.36.: Particle size (d) dependence of the radiative lifetime of the $^5\text{D}_4 a$ level for powders from method 1 (red circles) and powders from method 2 (blue squares). The solid line shows the expected dependence.

with the emergence of relaxation that is facilitated by amorphous phases and surface defects (see main text). However, as shown in the inset of Fig. 5.37, the splitting Δ between the $^5\text{D}_4 a/b$ levels does not change with particle size, which indicates that the ions' crystal field splittings and local lattice symmetry are not measurably different in the small powders.

5.7.10. APPENDIX C: Local temperature measurement

In past measurements, the thermal conductivity of small powders in a gas environment was observed to decrease with particle size due to two effects. First, the phonon scattering length is reduced in small powders, and second, heat flow is hindered

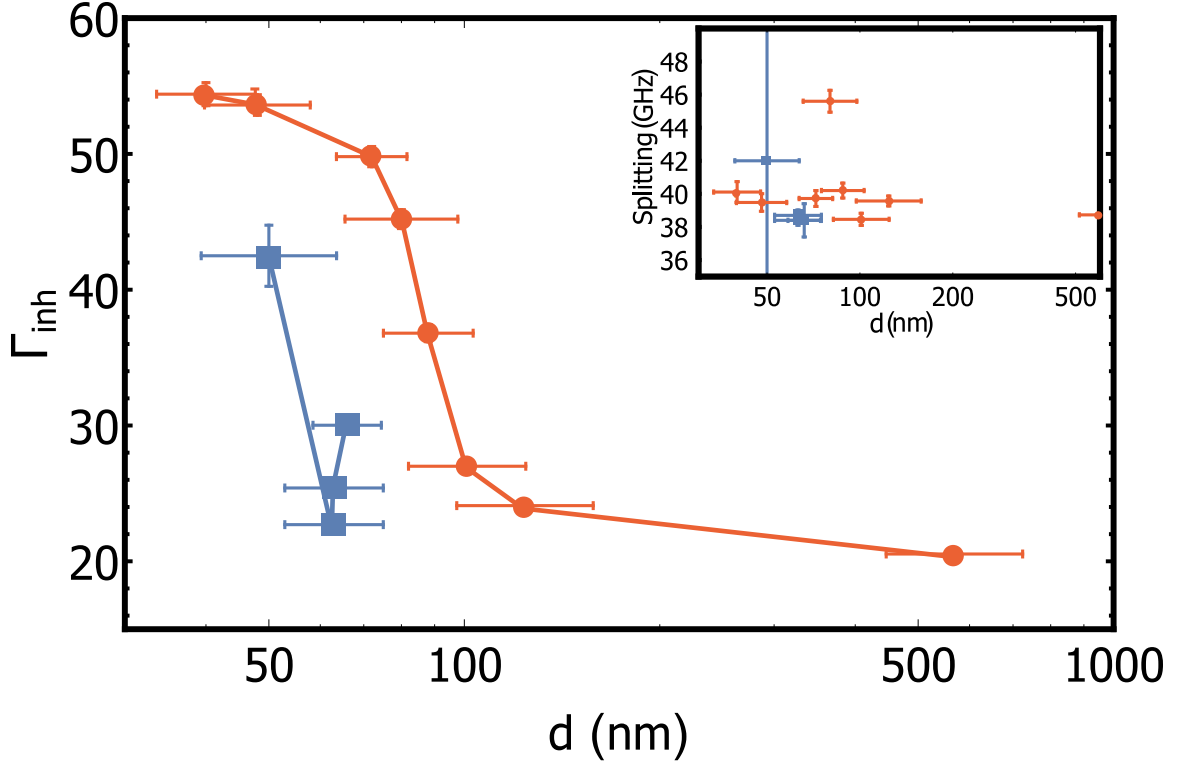


Figure 5.37.: Particle-size-dependence of the inhomogeneous linewidth for powders from method 1 (red circles) and powders from method 2 (blue squares). Inset: Splitting Δ between the $^5D_4 a/b$ levels versus particle size. The solid lines are guides to the eye.

by the surface resistance of the small particles contained in the powder [38, 39, 40]. These effects could lead to a locally elevated powder temperature, especially when the powder is probed using a high power laser. An elevated sample temperature in turn would produce significant changes in population relaxation and thermalization that could potentially be misinterpreted as arising from other effects. To ensure that the laser excitation did not induce localized heating, a direct temperature measurement that enables the true internal temperature of the particles to be monitored is required. We measured the internal temperature for each sample by recording the absorption spectrum $^7F_6 a, b \rightarrow ^5D_4 f$ and comparing the populations n_1 and n_2 in the first

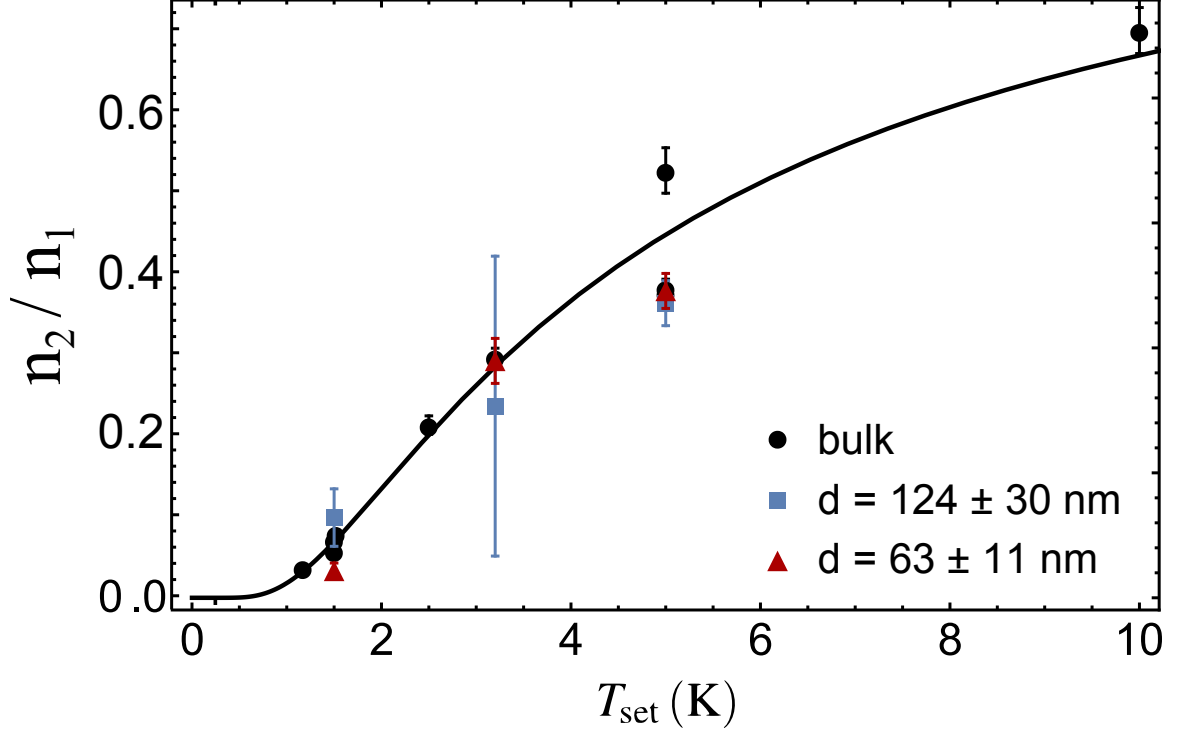


Figure 5.38.: Ratio n_2/n_1 of populations in the ground manifold ${}^7\text{F}_6$ b/a levels as a function of the temperature T_{set} read by the cryostat sensor for a bulk crystal (black dots) and nanocrystalline powder samples with diameters $d = 124 \pm 30 \text{ nm}$ and produced by method 1 (blue squares) and $d = 63 \pm 11 \text{ nm}$, produced by method 2 (red triangles). The solid line is the fit to a Boltzmann distribution with $\Delta_g = 83.5 \text{ GHz}$. Note that the large error bar for 3.2 K and $d = 124 \text{ nm}$ is caused by a large uncertainty of the fit to that particular absorption spectrum.

and second crystal field level ${}^7\text{F}_6 a$ and b of the ground state multiplet, which are separated by $\Delta_g = 83 \text{ GHz}$. This allowed us to determine the effective internal sample temperature T via the Boltzmann law $n_2/n_1 = A \exp\{-\Delta_g/k_B T\}$ with k_B the Boltzmann constant. We obtained the coefficient A , which depends on the relative oscillator strengths of the transitions, from a calibration measurement using a 1% Tb:YAG bulk crystal, that we assumed to thermalize quickly to the temperature T_{set} that was measured by the cryostat sensor. The temperature-dependent population ratio n_2/n_1 is shown in Fig. 5.38 for a selected set of nanocrystals. The close overlap

between the bulk and powder results confirms that all powders thermalize as well as the bulk when immersed in liquid helium or vapor and that the laser is not measurably heating the nanocrystals, even for the smallest sizes. Since these measurements are conducted using the same laser power and focusing parameters as those used for all other measurements described in the main text, they confirm that the changes in dynamics that we observe in the powders are not caused by local heating. Also, with this method, we ensure that the ions that are studied in the relaxation dynamics measurements (as in the main text) are also the same ions that are used to measure the temperature.

Bibliography

- [1] H. de Riedmatten and M. Afzelius, *Quantum Light Storage in Solid State Atomic Ensembles* (Springer International Publishing, Cham, 2015), pp. 241–273.
- [2] K. Heshami, D. G. England, P. C. Humphreys, P. J. Bustard, V. M. Acosta, J. Nunn, and B. J. Sussman, *Journal of Modern Optics* **0**, 1 (2016).
- [3] A. Sipahigil, R. E. Evans, D. D. Sukachev, M. J. Burek, J. Borregaard, M. K. Bhaskar, C. T. Nguyen, J. L. Pacheco, H. A. Atikian, C. Meuwly, R. M. Camacho, F. Jelezko, E. Bielejec, H. Park, M. Lončar, and M. D. Lukin, *Science* **354**, 847 (2016).
- [4] B. Hensen, H. Bernien, A. E. Dreau, A. Reiserer, N. Kalb, M. S. Blok, J. Ruitenberg, R. F. L. Vermeulen, R. N. Schouten, C. Abellan, W. Amaya, V. Pruneri, M. W. Mitchell, M. Markham, D. J. Twitchen, D. Elkouss, S. Wehner, T. H. Taminiau, and R. Hanson, *Nature* **526**, 682 (2015).
- [5] M. P. Hedges, J. J. Longdell, Y. Li, and M. J. Sellars, *Nature* **465**, 1052 (2010).

- [6] E. Saglamyurek, N. Sinclair, J. Jin, J. A. Slater, D. Oblak, F. Bussi eres, M. George, R. Ricken, W. Sohler, and W. Tittel, *Nature* **469**, 512 (2011).
- [7] P. C. Maurer, G. Kucsko, C. Latta, L. Jiang, N. Y. Yao, S. D. Bennett, F. Pastawski, D. Hunger, N. Chisholm, M. Markham, D. J. Twitchen, J. I. Cirac, and M. D. Lukin, *Science* **336**, 1283 (2012).
- [8] S. Hong, M. S. Grinolds, L. M. Pham, D. Le Sage, L. Luan, R. L. Walsworth, and A. Yacoby, *MRS Bulletin* **38**, 155161 (2013).
- [9] R. C. Powell, *Physics of Solid-State Laser Materials* (Springer-Verlag New York, 1998).
- [10] A. J. Kenyon, *Progress in Quantum Electronics* **26**, 225 (2002).
- [11] T. J ustel, H. Nikol, and C. Ronda, *Angewandte Chemie International Edition* **37**, 3084 (1998).
- [12] F. Wang, Y. Han, C. S. Lim, Y. Lu, J. Wang, J. Xu, H. Chen, C. Zhang, M. Hong, and X. Liu, *Nature* **463**, 1061 (2010).
- [13] E. Downing, L. Hesselink, J. Ralston, and R. Macfarlane, *Science* **273**, 1185 (1996).
- [14] X. L. Ruan and M. Kaviani, *Phys. Rev. B* **73**, 155422 (2006).
- [15] T. Lutz, L. Veissier, C. W. Thiel, P. J. T. Woodburn, R. L. Cone, P. E. Barclay, and W. Tittel, *Science and Technology of Advanced Materials* **17**, 63 (2016).

- [16] T. Lutz, L. Veissier, C. W. Thiel, P. J. Woodburn, R. L. Cone, P. E. Barclay, and W. Tittel, *Journal of Luminescence* pp. 2–12 (2017).
- [17] T. Zhong, J. M. Kindem, E. Miyazono, and A. Faraon, *Nat Commun* **6** (2015).
- [18] A. Ferrier, C. W. Thiel, B. Tumino, M. O. Ramirez, L. E. Bausá, R. L. Cone, A. Ikesue, and P. Goldner, *Phys. Rev. B* **87**, 041102 (2013).
- [19] T. Lutz, L. Veissier, C. W. Thiel, R. L. Cone, P. E. Barclay, and W. Tittel, *Phys. Rev. A* **94**, 013801 (2016).
- [20] H.-S. Yang, S. P. Feofilov, D. K. Williams, J. C. Milora, B. M. Tissue, R. S. Meltzer, and W. M. Dennis, *Physica B: Condensed Matter* **263**, 476 (1999).
- [21] H.-S. Yang, K. Hong, S. Feofilov, B. M. Tissue, R. Meltzer, and W. Dennis, *Journal of Luminescence* **83**, 139 (1999).
- [22] G. K. Liu, H. Z. Zhuang, and X. Y. Chen, *Nano Letters* **2**, 535 (2002).
- [23] B. Mercier, C. Dujardin, G. Ledoux, C. Louis, O. Tillement, and P. Perriat, *Journal of Luminescence* **119**, 224 (2006).
- [24] T. Förster, *Annalen der Physik* **437**, 55 (1948).
- [25] L. Mezeix and D. J. Green, *International Journal of Applied Ceramic Technology* **3**, 166 (2006).
- [26] N. Kaithwas, M. Dave, S. Kar, S. Verma, and K. S. Bartwal, *Crystal Research and Technology* **45**, 1179 (2010).

- [27] H. Gong, D.-Y. Tang, H. Huang, and J. Ma, Journal of the American Ceramic Society **92**, 812 (2009).
- [28] T. W. Hänsch, Appl. Opt. **11**, 895 (1972).
- [29] H. Lamb, Proceedings of the London Mathematical Society **s1-13**, 189 (1881).
- [30] P. W. Anderson, B. I. Halperin, and C. M. Varma, Philosophical Magazine **25**, 1 (1972).
- [31] W. A. Phillips, Journal of Low Temperature Physics **7**, 351 (1972).
- [32] X. C. G. Liu, *Handbook on the Physics and Chemistry of Rare Earths* (ELSEVIER SCIENCE & TECHNOLOGY, 2007).
- [33] S. J. Strickler and R. A. Berg, The Journal of Chemical Physics **37**, 814 (1962).
- [34] H. Schniepp and V. Sandoghdar, Phys. Rev. Lett. **89**, 257403 (2002).
- [35] A. Aubret, A. Pillonnet, J. Houel, C. Dujardin, and F. Kulzer, Nanoscale **8**, 2317 (2016).
- [36] S. Scheel, L. Knöll, and D.-G. Welsch, Phys. Rev. A **60**, 4094 (1999).
- [37] F. de Fornel, *Evanescent Waves* (Springer-Verlag Berlin Heidelberg, 2001).
- [38] K. W. Garrett and H. M. Rosenberg, Journal of Physics D: Applied Physics **7**, 1247 (1974).
- [39] T. Rettelbach, J. Säuberlich, S. Korder, and J. Fricke, Journal of Non-Crystalline Solids **186**, 278 (1995).

- [40] D. E. Brodie and C. F. Mate, Canadian Journal of Physics **43**, 2344 (1965).

5.8. Silicon vacancy centres in diamond

Even though we saw signatures of phonon suppression with REI doped host materials, we were not able to suppress non-radiative relaxation between closely spaced levels completely since other relaxation processes, related to crystal damage, arose. Our measurements showed that REI are very sensitive to any kind of mechanical processing. As described previously, we also found that fabrication methods increase the inhomogeneous broadening in the smallest powders which complicates the interpretation of measurements. Unfortunately, more gentle nano-fabrication methods such as chemical etching have yet to be developed for the most common REI host materials. Due to this lack of fabrication methods, the use of phononic crystals is thus not within immediate reach.

In order to perform a proof-of-principle experiment that demonstrates phonon suppression and lays the foundation for future applications, silicon vacancy centers in diamond are well suited. The silicon vacancy center (SiV) features two doubly degenerate orbital ground states ($|g_1\rangle, |g_2\rangle$) that are spaced by ~ 50 GHz (see Fig. 5.39). Jahnke *et al.* [63] showed that transitions between these two states are mainly driven by the direct phonon process. This limits the population lifetime in the upper orbital state, and, more importantly, the coherence time of the spin states that arise when a magnetic field is applied. The coherence time of the spin states has been measured to be around 40 ns at temperatures around 4 K. The latter is too short to enable the SiV as a quantum memory or efficient quantum information processing device. How-

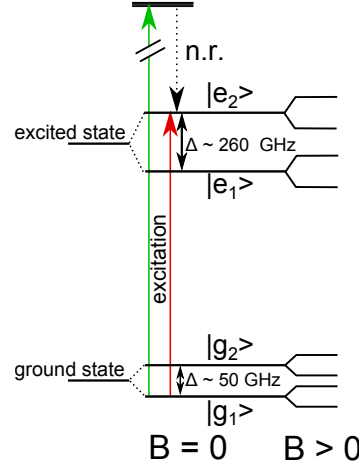


Figure 5.39.: Relevant energy levels of the SiV center in diamond.

ever, by suppressing the direct phonon process, coherence times up to milliseconds are expected [64].

Such coherence times together with the other advantages of the SiV, e.g. its strong zero phonon line and robustness against charge fluctuations in its environment (due to its inversion symmetry) would make this center a very promising candidate for applications such as quantum memories, quantum gates, single photon sources and on-chip implementations thereof.

5.9. Phonon suppression in silicon vacancy centers in diamond

Phonon suppression in SiVs can be achieved via the same principles as in REIs. However, due to their strong oscillator strength, one can use single SiVs for all investigations, which greatly simplifies measurements and avoids ambiguities arising from

inhomogeneous broadening. Furthermore, the splitting of ~ 50 GHz between the orbital ground states together with the high speed of sound in diamond (12000 m/s [65]) makes it possible to achieve phonon suppression in relatively large structures with dimensions around 150 nm. An additional benefit of the SiV is its inversion symmetry, which makes its properties largely insensitive to fabrication methods. Nanofabrication tools such as chemical etching and focused ion beam milling have been developed during the last decade [66] and the fabrication of structures on the scale of hundreds of nanometers is established. The work by Alp Sipahigil et.al [64] demonstrated that SiV can maintain their bulk properties in structures with sizes of only a few hundred nm.

Taking advantage of these properties, we also used the SiV in diamond to investigate the possibility for complete phonon suppression in small structures and whether this effect can be exploited for applications. First, we performed numerical simulations using various geometries to find a structure that is easy to fabricate but still capable to suppress phonons. These simulations (see Fig. 5.40) predict that small nanopillars with dimensions < 150 nm should result in a strongly reduced density of states for phonon frequencies around 50 GHz, i.e. the transition frequency between the two lowest orbital states (see Fig. 5.39).

In initial experiments, we fabricated small pillars containing SiVs on a diamond substrate. Towards this end, we purchased commercially available diamond chips that are grown using chemical vapor deposition (Element 6: electronic grade, i.e. < 0.03 ppb nitrogen vacancy center (NV) concentration). The low NV concentration is im-

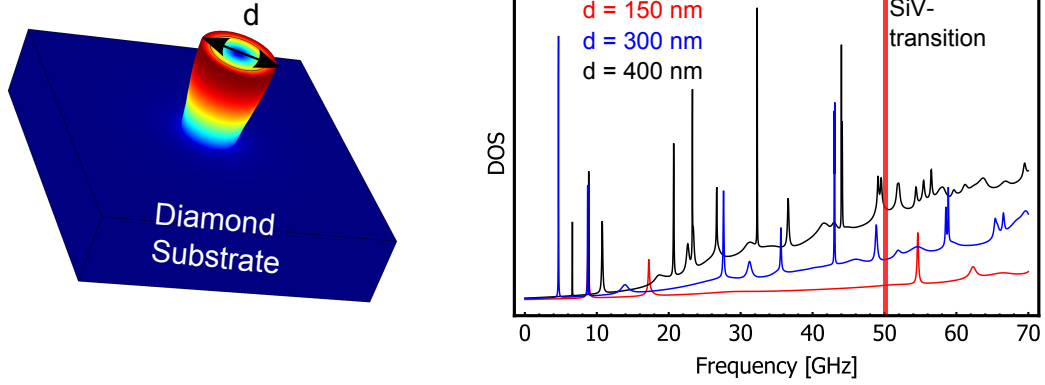


Figure 5.40.: Vibrational density of states (DOS) simulations for nanopillars with varying diameter d on a bulk diamond substrate.

portant since the presence of many NVs in the sample can mask the SiV signal. Subsequently, the sample was implanted with silicon ions ($^{28}\text{Si}^+$) with a dose of 10^{11} ions/cm² and an energy of 180 keV, which results in an implantation depth of around 150 nm. After implantation, the sample was cleaned using a mixture of perchloric, nitric, and sulphuric acid (1:1:1) heated to ~ 250 C, and then annealed at temperatures up to 1100 C and under vacuum ($< 10^{-6}$ torr) [67]. We fabricated nanopillars with diameters varying from 120 to 900 nm and heights of around 1 μm using the same fabrication process as described in [68], except that we omitted the isotropic diamond etching step that creates free standing structures. The sample was then cleaned using again the heated acid mixture. A scanning electron image of the resulting nanopillars is shown in Fig. 5.41.

In order to demonstrate phonon suppression in the fabricated pillars, we mounted the samples in a cryostat (Montana Instruments Cryostation) and cooled them down to around 5 K. The confocal microscope setup that was used for all investigations is shown in Fig. 5.42.

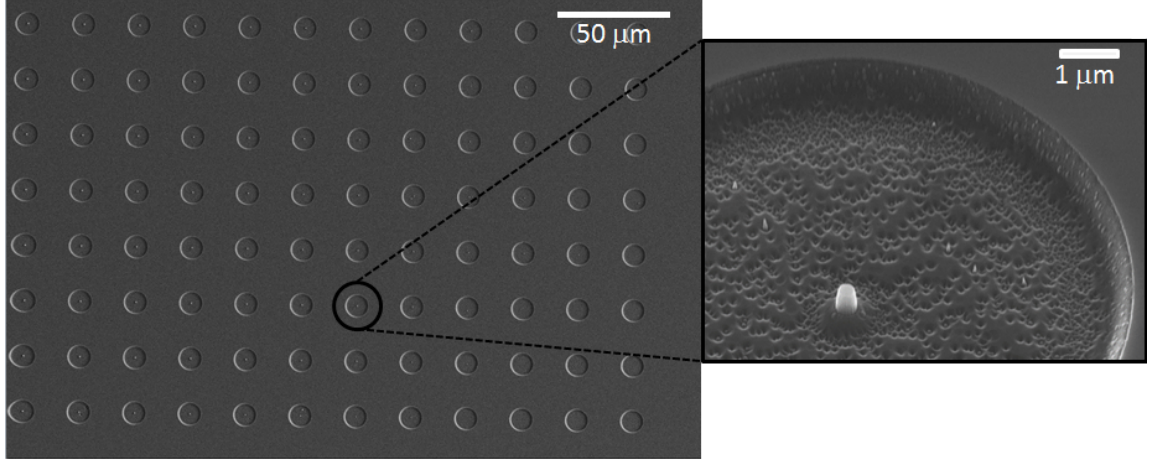


Figure 5.41.: Scanning electron microscope images of the fabricated nano pillars.

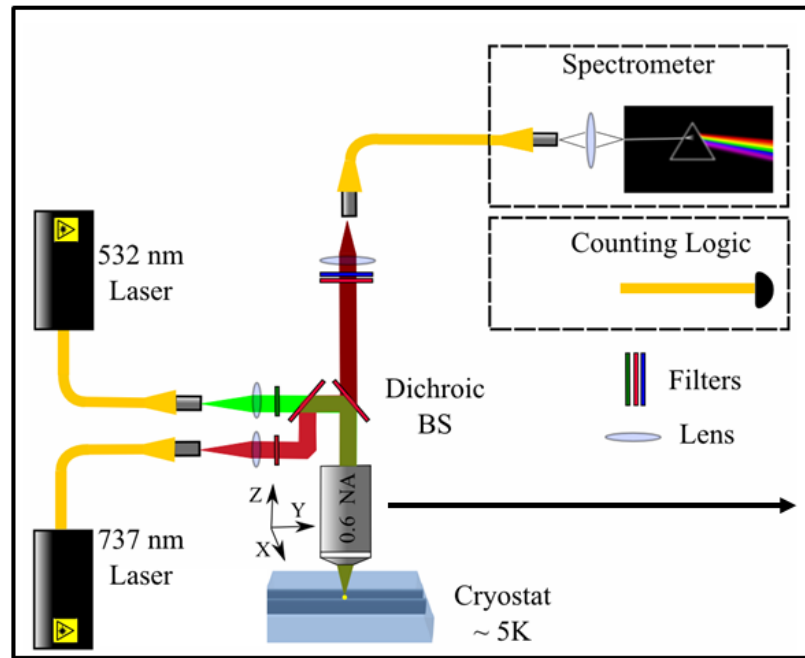


Figure 5.42.: Schematic of the setup used to probe SiV centers in diamond.

5.9.1. Resonant interaction

We excited the SiV resonantly on the transition $|g_i\rangle \rightarrow |e_i\rangle$ ($i=1,2$) using a tunable laser at a wavelength of 737 nm (New Focus Velocity TLB-6700), as shown in Fig. 5.42. The fluorescence from the phonon sideband was collected through the same

objective and measured using a silicon avalanche photo diode. When tuning the wavelength of the excitation laser across the four transitions of the SiV $|g_i\rangle \leftrightarrow |e_i\rangle$ ($i=1,2$) (see Fig. 5.39) the measured fluorescence increases whenever the laser is resonant with a transition. Using this photoluminescence excitation measurement, one can determine the exact wavelength of the individual transitions and, more importantly, the splittings between the energy levels in the ground- and excited state. A typical photoluminescence excitation spectrum of SiV in bulk diamond is shown in Fig. 5.43.

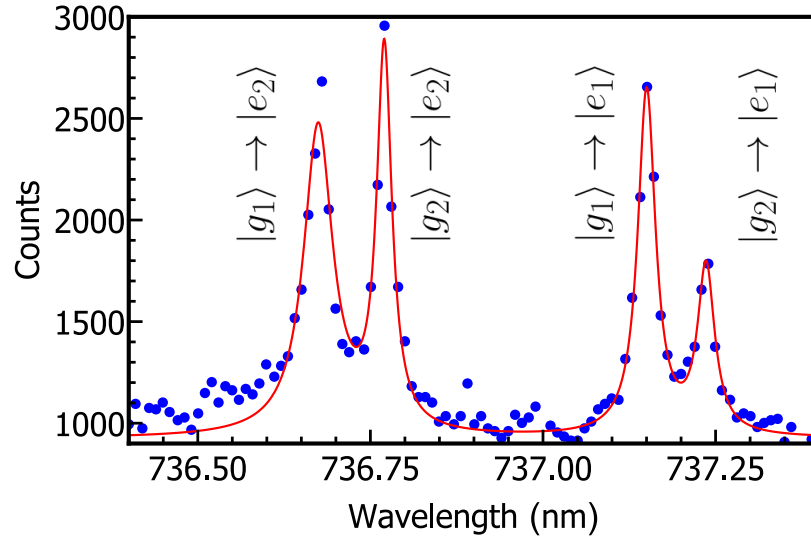


Figure 5.43.: Photoluminescence scan across the four transitions of a SiV center in bulk diamond.

Note that under resonant excitation the SiV can change its charge state and subsequently turn dark. It is possible to reset the charge state using excitation at 532 nm. For the spectrum shown in Fig. 5.43 and for all subsequent measurements, we switched between resonant excitation (160 μ s, 37 μ W cw-power) and charge state resets, i.e. green excitation (45 μ s, 20 μ W cw-power).

5.9.2. Orbital state lifetime measurements

The effect of phonon suppression in small nano pillars can be observed by measuring the lifetime of the upper orbital state $|g_2\rangle$. First, population is transferred from the ground state $|g_1\rangle$ into the upper orbital state via the application of a laser pulse resonant with the transition $|g_1\rangle \rightarrow |e_2\rangle$ (pump pulse in panel a) of Fig. 5.39). As shown in Fig. 5.44 b), population then decays from the excited state $|e_2\rangle$ into either orbital ground state. When pumping long enough (~ 80 ns), most population will be found in the level $|g_2\rangle$. Due to this population inversion, the fluorescence collected from the phonon sideband decreases during the excitation pulse, as shown in Fig. 5.44 c).

To measure the lifetime of the upper orbital state, another pulse (probe pulse in panel a) of Fig. 5.44) is applied on the same transition after a wait time τ . Depending on the wait time and the lifetime of the orbital state, some population will have relaxed back into the ground state, which manifests itself in an increase in fluorescence compared to the steady state fluorescence at the end of the first pulse. The lifetime T_1 can then be extracted by fitting an exponential

$$\frac{A_1}{A_2}(\tau) = 1 + A \exp\left(-\frac{\tau}{T_1}\right) \quad (5.30)$$

to the fraction of the area of the fluorescence signal during first pulse (that created the population inversion) A_1 and the fluorescence signal during the second pulse (that probed the population inversion) A_2 . A is the maximum observed population inversion in percent. Figure 5.45 shows an exemplary decay for a SiV center in bulk

diamond.

In an initial experiment we measured this lifetime in fabricated nanopillars of varying diameter and compared it to the result obtained with a bulk crystal (i.e. in an implanted area on the same chip but far from the fabricated pillars). All measurements were performed at a temperature of 5.8 K. The lifetime of the upper orbital state and its dependence on the pillar diameter is shown in Fig. 5.46. The bulk lifetime is represented as horizontal line. We also show the results of numerical simulations that predict a strong increase in lifetime in the smallest pillars due to phonon suppression. Fig. 5.46 shows clearly that, contrary to our expectations, the lifetime decreases for the smallest pillars. We believe that this trend is caused by imperfections in the crystal lattice surrounding the SiV. Furthermore, due to surface imperfections, there could be increased phonon leakage into the surrounding bulk substrate. To prove phonon suppression in this material, fabrication techniques have to be improved; specifically, the surface roughness of the pillars has to be reduced. In the future, we will pursue two avenues towards that goal. Firstly, we will study thermal annealing methods and determine to what degree they can help to improve the diamond lattice surrounding the SiV after implantation and fabrication of the nanopillars. Secondly, we hope to improve the fabrication process itself by studying different etching gases and by optimizing parameters of the etching step such as gas flow rates and the voltages of the electrodes that create and accelerate the etching plasma. Finally, we will continue to study different geometries, such as inverted pyramids on a diamond substrate that might be better suited to fully suppress phonons.

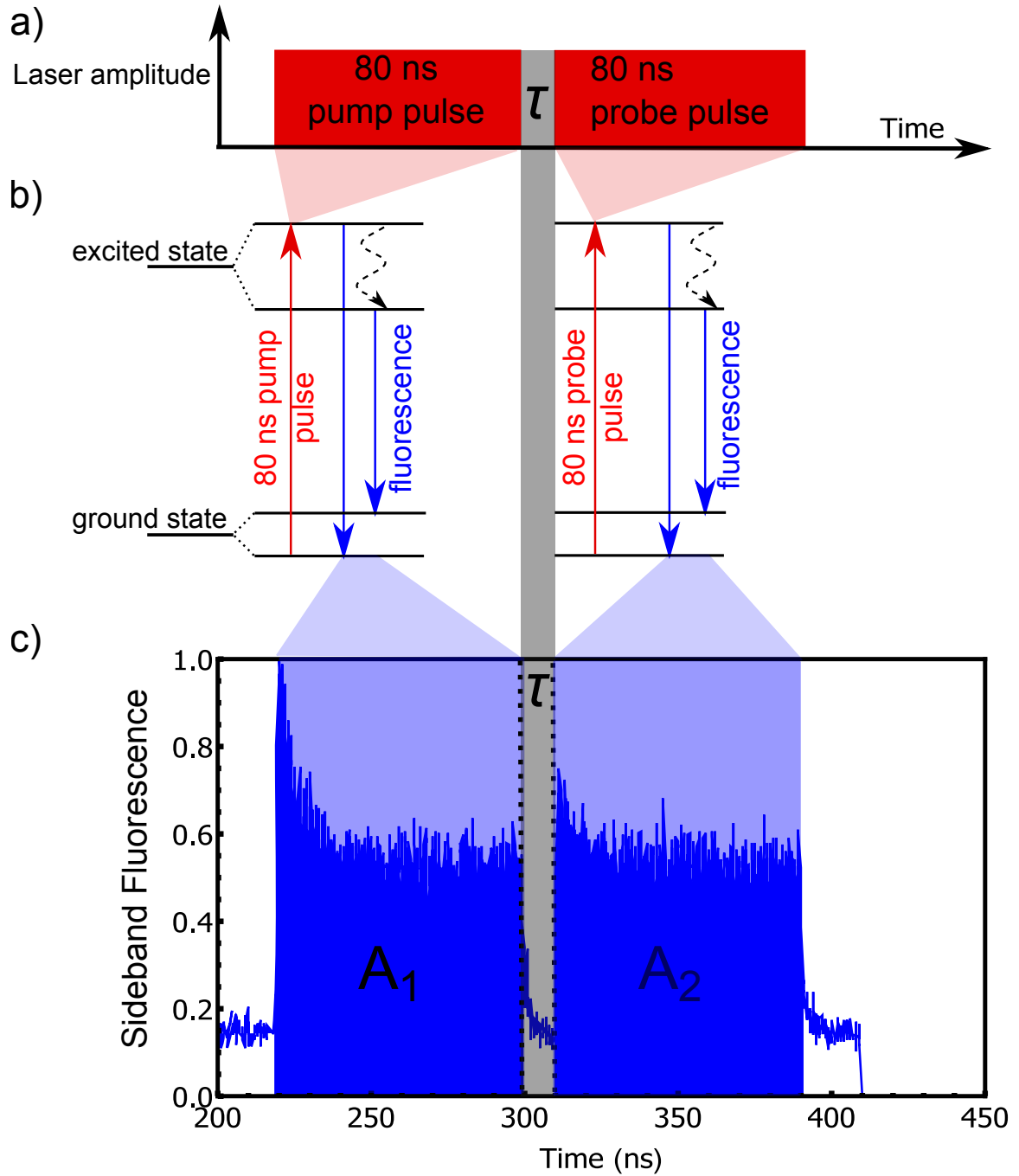


Figure 5.44.: a) Time sequence of the two laser pulses used to extract the orbital state lifetime of a SiV center. b) Simplified energy level structure of the SiV. For lifetime measurements, population is excited from the ground state $|g_1\rangle$ (red arrow) and fluorescence from the two excited states $|e_{1/2}\rangle$ (blue arrows) is collected from the phonon sideband. c) Time-resolved fluorescence collected from the phonon sideband. The pump pulse leads to a population inversion in the ground states that manifests itself in a decreased fluorescence during the second pulse. Due to population relaxation $|g_2\rangle \rightarrow |g_1\rangle$, the fluorescence during the probe pulse will increase with increasing spacing between the pulses τ .

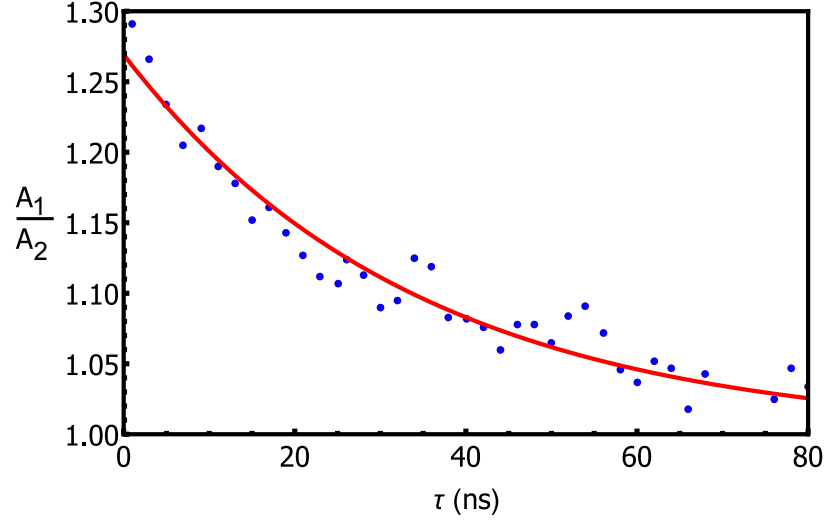


Figure 5.45.: Exemplary decay of the ratio A_1/A_2 for a SiV in bulk diamond. The population lifetime in the upper ground state $|g_2\rangle$ is extracted by a fit of Eq. 5.30.

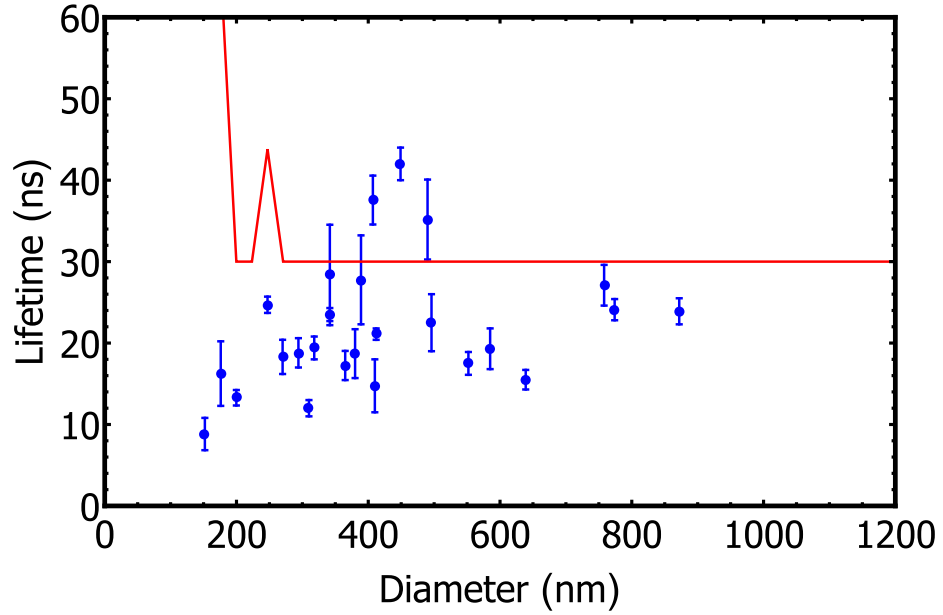


Figure 5.46.: Orbital state ($|g_2\rangle$) lifetime of SiV centers in nano-pillars of different diameters. Experimental data is displayed as blue dots, the red line shows the result of our simulations.

6. Effects of spin inhomogeneity in disordered materials on lifetimes and coherence times

As described in the previous chapter, phonons can influence lifetimes and linewidths in a detrimental way. For spin states, the effect of phonons is strongest at high magnetic fields. At low magnetic fields where the energy splitting between spin states is small, the phonon density of states is sufficiently small so that effects caused by lattice vibrations are not the dominant relaxation mechanisms. Nevertheless, spectroscopic properties of spin states are usually bad at low magnetic fields. This is due to the fact that without the presence of a strong external field, REI spins are more likely to randomly flip and two neighboring REI spins can exchange their orientation (spin flip-flop). Thus, spin lifetimes are limited and spin coherence times are reduced due to the magnetic field fluctuations in the environment of each spin.

It is thus desirable to reduce the interaction between individual REI spins. Reduced interaction would directly decrease the amount of spectral diffusion since each spin is less sensitive to its environment. Second, with decreased interaction between neighboring spins, so-called spin flip-flop processes in which neighboring, resonant ions exchange spin states are expected to happen at a much slower rate. Those flip-flop processes often prevent spectral tailoring at low magnetic fields. For the specific case of erbium-doped materials this is described in Papers 5.1 and 6.1.

The nature of spin flip-flops require the two spins that take part in such a process to be on resonance. In a high-quality crystalline material the spin inhomogeneous broadening is relatively small since the local environment is very similar for each ion and thus it is likely for spins to be on resonance. However, in a disordered host, no long-range crystal lattice is present and thus each ion will see a different local environment. This strongly increases not only the inhomogeneous broadening of the optical transition that can reach up to THz (see Paper 6.1) but also the inhomogeneous broadening of the spin transition. Thus, in a disordered material, it will be less likely to find two neighboring spins whose transition is on resonance compared to a bulk crystal with identical doping concentration. In the following papers, we investigated to which degree a disordered material can inhibit spin flip-flops and thus allow efficient spectral tailoring and enable the corresponding applications using an erbium doped silica fiber.

6.1. Paper 6: Efficient and long-lived Zeeman-sublevel atomic population storage in an erbium-doped glass fiber

Physical Review B. Rapid Communications, **92**, 241111(R), 14 Dec 2015

6.1.1. Summary

Paper 6 shows that in an erbium-doped fiber, efficient spectral tailoring can be performed due to the suppression of spin flip-flops that otherwise make spectral hole burning impossible at low magnetic fields. We demonstrate that up to 80% deep spectral holes that persist for up to 30 seconds can be created. Persistent and deep spectral holes are the prerequisite for applications such as quantum memories and processors for quantum states, both of which have been implemented using one of the fibers investigated in this paper (see [69, 70, 71] and [22] respectively). We identify the states that allow efficient population storage to be electronic Zeeman states and characterize the various processes limiting the latter. Furthermore, a set of parameters (magnetic field, temperature and concentration) that are optimal for spectral hole burning is identified.

The preparation and initial set-up for all experiments mentioned in this paper were performed by Erhan Saglamyurek and myself. The subsequent spectroscopic investigations were performed by the first three authors with equal contributions. Finally, the

data analysis and interpretation was done by Lucile Veissier and myself. Both of us also wrote the first draft of the manuscript with equal contributions.

Erhan Saglamyurek^{1‡}, Thomas Lutz¹, Lucile Veissier^{1†}, Morgan P. Hedges^{1⋈}, Charles
W. Thiel², Rufus L. Cone² and Wolfgang Tittel^{1*}

¹*Institute for Quantum Science and Technology, and Department of Physics &
Astronomy, University of Calgary, Calgary Alberta T2N 1N4, Canada*

²*Department of Physics, Montana State University, Bozeman, MT 59717 USA*

[†] *Present address: Department of Physics, University of Alberta, Edmonton,
Alberta, T6G 2E1, Canada*

[‡] *Present address: Laboratoire Aimé Cotton, CNRS-UPR 3321, Univ. Paris-Sud,
Bât. 505, F-91405 Orsay Cedex, France*

[⋈] *Present address: Department of Physics, Princeton University, Princeton, New
Jersey 08554, USA*

**Corresponding author: wtittel@ucalgary.ca*

Abstract: Long-lived population storage in optically pumped levels of rare-earth ions doped into solids, referred to as persistent spectral hole burning, is of significant fundamental and technological interest. However, the demonstration of deep and persistent holes in rare-earth ion doped amorphous hosts, e.g. glasses, has remained an open challenge since many decades – a fact that motivates our work towards a better understanding of the interaction between impurities and vibrational modes in glasses. Here we report the first observation and detailed characterization of such holes in an erbium-doped silica glass fiber cooled to below 1 K. We demonstrate population storage in electronic Zeeman-sublevels of the erbium ground state with lifetimes up to 30 seconds and 80% spin polarization. In addition to its fundamental

aspect, our investigation reveals a potential technological application of rare-earth ion doped amorphous materials, including at telecommunication wavelength.

Persistent spectral hole burning in cryogenically cooled rare-earth ion (REI) doped solids, the process of transferring atomic population via optical pumping from the ground level of the REI into a long-lived (metastable) level, has been extensively studied for five decades [1, 2]. The observation of persistent holes is of fundamental interest as they allow characterizing the interaction between REIs and their environment, and they find applications in both classical and quantum information processing [3]. Deep, narrow, and long-lived holes have been observed for various REIs doped into crystalline hosts [4, 5, 6]. These holes generally result from population storage in nuclear spin hyperfine levels, or, for REIs having an unpaired electron spin (so-called Kramers ions), in electronic Zeeman sublevels. Compared to REI-doped crystals, REIs in glasses experience much larger inhomogeneity of optical and spin transitions, as well as coupling with inelastic tunneling modes (also referred-to as two-level systems – TLS) [7, 8, 9] that results in significantly different decoherence and population relaxation properties. Persistent population transfer due to coupling with TLS, photochemical hole burning, and using spin states have been reported more than two decades ago [10, 11, 12], but the interaction between REIs and vibrational modes in amorphous media – the generalization of the well-known phonons that are present in crystals – is still not well understood. Furthermore, the observed holes have been shallow or hundreds of MHz wide, making them unlikely to be suitable for information processing applications.

6.1.2. Introduction

An exception is the erbium-doped fiber that we have used recently for quantum state storage [13, 14]. The goal of the present paper is to detail its hole-burning mechanism. We observe deep, persistent holes with 15 MHz width (limited by power-broadening) and lifetimes approaching a minute that arise from population redistribution among the Zeeman-split electronic sublevels of the Er^{3+} ground state. This improves upon the properties observed before for REI-doped glasses in terms of spin polarization (i.e. hole depth) and spectral width [15, 12]. We furthermore characterize the dependence of the spin relaxation rate on magnetic field, temperature, wavelength, and erbium ion concentration. This allows us to determine the processes responsible for electron spin state relaxation in this amorphous medium and provides the necessary information to optimize operation parameters for practical applications.

Except where mentioned otherwise, our experiments employ a commercially available, 20 m-long silica fiber co-doped with 190 ppm erbium (INO S/N 404-28252). The fiber is cooled to temperatures T as low as 0.65 K using an adiabatic demagnetization refrigerator, and a magnetic field B of up to 0.25 T that lifts the Kramers degeneracy of the ground and excited electronic levels, splitting each into two Zeeman sublevels. We burn spectral holes into the erbium ions' inhomogeneously broadened $^4I_{15/2} \leftrightarrow ^4I_{13/2}$ zero phonon line using 500 ms long laser pulses with a peak power of 1-5 μW derived from a narrowband, intensity-modulated, continuous wave laser operating, except where otherwise specified, at 1532 nm wavelength. After a variable waiting time that exceeds the 11 ms excited state lifetime, we probe the absorption

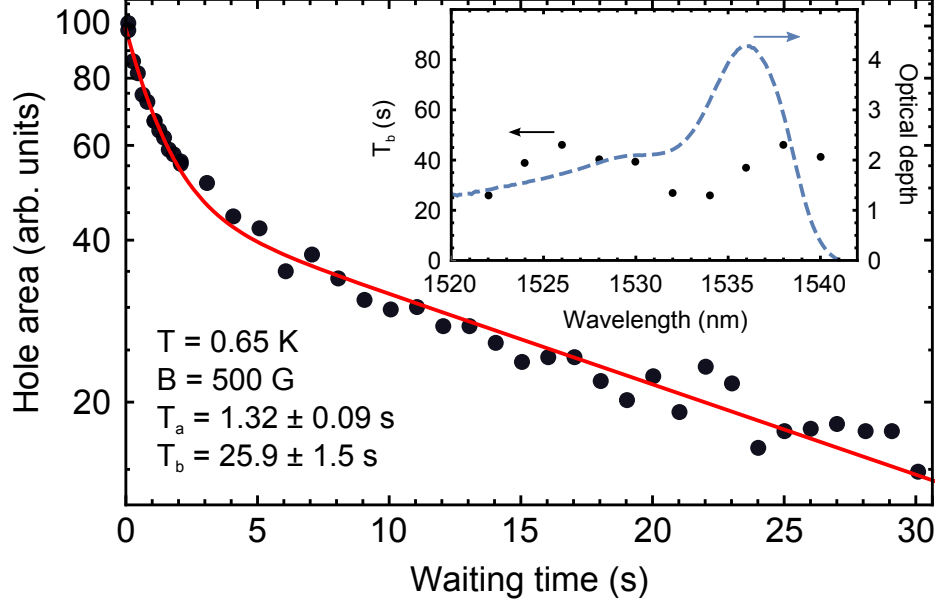


Figure 6.1.: Spectral hole area as a function of the waiting time for $B = 500 \text{ G}$ and $T = 0.65 \text{ K}$. The experimental data is fitted by the sum of two exponential decays with characteristic times $T_a = 1.32 \pm 0.09 \text{ s}$ and $T_b = 25.9 \pm 1.5 \text{ s}$. The inset shows the fiber absorption profile at $T = 0.8 \text{ K}$ (dashed blue line) and the hole lifetime T_b for various wavelengths (black dots).

profile by linearly chirped the frequency of the laser light over 500 MHz across the generated hole. The 1 ms-long scans are implemented using a phase modulator driven by a serrodyne signal [16]. Depending on the experimental conditions, we observe persistent spectral holes with line widths as narrow as 15 MHz, including the effect of power broadening. However, from coherence lifetime measurements, we know that homogeneous linewidths as narrow as a few MHz can be achieved in our fiber [17]. By measuring the area of the spectral hole with respect to the waiting time, we characterize the decay dynamics of the spectral hole and extract the underlying population relaxation processes.

First, we determine the decay dynamics for persistent holes, with a typical example shown in Fig. 6.1. We find that all decays, for temperatures ranging from 0.65 to

3.5 K and magnetic fields from 0 to 0.25 T, can be described by two exponential functions with similar weights and decay times (T_a) on the order of a second and (T_b) on the order of a few tens of seconds. This observation could indicate the presence of two different classes of erbium ions in the fiber, or could result from the average over a non-uniform, continuous distribution of decays corresponding to ions with different spin-state lifetimes. In addition, we characterize the wavelength dependence of the persistent hole lifetimes T_b at a temperature of 0.8 K; see inset of Fig. 6.1. We observe long-lived spectral holes with comparable lifetimes across the entire THz-wide inhomogeneous absorption line.

Second, we assess the efficiency of the hole burning mechanism, which we define as the maximum degree of spin polarization. It characterizes how deep a persistent spectral hole can be burnt. Spectral holes with absorption reduced by as much as 80% compared to the optical depth of the erbium-doped fiber before spectral hole burning were observed at $T = 0.7$ K, and with a probing delay of 50 ms. Furthermore, as the temperature rises from 0.7 to 3.5 K, the hole depth decreases linearly. In consequence, we extrapolate that it is, at least in principle, possible to burn a 100% deep hole at an optimal temperature of 0 K. This fact alone excludes population redistribution via the TLS mechanism, as the latter generally only allows for persistent holes with a maximum depth of 50%, and typically much less – even at $T = 0$ K [18]. Furthermore, given the width of the observed holes and the small intensity used to create them, we can also exclude photochemical hole burning.

6.1.3. Hole burning mechanism and limiting processes

An unambiguous way to confirm our hypothesis of Zeeman level storage as the hole burning mechanism would be to burn one narrow spectral hole, observe the regions of increased absorption due to population redistribution, i.e. anti-holes, and extract their magnetic field-dependent shift. However, this was not possible in our case due to the disorder in the amorphous material, which leads to very broad anti-holes that cannot be resolved. To indirectly verify the presence and positions of these anti-holes, we employ a novel method that is based on burning a wide hole and measuring its depth as a function of magnetic field. The results for a 200 MHz-wide hole are shown in Fig. 6.2. As the field decreases, the anti-holes begin to overlap with the central hole, causing it to become more shallow (due to the first-order electronic Zeeman splitting, the frequency shift between the hole and anti-hole depends linearly on the magnetic field strength). Modeling the hole and the anti-holes with Lorentzians of magnetic field-dependent width and position, we can predict the change in hole-depth as a function of the magnetic field, see Fig. 6.2. This allows estimating a mean hole/anti-hole splitting of 25 GHz/T, which is comparable to the values typically measured in erbium doped crystals [19, 20]. This further supports our conclusion of population storage in Zeeman levels. We also find that the anti-hole width is about six times larger than the splitting between hole and anti-hole, which reflects the large inhomogeneous broadening of the Zeeman transition in the fiber, as discussed earlier. To gain insight into the relaxation mechanisms that determine the observed spin lifetimes as well as to identify optimal conditions for potential applications based on

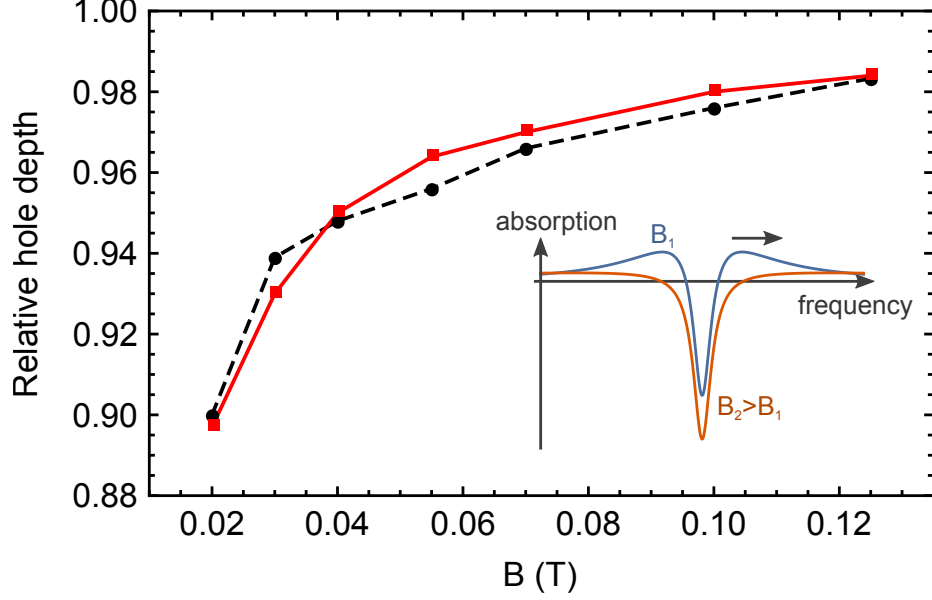


Figure 6.2.: Magnetic field dependent depth of a 200 MHz-wide hole normalized to the depths of a 100 MHz-wide hole at each field, which is not significantly affected by population transfer from an anti-hole. Please note that the absolute hole depth of a narrow hole decreases at $B > 0.06$ T due to decreasing lifetimes, as shown in Fig. 6.5 c). Experimental data is shown by black dots; simulated results are in red.

persistent spectral hole burning, we experimentally and theoretically study magnetic field and temperature dependence of hole decay rates (the inverse of the hole lifetime); examples of the experimental data are shown in Figs. 6.10 and 6.9. We note that the two decay components T_a and T_b exhibit very similar behavior as a function of magnetic field and temperature for the assessed range of parameters. Given the difficulty of measuring the longer Zeeman lifetime T_b with high precision at high temperature, we consider only the fast decay component T_a in the following analysis. To describe our experimental data, we develop a model based on the framework proposed in [21] for an Er:Y₂SiO₅ crystal, but adapt it to an amorphous host, in which the Debye model of phonons is not applicable and has to be replaced by TLS

and local vibrational modes. We assume the spin relaxation rate to be described by

$$\frac{1}{T_{a/b}} = \frac{\alpha_1}{\Gamma_S^0 + \gamma B} \text{sech}^2 \left(\frac{g\mu_B B}{2kT} \right) + \alpha_2 B^l T^m + \alpha_3 T^n. \quad (6.1)$$

The first term corresponds to the average mutual spin flip-flop rate due to magnetic dipole-dipole interactions between erbium ions, with g the g -factor of the Er ions, μ_B the Bohr magneton and k the Boltzmann constant. We assume $g = 9$, which is consistent with averaging over all possible direction-dependent values, ranging from 0 to 18 [22, 23, 24, 25, 26, 27]. Provided the erbium ions are uniformly distributed, the coefficient α_1 scales quadratically with Er concentration (we will examine this assumption below). In addition, the spin flip-flop term includes broadening of the inhomogeneous linewidth Γ_S of the spin transition with magnetic field, i.e. $\Gamma_S = \Gamma_S^0 + \gamma B$. This also leads to the anti-hole broadening discussed in the previous analysis, from which we extracted $\gamma = 6 \times 25 \text{ GHz/T}$.

The second term describes the direct coupling between Er ions and resonant, thermally-driven vibrational or TLS modes of the glass matrix. While this effect is in some ways analogous to the coupling with phonons in crystals, one cannot expect it to have the same dependence on the magnetic field and temperature due to a different density of states of vibrational modes in the amorphous medium [28]. We therefore include free parameters l and m in Eq. 6.8.

The third term describes the process where the Er ion relaxes through higher-energy vibrational or TLS modes of the glass via a second-order Raman-type interaction. It is equivalent to the phonon mediated inelastic Raman relaxation in crystals, which

involves two off-resonant vibrational modes. In the case of a crystal doped with a Kramers ion such as erbium, the Raman process scales as T^9 [29]; however, since the density of states of vibrational modes might be very different in the fiber, the temperature dependence of the Raman process is described by the free parameter n .

g	9	l	1 ± 0.1
γ (GHz/T)	150	m	1.2 ± 0.2
Γ_S^0 (GHz)	1.3 ± 0.2	n	3 ± 0.5
$1/T_a$	α_1	α_2	α_3
fiber 1	3.80 ± 0.2	12.4 ± 0.5	0.06 ± 0.01
$1/T_b$	fiber 1	fiber 2	fiber 3
α_1	0.160 ± 0.2	0.234 ± 0.2	1.67 ± 0.2
α_2	0.72 ± 0.5	0.82 ± 0.5	4.7 ± 0.5

Table 6.1.: Parameters for Eq. 6.8 to fit the experimental data, with α_1 in 10^9 s^{-2} , α_2 in $\text{Hz T}^{-1} \text{ K}^{-1}$ and α_3 in Hz T^{-4} .

By iteratively fitting Eq. 6.8 to several subsets of experimental data, we obtain the single set of parameters given in Table 6.2 that allows describing all experimental data. The good agreement is exemplified with the two datasets shown in Figs. 6.9 and 6.10. We note that the value for the inhomogeneous line width at zero field, Γ_S^0 , exceeds the value for REI-doped crystals by several orders of magnitude [30, 31, 32]. While we have no explanation yet for why $l=1$, we note that it is not possible to attribute this dependence to a direct-phonon-type process as observed in crystals because such a process must scale at least quadratically [29] with the magnetic field. This argument is based on the assumption that the phonon density of states is not decreasing with frequency, which is correct for silica glass at our temperatures [33]. Furthermore, we find that the fitted value for m , describing the temperature-dependent part of the coupling to TLS, is consistent with values that allow modeling coherence properties

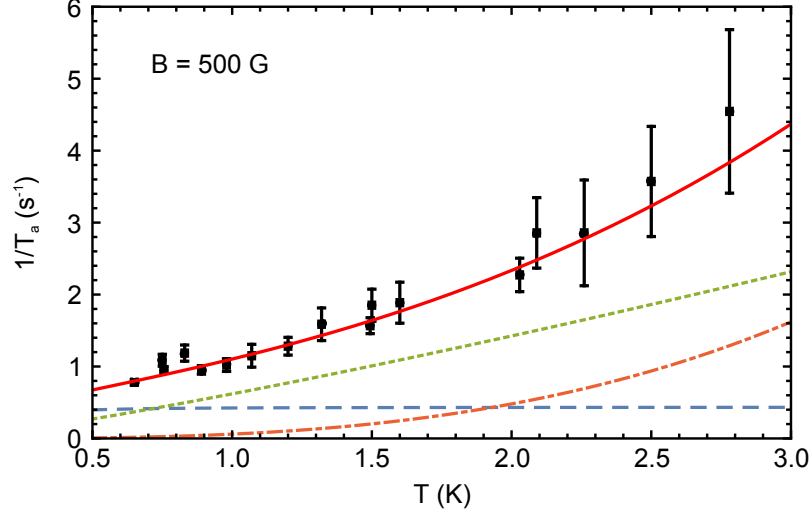


Figure 6.3.: Spin relaxation rate $1/T_a$ as a function of temperature at $B = 500$ G. The dashed lines correspond to the different terms of Eq. 6.8: the Er-Er coupling (blue dashed), the direct process (green dotted), and the Raman process (orange dashed dotted).

in REI-doped glasses [12, 22, 34], and that a difference of n from the value in crystals (i.e. $n_{crystal}=9$) has also been observed in nanometer size particles [35].

Let us now have a look how the interplay of the three different processes in Eq. 6.8 – represented as individual lines in Figs. 6.10 and 6.9 – determines the lifetime of the spectral hole. Fig. 6.10 shows that the decay rate increases monotonically with temperature, and that, for higher temperature, it is dominated by the Raman-type interaction. Furthermore, Fig. 6.9 shows that spin flip-flops, i.e. the exchange of spin states between neighboring, resonant erbium ions through magnetic dipole-dipole interactions, dominate the decay rate at small magnetic fields and 0.8 K. However, the contribution of this process decreases rapidly as the field is increased due to the additional inhomogeneous broadening described by γB , i.e. a decreasing probability for neighboring ions to be resonant. For higher fields, the decay rate is dominated by coupling to thermally-driven TLS and vibrational modes. Hence, for long-lived

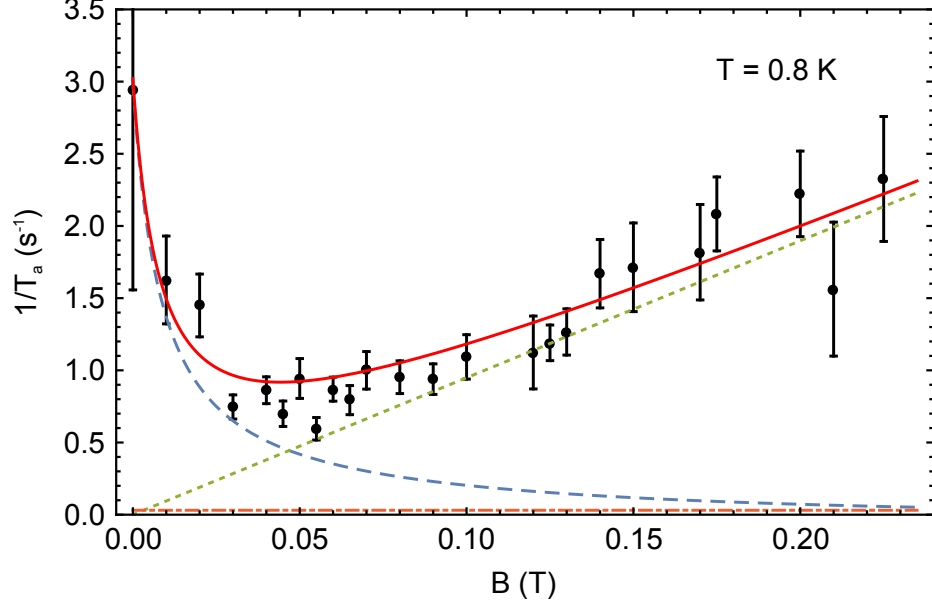


Figure 6.4.: Dependence of the rate $1/T_a$ on the magnetic field at $T = 0.8$ K. The solid line shows the theoretical prediction of Eq. 6.8 with the set of parameters in Table 6.2, and the dashed and dotted lines correspond to the individual terms (first term: blue dashed, second term: green dotted, third term: orange dashed dotted).

holes, it is always beneficial to work at the lowest possible temperature, but there is an optimum magnetic field. For our fiber, the best value for T_a is obtained at 0.65 K and around 500 G.

6.1.4. Concentration dependence

Next, we characterize and compare the magnetic field dependence of the long decay rates T_b at $T = 0.8$ K for three fibers of different Er-doping concentration: fiber 1 (the same as in the investigations described above) – 190 ppm (INO S/N 404-28252), fiber 2 – 200 ppm (INO S/N 402-28254) and fiber 3 – 1200 ppm (INO S/N 502-28255). Fig. 6.5 b) shows the absorption profiles for the three fibers. The profiles for the two low-concentration fibers (fiber 1 and 2) differ greatly, which we attribute

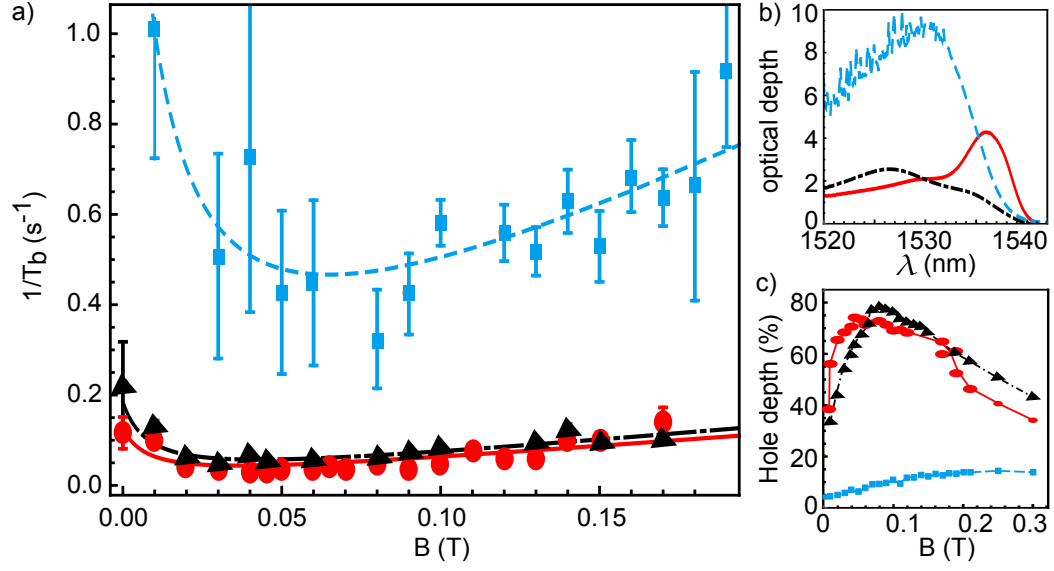


Figure 6.5.: a) Dependence of the rate $1/T_b$ on the magnetic field for fibers with different erbium doping concentrations and lengths. b) Absorption profiles of the three fibers. c) Hole depth as a function of magnetic field. All measurements are taken at 0.8 K, at 1532 nm for fibers 1 and 2, and at 1536 nm for fiber 3. Red: fiber 1 (190 ppm, 20 m), black: fiber 2 (200 ppm, 10 m), blue: fiber 3 (1200 ppm, 3 m).

to a difference in the co-dopants, and those of fiber 2 and 3, which features a very different erbium concentration, are comparable, suggesting similar co-dopants. The results of the rate measurements are shown in Fig. 6.5 a). We emphasize that the rates for fibers 1 and 2, which feature almost identical Er ion concentrations, are very similar over the entire range of magnetic field strength. Contrary to what one might expect, this seems to suggest that the spectral hole burning properties are not much affected by the co-dopants. However, comparing with the data obtained for fiber 3, we find that the decay rates strongly depend on the erbium doping concentration. To fit the data, we therefore include the concentration dependence only into α_1, α_2 and α_3 , and we assume that the spin inhomogeneous broadening, characterized by Γ_S^0 and γ , is the same for the three fibers.

As shown in Table 6.2, we find that the value for α_1 increases with Er doping concentration, which is consistent with the assumption that the first term in Eq. 6.8 describes spin flip flops. The concentration dependence of α_2 suggests that the dominant relaxation mechanism at high magnetic fields is through spin-elastic TLS involving motion of Er ions rather than simple vibrational modes of glass – or TLS modes created by Er ions [22]. For conclusive information about the scaling of these parameters, more investigations using fibers with other doping concentrations are needed. Furthermore, we find that the third term does not contribute to the decay rates measured at 0.8 K. Finally, we assess the quality of the spectral hole burning in terms of the hole depth for these three fibers after 50 ms waiting time and at $T = 0.8$ K – the results are shown in Fig. 6.5 c). We find that the erbium ion concentration has a direct impact on the hole depth – the smaller the concentration, the deeper the hole, which is due to reduced spin flip flops. Furthermore, we see that the optimum magnetic field also depends on the doping concentration, which is a consequence of the change in relative importance of the spin flip-flop process versus coupling with TLS.

6.1.5. Conclusion

In conclusion, we established the existence of long-lived, narrow and deep persistent spectral holes generated via spin-level storage in a rare-earth-ion doped amorphous host material. More precisely, using a weakly doped silica fiber under an optimized magnetic field, we observed population storage in electronic Zeeman levels of erbium ions with lifetimes approaching a minute. We furthermore developed a model that

identifies lifetime-limiting mechanisms, in particular spin flip-flops at low magnetic fields and coupling to TLS and vibrational modes at high fields. The model shows that the use of an amorphous host, which results in large spin inhomogeneous broadening, and low doping concentration leads to small spin flip-flop rates even at low magnetic fields, and hence to the possibility of observing deep and long-lived spectral holes. Our study shines light on the fundamental interaction between impurities and vibrational modes in glasses, which, as opposed to crystals, is still not well understood. Furthermore, our findings allow parameter optimization in future applications of persistent spectral hole burning, including optical quantum memories, photonic processors, configurable filters, and long-lived optical storage elements for fiber-optic communication. We emphasize that our investigations have been carried out on the 1532 nm transition in erbium, which opens these applications to the convenient telecommunication c-band.

Acknowledgements

The authors thank Daniel Oblak, Neil Sinclair, and Roger Macfarlane for discussions, and acknowledge support from Alberta Innovates Technology Futures (ATIF), the National Engineering and Research Council of Canada (NSERC), and the National Science Foundation of the USA (NSF) under award nos. CHE-1416454 and PHY-1415628. W.T. is a senior fellow of the Canadian Institute for Advanced Research (CIFAR).

E.S., T.L. and L.V. contributed equally to this work.

Bibliography

- [1] R. M. Macfarlane and R. M. Shelby, in *Modern Problems in Condensed Matter Sciences*, vol. 21 of *Spectroscopy of Solids Containing Rare Earth Ions*, A. A. Kaplyanskii and R. M. Macfarlane, eds. (Elsevier, 1987), pp. 51–184.
- [2] Y. C. Sun, in *Spectroscopic Properties of Rare Earths in Optical Materials*, P. R. Hull, P. J. Parisi, P. R. M. O. Jr, P. H. Warlimont, D. G. Liu, and P. B. Jacquier, eds. (Springer Berlin Heidelberg, 2005), no. 83 in Springer Series in Materials Science, pp. 379–429.
- [3] M. Nilsson, L. Rippe, N. Ohlsson, T. Christiansson, and S. Kröll, *Physica Scripta* **2002**, 178 (2002).
- [4] R. M. Macfarlane and J. C. Vial, *Physical Review B* **36**, 3511 (1987).
- [5] S. R. Hastings-Simon, M. Afzelius, J. Minar, M. U. Staudt, B. Lauritzen, H. de Riedmatten, N. Gisin, A. Amari, A. Walther, S. Kröll, E. Cavalli, and M. Bettinelli, *Physical Review B* **77**, 125111 (2008).

- [6] F. Könz, Y. Sun, C. W. Thiel, R. L. Cone, R. W. Equall, R. L. Hutcheson, and R. M. Macfarlane, Physical Review B **68**, 085109 (2003).
- [7] P. M. Selzer, D. L. Huber, D. S. Hamilton, W. M. Yen, and M. J. Weber, Physical Review Letters **36**, 813 (1976).
- [8] M. M. Broer, B. Golding, W. H. Haemmerle, J. R. Simpson, and D. L. Huber, Physical Review B **33**, 4160 (1986).
- [9] K. A. Littau, M. A. Dugan, S. Chen, and M. D. Fayer, The Journal of Chemical Physics **96**, 3484 (1992).
- [10] J. M. Hayes, and G. J. Small, Chemical Physics Letters **54**, 435-438 (1978).
- [11] R. Jankowiak, J. M. Hayes, and G. J. Small, Chemical Reviews **93**, 1471 (1993).
- [12] T. Schmidt, R. M. Macfarlane, and S. Völker, Physical Review B **50**, 15707 (1994).
- [13] E. Saglamyurek, J. Jin, V. B. Verma, M. D. Shaw, F. Marsili, S. W. Nam, D. Oblak, and W. Tittel, Nature Photonics **9**, 83-87 (2015).
- [14] J. Jin, E. Saglamyurek, M. Grimaud Puigibert, V. B. Verma, F. Marsili, S. W. Nam, D. Oblak, and W. Tittel, Physical Review Letters **115**, 140501 (2015)
- [15] R. Macfarlane and R. Shelby, Journal of Luminescence **36**, 179 (1987).
- [16] L. M. Johnson and C. H. Cox, Journal of Lightwave Technology **6**, 109 (1988).

- [17] L. Veissier, M. Falamarzi, T. Lutz, E. Saglamyurek, C. W. Thiel, R. L. Cone, and W. Tittel, *Physical Review B* **94**, 195138 (2016)
- [18] J. M. Hayes and G. J. Small, *Chemical Physics* **27**, 151 (1978).
- [19] T. Böttger, Y. Sun, C. W. Thiel, and R. L. Cone, *Physical Review B* **74**, 075107 (2006).
- [20] S. R. Hastings-Simon, B. Lauritzen, M. U. Staudt, J. L. M. van Mechelen, C. Simon, H. de Riedmatten, M. Afzelius, and N. Gisin, *Physical Review B* **78**, 085410 (2008).
- [21] T. Böttger, C. W. Thiel, Y. Sun, and R. L. Cone, *Phys. Rev. B* **73**, 075101 (2006).
- [22] R. M. Macfarlane, Y. Sun, P. B. Sellin, and R. L. Cone, *Phys. Rev. Lett.* **96**, 033602 (2006).
- [23] M. U. Staudt, S. R. Hastings-Simon, M. Afzelius, D. Jaccard, W. Tittel, and N. Gisin, *Optics Communications* **266**, 720 (2006).
- [24] I. Kurkin and K. Chernov, *Physica B+C* **101**, 233 (1980).
- [25] T. Böttger, “Laser frequency stabilization to spectral hole burning frequency references in erbium-doped crystals: Material and device optimization”, Ph.D. thesis (2002).
- [26] D. M. B. P. Milori, I. J. Moraes, A. C. Hernandez, R. R. de Souza, M. S. Li, M. C. Terrile, and G. E. Barberis, *Physical Review B* **51**, 3206 (1995).

- [27] M. Ball, G. Garton, M. J. M. Leask, D. Ryan, and W. P. Wolf, *Journal of Applied Physics* **32**, S267 (1961).
- [28] U. Buchenau, M. Prager, N. Nücker, A. J. Dianoux, N. Ahmad, and W. A. Phillips, *Physical Review B* **34**, 5665 (1986).
- [29] R. Orbach, *Proceedings of the Royal Society of London. Series A. Mathematical and Physical Sciences* **264**, 458 (1961).
- [30] E. Fraval, M. J. Sellars, and J. J. Longdell, *Physical Review Letters* **95**, 030506 (2005).
- [31] S. Probst, H. Rotzinger, S. Wünsch, P. Jung, M. Jerger, M. Siegel, A. V. Ustinov, and P. A. Bushev, *Physical Review Letters* **110**, 157001 (2013).
- [32] P. Jobez, C. Laplane, N. Timoney, N. Gisin, A. Ferrier, P. Goldner, and M. Afzelius, *Physical Review Letters* **114**, 230502 (2015).
- [33] R. Haworth, G. Mountjoy, M. Corno, P. Ugliengo, and R. J. Newport, *Phys. Rev. B* **81**, 060301 (2010).
- [34] Y. Sun, R. L. Cone, L. Bigot, and B. Jacquier, *Optics Letters* **31**, 3453 (2006).
- [35] R. S. Meltzer and K. S. Hong, *Physical Review B* **61**, 3396 (2000).

6.2. Coherence limiting two-level systems

As described in the previous sections, disordered host materials can make spectral hole burning in REIs possible due to the increased spin inhomogeneous broadening. However, in terms of the minimum achievable homogeneous linewidths, disordered materials generally have worse properties compared to crystalline hosts. Paper 7 (chapter 6.3) shows that the narrowest measured homogeneous linewidth in our erbium doped glass fiber is $\sim 1\text{MHz}$ compared to 73 kHz in an erbium doped Y_2SiO_5 crystal [72]. It is known that in glassy hosts so-called two-level systems (TLS) or local vibrational modes strongly limit coherence lifetimes. These TLS couple to the REI spins and thus cause rapid spectral diffusion that results in broad homogeneous lines and fast decoherence.

Already more than 30 years ago, the concept of TLS has been used to describe phenomena related to the specific heat in amorphous materials at low temperature [73]. Since then, there have been many efforts to develop a theory that describes how TLS affect spins of REIs and contribute to decoherence in a microscopic way. Up to now, however, there is no model available that describes all observed phenomena such as the temperature or magnetic field dependence of TLS-driven decoherence in a universal way. Therefore, this section will omit an in-depth theoretical treatment and will only provide a brief introduction to TLS and concentrate on how TLS are responsible for spectral diffusion. A detailed review on theoretical and experimental investigations on TLS can be found in [74] and, more recently, in [75]

TLS can be understood as two possible arrangements of the local environment (i.e. the molecules that form the disordered host) of a REI. Due to the two possible arrangements, the potential energy of the system has two minima in which the system is temporarily stable, hence the term two-level system. Since the temperature of the sample is not zero, the system can tunnel from one minimum into the other.

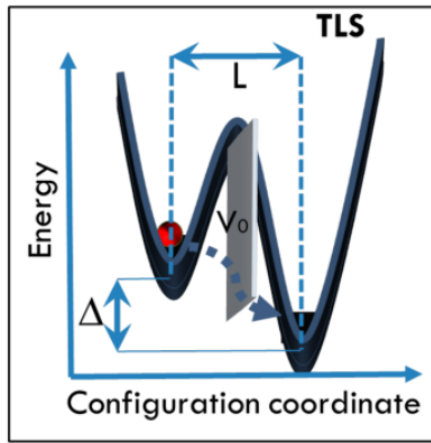


Figure 6.6.: Schematic of a TLS with barrier height V_0 , well separation L and energy difference Δ .

The tunneling rate depends on the barrier height V_0 , well separation L , the difference in energy Δ and the sample temperature. As observed in the measurements presented in Paper 7 (chapter 6.3) the tunneling rate can also be influenced by an external magnetic field. The different models are mostly distinguished by their assumption on the distributions of barrier height, and energy differences. With a given distribution of TLS tunneling rates R and energy differences $E = \sqrt{\Delta^2 + L^2}$ between the eigenstates of the double well one can then compute the contribution of all TLSs to spectral

diffusion-based broadening the homogeneous linewidth [76]

$$\Gamma_h^{TLS}(T, t) \propto \int_0^{E_{max}} \text{sech}^2\left(\frac{E}{2k_B t}\right) \int dR P(R, E) (1 - e^{-Rt}) dE. \quad (6.2)$$

Early models [76] resulted in the correct, logarithmic time-dependence of the homogeneous linewidth but predicted a linear temperature dependence whereas experiments resulted in $\Gamma_h^{TLS} \propto T^{1+\nu}, \nu < 1$. It was shown by Silbey *et al.* that the correct temperature dependence can be achieved using modified distributions for the barrier height and energy difference [75].

Since TLS are a material property and inevitably linked to the amorphous nature of the host, they pose strict limitations on the use of disordered hosts for quantum memories or any application requiring long coherence times. However, due to their broad inhomogeneous absorption profile and capability to enable spectral tailoring using spin states, specifically in the case of erbium, these materials can still be useful for broadband light-matter interfaces and quantum memories with short storage times. Furthermore, TLS-driven decoherence can in principle be reduced by cooling the medium to a lower temperature.

6.3. Paper 7: Optical decoherence and spectral diffusion in an erbium-doped silica glass fiber featuring long-lived spin sublevels

Physical Review B, **94**, 195138, 21 Nov 2016

6.3.1. Summary

The ultimate goal of our research on the erbium doped fibers presented in the previous sections was to determine if it can be used to implement a broadband light-matter interface that can be used to store qubits at telecom wavelengths around 1550 nm. After we showed how to optimize spectral tailoring in this material, this paper investigates the coherence properties and the processes limiting the latter. We measured coherence times and spectral diffusion and mapped out their dependence on temperature, magnetic field and concentration. These measurements allowed us to determine the parameters under which coherence times are optimal. It was found that those parameters coincide with the ones that are optimal for spectral tailoring. In particular, we found that at temperatures around 700 mK and magnetic fields around 500 Gauss, spectral features persist for up to 30 seconds and can be as narrow as 1 MHz (corresponding to $T_2 = 0.3 \mu\text{s}$). This made it possible to use the erbium doped fiber as a quantum memory for photons at telecom wavelengths [69, 70, 71].

Furthermore, the manuscript includes a detailed model describing the various pro-

cesses, including TLSs, contributing to the linewidth broadening. The model combines the semi-empirical framework developed for amorphous hosts (see Eq. 6.2) and the theory describing spectral diffusion in erbium doped crystals [42] and successfully reproduced the experimental data.

The experiments presented in this manuscript were performed by the first three authors with equal contribution. Lucile Veissier and I developed the model describing the experimental data. Lucile focused on the part describing spectral diffusion in erbium doped crystals whereas I concentrated on the explanation of spectral diffusion caused by TLSs. The first draft of the manuscript was written by Lucile Veissier and myself.

**Optical decoherence and spectral diffusion in an erbium-doped silica
glass fiber featuring long-lived spin sublevels**

Lucile Veissier^{1†}, Mohsen Falamarzi¹, Thomas Lutz¹, Erhan Saglamyurek^{1‡}, Charles

W. Thiel², Rufus L. Cone², Wolfgang Tittel¹

¹*Institute for Quantum Science and Technology, and Department of Physics &
Astronomy, University of Calgary, Calgary Alberta T2N 1N4, Canada*

²*Department of Physics, Montana State University, Bozeman, MT 59717 USA*

[†]*Present address: Laboratoire Aimé Cotton, CNRS-UPR 3321, Univ. Paris-Sud,
Bât. 505, F-91405 Orsay Cedex, France*

[‡] *Present address: Department of Physics, University of Alberta, Edmonton,
Alberta, T6G 2E1, Canada*

**Corresponding author: thomasl@ucalgary.ca*

Abstract: Understanding decoherence in cryogenically-cooled rare-earth-ion doped glass fibers is of fundamental interest and a prerequisite for applications of these material in quantum information applications. Here we study the coherence properties in a weakly doped erbium silica glass fiber motivated by our recent observation of efficient and long-lived Zeeman sublevel storage in this material and by its potential for applications at telecommunication wavelengths. We analyze photon echo decays as well as the potential mechanisms of spectral diffusion that can be caused by coupling with dynamic disorder modes that are characteristic for glassy hosts, and by the magnetic dipole-dipole interactions between Er^{3+} ions. We also investigate the effective linewidth as a function of magnetic field, temperature and time, and then

present a model that describes these experimental observations. We highlight that the operating conditions (0.6 K and 0.05 T) at which we previously observed efficient spectral hole burning coincide with those for narrow linewidths (1 MHz) – an important property for applications that has not been reported before for a rare-earth-ion doped glass.

6.3.2. Introduction

Cryogenically-cooled rare-earth-ion (REI) doped materials offer unique spectroscopic properties, such as narrow optical linewidths and long-lived shelving levels that allow for spectral tailoring of their inhomogeneously broadened absorption lines. These properties are required simultaneously in order to implement many of the potential applications of REI-doped materials, including optical quantum memories [1, 2], as well as classical and quantum signal processing [3, 4]. Compared to crystals, the properties of REI's in amorphous hosts are generally very different because of the intrinsic disorder of the environment. This disorder comes with some advantages, in particular larger inhomogeneous broadening that is required for high-bandwidth or spectrally multiplexed applications. Furthermore, the increased inhomogeneous broadening of electron and nuclear spin transitions can inhibit spin diffusion that leads to decoherence [5]. This reduction was a key factor in our recent observation of efficient optical pumping into Zeeman sublevels with spin lifetimes reaching 30 s in an erbium-doped fiber [6]. However, in addition to long-term storage mechanisms, another prerequisite for the above-mentioned applications is a narrow homogeneous

linewidth. REI-doped amorphous materials generally exhibit much larger homogeneous linewidths at liquid helium temperatures compared to REI-doped crystalline hosts due to interactions with dynamic fluctuations in the environment that are traditionally modeled as bistable two-level systems (TLS) [7, 8].

Motivated by our recent observation of slow spin relaxation [6] in a weakly-doped erbium-doped fiber that has allowed storing members of entangled photon pairs [9], we now investigate coherence properties of such a fiber with special attention to the regime of low magnetic fields where long Zeeman lifetimes were observed. More precisely, we report the magnetic field and temperature dependence of the optical coherence using two pulse photon echo (2PPE) and three pulse photon echo (3PPE) techniques. The fiber studied here has very similar composition and Er-doping concentration as the one used in our previous studies [6, 9]. In particular, both fibers feature long-lived persistent spectral holes with very similar characteristics.

Our paper is organized as follows. First, we discuss the results of the 2PPE measurements including the observed non-exponential echo decays in the context of spectral diffusion. We then present a detailed analysis describing the observed behaviors that combines elements from theoretical and semi-empirical models that have been developed in the past for glassy and crystalline hosts. In agreement with results of previous studies [10, 11], we find that coupling with TLS significantly limits the coherence lifetimes to less than $1\ \mu\text{s}$ even at high magnetic fields and temperatures as low as 600 mK. However, an important new finding is that the best coherence properties exist at weak magnetic fields of around 0.05 T, which correspond to the optimal field strength for persistent spectral hole burning in this material [6]. This result is highly desir-

able for applications requiring both long coherence times as well as long spin state lifetimes.

6.3.3. Experimental details

Our silica glass fiber (INO Canada, S/N 404-28565) is 25 m long and contains erbium, aluminium, germanium and phosphorus co-dopants. The Er and Al doping concentrations in the core are 80 ppm and 1800 ppm, respectively, and the concentrations of Ge and P are unknown. The fiber is cooled to temperatures as low as $T = 600$ mK using an adiabatic demagnetization refrigerator (please note that, unlike fluoride and tellurite glass fibers, silica glass fibers are easy to use at cryogenic temperatures), resulting in an optical depth of $\alpha L = 1.6$ at $\lambda = 1536$ nm wavelength. Magnetic fields B of up to 2 T are applied by means of a superconducting solenoid.

To perform the 2PPE (or 3PPE) measurements, we used two fiber-coupled electro-optic modulators to generate excitation pulses from a continuous wave external-cavity diode laser operating at $\lambda = 1536$ nm. The light was then amplified using an erbium-doped fiber amplifier (EDFA). In order to suppress spontaneously emitted and amplified light from the EDFA, we filtered the output in polarization with a polarizing beam-splitter, in frequency with a 1 nm bandpass filter, and in time using an additional intensity modulator before sending the excitation pulses into the Er^{3+} -doped fiber. The first pulse was 4 ns long, and the duration of the second (and third in case of 3PPE) pulse was 8 ns. All pulses emerging from the fiber were detected with an amplified photodetector (Newport AD-200xr). Since any persistent hole-burning will

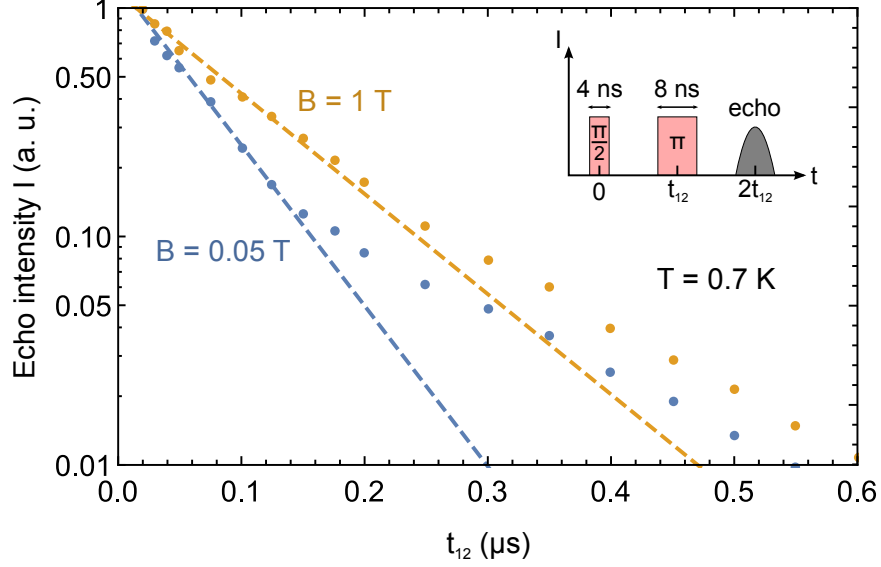


Figure 6.7.: Two-pulse photon echo peak intensity as a function of the time delay between the two excitation pulses at $T = 0.7$ K for $B = 0.05$ T (blue dots) and $B = 1$ T (yellow dots). The pulse sequence is shown in the inset. The experimental data are fitted by a single-exponential function (dashed lines) with characteristic decay constants $T_2 = 247 \pm 14$ ns and $T_2 = 396 \pm 16$ ns.

affect the echo signal strength, we ensured that the repetition period of the experiment exceeds the characteristic (magnetic field dependent [6]) persistence lifetime.

6.3.4. Two-pulse photon echo measurements – analysis and model

The optical coherence properties of the fiber can be extracted from two-pulse photon echo measurements. In a 2PPE sequence, two short pulses, separated by a waiting time t_{12} are sent into an inhomogeneously-broadened ensemble of absorbers. This gives rise to the emission of an echo at time t_{12} after the second pulse. The variation

of its intensity as a function of t_{12}

$$I(t_{12}) = I_0 e^{-4\pi\Gamma_h t_{12}} \quad (6.3)$$

reveals the homogeneous linewidth Γ_h (which is inversely proportional to the coherence lifetime: $\Gamma_h = (\pi T_2)^{-1}$) assuming that all absorbers have the same coherence properties. Fig. 6.7 shows typical examples of the echo intensity as a function of the pulse separation t_{12} for $B = 0.05$ T and $B = 1$ T. The echo decays clearly show a non-exponential behavior: they deviate from a single exponential fit (see dashed lines) roughly at $t_{12} \geq 0.2 \mu\text{s}$, and feature a slower decay after this point. This differs from what has been observed in previous investigations of coherence properties in Er-doped fibers, where simple exponential decays were reported [12, 11] – most likely because the dynamic range of the echo decays in these past studies was smaller. In our case, the experimental echo decays can be fitted by the sum of multiple exponential functions, which could suggest the presence of several classes of ions with distinct coupling strengths to their environment, or of several distinct perturbing processes. However, these explanations are not likely for an amorphous host where a random distribution of different site environments is usually assumed.

Due to the amorphous nature of the fiber, we expect a broad, continuous distribution of coherence-limiting processes to affect the Er^{3+} ions. Of particular importance are changes in the local electric or magnetic field at the Er^{3+} ion position; they result in time-dependent shifts of its optical transition frequency – so-called spectral diffusion – which is taken into account by using an effective homogeneous linewidth Γ_{eff} . As

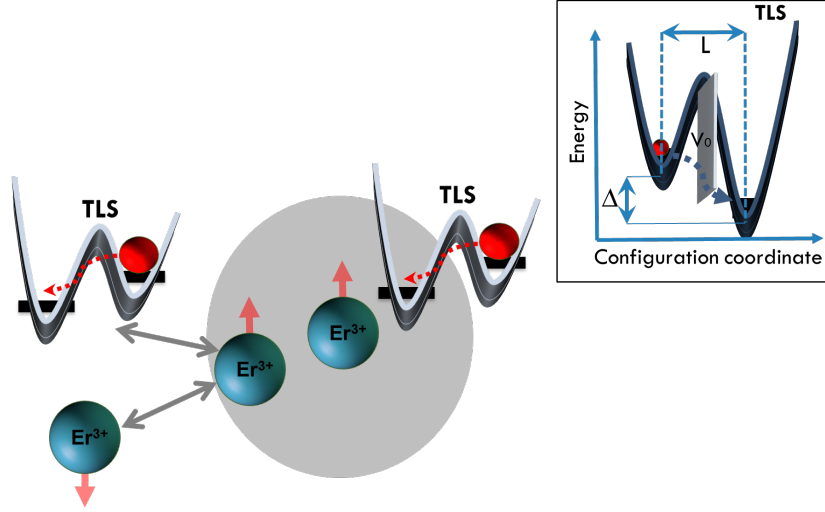


Figure 6.8.: Spectral diffusion processes in a rare-earth ion doped glass. The local environments of the optically probed Er^{3+} ions in the center of the grey circle are perturbed by either direct interaction with fluctuations in the state of neighboring TLS (depicted on the right-hand side), or interaction with fluctuations in the state of other Er^{3+} spins in the local environment driven by TLS or another Er^{3+} ion. Inset: double-well potential-energy structure of the TLS, with asymmetry energy Δ , barrier energy V_0 and well separation L .

depicted in Fig. 6.8, these shifts can arise due to interactions with neighboring TLS's (or tunneling modes) and Er^{3+} spins, each described by two states featuring a certain energy splitting and random population fluctuations at a certain local rate [13, 14]. Two-level systems [7, 8] are intrinsic to amorphous materials and are present with a continuous distribution of flip rates R and energy splittings E that both depend on the asymmetry energy Δ , well separation L , and barrier energy V_0 (see inset of Fig. 6.8), as well as on the magnetic field in certain cases (so-called spin-elastic or magnetic TLSs) [15, 11, 12]. Thus, the calculation of the intensity of a 2PPE must

include integration over a continuous distribution of rates and energy splittings:

$$I(t_{12}) = I_0 \int \int e^{-4\pi\Gamma_{\text{eff}}(R,E,T,t)t_{12}} dR dE , \quad (6.4)$$

where

$$\Gamma_{\text{eff}}(R, E, T, t) = \Gamma_0(T) + \Gamma_{\text{SD}}(E, T)P(R, E)(1 - e^{-Rt}) . \quad (6.5)$$

$\Gamma_0(T)$ is the intrinsic homogeneous linewidth (without spectral diffusion), and the spectral diffusion linewidth Γ_{SD} is given by

$$\Gamma_{\text{SD}}(E, T) = \Gamma_{\text{max}} \text{sech}^2 \left(\frac{E}{2kT} \right) , \quad (6.6)$$

where Γ_{max} is the maximum possible linewidth broadening caused by spectral diffusion, k the Boltzmann constant, and T the temperature [16]. Furthermore, the probability distribution for finding a TLS with energy E and flipping rate R , $P(R, E)$, is given by

$$P(R, E) = \frac{1}{R\sqrt{1 - R/R_{\text{max}}(E)}} , \quad (6.7)$$

with $R_{\text{max}}(E) \propto E^3 \coth \left(\frac{E}{2kT} \right)$ [17]. In the case of interactions with a magnetic TLS or the spin of another Er^{3+} ion, the energy E is given by $g\mu_B B$, where g is the effective g -value for the perturbing TLS or Er^{3+} ion, μ_B the Bohr magneton, and B the applied magnetic field. Using Eq. 6.4, one can fit Γ_{eff} to the individual echo decays by summing over five individual processes: spectral diffusion due to direct interaction of the probed Er^{3+} ions with non-magnetic (process 1) or magnetic (process 2) TLSs;

spectral diffusion due to interaction of the probed Er^{3+} ions with pairs of coupled Er^{3+} spins in the environment that randomly exchange spin states (Er^{3+} - Er^{3+} spin flip flops) (process 3); and spectral diffusion due to interaction of the probed Er^{3+} ions with Er^{3+} spins that are strongly coupled to magnetic (process 4) or non-magnetic (process 5) TLSs that drive spin flips (i.e. Er^{3+} -TLS flip flops). Due to the data set being limited in size and quality as well as computational complexity, we did not succeed in fitting all echo decays with one unique set of model parameters. However, as we will describe next, restricting the coherence-limiting processes to (1), (3) and (4), we were able to reproduce the magnetic field and temperature dependence of the single-exponential fits to our data shown in Fig.6.7 for the effective homogeneous linewidth $\Gamma_{\text{eff}}(B, T)$.

6.3.5. Temperature and magnetic field dependence of the effective homogeneous linewidth

To extract the effective homogeneous linewidth as a function of magnetic field and temperature, we fit all measured echo decays using the single exponential function described in Eq. 6.4 (after replacing Γ_{h} with Γ_{eff}). These fits describe the coherence data over the first decade of the decays, thereby restricting the assessment of coherence-limiting processes to that region of the data; nevertheless, we should note that the first decade of the decay represents the dominant decoherence mechanisms that are primarily responsible for the performance in applications, with the different behaviors observed at longer times resulting from either higher-order processes and

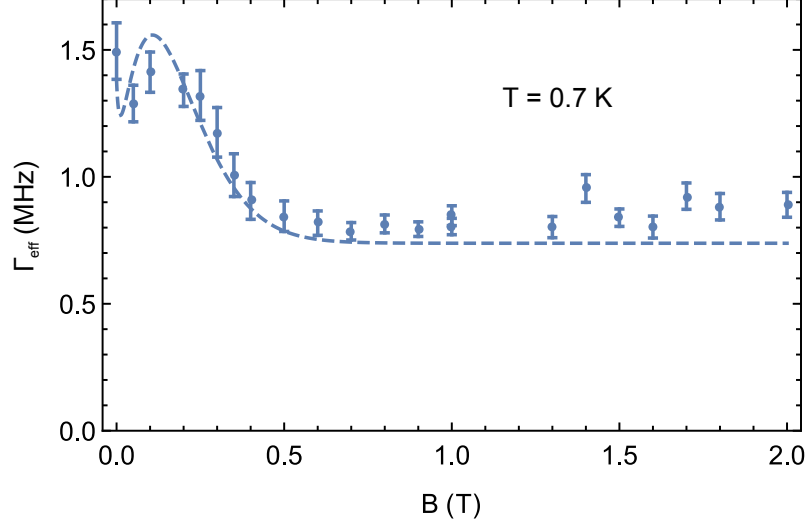


Figure 6.9.: Magnetic field dependence of the effective homogeneous linewidth Γ_{eff} at $T = 0.7 \pm 0.05$ K. The dashed lines shows the theoretical prediction of Eq. 6.8 with the set of parameters in Table 6.2.

correlations or groups of minority ion sites in the material.

In Figs. 6.9 and 6.10 we plot examples of the experimentally obtained effective linewidth Γ_{eff} as a function of magnetic field for a fixed temperature and as a function of temperature for two different magnetic fields. In the case of varying magnetic field (Fig. 6.9), we observe two components. The first one is magnetic field independent and has been attributed to dephasing due to non-magnetic, or elastic, TLS [12, 11]. At 0.7 K its contribution to the Er^{3+} homogeneous linewidth in our fiber is roughly 0.75 MHz. The second component is magnetic field dependent: it dominates at small magnetic fields and is rapidly suppressed as the field increases. This behavior has been attributed to spectral diffusion due to the interaction of Er^{3+} ions with magnetic TLS [12, 11], or other Er^{3+} ions in the environment [15]. The latter process is regularly observed in Er^{3+} -doped crystals [18, 19, 20]. In the region of low magnetic field, we observe a local minimum at $B \approx 0.05$ T, followed by a local maximum at $B \approx 0.15$ T.

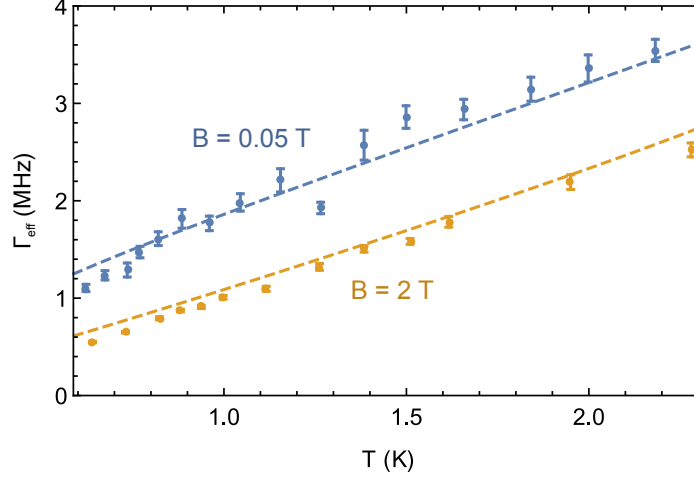


Figure 6.10.: Temperature dependence of the effective homogeneous linewidth Γ_{eff} at $B = 0.05$ T and $B = 2$ T. The dashed lines show the theoretical prediction of Eq. 6.8 with the set of parameters in Table 6.2.

This behavior is similar to what has been observed in Er^{3+} -doped crystals, such as $\text{Er}^{3+}:\text{LiNbO}_3$ and $\text{Er}^{3+}:\text{KTP}$ [19, 20], and can be explained by the competition between two mechanisms: the interaction between Er^{3+} ions, which decreases with B , and the interaction between Er^{3+} ions and resonant TLS, which increases with B according to the TLS density of states [6]. Note that the overall effect of the spectral diffusion caused by Er-Er interactions i.e. processes (3,4,5) is 0.7 MHz at 0.1 T and 0.7 K in our 80 ppm Er-doped fiber, whereas it is about 40 kHz at the same magnetic field and at 3 K in a 80 ppm $\text{Er}^{3+}:\text{LiNbO}_3$ crystal [19]. Thus, this contribution is larger in the fiber, but due to the broadening of the spin transition reducing spin flip flops, it is suppressed more rapidly with the application of a magnetic field.

Investigating Γ_{eff} at low and high magnetic fields as a function of temperature (Fig. 6.10), we observe that both components increase nearly linearly with temperature. This agrees with the characteristic behavior of TLS-limited coherence [21], in which the effective linewidth is proportional to T^n , with values of n reported between 1 and 1.5

[12, 13, 11].

6.3.5.1. Spectral diffusion model

Next, we fit the effective linewidths using a model that takes into account the three processes described previously (1, 3, and 4). Our model combines what has been proposed for amorphous media [21] and crystals (in particular in the case of Er:YSO [18]). We write the coherence lifetime as

$$T_2 = \frac{2(\Gamma_0 + \alpha_0 T^n)}{\Gamma_{SD} R} \left(\sqrt{1 + \frac{\Gamma_{SD} R}{\pi(\Gamma_0 + \alpha_0 T^n)^2}} - 1 \right). \quad (6.8)$$

Here, Γ_0 is the homogeneous linewidth at $T = 0$ K, α_0 is a constant describing the direct interaction with non-magnetic TLS (process 1), and $1 \leq n \leq 1.5$. The term $\frac{1}{2}\Gamma_{SD}R$ represents the shortening of the coherence lifetime through spectral diffusion caused by magnetic dipole-dipole interactions (since the Zeeman energy level splittings are on the order of kT, only spins are thermally activated and thus, the dynamics are dominated by magnetic dipole-dipole interactions between co-dopants) with surrounding Er^{3+} spins, which are flipped by neighboring Er-ions or TLS (processes 3 and 4). The associated flipping rate R can be described by

$$R(B, T) = \frac{\alpha_1}{\Gamma_S^0 + \gamma_S B} \text{sech}^2 \left(\frac{g_{\text{env}} \mu_B B}{2kT} \right) + \alpha_2 B T. \quad (6.9)$$

The first term corresponds to spin flip-flops between Er^{3+} ions, with a coupling coefficient α_1 (process 3). We include broadening of the inhomogeneous linewidth Γ_S

Γ_0	$(0.0 \pm 0.5) \text{ MHz}$
α_0	$(1.1 \pm 0.5) \text{ MHz/T}^n$
n	1.1 ± 0.4
g_{env}	14.4 ± 1.6
$\alpha_1/\Gamma_{\text{max}}$	$11 \pm 5 \text{ GHz}$
$\alpha_2/\Gamma_{\text{max}}$	$348 \pm 42 \text{ (T K)}^{-1}$

Table 6.2.: Parameters resulting from the 2-dimensional fit of Eq. 6.8 to $\Gamma_{\text{eff}}(B, T)$.

of the spin transition with magnetic field, i.e. $\Gamma_{S_0} = \Gamma_S^0 + \gamma_S B$, with $\Gamma_S^0 = 1.5 \text{ GHz}$ and $\gamma_S = 150 \text{ GHz/T}$, as observed in our previous work on spin relaxation in erbium-doped fiber [6]. The second term corresponds to flip flops with magnetic TLS, with a coupling coefficient α_2 (process 4). While this effect is in some ways analogous to the coupling with phonons in crystals, we observed in the same previous work that it is proportional to B , i.e. has a different dependence on the magnetic field due to the difference in the density of states of the TLS [22]. The flip-flop rate increases with magnetic field for $B > 0.05 \text{ T}$, which opposes the reduction of the linewidth Γ_{SD} with B , hence giving rise to the local maximum observed in the magnetic field dependence of the homogeneous linewidth (see Fig. 6.9). Fitting Eq. 6.8 to the magnetic field and temperature dependence of the homogeneous linewidth $\Gamma_{\text{eff}}(B, T)$ results in the parameters listed in Table 6.2. The values of Γ_S^0 and γ_S have been fixed to the values found in our previous investigation of 1.5 GHz and 150 GHz/T, respectively [6].

The agreement between our model and the experimental data is exemplified by the data sets shown in Figs. 6.9 and 6.10. Furthermore, the value of 1.1 for the exponent n is in agreement with previous work [12, 13, 11], and the value of $g_{\text{env}} = 14.4$, while large, is within the allowed range from 0 to 18 for the $^4\text{I}_{15/2}$ levels of Er^{3+} ions

[23, 24, 25, 26, 27, 28]. We also note that the rate of Er^{3+} spin flips, characterized by α_1 and α_2 , is on the order of MHz to GHz. However, we reported spin relaxation (i.e. spin flip) rates on the order of Hz in our previous study of persistent spectral hole burning in a similar fiber [6]. We believe that this large difference in behavior can be explained by the broad distribution of spin relaxation rates spanning the entire range from Hz to GHz. The coherence lifetime is limited by spectral diffusion that occurs at the fastest rate whereas the possibility for persistent spectral hole burning is determined by Er^{3+} ions with the slowest rates; in addition to causing spectral diffusion, the small fraction of rapidly relaxing ions leads to the observed temperature-dependent limit on the maximum hole depth.

Overall, the coherence properties improve at low temperature and high magnetic fields, with an optimum of $\Gamma_{\text{eff}} = 0.55$ MHz at $T = 0.64$ K and $B = 2$ T (see Fig. 6.10). However, the broadening of the effective linewidth at magnetic fields of around 0.05 T (at which persistent spectral hole burning is possible) is small enough to allow linewidths of approximately 1 MHz at $T = 0.64$ K (see Fig. 6.10). This property has not been previously observed [10, 11], possibly due to differences in co-dopants (phosphorus in our fiber and lanthanum in the fiber studied, e.g., in [10]). Another interesting observation is that the value for Γ_0 predicts a very narrow linewidth for $T \rightarrow 0$ K. However, note that this is only an extrapolation of our observations down to $T = 0.6$ K, and it is likely that other processes limit the linewidth to a constant value at lower temperatures.

6.3.6. Three-pulse photon echo measurements – spectral

diffusion at large timescales

Finally, to investigate spectral diffusion at timescales comparable to the excited-state lifetime of Er^{3+} (11 ms), 3PPE measurements were carried out at a temperature of $T = 0.76$ K. We chose two values of the magnetic field: $B = 0.06$ T for which the coherence lifetime exhibits a local maximum, and $B = 2$ T for which the effect of spectral diffusion due to Er^{3+} - Er^{3+} interaction is small and the coherence is limited by the interaction with TLS. For these measurements, the separation time t_{12} between the first two pulses was held constant at 50 ns and the echo intensity was measured as a function of the time t_{23} between the second and third pulse, with t_{23} varying between 0.001 ms and 35 ms. The echo intensity is given by

$$I(t_{12}, t_{23}) = I_0 \left\{ e^{-t_{23}/T_1} + \frac{\beta}{2} \frac{T_Z}{T_Z - T_1} (e^{-t_{23}/T_Z} - e^{-t_{23}/T_1}) \right\}^2 \times e^{-4 t_{12} \pi \Gamma_{\text{eff}}(t_{12}, t_{23})}. \quad (6.10)$$

where I_0 is a scaling coefficient and β the branching ratio from the excited-level (with lifetime T_1) to the other Zeeman sublevel of the ground state (with lifetime T_Z) [18]. A fit to our data with $T_1 = 11$ ms yields the effective homogeneous linewidth Γ_{eff} that depends on t_{12} and t_{23} .

The measurement results are shown in Fig. 6.11, which also includes fits of the ex-

pected logarithmic dependence of Γ_{eff} on t_{23} due to coupling to TLS in fiber [16, 29]:

$$\Gamma_{\text{eff}}(t_{12}, t_{23}) = \Gamma(t_0) + \gamma \log_{10} \left(\frac{t_{23}}{t_0} \right). \quad (6.11)$$

Here, $\Gamma(t_0)$ is the effective linewidth at the minimum value of $t_{12} + t_{23} \equiv t_0$, and γ is a coupling coefficient. The value of $\Gamma(t_0)$ is set to the one we measured in the 2PPE at the same magnetic field. We find excellent agreement for $\gamma = 0.376$ MHz/decade at $B = 0.06$ T and $\gamma = 0.410$ MHz/decade at 2 T. We find that, as in the case of short waiting times, our Er^{3+} -doped fiber features better coherence properties for small magnetic fields. Furthermore, effective linewidths at long waiting times barely improve when increasing the field to 2 T. This implies that spectral tailoring of the absorption profile with MHz resolution is possible even after large delays of up to hundreds of ms. In particular, this allows our fiber to be used as a quantum memory for light [9].

6.3.7. Conclusion

In conclusion, we have experimentally and theoretically investigated decoherence and spectral diffusion over a large range of timescales in an erbium-doped fiber similar to the one in which persistent hole burning has recently been demonstrated [6]. Our model combines the semi-empirical model framework developed for amorphous hosts, where spectral diffusion is caused by the interaction with two-level systems, and the theoretical framework successfully applied previously for Er^{3+} -doped crystals, where spectral diffusion is due to Er^{3+} - Er^{3+} magnetic dipole interactions. Most importantly,

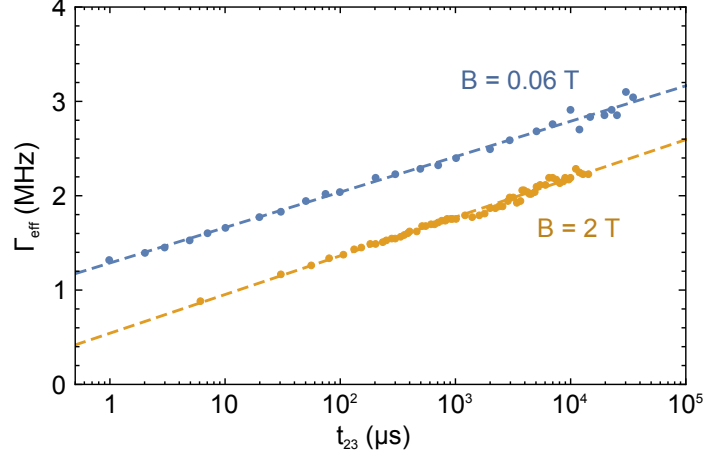


Figure 6.11.: Effective homogeneous linewidth as a function of t_{23} , derived from 3PPE measurements at $T = 0.76$ K at $B = 0.06$ T (empty circles) and $B = 2$ T (filled circles). The experimental data is fitted by Eq. 6.10 with $\gamma = 0.376$ MHz/decade and 0.410 MHz/decade at $B = 0.06$ T and 2 T respectively.

we found coherence lifetimes at small magnetic fields, at which Zeeman lifetimes can be as long as seconds, that are comparable to those at high magnetic fields. This is crucial for applications in the field of quantum information processing, in particular quantum memory for light [9].

6.3.8. Acknowledgments

The authors thank Daniel Oblak and Neil Sinclair for discussions and acknowledge support from Alberta Innovates Technology Futures (ATIF), the National Engineering and Research Council of Canada (NSERC), the US National Science Foundation (NSF) under award nos. PHY-1415628 and CHE-1416454, and the Montana Research and Economic Development Initiative. Furthermore, W.T. acknowledges support as a Senior Fellow of the Canadian Institute for Advanced Research (CIFAR).

Bibliography

- [1] W. Tittel, M. Afzelius, T. Chanelière, R. L. Cone, S. Kröll, S. Moiseev, and M. Sellars, *Laser & Photonics Reviews* **4**, 244 (2010).
- [2] A. I. Lvovsky, B. C. Sanders, and W. Tittel, *Nature Photonics* **3**, 706 (2009).
- [3] C. W. Thiel, T. Böttger, and R. L. Cone, *Journal of Luminescence Selected papers from DPC'10*, **131**, 353 (2011).
- [4] E. Saglamyurek, N. Sinclair, J. A. Slater, K. Heshami, D. Oblak, and W. Tittel, *New Journal of Physics* **16**, 065019 (2014).
- [5] C. Thiel, W. Babbitt, and R. Cone, *Physical Review B* **85**, 174302 (2012).
- [6] E. Saglamyurek, T. Lutz, L. Veissier, M. P. Hedges, C. W. Thiel, R. L. Cone, and W. Tittel, *Physical Review B* **92**, 241111 (2015a).
- [7] P. W. Anderson, B. I. Halperin, and C. M. Varma, *Philosophical Magazine* **25**, 1 (1972).
- [8] W. A. Phillips, *Journal of Low Temperature Physics* **7**, 351 (1972).

- [9] E. Saglamyurek, J. Jin, V. B. Verma, M. D. Shaw, F. Marsili, S. W. Nam, D. Oblak, and W. Tittel, *Nature Photonics* **9**, 83 (2015b).
- [10] R. M. Macfarlane, Y. Sun, P. B. Sellin, and R. L. Cone, *Physical Review Letters* **96**, 033602 (2006).
- [11] M. U. Staudt, S. R. Hastings-Simon, M. Afzelius, D. Jaccard, W. Tittel, and N. Gisin, *Optics Communications* **266**, 720 (2006).
- [12] R. M. Macfarlane, Y. Sun, P. B. Sellin, and R. L. Cone, *Journal of Luminescence Proceedings of the Ninth International Meeting on Hole Burning, Single Molecule, and Related Spectroscopies: Science and Applications* **127**, 61 (2007).
- [13] M. M. Broer, B. Golding, W. H. Haemmerle, J. R. Simpson, and D. L. Huber, *Physical Review B* **33**, 4160 (1986).
- [14] J. L. Zyskind, E. Desurvire, J. W. Sulhoff, and D. J. D. Giovanni, *IEEE Photonics Technology Letters* **2**, 869 (1990).
- [15] Y. Sun, R. L. Cone, L. Bigot, and B. Jacquier, *Optics Letters* **31**, 3453 (2006).
- [16] J. L. Black and B. I. Halperin, *Physical Review B* **16**, 2879 (1977).
- [17] J. Jackle, *Zeitschrift für Physik* **257**, 212 (1972).
- [18] T. Böttger, C. W. Thiel, Y. Sun, and R. L. Cone, *Physical Review B* **73**, 075101 (2006).

- [19] C. W. Thiel, R. M. Macfarlane, T. Böttger, Y. Sun, R. L. Cone, and W. R. Babbitt, Journal of Luminescence Special Issue based on the Proceedings of the Tenth International Meeting on Hole Burning, Single Molecule, and Related Spectroscopies: Science and Applications (HBSM 2009) - Issue dedicated to Ivan Lorgere and Oliver Guillot-Noel, **130**, 1603 (2010).
- [20] T. Böttger, C. W. Thiel, Y. Sun, R. M. Macfarlane, and R. L. Cone, Journal of Luminescence The 17th International Conference on Luminescence and Optical Spectroscopy of Condensed Matter (ICL'14), **169, Part B**, 466 (2016).
- [21] W. A. Phillips, Reports on Progress in Physics **50**, 1657 (1987).
- [22] U. Buchenau, M. Prager, N. Nücker, A. J. Dianoux, N. Ahmad, and W. A. Phillips, Physical Review B **34**, 5665 (1986).
- [23] H. Asatryan, R. Zakharchenya, A. Kutsenko, R. Babunts, and P. Baranov, Physics of the Solid State **49**, 1074 (2007).
- [24] C. Ammerlaan and I. de Maat-Gersdorf, Applied Magnetic Resonance **21**, 13 (2001).
- [25] T. Nolte, T. Pawlik, and J.-M. Spaeth, Solid state communications **104**, 535 (1997).
- [26] D. Bravo and F. Lopez, The Journal of chemical physics **99**, 4952 (1993).
- [27] R. Reynolds, L. Boatner, C. Finch, A. Chatelain, and M. Abraham, The Journal of Chemical Physics **56**, 5607 (1972).

- [28] A. Belyaeva, V. Eremenko, V. Pavlov, and A. Antonov, Optics and Spectroscopy **25**, 55 (1968).
- [29] R. J. Silbey, J. M. A. Koedijk, and S. Völker, The Journal of Chemical Physics **105**, 901 (1996).

7. Conclusion

The overall goal of this thesis was to show that spectroscopic properties such as population lifetimes and homogeneous linewidths of REIs can be improved by engineering host materials. The specific focus was to develop materials that allow for high-quality spectral tailoring thus benefit applications such as quantum memories. Towards that goal, two approaches were pursued: Suppression of direct phonon processes and suppression of interaction between neighboring REI spins. Both relaxation mechanisms cause transitions between energy levels and thus reduce population lifetimes and broaden homogeneous linewidths via spectral diffusion.

Towards the goal of phonon suppression in small, REI doped powders, we first showed theoretically that such a restriction can be achieved if powders are sufficiently small and hence the phonon density of states is zero at the desired frequencies. Various methods such as chemical synthesis and mechanical grinding were studied in order to produce powders that satisfy this condition along with that of good crystal quality. We found that any kind of mechanical processing creates amorphous phases and residual strain in the crystallites. This damage could be partially repaired through

thermal annealing.

By studying relaxation processes between crystal field levels in $\text{Tb}^{3+}:\text{Y}_3\text{Al}_5\text{O}_{12}$, we found that imperfect powders can lead to observations that can wrongfully be interpreted as signatures of phonon suppression. We show that sensitive powder characterization methods are needed together with several complementary measurements to unambiguously demonstrate phonon suppression. Our time-resolved fluorescence measurements of relaxation dynamics are consistent with phonon suppression in small particles. However, we also observe that relaxation between crystal field levels is still possible via nonradiative processes — most likely related to glass-like dynamics in the nanocrystals. To exploit the effect of phonon suppression for possible applications, fabrication and annealing methods must be further improved and materials that are less sensitive to host imperfections must be chosen.

As a result of these investigations, we performed initial experiments on SiV centers in nano-structured diamond since their symmetry makes them largely insensitive to nanofabrication methods. Furthermore, SiVs allow for experiments with single emitters in a diamond nanopillar that is produced via electronbeam lithography and chemical etching. Our numerical simulations predicted phonon suppression in pillars below 150 nm diameter. However, up to now we were not able to observe this effect experimentally. As described in the outlook, we expect to show and apply phonon suppression through improvements in our fabrication methods.

In order to demonstrate the reduction of interaction between neighboring spins, we also studied erbium-doped glass fibers. Erbium is of specific interest since it features an optical transition that is compatible with the wavelengths used for existing telecommunication infrastructure. However, in crystals, interaction between neighboring erbium spins prevent applications, specifically at low magnetic fields. Our studies revealed that in a disordered material, i.e. the glass fiber, the spin inhomogeneous broadening is much larger than in a bulk crystal. This increase in broadening was found to significantly reduce spin-spin interactions to a degree where spin flip-flops are slow enough to enable efficient and persistent spectral tailoring, a prerequisite for many applications.

To assess the possibility for implementations of a quantum memory protocol with the erbium doped fiber, we also investigated coherence-limiting processes in that medium. It was found that two-level systems common to amorphous hosts strongly limit coherence properties and cause homogeneous linewidths of at best 1 MHz. However, our experiments identified a set of operational parameters that made it possible to use the studied fiber for proof of principle experiments of a single- and multimode quantum memory and an integrated processor for photonic quantum states.

Ultimately, we conclude that it is indeed possible to engineer spectroscopic properties of impurities in solid-state hosts through modifications of the host material, although significant efforts have to be undertaken to ensure that fabrication processes do not degrade the overall quality of the material.

8. Outlook

Up to now, imperfect material quality prevented us from demonstrating complete phonon suppression in REI-doped materials. In future, the various powder materials could be improved by performing the chemical synthesis with ultra pure precursors. In addition, systematic studies on thermal annealing are expected to lead to materials with better crystal quality. As a long-term goal, however, it would be highly beneficial to explore the use of nano-machining tools such as focused ion beam milling and chemical etching for the fabrication of phononic crystals. Such structures would have a deterministic crystal orientation and scatter light less strongly compared to powders. Together with the suppression of detrimental phonons, these advantages should make applications possible.

Future work on this project should also focus on optimization of the diamond substrates and the fabrication process to create nano-pillars that suppress the undesired lattice vibrations. Initial efforts could concentrate on reducing strain in the diamond samples that is caused by mechanical polishing. We believe that most of the damage is contained on the surface of the diamond chip. Thus, we hope to be able to access regions that are less strained by etching away several micrometers of material from

the diamond top surface. In addition, thermal annealing methods, which have successfully relieved strain in REI host materials, should be explored in order to further improve the samples. Subsequently, fabrication methods used to create nano-pillars can be optimized by tuning the parameters of the chemical etching, such as flow rates of the various gases, and by exploring new etching chemistries, i.e. alternative gases. The goal of this step is to achieve the smoothest possible surfaces. At the same time it would be advantageous to optimize the electron beam lithography process such that smaller pillars can be obtained, which should make the observation of phonon suppression easier.

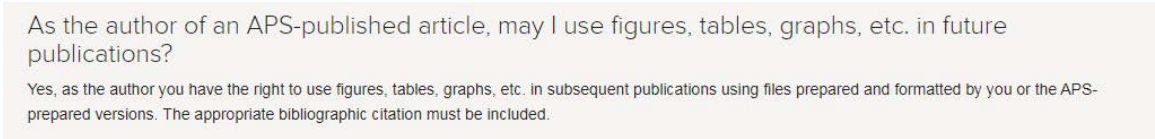
In parallel, one should start studying ensembles of SiVs with the goal of using them as a quantum memory, potentially based on the AFC protocol. Through this approach it may become possible to combine a multimode quantum memory based on SiV ensembles, which would be very beneficial for high-rate quantum communication, with individual SiVs that feature enhanced spin coherence times due to phonon suppression. The latter could be used for local processing of quantum information. Such a hybrid system would pave the way towards a quantum network with distributed computing nodes connected by high-rate communication channels.

A. Copyright permissions

This appendix lists copyright permissions required to include papers 1-7 in this thesis:

A.1. Papers 1,4,5,6,7

Papers 1,4,5,6,7 were published in Journals of the American Physical Society (APS), i.e. Physical Review A and Physical Review B. Fig. A.1 shows the part of the copyright agreement granting me permission to use these papers in my thesis.



As the author of an APS-published article, may I use figures, tables, graphs, etc. in future publications?

Yes, as the author you have the right to use figures, tables, graphs, etc. in subsequent publications using files prepared and formatted by you or the APS-prepared versions. The appropriate bibliographic citation must be included.

Figure A.1.: Part of the APS copyright agreement granting me permission to use papers 1,4,5,6,7 in my thesis.

A.2. Paper 2

Paper 2 was submitted to the journal Science and Technology of Advanced Materials (STAM). Fig. A.2 shows the part of the copyright agreement granting me permission to use this paper in my thesis.



LICENSE TO PUBLISH AGREEMENT FOR JOURNALS

This License to Publish must be signed, either electronically within the Peer X-Press manuscript submission system, or as a PDF to be uploaded into Peer X-Press as an alternate form, before the manuscript can be published. If you have questions about how to submit the form, please contact the journal's editorial office. For questions regarding the copyright terms and conditions of this License, please contact AIP Publishing LLC's Office of Rights and Permissions, 1305 Walt Whitman Road, Suite 300, Melville, NY 11747-4300 USA; Phone 516-576-2268; Email: rights@aip.org.

Article Title ("Work"):

(Please indicate the final title of the Work. Any substantive changes made to the title after acceptance of the Work may require the completion of a new agreement.)

All Author(s):

(Please list all the authors' names in order as they will appear in the Work. All listed authors must be fully deserving of authorship and no such authors should be omitted. For large groups of authors, attach a separate list to this form.)

Journal:

Manuscript ID#

All Copyright Owner(s), if not Author(s):

(Please list all copyright owner(s) by name. In the case of a Work Made for Hire, the employer(s) or commissioning party(ies) are the copyright owner(s). For large groups of copyright owners, attach a separate list to this form.)

Copyright Ownership and Grant of Rights

For the purposes of this License, the "Work" consists of all content within the article itself and made available as part of the article, including but not limited to the abstract, tables, figures, graphs, images, and multimedia files, as well as any subsequent errata. The Work refers to the content contained in both the Accepted Manuscript (AM) and the Version of Record (VOR). "Supplementary Material" consists of material that is associated with the article but linked to or accessed separately (available electronically only), including but not limited to data sets and any additional files.

This Agreement is an Exclusive License to Publish not a Transfer of Copyright. Copyright to the Work remains with the Author(s) or, in the case of a Work Made for Hire, with the Author(s)' employer(s). AIP Publishing LLC shall own and have the right to register in its name the copyright to the journal issue or any other collective work in which the Work is included. Any rights granted under this License are contingent upon acceptance of the Work for publication by AIP Publishing. If for any reason and at its own discretion AIP Publishing decides not to publish the Work, this License is considered void.

Each Copyright Owner hereby grants to AIP Publishing LLC the following irrevocable rights for the full term of United States and foreign copyrights (including any extensions):

1. The exclusive right and license to publish, reproduce, distribute, transmit, display, store, translate, edit, adapt, and create derivative works from the Work (in whole or in part) throughout the world in all formats and media whether now known or later developed, and the nonexclusive right and license to do the same with the Supplementary Material.
2. The right for AIP Publishing to freely transfer and/or sublicense any or all of the exclusive rights listed in #1 above. Sublicensing includes the right to authorize requests for reuse of the Work by third parties.
3. The right for AIP Publishing to take whatever steps it considers necessary to protect and enforce, at its own expense, the exclusive rights granted herein against third parties.

Author Rights and Permitted Uses

Subject to the rights herein granted to AIP Publishing, each Copyright Owner retains ownership of copyright and all other proprietary rights such as patent rights in the Work.

Each Copyright Owner retains the following nonexclusive rights to use the Work, without obtaining permission from AIP Publishing, in keeping with professional publication ethics, and provided clear credit is given to its first publication in an AIP Publishing journal. Any reuse must include a full credit line acknowledging AIP Publishing's publication and a link to the VOR on AIP Publishing's site.

Each Copyright Owner may:

1. Reprint portions of the Work (excerpts, figures, tables) in future works created by the Author, in keeping with professional publication ethics.
2. Post the Accepted Manuscript (AM) to their personal web page or their employer's web page immediately after acceptance by AIP Publishing.
3. Deposit the AM in an institutional or funder-designated repository immediately after acceptance by AIP Publishing.

4. Use the AM for posting within scientific collaboration networks (SCNs). For a detailed description of our policy on posting to SCNs, please see our Web Posting Guidelines (<https://publishing.aip.org/authors/web-posting-guidelines>).
5. Reprint the Version of Record (VOR) in print collections written by the Author, or in the Author's thesis or dissertation. It is understood and agreed that the thesis or dissertation may be made available electronically on the university's site or in its repository and that copies may be offered for sale on demand.
6. Reproduce copies of the VOR for courses taught by the Author or offered at the institution where the Author is employed, provided no fee is charged for access to the Work.
7. Use the VOR for internal training and noncommercial business purposes by the Author's employer.
8. Use the VOR in oral presentations made by the Author, such as at conferences, meetings, seminars, etc., provided those receiving copies are informed that they may not further copy or distribute the Work.
9. Distribute the VOR to colleagues for noncommercial scholarly use, provided those receiving copies are informed that they may not further copy or distribute the Work.
10. Post the VOR to their personal web page or their employer's web page 12 months after publication by AIP Publishing.
11. Deposit the VOR in an institutional or funder-designated repository 12 months after publication by AIP Publishing.
12. Update a prior posting with the VOR on a noncommercial server such as arXiv, 12 months after publication by AIP Publishing.

Author Warranties

Each Author and Copyright Owner represents and warrants to AIP Publishing the following:

1. The Work is the original independent creation of each Author and does not infringe any copyright or violate any other right of any third party.
2. The Work has not been previously published and is not being considered for publication elsewhere in any form, except as a preprint on a noncommercial server such as arXiv, or in a thesis or dissertation.
3. Written permission has been obtained for any material used from other sources, and copies of the permission grants have been supplied to AIP Publishing to be included in the manuscript file.
4. All third-party material for which permission has been obtained has been properly credited within the manuscript.
5. In the event that an Author is subject to university open access policies or other institutional restrictions that conflict with any of the rights or provisions of this License, such Author has obtained the necessary waiver from his or her university or institution.

This License must be signed by the Author(s) and, in the case of a Work Made for Hire, also by the Copyright Owners. One Author/Copyright Owner may sign on behalf of all the contributors/owners only if they all have authorized the signing, approved of the License, and agreed to be bound by it. The signing Author and, in the case of a Work Made for Hire, the signing Copyright Owner warrants that he/she/it has full authority to enter into this License and to make the grants this License contains.

1. The Author must please sign here (except if an Author is a U.S. Government employee, then please sign under #3 below):

Author Signature	Print Name	Date
------------------	------------	------

2. The Copyright Owner (if different from the Author) must please sign here:

Name of Copyright Owner	Authorized Signature and Title	Date
-------------------------	--------------------------------	------

3. If an Author is a U.S. Government employee, such Author must please sign below. The signing Author certifies that the Work was written as part of his/her official duties and is therefore not eligible for copyright protection in the United States.

Name of U.S. Government Institution (e.g., Naval Research Laboratory, NIST)

Author Signature	Print Name	Date
------------------	------------	------

PLEASE NOTE: NATIONAL LABORATORIES THAT ARE SPONSORED BY U.S. GOVERNMENT AGENCIES BUT ARE INDEPENDENTLY RUN ARE NOT CONSIDERED GOVERNMENT INSTITUTIONS. (For example, Argonne, Brookhaven, Lawrence Livermore, Sandia, and others.) Authors at these types of institutions should sign under #1 or #2 above.

If the Work was authored under a U.S. Government contract, and the U.S. Government wishes to retain for itself and others acting on its behalf, a paid-up, nonexclusive, irrevocable, worldwide license in the Work to reproduce, prepare derivative works from, distribute copies to the public, perform publicly, and display publicly, by or on behalf of the Government, please check the box below and add the relevant Contract numbers.

☐ Contract #(s) _____ [1, 16, 1]

Figure A.2.: Part of the Journal of Luminescence copyright agreement granting me permission to use paper 2 in my thesis.

A.3. Paper 3

Paper 3 was submitted to the Journal of Luminescence. Fig. A.3 shows the part of the copyright agreement granting me permission to use this paper in my thesis.

Journal author rights

In order for Elsevier to publish and disseminate research articles, we need publishing rights. This is determined by a publishing agreement between the author and Elsevier. This agreement deals with the transfer or license of the copyright to Elsevier and authors retain significant rights to use and share their own published articles. Elsevier supports the need for authors to share, disseminate and maximize the impact of their research and these rights, in Elsevier proprietary journals* are defined below:

For subscription articles	For open access articles
<p>Authors transfer copyright to the publisher as part of a journal publishing agreement, but have the right to:</p> <ul style="list-style-type: none">• Share their article for Personal Use, Internal Institutional Use and Scholarly Sharing purposes, with a DOI link to the version of record on ScienceDirect (and with the Creative Commons CC-BY-NC-ND license for author manuscript versions)• Retain patent, trademark and other intellectual property rights (including research data).• Proper attribution and credit for the published work.	<p>Authors sign an exclusive license agreement, where authors have copyright but license exclusive rights in their article to the publisher**. In this case authors have the right to:</p> <ul style="list-style-type: none">• Share their article in the same ways permitted to third parties under the relevant user license (together with Personal Use rights) so long as it contains a CrossMark logo, the end user license, and a DOI link to the version of record on ScienceDirect.• Retain patent, trademark and other intellectual property rights (including research data).• Proper attribution and credit for the published work.

Figure A.3.: Part of the STAM copyright agreement granting me permission to use paper 2 in my thesis.

A.4. Permission of co-authors

The following includes the permission of all co-authors (in alphabetical order) to use the respective papers in this thesis.

- Paul Barclay see Fig. A.4 and A.5

- Rufus Cone see Fig. A.6 and A.7
- Mohsen Falamarzi see Fig. A.8
- Morgan Hedges see Fig. A.9
- Erhan Saglamyurek see Fig. A.10
- Charles Thiel see Fig. A.11 and A.12
- Wolfgang Tittel see Fig. A.13 and A.14
- Lucile Veissier see Fig. A.15
- Philip Woodburn see Fig. A.16

Re: permission to use papers

Subject: Re: permission to use papers

From: [REDACTED]

Date: 12/4/2017 11:58 AM

To: [REDACTED]

Hi Thomas,

I grant permission.

Paul

On Dec 4, 2017 11:41 AM [REDACTED] wrote:

Hi Paul,

I am just finishing up the last corrections for the thesis. However, I would also need your permission to include the following papers:

- 1) Modification of phonon processes in nanostructured rare-earth-ion-doped crystals
Thomas Lutz, Lucile Veissier, Charles W. Thiel, Rufus L. Cone, Paul E. Barclay, and Wolfgang Tittel
Phys. Rev. A 94, 013801 – Published 1 July 2016
- 2) Effects of fabrication methods on spin relaxation and crystallite quality in Tm-doped powders studied using spectral hole burning
Thomas Lutz, Lucile Veissier, Charles W. Thiel, Philip J. T. Woodburn, Rufus L. Cone, Paul E. Barclay & W. Tittel, Science and Technology of Advanced Materials, Pages 63-70 | Received 26 Sep 2015, Accepted 23 Jan 2016, Published online: 16 Mar 2016
- 3) Effects of mechanical processing and annealing on optical coherence properties of Er³⁺:LiNbO₃ powders, Thomas Lutz, Lucile Veissier, Charles W. Thiel, Philip J.T. Woodburn, Rufus L. Cone, Paul E. Barclay, Wolfgang Tittel, Journal of Luminescence, 2017
- 4) Quadratic Zeeman effect and spin-lattice relaxation of Tm³⁺:YAG at high magnetic fields
Lucile Veissier, Charles W. Thiel, Thomas Lutz, Paul E. Barclay, Wolfgang Tittel, and Rufus L. Cone
Phys. Rev. B 94, 205133 – Published 22 November 2016
- 5) Modification of relaxation dynamics in Tb³⁺:Y₃Al₅O₁₂ nanopowders T. Lutz, L. Veissier, P. J. T. Woodburn, R. L. Cone, P.E. Barclay, W. Tittel, C.W. Thiel
- 6) Efficient and long-lived Zeeman-sublevel atomic population storage in

1 of 2

12/4/2017 11:59 AM

Figure A.4.: Email (part 1) from Paul Barclay granting me permission to publish the papers of which he is a co-author.

Re: permission to use papers

an erbium-doped glass fiber
Erhan Saglamyurek, Thomas Lutz, Lucile Veissier, Morgan P. Hedges,
Charles W. Thiel, Rufus L. Cone, and Wolfgang Tittel
Phys. Rev. B 92, 241111(R) – Published 14 December 2015

7) Optical decoherence and spectral diffusion in an erbium-doped silica
glass fiber featuring long-lived spin sublevels
Lucile Veissier, Mohsen Falamarzi, Thomas Lutz, Erhan Saglamyurek,
Charles W. Thiel, Rufus L. Cone, and Wolfgang Tittel
Phys. Rev. B 94, 195138 – Published 21 November 2016

Could you please send me a brief email granting me permission to use
these in my thesis?

Thank you very much,

Thomas

2 of 2

12/4/2017 11:59 AM

Figure A.5.: Email (part 2) from Paul Barclay granting me permission to publish the papers of which he is a co-author.

RE: permission to use papers in thesis

Subject: RE: permission to use papers in thesis

From: [REDACTED]

Date: 8/30/2017 4:08 PM

To: Thomas [REDACTED]

Dear Thomas,
This email is to grant you permission to use the requested papers which you listed below.
Sincerely,
Rufus

-----Original Message-----

From [REDACTED]

August 30, 2017 4:04 PM

To: Cone, [REDACTED]

Subject: permission to use papers in thesis

Dear Rufus,

I am currently working on my thesis in which I would like to include the papers we wrote together. As you probably know, I require your permission to do that. Specifically, I want to include the following papers:

1) Modification of phonon processes in nanostructured rare-earth-ion-doped crystals Thomas Lutz, Lucile Veissier, Charles W. Thiel, Rufus L. Cone, Paul E. Barclay, and Wolfgang Tittel
Phys. Rev. A 94, 013801 – Published 1 July 2016

2) Effects of fabrication methods on spin relaxation and crystallite quality in Tm-doped powders studied using spectral hole burning
Thomas Lutz, Lucile Veissier, Charles W. Thiel, Philip J. T. Woodburn, Rufus L. Cone, Paul E. Barclay & W. Tittel, Science and Technology of Advanced Materials, Pages 63-70 | Received 26 Sep 2015, Accepted 23 Jan 2016, Published online: 16 Mar 2016

3) Effects of mechanical processing and annealing on optical coherence properties of Er³⁺:LiNbO₃ powders, Thomas Lutz, Lucile Veissier, Charles W. Thiel, Philip J.T. Woodburn, Rufus L. Cone, Paul E. Barclay, Wolfgang Tittel, Journal of Luminescence, 2017

4) Quadratic Zeeman effect and spin-lattice relaxation of Tm³⁺:YAG at high magnetic fields
Lucile Veissier, Charles W. Thiel, Thomas Lutz, Paul E. Barclay, Wolfgang Tittel, and Rufus L. Cone
Phys. Rev. B 94, 205133 – Published 22 November 2016

5) Modification of relaxation dynamics in Tb³⁺:Y₃Al₅O₁₂ nanopowders T. Lutz, L. Veissier, P. J. T. Woodburn, R. L. Cone, P.E. Barclay, W. Tittel, C.W. Thiel

1 of 2

8/30/2017 4:08 PM

Figure A.6.: Email (part 1) from Rufus Cone granting me permission to publish the papers of which he is a co-author.

RE: permission to use papers in thesis

6) Efficient and long-lived Zeeman-sublevel atomic population storage in an erbium-doped glass fiber
Erhan Saglamyurek, Thomas Lutz, Lucile Veissier, Morgan P. Hedges, Charles W. Thiel, Rufus L. Cone, and Wolfgang Tittel
Phys. Rev. B 92, 241111(R) - Published 14 December 2015

7) Optical decoherence and spectral diffusion in an erbium-doped silica glass fiber featuring long-lived spin sublevels
Lucile Veissier, Mohsen Falamarzi, Thomas Lutz, Erhan Saglamyurek, Charles W. Thiel, Rufus L. Cone, and Wolfgang Tittel
Phys. Rev. B 94, 195138 - Published 21 November 2016

Thank you very much,

Thomas

2 of 2

8/30/2017 4:08 PM

Figure A.7.: Email (part 2) from Rufus Cone granting me permission to publish the papers of which he is a co-author.

Hi Thomas,

I am writing this email to give you permission to place the following paper into your thesis.

Optical decoherence and spectral diffusion in an erbium-doped silica
glass fiber featuring long-lived spin sublevels
Lucile Veissier, Mohsen Falamarzi, Thomas Lutz, Erhan Saglamyurek,
Charles W. Thiel, Rufus L. Cone, and Wolfgang Tittel
Phys. Rev. B 94, 195138 – Published 21 November 2016

Cheers,

Mohsen

Figure A.8.: Email from Mohsen Falamarzi granting me permission to publish the papers of which he is a co-author.

Re: permission to use papers in thesis

Subject: Re: permission to use papers in thesis

From: Morgan Hedges [REDACTED]

Date: 7/11/2017 4:10 PM

To: Thomas Lutz [REDACTED]

Yep, of course. Does that mean your submitting by publication? Glad you're getting that thesis thing done in any case. They can sometimes be... unpleasant

Need any proof reading yet? I'd love to find out what you've been up to. Last time I spoke to Charles it sounded like you'd been doing interesting stuff.

Morgan

On Wednesday, July 12, 2017, [REDACTED] :

Hi Morgan,

it has been quite a while. I hope you are doing well.

I am currently working on my thesis in which I would like to include the papers we wrote on the erbium doped fiber. As you probably know, I require your permission to do that. Specifically, I want to include the following paper:

1) Efficient and long-lived Zeeman-sublevel atomic population storage in an erbium-doped glass fiber

Erhan Saglamyurek, Thomas Lutz, Lucile Veissier, Morgan P. Hedges, Charles W. Thiel, Rufus L. Cone, and Wolfgang Tittel

Phys. Rev. B 92, 241111(R) – Published 14 December 2015

Thank you very much,

Thomas

1 of 1

7/11/2017 4:11 PM

Figure A.9.: Email from Morgan Hedges granting me permission to publish the papers of which he is a co-author.

Re: Permission to use papers in thesis

Subject: Re: Permission to use papers in thesis

From: Erhan Saglamyurek [REDACTED]

Date: 7/10/2017 9:23 PM

To: Thomas Lutz [REDACTED]

Hi Thomas,

I give you my permission to use these two publications in your thesis. Good luck with your thesis writing !

with my best wishes,

Erhan

On Mon, Jul 10, 2017 at 3:33 PM, [REDACTED] wrote:

Hi Erhan,

I am currently working on my thesis in which I would like to include the papers we wrote on the erbium doped fiber. As you probably know, I require your permission to do that. Specifically, I want to include the following 2 papers:

1) Efficient and long-lived Zeeman-sublevel atomic population storage in an erbium-doped glass fiber

Erhan Saglamyurek, Thomas Lutz, Lucile Veissier, Morgan P. Hedges, Charles W. Thiel, Rufus L. Cone, and Wolfgang Tittel

Phys. Rev. B 92, 241111(R) – Published 14 December 2015

2) Optical decoherence and spectral diffusion in an erbium-doped silica glass fiber featuring long-lived spin sublevels

Lucile Veissier, Mohsen Falamarzi, Thomas Lutz, Erhan Saglamyurek, Charles W. Thiel, Rufus L. Cone, and Wolfgang Tittel

Phys. Rev. B 94, 195138 – Published 21 November 2016

Thank you very much,

Thomas

1 of 1

7/10/2017 9:40 PM

Figure A.10.: Email from Erhan Saglamyurek granting me permission to publish the papers of which he is a co-author.

Re: permission to use papers in thesis

Subject: Re: permission to use papers in thesis

From: Charles [REDACTED]
[REDACTED]

Thomas,

Yes, of course you have my permission to use all of the papers in your thesis.

Charles

On 8/30/2017 4:03 PM, Thomas Lutz wrote:

Hi Charles,

I am currently (partially) working on my thesis in which I would like to include the papers we wrote together. As you probably know, I require your permission to do that. Specifically, I want to include the following papers:

- 1) Modification of phonon processes in nanostructured rare-earth-ion-doped crystals
Thomas Lutz, Lucile Veissier, Charles W. Thiel, Rufus L. Cone, Paul E. Barclay, and Wolfgang Tittel
Phys. Rev. A 94, 013801 – Published 1 July 2016
- 2) Effects of fabrication methods on spin relaxation and crystallite quality in Tm-doped powders studied using spectral hole burning
Thomas Lutz, Lucile Veissier, Charles W. Thiel, Philip J. T. Woodburn, Rufus L. Cone, Paul E. Barclay & W. Tittel, Science and Technology of Advanced Materials, Pages 63-70 | Received 26 Sep 2015, Accepted 23 Jan 2016, Published online: 16 Mar 2016
- 3) Effects of mechanical processing and annealing on optical coherence properties of Er³⁺:LiNbO₃ powders, Thomas Lutz, Lucile Veissier, Charles W. Thiel, Philip J.T. Woodburn, Rufus L. Cone, Paul E. Barclay, Wolfgang Tittel, Journal of Luminescence, 2017
- 4) Quadratic Zeeman effect and spin-lattice relaxation of Tm³⁺:YAG at high magnetic fields
Lucile Veissier, Charles W. Thiel, Thomas Lutz, Paul E. Barclay, Wolfgang Tittel, and Rufus L. Cone
Phys. Rev. B 94, 205133 – Published 22 November 2016
- 5) Modification of relaxation dynamics in Tb³⁺:Y₃Al₅O₁₂ nanopowders T. Lutz, L. Veissier, P. J. T. Woodburn, R. L. Cone, P.E. Barclay, W. Tittel, C.W. Thiel
- 6) Efficient and long-lived Zeeman-sublevel atomic population storage in an erbium-doped glass fiber
Erhan Saglamyurek, Thomas Lutz, Lucile Veissier, Morgan P. Hedges, Charles W. Thiel, Rufus L. Cone, and Wolfgang Tittel
Phys. Rev. B 92, 241111(R) – Published 14 December 2015

1 of 2

8/31/2017 8:22 AM

Figure A.11.: Email (part 1) from Charles Thiel granting me permission to publish the papers of which he is a co-author.

Re: permission to use papers in thesis

7) Optical decoherence and spectral diffusion in an erbium-doped silica glass fiber
featuring long-lived spin sublevels
Lucile Veissier, Mohsen Falamarzi, Thomas Lutz, Erhan Saglamyurek, Charles W. Thiel,
Rufus L. Cone, and Wolfgang Tittel
Phys. Rev. B 94, 195138 - Published 21 November 2016

Thank you very much,

Thomas

.

2 of 2

8/31/2017 8:22 AM

Figure A.12.: Email (part 2) from Charles Thiel granting me permission to publish the papers of which he is a co-author.

Re: permission to include papers

Subject: Re: permission to include papers

From: [REDACTED]

Date: 12/4/2017 12:58 PM

To: [REDACTED]

Dear Thomas,

I hereby give you permission to include these papers into your thesis.

All the best,
Wolfgang

—

Dr Wolfgang Tittel

[REDACTED]
in Quantum Secured Com
University of Calgary, Canada
<http://www.qc2lab.com>

On Dec 4, 2017, at 11:40, [REDACTED] :

Hi Wolfgang,

I am just finishing up the last corrections for the thesis. However, I would also need your permission to include the following papers:

- 1) Modification of phonon processes in nanostructured rare-earth-ion-doped crystals
Thomas Lutz, Lucile Veissier, Charles W. Thiel, Rufus L. Cone, Paul E. Barclay, and Wolfgang Tittel
Phys. Rev. A 94, 013801 – Published 1 July 2016
- 2) Effects of fabrication methods on spin relaxation and crystallite quality in Tm-doped powders studied using spectral hole burning
Thomas Lutz, Lucile Veissier, Charles W. Thiel, Philip J. T. Woodburn, Rufus L. Cone, Paul E. Barclay & W. Tittel, Science and Technology of Advanced Materials, Pages 63-70 | Received 26 Sep 2015, Accepted 23 Jan 2016, Published online: 16 Mar 2016
- 3) Effects of mechanical processing and annealing on optical coherence properties of Er³⁺:LiNbO₃ powders, Thomas Lutz, Lucile Veissier, Charles W. Thiel, Philip J.T. Woodburn, Rufus L. Cone, Paul E. Barclay, Wolfgang Tittel, Journal of Luminescence, 2017
- 4) Quadratic Zeeman effect and spin-lattice relaxation of Tm³⁺:YAG at high magnetic fields
Lucile Veissier, Charles W. Thiel, Thomas Lutz, Paul E. Barclay, Wolfgang Tittel, and Rufus L. Cone
Phys. Rev. B 94, 205133 – Published 22 November 2016
- 5) Modification of relaxation dynamics in Tb³⁺:Y₃Al₅O₁₂ nanopowders T. Lutz, L. Veissier,

1 of 2

12/4/2017 1:05 PM

Figure A.13.: Email (part 1) from Wolfgang Tittel granting me permission to publish the papers of which he is a co-author.

Re: permission to include papers

P. J. T. Woodburn, R. L. Cone, P.E. Barclay, W. Tittel, C.W. Thiel

6) Efficient and long-lived Zeeman-sublevel atomic population storage in an erbium-doped glass fiber

Erhan Saglamyurek, Thomas Lutz, Lucile Veissier, Morgan P. Hedges, Charles W. Thiel, Rufus L. Cone, and Wolfgang Tittel

Phys. Rev. B 92, 241111(R) – Published 14 December 2015

7) Optical decoherence and spectral diffusion in an erbium-doped silica glass fiber featuring long-lived spin sublevels

Lucile Veissier, Mohsen Falamarzi, Thomas Lutz, Erhan Saglamyurek, Charles W. Thiel, Rufus L. Cone, and Wolfgang Tittel

Phys. Rev. B 94, 195138 – Published 21 November 2016

Could you please send me a brief email granting me permission to use these in my thesis?

Thank you very much,

Thomas

2 of 2

12/4/2017 1:05 PM

Figure A.14.: Email (part 2) from Wolfgang Tittel granting me permission to publish the papers of which he is a co-author.

Re: permission to use papers

Subject: Re: permission to use papers

From: Lucile Veissier [REDACTED]

Date: 12/4/2017 4:12 PM

To: Thomas Lutz [REDACTED]

Thomas,

I give you permission to include the following papers in your thesis:

- 1) Modification of phonon processes in nanostructured rare-earth-ion-doped crystals
Thomas Lutz, Lucile Veissier, Charles W. Thiel, Rufus L. Cone, Paul E. Barclay, and Wolfgang Tittel
Phys. Rev. A 94, 013801 – Published 1 July 2016
- 2) Effects of fabrication methods on spin relaxation and crystallite quality in Tm-doped powders studied using spectral hole burning
Thomas Lutz, Lucile Veissier, Charles W. Thiel, Philip J. T. Woodburn, Rufus L. Cone, Paul E. Barclay & W. Tittel, Science and Technology of Advanced Materials, Pages 63-70 | Received 26 Sep 2015, Accepted 23 Jan 2016, Published online: 16 Mar 2016
- 3) Effects of mechanical processing and annealing on optical coherence properties of Er³⁺:LiNbO₃ powders, Thomas Lutz, Lucile Veissier, Charles W. Thiel, Philip J.T. Woodburn, Rufus L. Cone, Paul E. Barclay, Wolfgang Tittel, Journal of Luminescence, 2017
- 4) Quadratic Zeeman effect and spin-lattice relaxation of Tm³⁺:YAG at high magnetic fields
Lucile Veissier, Charles W. Thiel, Thomas Lutz, Paul E. Barclay, Wolfgang Tittel, and Rufus L. Cone
Phys. Rev. B 94, 205133 – Published 22 November 2016
- 5) Modification of relaxation dynamics in Tb³⁺:Y₃Al₅O₁₂ nanopowders T. Lutz, L. Veissier, P. J. T. Woodburn, R. L. Cone, P.E. Barclay, W. Tittel, C.W. Thiel
- 6) Efficient and long-lived Zeeman-sublevel atomic population storage in an erbium-doped glass fiber
Erhan Saglamyurek, Thomas Lutz, Lucile Veissier, Morgan P. Hedges, Charles W. Thiel, Rufus L. Cone, and Wolfgang Tittel
Phys. Rev. B 92, 241111(R) – Published 14 December 2015
- 7) Optical decoherence and spectral diffusion in an erbium-doped silica glass fiber featuring long-lived spin sublevels
Lucile Veissier, Mohsen Falamarzi, Thomas Lutz, Erhan Saglamyurek, Charles W. Thiel, Rufus L. Cone, and Wolfgang Tittel
Phys. Rev. B 94, 195138 – Published 21 November 2016

Lucile Veissier

On 4 December 2017 at 19:41, [REDACTED] :

Hi Lucile,

So, the day came and I am just finishing up the last corrections for the thesis. I would need your permission to include the following papers:

- 1) Modification of phonon processes in nanostructured rare-earth-ion-doped crystals

1 of 2

12/4/2017 4:20 PM

Figure A.15.: Email from Lucile Veissier granting me permission to publish the papers of which she is a co-author.

Thomas!

I hope you can get it written quickly so you can get a high paying job so the only powder you have to think about is the fresh powder falling from the sky!

Yes you have my permission.

Good luck sir,

Tino

On Wed, Aug 30, 2017 at 4:05 PM, Thomas Lutz [REDACTED] wrote:
Hi Tino,

I hope you are doing well and are enjoying Montana's summer. I am currently (partially) working on my thesis in which I would like to include the papers we wrote together. I require your permission to do that. Specifically, I want to include the following papers:

- 1) Effects of fabrication methods on spin relaxation and crystallite quality in Tm-doped powders studied using spectral hole burning
Thomas Lutz, Lucile Veissier, Charles W. Thiel, Philip J. T. Woodburn, Rufus L. Cone, Paul E. Barclay & W. Tittel, Science and Technology of Advanced Materials, Pages 63-70 | Received 26 Sep 2015, Accepted 23 Jan 2016, Published online: 16 Mar 2016
- 2) Effects of mechanical processing and annealing on optical coherence properties of Er³⁺:LiNbO₃ powders, Thomas Lutz, Lucile Veissier, Charles W. Thiel, Philip J.T. Woodburn, Rufus L. Cone, Paul E. Barclay, Wolfgang Tittel, Journal of Luminescence, 2017
- 3) Modification of relaxation dynamics in Tb³⁺:Y₃Al₅O₁₂ nanopowders T. Lutz, L. Veissier, P. J. T. Woodburn, R. L. Cone, P.E. Barclay, W. Tittel, C.W. Thiel

Thank you very much,

Thomas

Figure A.16.: Email from Philip Woodburn granting me permission to publish the papers of which he is a co-author.

Bibliography

- [1] A. J. Freeman and R. E. Watson, Phys. Rev. **127**, 2058 (1962).
- [2] W. Moerner, ed., *Persistent Spectral Hole-Burning: Science and Applications* (Springer, 2012).
- [3] S. R. Hastings-Simon, M. Afzelius, J. Minář, M. U. Staudt, B. Lauritzen, H. de Riedmatten, N. Gisin, A. Amari, A. Walther, S. Kröll, E. Cavalli, and M. Bettinelli, Phys. Rev. B **77**, 125111 (2008).
- [4] G. Liu and B. Jacquier, *Spectroscopic Properties of Rare Earths in Optical Materials* (Springer Berlin Heidelberg, 2005).
- [5] H. J. Kimble, Nature **453**, 1023 (2008).
- [6] M. A. Nielsen and I. L. Chuang, *Quantum Computation and Quantum Information* (Cambridge University Pr., 2001).
- [7] C. Monroe, Nature **416**, 238 (2002).
- [8] P. W. Shor, SIAM Journal on Computing **26**, 1484 (1997).

- [9] L. K. Grover (1996).
- [10] H.-K. Lo, M. Curty, and K. Tamaki, Nat Photon **8**, 595 (2014). Review.
- [11] L. Chen, S. Jordan, Y.-K. Liu, D. Moody, R. Peralta, R. Perlmutter, and D. Smith-Tone, “Report on post-quantum cryptography”, Tech. rep. (2016).
- [12] W. K. Wootters and W. H. Zurek, Nature **299**, 802 (1982).
- [13] W. Heisenberg, Zeitschrift für Physik **43**, 172 (1927).
- [14] C. Simon, H. de Riedmatten, M. Afzelius, N. Sangouard, H. Zbinden, and N. Gisin, Phys. Rev. Lett. **98**, 190503 (2007).
- [15] N. Sangouard, C. Simon, H. de Riedmatten, and N. Gisin, Rev. Mod. Phys. **83**, 33 (2011).
- [16] R. M. Macfarlane and R. M. Shelby, in *Modern Problems in Condensed Matter Sciences*, vol. 21 of *Spectroscopy of Solids Containing Rare Earth Ions*, A. A. K. a. R. M. Macfarlane, ed. (Elsevier, 1987), pp. 51–184.
- [17] Y. Sun, C. Thiel, R. Cone, R. Equall, and R. Hutcheson, Journal of Luminescence **98**, 281 (2002).
- [18] T. Böttger, C. W. Thiel, R. L. Cone, and Y. Sun, Phys. Rev. B **79**, 115104 (2009).
- [19] R. W. Equall, Y. Sun, R. L. Cone, and R. M. Macfarlane, Phys. Rev. Lett. **72**, 2179 (1994).

- [20] R. L. Ahlefeldt, M. R. Hush, and M. J. Sellars, Phys. Rev. Lett. **117**, 250504 (2016).
- [21] E. Saglamyurek, N. Sinclair, J. Jin, J. A. Slater, D. Oblak, F. Bussieres, M. George, R. Ricken, W. Sohler, and W. Tittel, Nature **469**, 512 (2011).
- [22] E. Saglamyurek, N. Sinclair, J. A. Slater, K. Heshami, D. Oblak, and W. Tittel, New Journal of Physics **16**, 065019 (2014).
- [23] P. B. Sellin, N. M. Strickland, J. L. Carlsten, and R. L. Cone, Opt. Lett. **24**, 1038 (1999).
- [24] V. Lavielle, I. Lorgeré, J.-L. Le Gouët, S. Tonda, and D. Dolfi, Optics Letters **28**, 384 (2003).
- [25] A. I. Lvovsky, B. C. Sanders, and W. Tittel, Nature of Photonics **3**, 706 (2009).
- [26] M. Afzelius, C. Simon, H. de Riedmatten, and N. Gisin, Phys. Rev. A **79**, 052329 (2009).
- [27] F. Bussi eres, N. Sangouard, M. Afzelius, H. de Riedmatten, C. Simon, and W. Tittel, Journal of Modern Optics **60**, 1519 (2013).
- [28] R. H. Dicke, Phys. Rev. **93**, 99 (1954).
- [29] B. Kraus, W. Tittel, N. Gisin, M. Nilsson, S. Kr  ll, and J. I. Cirac, Phys. Rev. A **73**, 020302 (2006).
- [30] F. X. Kaertner, “6.977 ultrafast optics lecture notes”, (2005). Chapter 2.

- [31] P. E. Barclay, “Phys 673 quantum optics lecture notes”, (2014).
- [32] A. Yariv, *Quantum Electronics* (Wiley, 1989), 3rd ed.
- [33] F. Bloch, Phys. Rev. **70**, 460 (1946).
- [34] J. D. Joannopoulos, *Photonic Crystals* (University Press Group Ltd, 2008).
- [35] E. T. Jaynes and F. W. Cummings, Proceedings of the IEEE **51**, 89 (1963).
- [36] A. Szabo, Phys. Rev. B **11**, 4512 (1975).
- [37] C. Thiel, Y. Sun, T. Böttger, W. Babbitt, and R. Cone, Journal of Luminescence **130**, 1598 (2010). Special Issue based on the Proceedings of the Tenth International Meeting on Hole Burning, Single Molecule, and Related Spectroscopies: Science and Applications (HBSM 2009) - Issue dedicated to Ivan Lorgere and Oliver Guillot-Noel.
- [38] J. H. J.J. Zayhowski, D. Welford, *The Handbook of Photonics* (CRC Press, 2006), 2nd ed.
- [39] H. de Vries and D. A. Wiersma, The Journal of Chemical Physics **72**, 1851 (1980).
- [40] N. A. Kurnit, I. D. Abella, and S. R. Hartmann, Phys. Rev. Lett. **13**, 567 (1964).
- [41] W. B. Mims, Phys. Rev. **168**, 370 (1968).
- [42] T. Böttger, C. W. Thiel, Y. Sun, and R. L. Cone, Phys. Rev. B **73**, 075101 (2006).

- [43] R. Orbach, Proceedings of the Royal Society of London. Series A. Mathematical and Physical Sciences **264**, 458 (1961).
- [44] I. Waller, Zeitschrift für Physik **79**, 370 (1932).
- [45] W. Heitler and E. Teller, Proc. R. Soc **155**, 629 (1936).
- [46] M. Fierz, Physica **5**, 433 (1938).
- [47] C. Gorter, P. Teunissen, and L. Dijkstra, Physica **5**, 1013 (1938).
- [48] R. de L. Kronig, Physica **6**, 33 (1939).
- [49] J. H. V. Vleck, The Journal of Chemical Physics **7**, 72 (1939).
- [50] J. H. Van Vleck, Phys. Rev. **57**, 426 (1940).
- [51] R. J. Elliott and K. W. H. Stevens, Proceedings of the Royal Society of London A: Mathematical, Physical and Engineering Sciences **215**, 437 (1952).
- [52] J. Ziman, *Electrons and Phonons* (Oxford, 1960).
- [53] A. Abragam and B. Bleaney, *Electron Paramagnetic Resonance of Transition Ions* (Oxford University Press, 2012).
- [54] L. K. Aminov, I. N. Kurkin, and D. A. Lukoyanov, Applied Magnetic Resonance **14**, 447 (1998).
- [55] M. Veith, S. Mathur, A. Kareiva, M. Jilavi, M. Zimmer, and V. Huch, Journal of Materials Chemistry **9**, 3069 (1999).

- [56] A. A. V. Tucureanu, A. Matei, Opto-Electronics Review **23**, 239 (2015).
- [57] S. Cheng, https://www.ch.ntu.edu.tw/~sfcheng/HTML/material95/Solid_synthesis.pdf.
- [58] M. Liu and D. Xue, Solid State Ionics **177**, 275 (2006).
- [59] H.-S. Yang, S. P. Feofilov, D. K. Williams, J. C. Milora, B. M. Tissue, R. S. Meltzer, and W. M. Dennis, Physica B: Condensed Matter **263**, 476 (1999).
- [60] H.-S. Yang, K. Hong, S. Feofilov, B. M. Tissue, R. Meltzer, and W. Dennis, Journal of Luminescence **83**, 139 (1999).
- [61] G. K. Liu, H. Z. Zhuang, and X. Y. Chen, Nano Letters **2**, 535 (2002).
- [62] B. Mercier, C. Dujardin, G. Ledoux, C. Louis, O. Tillement, and P. Perriat, Journal of Luminescence **119**, 224 (2006).
- [63] K. D. Jahnke, A. Sipahigil, J. M. Binder, M. W. Doherty, M. Metsch, L. J. Rogers, N. B. Manson, M. D. Lukin, and F. Jelezko, New Journal of Physics **17**, 043011 (2015).
- [64] A. Sipahigil, R. E. Evans, D. D. Sukachev, M. J. Burek, J. Borregaard, M. K. Bhaskar, C. T. Nguyen, J. L. Pacheco, H. A. Atikian, C. Meuwly, R. M. Camacho, F. Jelezko, E. Bielejec, H. Park, M. Lončar, and M. D. Lukin, Science **354**, 847 (2016).
- [65] R. A. Serway, R. J. Beichner, and J. W. Jewett, *Physics for Scientists and Engineers* (Brooks Cole, 1999).

- [66] T. Schröder, S. L. Mouradian, J. Zheng, M. E. Trusheim, M. Walsh, E. H. Chen, L. Li, I. Bayn, and D. Englund, *J. Opt. Soc. Am. B* **33**, B65 (2016).
- [67] R. E. Evans, A. Sipahigil, D. D. Sukachev, A. S. Zibrov, and M. D. Lukin, *Phys. Rev. Applied* **5**, 044010 (2016).
- [68] B. Khanaliloo, H. Jayakumar, A. C. Hryciw, D. P. Lake, H. Kaviani, and P. E. Barclay, *Phys. Rev. X* **5**, 041051 (2015).
- [69] J. Jin, E. Saglamyurek, M. I. G. Puigibert, V. Verma, F. Marsili, S. W. Nam, D. Oblak, and W. Tittel, *Phys. Rev. Lett.* **115**, 140501 (2015).
- [70] E. Saglamyurek, J. Jin, V. B. Verma, M. D. Shaw, F. Marsili, S. W. Nam, D. Oblak, and W. Tittel, *Nat Photon* **9**, 83 (2015). Letter.
- [71] E. Saglamyurek, M. Grimaud Puigibert, Q. Zhou, L. Giner, F. Marsili, V. B. Verma, S. Woo Nam, L. Oesterling, D. Nippa, D. Oblak, and W. Tittel, *Nature Communications* **7** (2016). Article.
- [72] T. Böttger, Y. Sun, C. W. Thiel, and R. L. Cone, *Phys. Rev. B* **74**, 075107 (2006).
- [73] W. A. Phillips, *Journal of Low Temperature Physics* **7**, 351 (1972).
- [74] W. A. Phillips, *Reports on Progress in Physics* **50**, 1657 (1987).
- [75] R. J. Silbey, J. M. A. Koedijk, and S. Völker, *The Journal of Chemical Physics* **105**, 901 (1996).

[76] J. L. Black and B. I. Halperin, Phys. Rev. B **16**, 2879 (1977).